University of Strathclyde

Department of Pure and Applied Chemistry

Nanosphere Lithography Fabricated Nanostructures for use in Surface-Enhanced Raman Scattering Biosensing Applications

by

Kirsty Gibson

A thesis presented in fulfilment of the requirements for the degree of Doctor of Philosophy

2012

Acknowledgements

Abstract

The use of plasmonic nanostructures in sensing applications has increased in recent years owing to improved fabrication methods. Reports in the literature have highlighted the great potential of film-over nanosphere (FON) and nanotriangle surfaces as sensitive and reproducible Surface-Enhanced Raman Scattering (SERS) substrates. The relationship between the physical and optical properties of nanostructured arrays is of great importance and it has a significant influence on the SERS enhancement exhibited by the arrays. However, there has been no comparative study on the plasmonic and Raman properties of closely related FON and nanotriangle substrates.

This research details a systematic investigation into the origin of SERS enhancement in a series of nanostructures fabricated via modified nanosphere lithography (NSL). The symbiotic relationship between SERS and plasmonics was exploited by using SERS to probe and evaluate the nanostructured plasmonic surfaces. The relationship between the physical and optical properties of the nanostructures was investigated to understand and determine the optimal structures for use in SERS analysis. The optimal substrates identified for every series investigated were not FON or nanotriangle arrays but instead the closely related film-over etched nanosphere (FOEN) and nanohole arrays which were the result of an etching step in the fabrication process. The transition between nanotriangle and nanohole was studied and the localisation of hot-spots on the structures was identified. Experimental SERS false-colour images showed that in nanotriangle arrays, the electric field was concentrated at the point at which two triangle apexes met. In nanohole arrays, the electric field was greatest on the metal lattice that surrounds the holes. As the diameter of the nanoholes decreased, the electric field was located around the rim of the holes and in nanohole arrays with very small diameters the electric field was concentrated in the centre of the hole. The experimental results were in good agreement with theoretical predications.

Nanohole arrays that were shown to have high SERS activity were used in a proof-of-concept SERS sensing study resulting in the detection of labelled Streptavidin at nanomolar concentrations. This method was then applied to a real-life system to probe the interaction of Aurora A with IKKβ peptides.

Abbreviations

AFM – Atomic force microscopy

CDA – Coupled dipole approximation

CV – Coefficient of variation

D – Aspartic acid

DCM – Dichloromethane

DDA – Discrete dipole approximation

ddH$_2$O – Doubly distilled water

DMF – Dimethyl formamide

DMSO – Dimethyl sulfoxide

D/P – Diameter/periodicity ratio

EDC – 1-Ethyl-3-(3-dimethylaminopropyl)carbodiimide

FDTD – Finite-difference time-domain

FOEN – Film over etched nanosphere

FON – Film over nanosphere

GST - Glutathione *S*-transferase

IgG – Immunoglobulin G

IKK – Inhibitory Kappa kinase

IP – Inter-particle distance

IR – Infra-red

K$_d$ – Dissociation constant

L – Leucine

LSPP – localised surface plasmon polariton

MG – Malachite green

MG ITC – Malachite green isothiocyanate

16-MHA – 16-Mercaptohexadecanoic acid

11-MUA – 11-Mercaptoundecanoic acid

MWCO – Molecular weight cut-off

NA – Numerical aperture

4-NBT – 4-Nitrobenzenethiol

NHS – *N*-hydroxysuccinimide

NP - Nanoparticle

NS – Nanostructure

NSL – Nanosphere lithography

OSR – Outside spectral range

P - Periodicity

PBS – Phosphate buffered saline

PBST – Phosphate buffered saline tween

PEG – Polyethylene glycol

RI – Refractive index

rpm – Rotations per minute

r.t. – Room temperature

S - Serine

SAM – Self-assembled monolayer

SDS – Sodium dodecylsulfate

SERRS – Surface-enhanced resonance Raman spectroscopy

SERS – Surface-enhanced Raman spectroscopy

StreptavidinMG – Streptavidin conjugated to malachite green

sulfoNHS – *N*-hydroxysulfosuccinimide

TA – Thioctic acid

UV-vis – Ultraviolet-visible

W - Tryptophan

WT – Wild type

λ_{ex} – Excitation wavelength

λ_{LSPR} – LSPR wavelength

Units

a.u. – Arbitrary unit

kDa – Kilodalton

℃ – Degree centigrade

counts s^{-1} – counts per second

g – Gram

Hz – Hertz

h – Hour

mM – Millimolar

mg/ml – Milligrams per millilitre

min - Minute

m – Meter

µm – Micrometer

nm – Nanometer

l – Litre

ml – Millilitre

µl - Microlitre

µM – Micromolar

nM – Nanomolar

pM – Picomolar

fM – Femtomolar

N – Newton

MΩ – Megaohm

RIU^{-1} – Refractive index unit

s – Second

W – Watt

mW – Milliwatt

μW – Microwatt

cm^{-1} – Wavenumber

Contents

CHAPTER 1 - INTRODUCTION

The study of the optical properties and applications of metals is an expanding and active research area known as plasmonics. In recent years, there has been great interest in nano-plasmonics which combines the fields of plasmonic and nanoscience by investigating the optical response of metallic structures in the nanometer size regime. This area has generated renewed interest in plasmonics and continues to fascinate researchers with the wealth of applications that have been developed. Nano-plasmonics has found popularity in numerous sensing applications, e.g. localised surface plasmon resonance (LSPR) spectroscopy and surface-enhanced Raman spectroscopy (SERS), due to the high sensitivity offered by these substrates. In parallel with the increase in interest in nano-plasmonics, there has been an increase in the development of fabrication methods that are able to prepare nano-plasmonic structures. Nanosphere lithography (NSL) has shown promise as a cheap, straightforward and reliable method of nanostructure preparation. NSL can be modified to prepare a range of nanostructured substrates which can be tuned to the needs of the desired application. Although several groups use NSL fabricated nanostructures in SERS applications, there has been no systematic study which focusses on the structure-property relationship of these structures with respect to the SERS enhancement. This research details the investigation into the structure-property relationship of a series of nanostructures fabricated by a modified NSL method to determine the optimal structures for use in SERS and to evaluate the potential of these substrates in sensing applications.

1.1 The interaction of plasmons with light

A plasmon has been defined as a "quantum quasi-particle representing the elementary excitations of charge density oscillations in a plasma".[1] The interaction of plasmons with light gives rise to interesting optical phenomena that have been harnessed in wide-ranging applications. When light in the visible or infra-red wavelength range interacts with the free electron plasma of a coinage metal, a plasmon-polariton is generated. The plasmon-polariton, also known as the surface plasmon (SP) is a collective oscillation of the free conducting electrons of the metal. In order to detail the

structure-property relationships in plasmonic materials, it is imperative to understand the properties of plasmons and their interaction with light.

The optical response of a metal is governed by its dielectic function. A surface plasmon can be excited at the surface of metals which possess the right material properties; a metal must have a negative real and small positive imaginary dielectric constant to support a surface plasmon. Both silver (Ag) and gold (Au) have a small negative real value of the dielectric function which allows these metals to support a SP in the visible wavelength range. As a result, these metals are of great interest in plasmonics as their optical response is easily investigated.

Metallic surfaces can support two types of surface plasmon polaritons as illustrated in Figure 1.1.
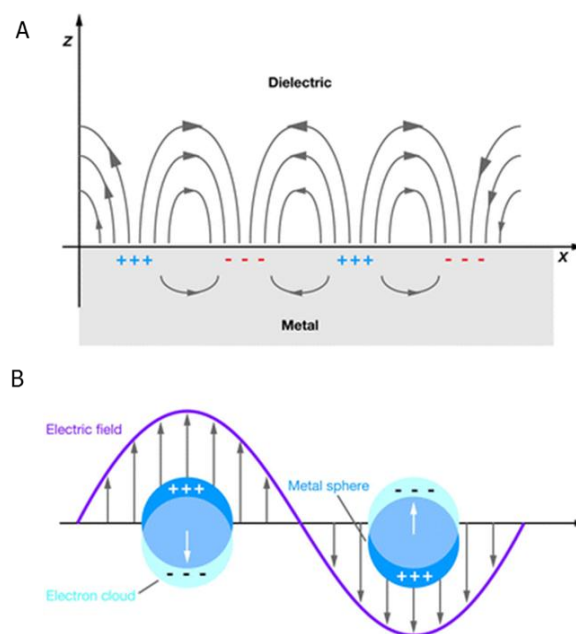
Figure 1.1 - Schematic of A) a surface plasmon polariton and B) a localised surface plasmon.[2]

A propagating surface plasmon oscillates in a coherent manner along the metal-dielectric interface in an *x*-, *y*- direction. This type of plasmon, also known as a propagating surface plasmon polariton (PSPP), occurs in surfaces that are planar over an area larger than the wavelength of the incident light. In theory, PSPP can propagate infinitely in the x- direction. However, in a real metal the surface PSPP is damped by absorption in the metal, decreasing the field intensity and shortening the propagation distance. PSPP have been reported to propagate up to a distance of approximately 40

µm and 150 µm in Au[3] and Ag[3, 4] metal films, respectively, when excited by light in the visible wavelength region.

In planar metallic surfaces, in order for light to couple to a plasmon and excite a PSPP, the momentum and energy of the incident radiation must be conserved. When this occurs, the coupling conditions are met and the excitation of the PSPP can be observed by a resonance peak. The wavelength of the resonance peak, or surface plasmon resonance (SPR), is highly dependent on the incident wavelength, the angle of incidence, the metal film thickness and the dielectric constant of the dielectric material. SPR have narrow bands and are highly sensitive to changes in the dielectric environment.

When electromagnetic radiation interacts with metallic particles that are comparable or much smaller than the wavelength of the incident radiation, a localized surface plasmon polariton (LSPP) arises. This type of plasmon is localized around nanoscale features and is observed in metallic nanoparticles and in surfaces that have nanostructured elements. Efficient coupling between the incident electromagnetic radiation and the plasmon is required to result in excitation of the LSPP which can subsequently be detected by a localized surface plasmon resonance (LSPR). The LSPR is dependent on the same factors as SPR in addition to other parameters e.g. size and shape of metallic particle. Both propagating and localised SPP are sensitive to the local dielectric environment, with PSPP showing higher sensitivity due to sharper resonances, and this trait can be exploited in SPR and LSPR sensing applications.

When the oscillation frequency of the surface plasmon at the metal surface is in resonance with the frequency of the incident radiation, a large enhancement of the local electric field at the metal surface occurs resulting in a large electric field intensity.

Electric field intensity

The electromagnetic energy at a metal-dielectric interface is confined to the surface resulting in large local electric field intensities at this point. The surface electric field inside the metal is parallel to the interface whereas the surface electric field outside the metal is perpendicular to the interface.[1] The intensity of the electric field is higher outside the metal and it is this feature that gives rise to surface-enhanced spectroscopies.

3

1.1.1 Surface Plasmon Resonance (SPR) spectroscopy

Surface plasmon resonance (SPR) spectroscopy is an optical analytical technique used to investigate and evaluate changes in refractive index (RI) at a metal surface. Thin Ag and Au films (50 nm in thickness) support a propagating surface plasmon which is excited by visible light.[5] Direct illumination of the SPP is not possible due to a mismatch of the wavevector of light with the wavevector of the SPP and hence, a failure to meet the coupling conditions, thus, the Kretschmann configuration, illustrated in Figure 1.2, is the set-up most commonly used to achieve resonance between the incident light and the SPP in practical applications.
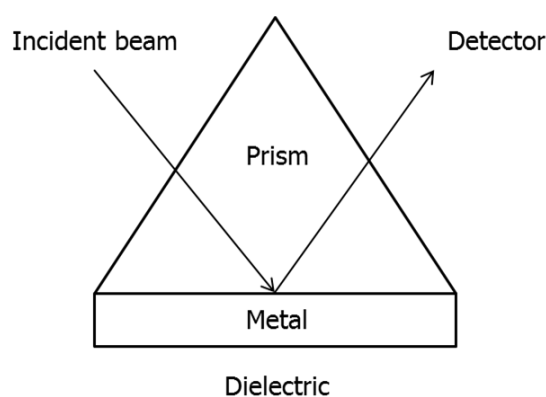
Figure 1.2 - Kretschmann configuration set-up for SPR spectroscopy.

In the Kretschmann configuration, the metal film is evaporated or mounted onto a glass prism. The incident light undergoes total internal reflection in the glass prism and the resulting evanescent wave penetrates the metal film and excites the SPP at the outer face of the metal film. The SPP decays evanescently in the *z*- direction from the metal-dielectric interface over a distance of approximately 200 nm and is therefore very sensitive to changes in the refractive index of the dielectric medium. The RI of the dielectric medium affects the wavelength of light absorbed by the SPP; increasing RI causes red-shifting of the light in resonance with the SPP. Hence, adsorption of molecules at the metal surface can be followed by analysis of the shift in SPP wavelength and the shift observed is proportional to the size/number of molecules adsorbed.[6] This process is shown schematically in Figure 1.3.

The metallic thin film has to be modified with chemical groups or molecules that are selective for the analyte to ensure wavelength shifts are not due to adsorption from the bulk material.
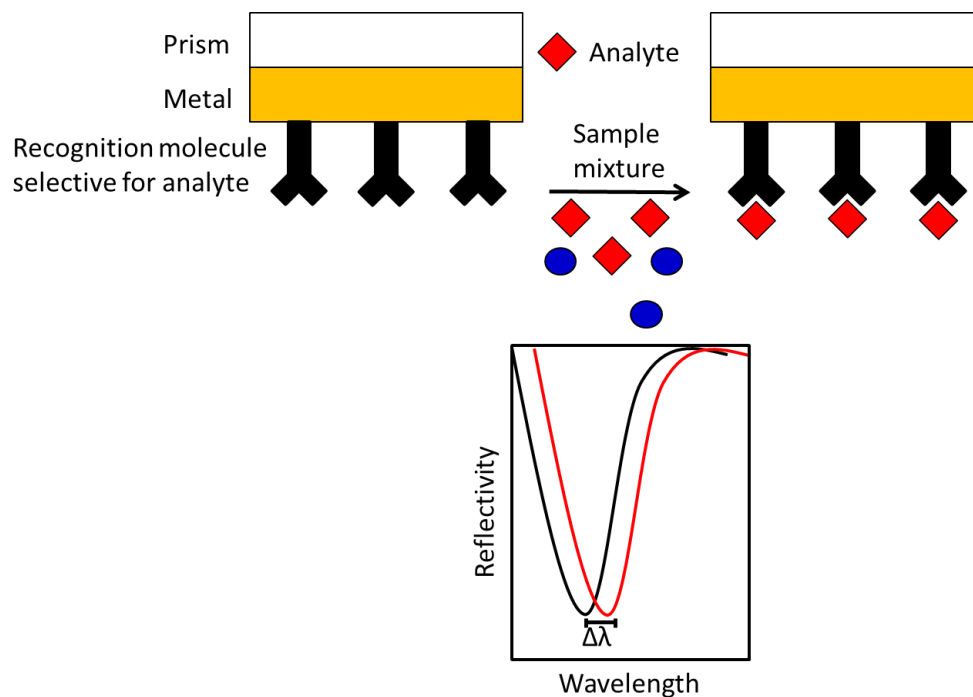
Figure 1.3 - Schematic of SPR spectroscopy

SPR spectroscopy is used to monitor and quantify binding in biological applications, e.g. protein-protein[7] and protein-DNA binding[8], small-ligand screening[9], and to detect the adsorption of chemical species.[10]

1.1.2 Localized surface plasmon spectroscopy (LSPR)

Localized surface plasmon resonance (LSPR) spectroscopy is used to investigate the change in RI of the dielectric at a nanostructured metal surface. It can sensitively detect and quantify changes in the molecular adsorbate layer on the metal surface. Like SPR spectroscopy, the analyte does not have to be tagged with an identifying label to enable detection. LSPR spectroscopy most commonly investigates the wavelength shift of transmitted/reflected light from the metal surface at a constant angle of incidence. LSPR spectroscopy measures the extinction spectra of a sample and can be performed using two-different experimental set-ups depending on the structure of the metal surface. Transmission ultraviolet-visible (UV-vis) spectroscopy, as shown in Figure 1.4A, is used when the metal takes the form of colloidal metallic nanoparticles in

solution or when the metal sample is transparent. Incident light with a wavelength in the UV-vis region illuminates the sample and the light transmitted from the sample is collected and analysed to determine the LSPR wavelength. Identification of the wavelength at which the maximum amount of light was transmitted results in the determination of the LSPR peak. For opaque samples, UV-vis spectroscopy is used in an epi-illumination configuration, as shown in Figure 1.4B, in which a probe fibre bundle is used to both illuminate the sample with incident radiation and collect the light reflected from the surface. The reflected light is analysed and the LSPR is determined by locating the wavelength at which the minimum amount of light was reflected.
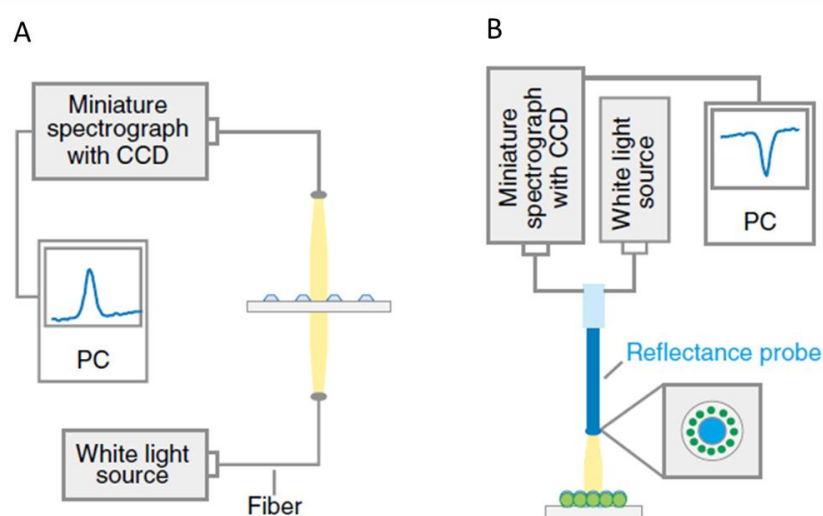
Figure 1.4 –A) LSPR spectroscopy instrumental set-up in transmission (trans-illumination) configuration.[2] B) LSPR spectroscopy instrumental set-up in epi-illumination configuration.[2]

Comparison of the LSPR wavelengths of a bare sample and the same sample after addition of the analyte results in a wavelength shift which is indicative of analyte concentration.

Both SPR and LSPR spectroscopy can afford quantitative measurements and real-time kinetic data for binding events that occur at the metal surface. SPR spectroscopy is more sensitive to changes in the bulk refractive index than LSPR spectroscopy. The electromagnetic field decay length of a LSPR sensor is around 40 times smaller than that of a SPR sensor.[11, 12] This results in LSPR surfaces interrogating smaller sensing volumes than SPR surfaces, leading to more efficient sensing of molecular adsorption processes by LSPR.[13] LSPR sensors can be tuned to a specific wavelength region, from the visible to the infra-red,[14] by controlling the morphology of the nanostructured surface. This provides an additional degree of flexibility in LSPR sensing strategies.

However, both techniques suffer from disadvantages. Only molecules with a molecular weight/size greater than a certain limit can be detected as small molecules do not cause a significant change in RI at the metal-dielectric interface. This can be overcome by conjugation of small molecules to metallic colloidal nanoparticles which dramatically increases the RI change allowing detection to occur. Secondly, it is impossible to confirm if an observed LSPR wavelength shift is a result of binding to the analyte molecule or non-specific binding from the bulk matrix. Both sensing techniques ultimately rely on the surface chemistry to selectively bind the analyte.

1.2 Raman Scattering

When light interacts with a molecule, several optical processes can occur. A molecule can absorb a photon causing an electron to be excited to a higher energy level. If the wavelength of the photon is within the UV or visible range, the electron is promoted to an electronic excited state. If the photon is within the infra-red wavelength range, the electron is promoted to a higher energy vibrational/rotational state in the same electronic energy level. For absorption to occur, the energy of a photon has to match the energy transition between energy levels. The energy of the absorbed photon can be emitted via several mechanisms which ultimately result in the excited electron being relaxed to a lower energy level. Emission of an absorbed photon is known as luminescence; a process in which the emitted photon has the same energy as the incident photon. Fluorescence is the most common form of luminescence in which the emitted photon is of equal or lower energy than the incident photon. The difference in energy between the incident and emitted photon is known as the Stokes shift. A photon can also be emitted by phosphorescence which is a slower process than fluorescence due to the electron undergoing a forbidden singlet to triplet transition. Similar to fluorescence, the emitted photon undergoes a Stokes shift when emitted *via* phosphorescence.

In addition to absorption, a second optical process can occur when light interacts with a molecule. The incident photon can cause distortion of the electron cloud surrounding the nucleus of the molecule resulting in scattering of the photon. Elastic scattering occurs when the scattered photon is of the same energy as the incident photon. This is known as Rayleigh scattering. If the scattered photon is different in energy to that of

the incident photon, the scattering process is known as Raman scattering. The energy of the incident photon does not have to be equal to that of an energy transition for scattering to occur. Instead, the excited electron is promoted to a virtual state which may or may not be equal in energy to that of an electronic, vibrational or rotational energy level. The Raman shift is the change in energy of a photon as a result of the scattering process. A Raman shift corresponds to a vibrational mode of a molecule allowing identification of a vibration in a molecule.

Raman scattering can occur via two mechanisms, Stokes or anti-Stokes scattering, as illustrated in Figure 1.5.

Virtual states

Ground electronic states

n

m

Rayleigh scattering

Stokes scattering

anti - Stokes scattering

$E = h\nu$ $E = h\nu - E_{n-m}$ $E = h\nu + E_{n-m}$
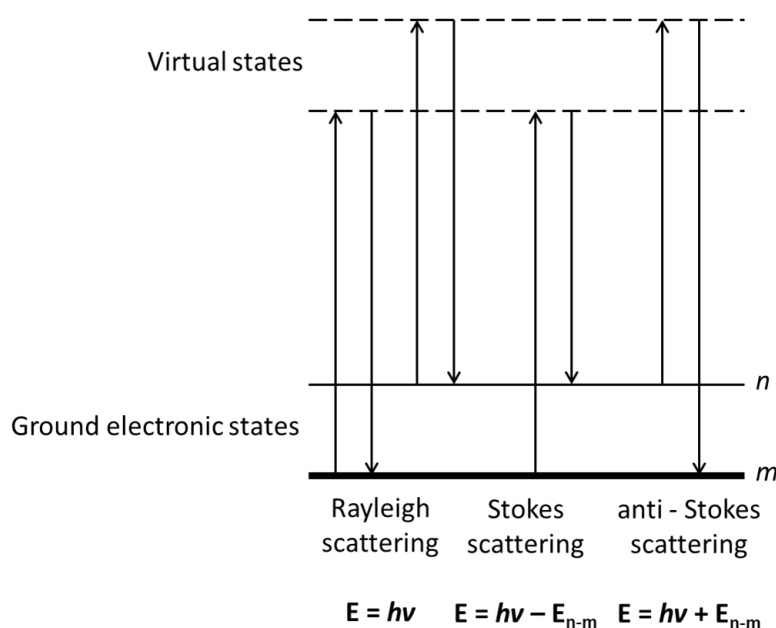
Figure 1.5 - Diagrammatical representation of scattering processes.

Stokes scattering occurs when the incident photon is of higher energy than that of the scattered photon resulting in a positive Raman shift whereas anti-Stokes scattering occurs if the incident photon is lower in energy than the scattered photon and results in a negative Raman shift. Stokes scattering is generally more intense as the majority of the molecules are in the ground state prior to the scattering interaction as predicted by the Boltzmann distribution.[1]

Each Raman-active vibration within a molecule results in a characteristic peak and so Raman scattering is a vibrational spectroscopic technique which gives a characteristic, fingerprint spectrum for the analyte molecule. One of the great advantages of Raman spectroscopy is that water is only weakly Raman active hence does not interfere in the

spectra obtained from molecules in an aqueous environment. This is hugely beneficial in a wide-range of applications, particularly so in the analysis of biomolecules as it allows them to be analysed in biologically-relevant buffers.

Raman scattering is an inherently weak process; at maximum efficiency, only one photon in every ten million undergoes Raman scattering. However, scattering efficiencies can be enhanced by the use of resonance Raman scattering (RRS), surface-enhanced Raman scattering (SERS), or a combination of both these techniques, surface-enhanced resonance Raman scattering (SERRS).

RRS occurs when an electron is excited to a virtual state and the energy transition is in resonance with an electronic transition within the analyte molecule. This results in a resonance contribution toward the Raman enhancement of approximately 10^3 - 10^4.[15]

1.2.1 Surface-enhanced Raman Scattering (SERS)

The Raman scattering enhancement obtained when a molecule is adsorbed onto a roughened metal surface was first observed by Fleischmann and co-workers in 1974.[16] Independent investigations in 1977 by Jeanmaire and Van Duyne[17] and by Albrect and Creighton[18] confirmed this observation. The effect was denoted surface-enhanced Raman scattering (SERS) and it has been shown to enhance the Raman scattering in the order of 10^6 – 10^7 and up to 10^{14} under certain conditions.[19]

1.2.1.1 Enhancement mechanisms

There are two proposed theories that explain the enhancement in Raman scattering observed when a molecule is adsorbed onto a roughened metal surface. Electromagnetic enhancement is postulated to originate from coupling of the incident and Raman scattered photons with the SPP of the roughened metal surface. As discussed in section 1.1, interaction of electromagnetic radiation with a Ag or Au surface generates a SPP which results in an enhanced local electric field at the metal surface. The metal surface has to be roughened at the nanoscale so as to trap the SPP and prevent it from propagating in the *x*-, *y*- direction. The trapped SPP gives rise to intense electric fields localised at the metal surface which enhances the Raman scattering efficiency. As a result of this local electric field, molecules which are adsorbed on or are in close proximity to the metal surface and so within the enhanced

electric field, undergo a large enhancement in Raman scattering. The electromagnetic mechanism is regarded to be the major contributing factor to the SERS enhancement.[20,][21] The second enhancement theory, charge transfer theory, is generally accepted to have a smaller contribution. This theory postulates that when a molecule is chemisorbed onto a roughened metal surface, a new species is formed which can undergo charge transfer from the molecule to the surface and vice versa. The charge-transfer causes resonance-type effects resulting in enhancement of the Raman scattering. The charge-transfer theory requires the analyte to be chemically adsorbed on the metal surface and so does not explain enhancement observed from molecules that are in close proximity to the metal surface. Both theories have undergone thorough fundamental investigation however it is difficult to separate the relative contributions of the electromagnetic mechanism and the chemical mechanism to the overall enhancement. Today, it is generally regarded that the electromagnetic contribution is dominant in the enhancement observed in SERS experiments.

1.2.1.2 SERS experimental considerations

A laser, typically in the visible or near infra-red wavelength region, is used as the incident light source. The laser photons simultaneously excite the LSPR of the SERS substrate and cause Raman scattering to occur within the analyte molecule. The SERS substrate must support a LSPR within the wavelength range of the laser and can take the form of a wide-range of surfaces.[22] Typically Ag or Au metallic colloidal nanoparticles are used but there has been recent interest in the use of ordered 2D or 3D Ag or Au nanostructures.[23] The flexible nature of SERS allows analytes to be in the form of solutions or dried onto a nanostructured surface. The only stipulation is that the analyte molecule must be adsorbed on or in very close proximity (within 10 nm) to the SERS substrate. SERS analysis can be performed using a trans- or epi-illumination set-up. A notch filter blocks the reflected laser photons as these would dominate the SERS spectra if present. A detector collects the scattered photons generating a plot of Raman shift versus intensity, known as a SERS spectrum. The intensity of the scattered photons is dependent on numerous factors and can be varied by controlling the incident laser power, the objective magnification used and the acquisition time of the measurement.

1.2.1.3 SERS distance dependence

An important factor to take into consideration when designing SERS experiments is the effect of the distance between analyte and metal surface on the SERS enhancement. The local enhanced electric field generated by coupling of incident photons with a LSPP originates at the metal-dielectric interface but extends beyond the metal surface. This creates a sensing distance of a few nm from the surface. It is not always practical for analytes to be adsorbed onto the metal surface. The ability to enhance the Raman scattering from molecules that are in close proximity to the metal surface is very important in many experiments. Often, the metal surface can be functionalised with a self-assembled monolayer of molecules designed to provide a specific attachment point for the analyte or improve biocompatibility of the substrate. This results in the analyte not being directly adsorbed. The distance dependence of SERS has been shown to behave according to the relationship shown in equation 1.1[24] where I = intensity of Raman scattering, a = radius of curvature of roughness feature on metal surface and r = distance of molecule from surface.

$$I = \left(\frac{a+r}{a}\right)^{-10}$$

(1.1)

Theory predicts that the intensity of Raman scattering decays as the distance between molecule and surface increases therefore practical consideration of this factor is required when performing SERS experiments.

1.2.1.4 SERS surface selection rule

The effect of the orientation of the analyte molecule adsorbed on the metal surface on the intensity of the SERS enhancement is described by the SERS surface selection rule. The most intense SERS enhancements are observed from vibrational modes within the analyte molecule that are perpendicular to the roughened metal surface.[25]

1.2.1.5 Metal selection

Ag and Au particles and nanostructures can both be used as SERS metals as they support a LSPR in the wavelength regions which corresponds to the most widely used and available laser excitation wavelengths. The use of Ag results in larger SERS enhancements compared to Au as Ag has a more favourable scattering-to-absorbance ratio and is more polarisable than Au.[26] However, Au is less prone to oxidation under

ambient conditions[27] than Ag therefore, there must be a balance between substrate stability and large SERS enhancements.

1.2.1.6 The relationship between LSPR and SERS

As discussed previously, the SERS enhancement is almost exclusively due to coupling between the incident photon and the local electric field at the metal surface. Therefore, the SERS enhancement is heavily dependent on the local electromagnetic field enhancements at the metal surface that occur on excitation of the LSPR by incident radiation. The SERS enhancement has maximised efficiency when the LSPR maximum is closely matched to the laser excitation wavelength.[28] There has been great interest in engineering both the LSPR and the local electric field enhancement of the SERS substrate to result in intense SERS enhancement factors.[29-33]

1.2.1.7 Enhancement Factor (EF)

SERS enhancement factors (EF) are often stated in literature reports to compare the enhancement obtained from different SERS substrates. The EF is defined as the enhancement obtained with respect to what would be obtained under non-SERS conditions (i.e. in the absence of the SERS active substrate) for the same analyte molecule under the same environmental conditions. The EF for a specific SERS substrate or system can be calculated using equation 1.2 where I_{SERS} is the intensity of the SERS signal (usually obtained from the peak height of a characteristic peak), I_{RS} is the intensity of the Raman signal (obtained from the peak height of the same characteristic peak), N_{Surf} is the average number of adsorbed molecules in the same scattering volume for the SERS measurement and N_{Vol} is the average number of molecules in the scattering volume for the Raman measurement ($N_{Vol} = c_{RS}V$ where c_{RS} is the concentration of the analyte and V is the scattering volume).

$$EF = \frac{I_{SERS}}{I_{RS}} \frac{N_{Surf}}{N_{Vol}}$$

(1.2)

The EF is heavily influenced by the local-field enhancements at the substrate and in turn, the local-field enhancement is strongly dependent on the exact position of the probe molecule on the surface which results in highly non-uniform SERS EFs across a surface. This can be overcome by calculating the average SERS EF for a surface. Reports

in the literature have claimed enhancement factors ranging from 10^6 for isolated metallic nanoparticles[34] to 10^8 for dimer nanoparticles[35] and up to 10^{14} for colloidal gold clusters.[19] Often, the relationship between SERS enhancement and reproducibility is inversely proportional to one another and it is important to find a balance between the two for the desired application.

Large EF in the region of 10^{14} can also be achieved through the use of surface-enhanced resonance Raman scattering (SERRS) in which a molecular resonant dye is used as the Raman reporter. SERRS occurs when the dye, which must be in close-proximity to the roughened metal surface, has an electronic transition which is in resonance with the incident radiation resulting in promotion of an electron within the dye molecule to an electronic excited state. Coupling occurs between the chromophore and the local-electric field at the metal surface resulting in large SERS enhancements.[36]

1.2.1.8 Applications

SERS is a sensitive spectroscopic technique that can give molecularly-specific information and can be applied to a variety of analytes. Reproducibility of the SERS enhancement can be problematic and further investigation is on-going to try to remedy this. The direct detection of a wide-range of analytes has been achieved using SERS, e.g. DNA,[37] proteins,[38] viruses,[39] drugs,[40] explosives[41] and water contaminants.[42] Additionally, analytes can be labelled with Raman reporter molecules, often small molecules or dyes, to further aid detection.[43-45] SERS has the ability to be used in the simultaneous analysis of multiple analytes, known as multiplexing, as SERS peaks are narrow and characteristic to a particular molecule.[46] The many multi-disciplinary applications of this technique highlight its potential as an extremely useful analytical technique, especially in the field of bioanalysis.

1.3 Ordered 2D plasmonic nanostructures

Plasmonic nanomaterials can take many forms, from colloidal nanoparticles in solution to highly ordered 1D, 2D and 3D metallic arrays. Figure 1.6 illustrates the form of selected nanomaterials.

| colloidal nanoparticles | 1D highly ordered metal nanoparticle string | 2D highly ordered close-packed nanoparticle array |
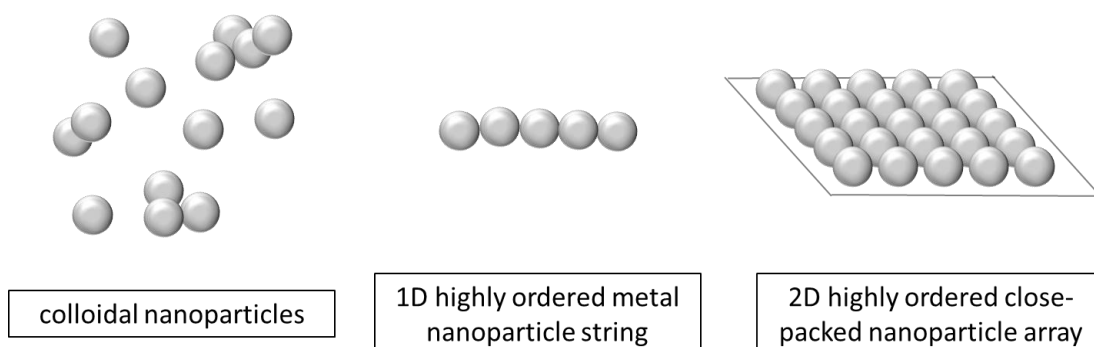
Figure 1.6 - Schematic images of plasmonic nanomaterials.

In recent years, the use of 2D ordered plasmonic substrates in analytical applications has grown.[47-49] In part this is due to a better fundamental understanding of the plasmonic nature of the substrates; however, the development of suitable lithographic fabrication processes has been instrumental in their increased popularity.

1.3.1 Fabrication of ordered plasmonic nanostructures

The fabrication method used to prepare a series of plasmonic nanostructures for research into substrate properties, use in sensing applications or commercialised analysis, should be inexpensive, straight-forward, highly reproducible and possess the ability to fabricate samples in parallel. Ideally, the method should also be easily adapted to alter sample parameters.

1.3.1.1 High-tech lithography methods

Photolithography, which is also known as UV lithography, is a technique often used to fabricate nanostructures.[50] The substrate is coated with a photoresist layer that reacts under irradiation with UV light and marks a pattern onto the substrate surface. The marked areas have a different chemistry to the bare areas and so can be selectively developed to create a nanostructured pattern. The fabrication of multiple samples in parallel can be achieved using photolithography. The main drawback to this

lithographic technique is that it suffers from diffraction-limited resolution that limits feature size to approximately 100 nm. Recent research, however, has demonstrated that this diffraction-limit can be overcome by the use of two excitation sources at different wavelengths.[51]

Focused ion-beam milling (FIB) is a hard lithographic technique that uses Ga^+ ions at a high beam current to mill through the target substrate to create nano-scale features. FIB is a very precise technique that can fabricate high-resolution nanostructures and has been used to fabricate nanohole-type arrays on both Ag and Au substrates.[52, 53]

Electron-beam lithography (EBL) is a commonly used alternative to FIB. The surface is coated with a resist layer that is exposed to a high energy electron beam resulting in the production of the required pattern. Deposition of a metal onto the surface results in metal accumulating in the gaps in the resist. The resist layer is then removed resulting in a surface with nano-patterned metal features. This technique has been employed to fabricate numerous types of nanostructure; Au nanoholes and nanocrescents,[54, 55] Ag nanoparticles[56] and quantum dot nanostructures[57] amongst others.

FIB and EBL are very precise methods of nanostructure fabrication which can create high-resolution defect-free patterns with a high-degree of reproducibility. However, samples cannot be prepared in parallel and both techniques require expensive equipment therefore these methods are not ideally suited to the preparation of nanostructured substrates for use in commercial applications.[58] Recently, research effort has been focussed on the development of lithographic techniques for nanostructure fabrication that are less expensive to run and can be performed in parallel.

1.3.1.2 A low-tech lithography method with excellent potential - Nanosphere Lithography (NSL)

Nanosphere lithography (NSL) was popularised by the Van Duyne group for the fabrication of plasmonic substrates[59] and it is now used extensively for the fabrication of several 2D close-packed nanostructured array formats. It is based on natural lithography, a microfabrication method developed by Deckmann and co-workers.[60] NSL is inexpensive, straightforward and capable of parallel sample preparation.

A schematic of the NSL process is shown in Figure 1.7.
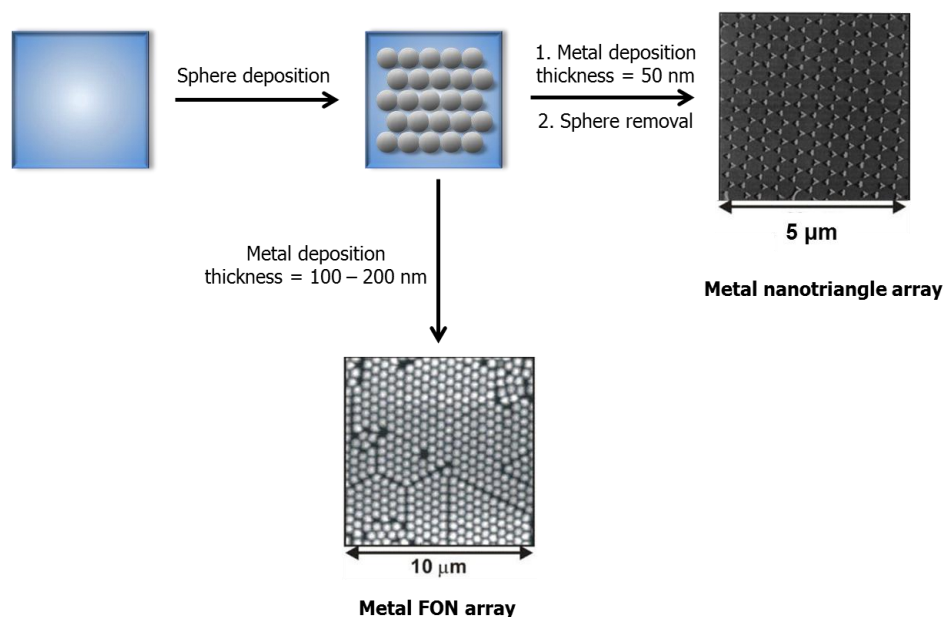
Figure 1.7 - Schematic of NSL procedure to fabricate metal FON array[14] and metal nanotriangle array.[61]

A solution of colloidal spheres is either drop-coated,[62] transferred from a Langmuir monolayer,[63] or spin-coated[59] onto a clean surface. It is essential that the surface is contaminant-free to promote a uniform sphere self-assembly process therefore surfaces are often cleaned in piranha solution prior to use. The deposited nanospheres freely rearrange themselves until they reach their lowest energy configuration. As the solvent evaporates from the substrate surface, capillary forces draw the nanospheres together. The nanospheres then crystallise and form a hexagonal close-packed monolayer. A metal layer is then deposited through the colloidal crystal mask using a physical vapour deposition method at 90° to the surface. The deposition process results in triangular metal prisms being formed in the voids between the colloidal spheres. Removal of the colloidal sphere mask by sonication of the substrates in a suitable solvent results in nanotriangle arrays.[61] If a thicker metal layer is deposited and the spheres are not removed by sonication, a film over nanosphere (FON) array is generated.[64] The diameter (D) of the colloidal spheres used determines the size and interparticle spacing of the nanotriangles and nanospheres.

The process is not perfect; dislocations and defects interrupt the well-ordered structure but it is possible to fabricate large areas of nanostructures (10 - 100 μm²) that are defect-free using this method.[61, 65]

16

NSL is a general fabrication process that can be applied to numerous materials. Glass,[59, 63] silica,[66, 67] mica[67] and indium tin oxide[68] have all been used as substrates onto which the colloidal crystals are assembled. The colloidal masks are usually polystyrene or silica spheres however modified polymers have also been used.[69] A variety of materials have been deposited through the mask to prepare nanotriangle arrays including noble metals,[59] magnetic[70, 71] or semiconductor materials[72] and polymers.[73]

1.3.1.3 Modified NSL to fabricate nanohole arrays

Nanohole arrays can be fabricated using modified NSL which incorporates a reactive plasma etching step of the colloidal spheres before metal deposition, as illustrated in Figure 1.8.

Metal nanohole array
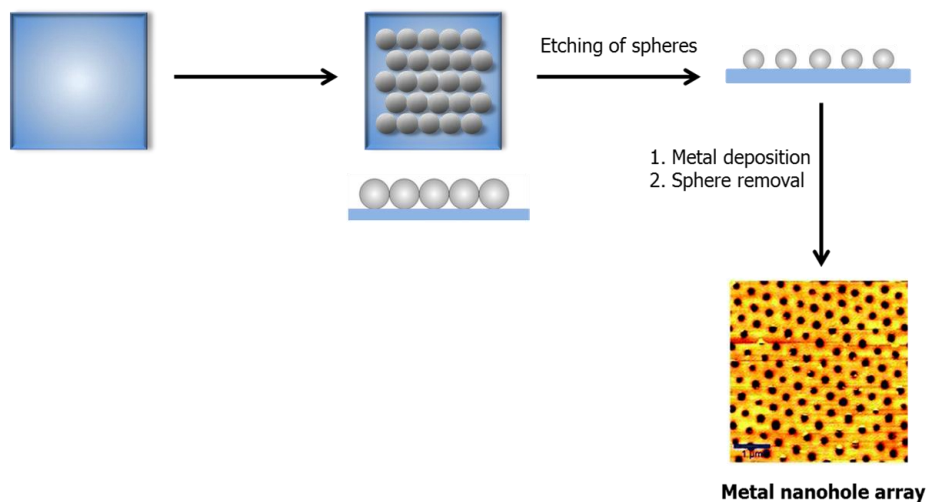
Figure 1.8 - Schematic of modified NSL process to fabricate metal nanohole array.[74]

Masson *et al*. have used a modified NSL method to fabricate nanohole arrays.[63, 74] In this technique, ambient air or oxygen plasma is used to generate ionic species which oxidise the latex spheres on the substrate. This results in spheres which retain the lattice spacing but have a decreased diameter. The diameter of the spheres is easily controlled by monitoring the etch time: the longer the etch time, the smaller the diameter of the spheres. Sonication of the arrays after metal deposition in a suitable solvent results in nanohole arrays. The etch step is an inhomogeneous process which results in rougher sphere surfaces as the etch time increases. This roughness is translated to the inner hole area of the nanohole arrays.

Modified NSL provides a simple method for the preparation of a series of samples with decreasing hole diameter. Using this method, the properties of samples that encompass the transition of nanotriangle to nanohole can be systematically investigated.

1.3.1.4 Other variations on NSL

Variations on the NSL process have been used by many groups to fabricate a plethora of nanostructured surfaces.[59, 63, 66, 75-78]

Modifications to the polymer sphere self-assembly step

Ormonde *et al.* developed a method to decrease defects in the colloidal crystal self-assembled monolayer created by NSL.[75] The method was based on convective self-assembly and was shown to increase the quality and uniformity of the monolayer. Using this method, the authors were able to fabricate a 1 cm² area of hexagonally close-packed nanospheres. Interesting nanostructured arrays can be fabricated using a more concentrated polymer sphere solution.[59] In this case, the spheres self-assemble to form a 2D bilayer structure in which the spheres of the upper layer lie in the depressions formed by the lower layer. Metal deposition occurs through the gaps in the bilayer resulting in metal nanoparticle arrays with one structure per unit cell compared to a nanotriangle array formed from a monolayer of polymer spheres which has two structures per unit cell as illustrated in Figure 1.9A and B.
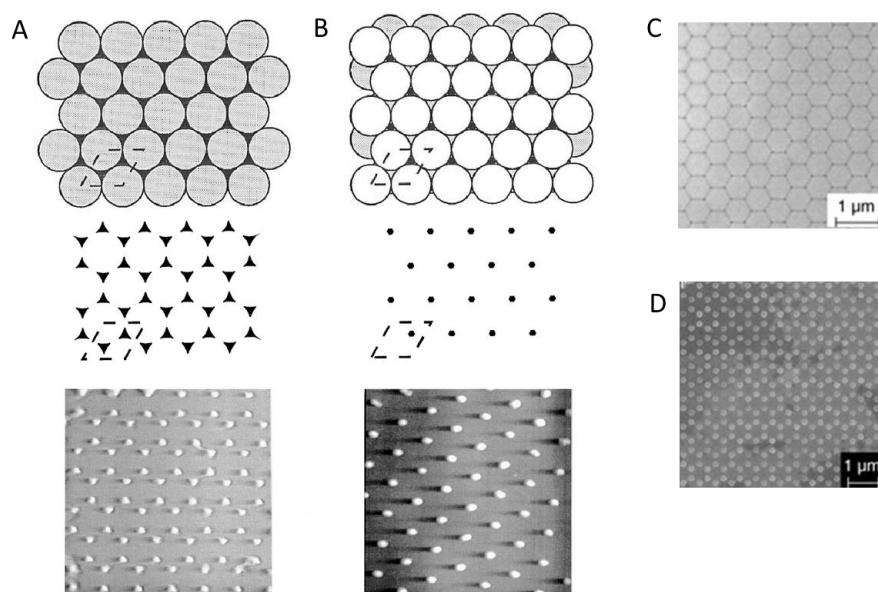
Figure 1.9 – A) Result of NSL using a single layer colloidal crystal mask. [59] B) Result of NSL using a double layer colloidal crystal mask.[59] C) SEM image of polystyrene NSL mask after thermal annealing.[78] D) SEM image of ordered Fe nanorings fabricated by NSL with the inclusion of a thermal annealing step.[78]

A thermal annealing step can be introduced after sphere self-assembly resulting in the apertures between the spheres shrinking and adopting a circular shape as illustrated in Figure 1.9C.[78] As shown in Figure 1.9D, this method has been used to create a well-ordered array of nanorings. As discussed previously, the polymer sphere self-assembly

can be performed on substrates other than glass. Metallic nanopore arrays have been fabricated by Bartlett et *al*[76] using NSL on an Au electrode followed by electro-chemical deposition of the metal layer. Nanopore arrays are prepared on a metal surface and so the entire surface of the pore is metal. This differs from nanohole arrays which are prepared on glass, therefore the base of the hole is glass whilst walls of the hole are metal.

Modifications to the etch step

Triangular nanopore arrays have been fabricated by Whitney and co-workers using a method that combines NSL and reactive ion etching (RIE).[66] Reactive CF_4 plasma was used to etch the exposed Si(111) substrate between the polymer spheres resulting in a well-ordered array of nanopores. A triangular nanopore array was produced after removal of the polymer spheres. It was further demonstrated that by etching the samples at an angle, the in-plane width of the triangular nanopore could be controlled.

Modifications to the metal deposition step

The samples can be tilted at an angle during the metal deposition step. This technique is known as glancing angle deposition (GLAD) and results in different morphologies of the deposited metal depending on the angle used. Masson and co-workers used GLAD to form an array of inter-connected nanotriangles using a deposition angle of 18°, nanohole arrays using a deposition angle of 30° and crossed nanowires at a deposition angle of 45°.[63] A range of nanostructures fabricated by GLAD are shown in Figure 1.10A. Angle-resolved NSL has been used by Haynes *et al*. to fabricate arrays with noteworthy nanoparticle structural motifs. Nanooverlap structures were formed when a second metal deposition was performed at an angle below that of the first deposition, nanogap structures were formed when a second metal deposition was performed at an angle above that of the first deposition and nanochain structures (shown in Figure 1.10B) were formed when more than two metal deposition steps were carried out at varying angles.[77]
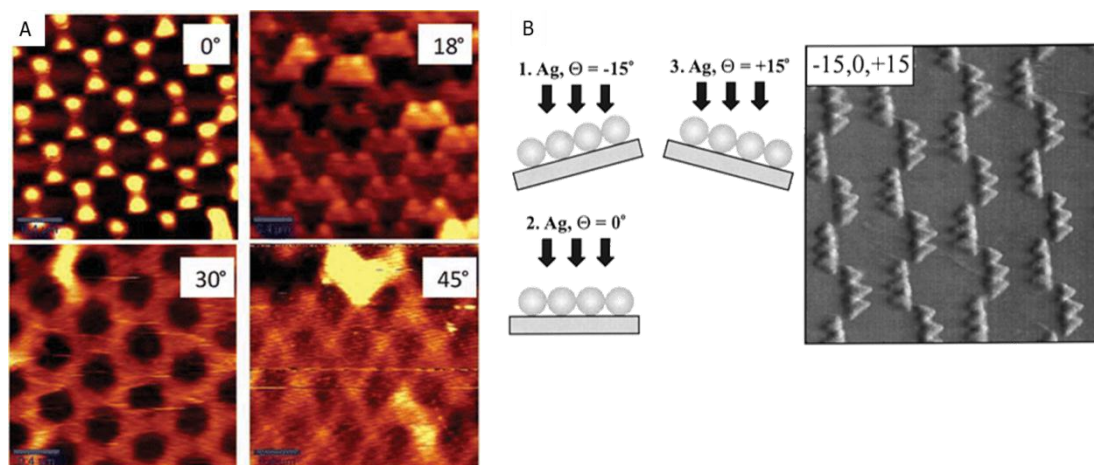
Figure 1.10 - Nanostructures fabricated by NSL with modifications to the metal deposition step A) Nanostructures fabricated using GLAD.[63] B) Nanochains fabricated using angle-resolved NSL. [77]

A combination of mask annealing after self-assembly and shadow NSL, which involves metal deposition whilst rotation of the samples at an angle, has been used by Kosiorek and co-workers to fabricate a wide-range of well-ordered nanostructured arrays including rings, dots and rods.[78]

1.3.1.5 Advantages of NSL as a fabrication technique

NSL is a cheap and facile nanostructure fabrication method. It can easily be performed in a standard lab without the need for expensive equipment, clean-room practices or extensive training. It can produce relatively large areas of defect-free nanostructured surface which is advantageous when compared to alternative fabrication methods. NSL allows samples to be prepared in parallel which lends itself to high-throughput production. FIB and EBL can only produce small areas of nanostructured surface and fabrication cannot be performed in parallel which is inconvenient when developing a high-throughput method of nanostructure fabrication. In addition, FIB is a time-consuming technique and both EBL and FIB require the use of expensive equipment. One of the great advantages of NSL is that there is exquisite control over sample properties. By controlling the diameter of the spheres and the thickness of the metal layer, substrates produced by NSL can be easily tuned to specific parameters. Further control over tuning of the samples can be achieved with modified versions of NSL resulting in tuning of the LSPR from visible to near-IR wavelengths dependent on experimental requirements.[74]

1.4 Substrate engineering for optimal use in sensing applications

The architecture of the nanostructure significantly influences both the LSPR position and the intensity of the electric field at the metal surface. Hence, there has been great interest in understanding the structure-property relationship of 2D ordered nanostructured surfaces.

1.4.1 Tuning the LSPR

In order to design optimal nanostructured materials for SERS sensing applications, fundamental understanding of the properties that govern the LSPR wavelength and the SERS enhancement factor (EF) is required. It is imperative that the effect of nanoparticle size, shape and periodicity on the LSPR wavelength is fully understood. The effects of nanostructure architecture on optical response have been extensively and systematically studied by the Van Duyne group.[79, 80] As discussed earlier, NSL allows the preparation of nanostructured arrays with excellent control of size, shape and periodicity hence, NSL fabricated structures were exploited by Van Duyne and co-workers to investigate the relationship between structure and optical properties.

The effect of size of nanostructures on LSPR wavelength

The effect of size of nanostructure on LSPR was evaluated by Van Duyne and co-workers by varying the in-plane width (labelled as a in Figure 1.11B) and out-of-plane height (labelled as b in Figure 1.11B) of Ag triangular nanostructures.[79] The LSPR red-shifted to longer wavelengths as the in-plane width of the nanostructures increased. Conversely, the LSPR blue-shifted to shorter wavelengths as the out-of-plane height increased. The authors demonstrated that the LSPR could be tuned from 426 to 782 nm, as shown in Figure 1.11A, by controlling the in-plane width and out-of-plane height of the nanostructures.
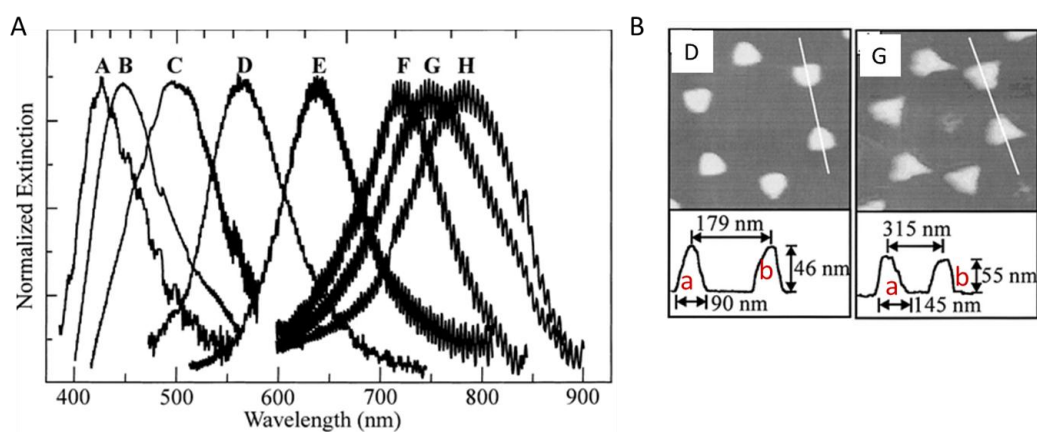
Figure 1.11 [79] - A) LSPR response of a series of Ag triangular nanostructures with different dimensions. B) AFM images and measured dimensions of nanostructures that correspond to LSPR peaks D and G. Labelled distance a represents in-plane width. Labelled distance b represents out-of-plane height.

The effect of shape of nanostructure on LSPR wavelength

It has been documented that different geometrical shapes of colloidal nanoparticle show distinct optical responses.[81] The effect of nanostructure shape on the LSPR peak was investigated by electrochemically oxidising the nanostructures to modify the shape in a controlled manner.[80] Selective oxidation of the triangular nanostructures occurred in the following order after a number of chronocoulometric runs; bottom edges, triangular tips, top face. This resulted in a series of nanostructures with different morphologies that could be utilised to investigate the optical response. It was demonstrated that the LSPR peak underwent a blue-shift as the number of oxidations increased and the sharp edges of the nanostructure were softened as shown in Figure 1.12.
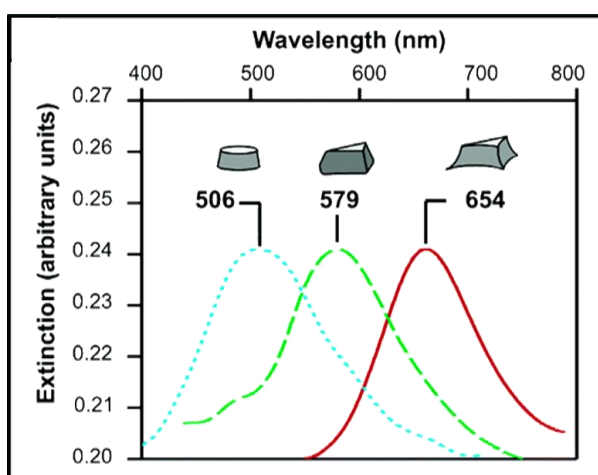
Figure 1.12 - LSPR response of triangular nanostructures that had undergone electrochemical oxidation to alter the shape.[80]

This method was shown to successfully tune the optical response from 654 to 506 nm using colloidal crystals with an initial diameter of 390 nm.

These studies highlight that the size and shape of the nanostructures are instrumental in determining the position of the LSPR peak. By controlling the size and shape of nanoparticles in NSL-fabricated arrays, the LSPR can be tuned from 400 to 800 nm encompassing the entire visible region of the electromagnetic spectrum.[79]

The effect of inter-particle distances on LSPR wavelength

A gap SPP occurs when two metallic particles are brought within close proximity to one another. A coupling occurs between the LSPP of each particle, resulting in a new coupled resonance which is red-shifted and broadened compared to the single particle LSPR. The outcome of this effect is a greatly enhanced electric field intensity.[1] The gap distance between the two particles greatly affects both the LSPR wavelength and the local electric field intensity. 2D nanostructures fabricated by EBL have been used by researchers to investigate the effect of inter-particle distance on LSPR wavelength as EBL allows exquisite control of the inter-particle gap diameter.

El-Sayed *et al.* investigated the effect of an inter-particle gap of between 2 and 212 nm, in Au nanodisc pairs, on the LSPR wavelength.[82] It was shown that on illumination by polarised light along the inter-particle axis, the LSPR red-shifts as the inter-particle distance decreases. This red-shift effect is observed in similar systems and occurs when the inter-particle distance is much smaller than the incident light wavelength due to static dipolar coupling between the particles.[83]

When the inter-particle distance is larger and approaches the wavelength of light, electromagnetic coupling between particles results in more complex behaviour. For inter-particle distances of greater than 200 nm, it was observed by Haynes and co-workers that the LSPR peak blue-shifts as the inter-particle distance decreases.[84] This observation holds true for various shapes and sizes of nanostructure.[85] Computational calculations were in good agreement with the experimental observations. In addition, the computational analyses revealed that the blue-shift of the LSPR peak was due to both radiative dipolar coupling between the particles and retardation effects in which the resonances of the particles are out-of-phase.

The observations, noted by El-Sayed[82] and Haynes[84] were in good agreement with research previously reported by Moerner *et al.* in which the coupling of a single Au

bow-tie nanoantenna with varying interparticle distances was investigated.[86] The bow-tie nanoantenna consisted of two tip-to-tip facing Au nanotriangles with a triangular length of 75 nm and an inter-particle gap distance ranging from 16 – 485 nm. The authors reported that on irradiation by light that was polarized along the inter-particle axis, two distinct LSPR shifts were observed; the LSPR initially blue-shifted as the inter-particle gap distance decreased from 485 to 293 nm followed by a LSPR red-shift as the inter-particle gap decreased under 97 nm. It was also noted that the effect of inter-particle distance on LSPR was dependent on the polarization direction of the incident radiation: when incident radiation polarised perpendicular to the length of the triangles was used, the LSPR demonstrated little dependence on the inter-particle distance. The results from theoretical finite-domain time difference (FDTD) and coupled dipole approximation (CDA) calculations were in agreement with the experimental conclusions.

El-Sayed conducted further research on the effects of inter-particle spacing on the LSPR wavelength and derived a plasmon ruler equation that estimated the inter-particle spacing between two Au nanospheres based on the shift of the LSPR peak.[82] The authors reported good agreement between the inter-particle gaps that were experimentally determined and calculated using the plasmon ruler equation. It was also demonstrated that inter-particle coupling decays via an exponential curve, as shown in Figure 1.13, as the distance between the particles increased.
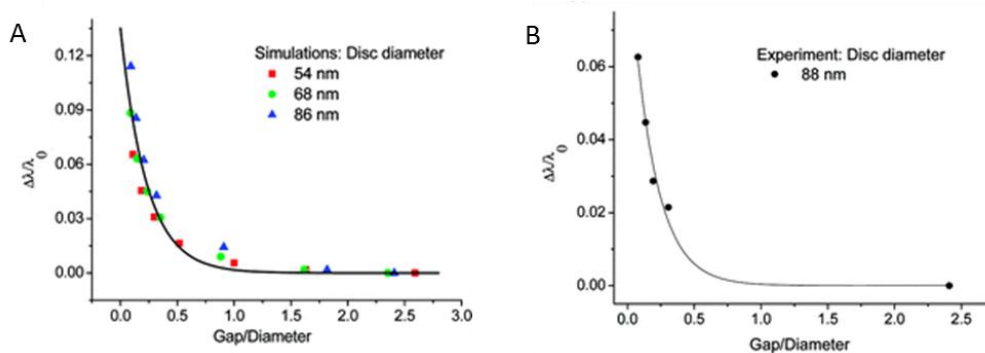
Figure 1.13 [82] - A) Simulated plasmon shift curve for Au nanodisc pair of various diameters. B) Experimental plasmon shift curve for Au nanodisc pair of 88 nm diameter.

From the resulting exponential curves, the decay length was determined to be around 0.2 in units of the particle size. This value was shown to hold true for nanoparticles of different shapes, sizes, metal types and dielectric constant.

1.4.2 Chemical and biosensing using LSPR spectroscopy

The use of nanostructured materials in chemical and biosensing applications is widespread. Again, the work of the Van Duyne group is very prominent in this field.[87-94] Initial biosensing experiments investigated the detection of Streptavidin[95] and anti-biotin[88] on biotin-functionalised nanotriangle arrays. Streptavidin could be detected in the high-femtomolar range using this method which was a significant result. Detection of anti-biotin, an antibody specific for biotin, was achieved in a physiologically relevant buffer which demonstrated the application of this method to biosensing strategies. This method was also applied to the detection of the lectin concanavalin A on mannose-functionalised nanotriangle arrays.[89] This group reported the sensitive and clinically relevant detection of a biomarker for Alzheimer's disease using a sandwich format LSPR assay and initial work reported a limit of detection of 100 fM.[96] This sensing strategy was further developed to detect the biomarker in biological samples highlighting the potential for this application in clinical diagnosis of a variety of diseases which have an associated biomarker and antibody pair.[91] This work demonstrated the first clinical diagnostic application of LSPR sensing. The detection of an electronically resonant molecule by LSPR spectroscopy was established by this group. The researchers showed that adsorption of a molecule with an electronic transition in resonance with the LSPR peak of the substrate resulted in an amplified wavelength shift.[97] This strategy could be used to benefit the detection of small molecules which under normal LSPR conditions cannot be sensed as they do not cause a large enough change in RI.[92] Recently, amplification of the LSPR response has been achieved by detection of surface-bound analytes with antibody-gold nanoparticle conjugates which significantly increases the change in RI at the surface. This method was shown to improve the limit-of-detection by 3 orders of magnitude demonstrating the potential of this method for biosensing applications.[93]

Chemical sensing using LSPR spectroscopy has also been achieved by the Van Duyne group. Modification of nanotriangle arrays with a metal-organic framework material resulted in a porous substrate that could sense carbon dioxide.[94]

The majority of reports of LSPR sensing in the literature are performed on nanotriangle arrays fabricated by NSL. In recent years, LSPR sensing has also been accomplished on alternative ordered substrates. An ordered gold-capped nanoparticle substrate was used by Minh and co-workers for the detection of casein in milk samples.[98] Prostate-

specific antigen (PSA) detection via an enzyme reaction was achieved on Au nanodisc arrays fabricated by nanoimprint lithography.[99] Most recently, Au nanoarrays of varying size and shape fabricated by EBL were used to sense neutravidin by LSPR spectroscopy.[100]

1.4.3 The use of ordered 2D nanostructures in SPR sensing

Ordered 2D nanostructured arrays have been used in SPR sensing applications. Au nanohole arrays prepared using FIB/EBL or soft-nanoimprint[71] lithography have been used as SPR substrates in sensing applications. They have been reported to have a sensitivity to refractive index of around 400 nm/refractive index unit (nmRIU^{-1}) which is comparable to that of other grating-based SPR surfaces but less than that of continuous thin films.[101] Antibodies,[54] IgG[102] and glutathione S-transferase (GST)[103] are amongst the biomolecules detected at nanomolar concentrations on Au nanohole arrays. The sensitivity can be increased by conjugation of the biomolecule to a nanoparticle.[104]

The use of Au nanohole arrays in flow-through SPR sensing is a recent development in the field that benefits from improved transport of the analyte to the activated surface.[105] This may result in lower sample volumes being required for analysis. In-hole detection of Streptavidin has been performed resulting in a smaller sensing area and a lower limit of detection compared to conventional flow-over detection.[106]

The use of nanostructured arrays in SPR sensing highlights the possibility of combined simultaneous analysis by SPR and a second complementary technique, e.g. SERS or surface-enhanced fluorescence. This would be advantageous as more experimental information could be gathered from one sample preparation. Recently, Meyer *et al.* published an experimental set-up capable of performing simultaneous SPR and SERS measurements highlighting the interest in the development of complementary analyses.[107]

1.5 The use of 2D ordered nanostructured arrays as SERS substrates

Ordered metallic arrays have distinct advantages over metallic colloidal nanoparticles and disordered metal structures as SERS substrates. The LSPR of ordered nanostructures prepared by NSL can be easily tuned to be in resonance with the laser excitation wavelength resulting in more efficient coupling between the incident radiation and the SPP of the metallic substrate. Colloidal nanoparticles suffer from aggregation issues and careful optimisation of the conditions is needed to achieve stable particles for each new system under investigation.[108] Metallic nanostructured arrays are supported on a solid substrate and so do not fall prey to unwanted aggregation. In addition, metallic array substrates benefit from straight-forward wash and separation steps. The density of intense local electromagnetic field regions (known as hot-spots) is maximised when the nanostructured features are well organised in a close-packed arrangement.[109] In addition, ordered nanostructures benefit from increased Raman enhancement due to the long-range effect, in which coupling and resulting propagation of LSPP occur over distances between nanoscale features in close proximity to each other.[110]

Metallic FON arrays have been shown to be stable to a range of conditions and so are attractive substrates for SERS analysis. Experiments concluded that these substrates were stable for weeks under standard conditions[29, 111] and retained SERS-activity at high temperatures[112] and large electrochemical potentials.[113] Bare Ag nanostructures are prone to oxidation over extended periods of time however deposition of a thin layer of alumina on top of the structures has been shown to prevent oxidation rendering the substrates stable for months without having a detrimental effect on the SERS activity.[114]

1.5.1 Maximising the SERS enhancement

The local electromagnetic field at the metal surface is the major contributor to the intense signals observed in SERS experiments. Maximisation of the electric field results in optimal SERS enhancement so allowing detection of analytes at lower concentrations. There has been great interest in understanding the factors that affect the local electric field with a view to engineer the nanostructures to obtain maximum

SERS enhancement. Comparison of EF values between substrates allows determination of the factors which have the greatest effect on the local electric field at the metal surface and, in turn, the SERS enhancement.

The effect of nanostructure feature size on SERS EF

The effect of feature size on the magnitude of the electric field was simulated using FDTD calculations by Dhawan and co-workers.[115] They modelled the electric field around dimers of metallic nanospheres. Au nanospheres with a diameter of 20 nm were evaluated to have a SERS EF of 10^3 whereas nanospheres with a diameter of 70 nm were calculated to have a SERS EF of 10^6 highlighting that the electric field enhancement is strongly influenced by the size of the nanostructured feature. This effect has also been observed experimentally in Ag hole arrays with a diameter range of 170 to 400 nm in which the SERS EF increased with increasing hole diameter.[116]

The effect of inter-particle (IP) distance on SERS EF

The electric field enhancement observed from a SERS-active nanostructured surface is known to be strongly influenced by the inter-particle distance between nanostructured features. Optimisation of the inter-particle distance is required to achieve substrates with the best possible EF. The effect of inter-particle spacing on the electric field enhancement in nanosphere dimers was investigated using FDTD simulations.[115] Simulations revealed the SERS EF decreased by a factor of 3.0 for Ag arrays and 4.3 for Au arrays as the inter-particle gap increased from 2.5 to 20 nm.

Bow-tie particles and arrays fabricated by EBL are useful structures for the experimental and theoretical investigation of the effect of gap distance on SERS enhancement as the inter-particle spacing can be easily controlled. A practical investigation by Hatab and co-workers demonstrated that EF decreased as the inter-particle distance increased highlighting that the optimal structures result when nanoparticles are in very close proximity.[30] The EF from an isolated bow-tie structure and a bow-tie array were shown to be 2×10^{11} and 7×10^{11} respectively. The authors attributed the increase in EF in the bow-tie array substrate to the presence of collective interactions between the individual bow-tie structures. They concluded that the maximum EF was achieved when the periodicity of the arrays matched the laser excitation wavelength. The optimum inter-particle distance determined from this work was 8 nm however, the fabrication method did not allow inter-particle distances of less than 8 nm therefore further research is needed to investigate the optimal gap distance.

The conclusions drawn from the experimental investigation conducted by Hatab and co-workers were in agreement with theoretical results from FDTD calculations performed by several groups.[117, 118] As bow-tie arrays resemble nanotriangle arrays to a high extent, insights gained from the investigation of bow-tie arrays can be applied to determining the optimal structure for nanotriangle arrays.

The effect of inter-particle distance was also investigated using an array of Ag semishells prepared by modified NSL.[31] It was observed that as the interparticle distance increased from 0 to 340 nm, the SERS EF decreased from 1.18×10^5 to 4.6×10^4. These results were in agreement with theoretical simulations based on similar structures[119] and with the general trend observed both experimentally and theoretically when similar experiments were conducted with bow-tie arrays. It is interesting to note that the optimum EF observed in the Au bow-tie array investigation was almost 6×10^6 times that observed in the Ag semisphere investigation.

Experimental investigation and theoretical simulations on a variety of nanostructured substrates has demonstrated that the highest electric field enhancement occurs when the gap between the nanostructured features is minimal. This highlights that the inter-particle distance is a major factor in the electric field enhancement of nanostructured substrates.

The effect of metal thickness on SERS

The effect of the thickness of the metal layer in AuFON arrays was investigated by Astilean *et al.*[29] The deposited metal layer was not thick enough to join the Au triangular islands resulting from metal deposition in the interstitial regions and the Au hemisphere layer. Therefore, in these particular substrates two spatially separate metallic gratings exist which increases the complexity of the optical response. The authors demonstrated that the SERS intensity was dependant on both the deposited metal thickness and the excitation wavelength for a set diameter of sphere. At 532 nm excitation, a deposited gold layer of 15 nm was shown to give the best SERS response whilst a 30 nm layer gave the highest SERS intensity at 633 nm excitation. At 830 nm excitation, a deposited metal layer of 60 nm demonstrated the highest SERS enhancement. The authors concluded that further research is needed to fully understand the optical properties of these complex nanostructured films.

It is clear that the size and shape of the nanostructures and the inter-particle distance influence the magnitude of the electric field and thus the achievable SERS EF to differing degrees.

1.5.1.2 Relating SERS EF and LSPR

Efficient coupling between the incident radiation and the LSPR is required to give rise to a strong electric field at the metal surface. Maximum SERS EF occur when the incident radiation and LSPR are in close resonance with one another. Numerous studies have been published investigating the relationship between LSPR wavelength and SERS EF. Aussenegg *et al*. demonstrated that maximum SERS enhancement was achieved when the LSPR was positioned exactly mid-way between the laser excitation wavelength and the wavelength of the Raman scattered photons.[120] This observation was further investigated by Van Duyne and co-workers using NSL-fabricated nanotriangle arrays.[32] Wavelength-scanned surface-enhanced Raman excitation spectroscopy was used to establish the excitation wavelength that resulted in maximum SERS intensity in a series of samples. The SERS EF was shown to vary by 3 orders of magnitude over the 500 nm spectral window investigated. It was concluded that the maximum SERS enhancement was observed in all samples when the λ_{ex} was blue-shifted with respect to the LSPR resulting in location of LSPR λ_{max} between λ_{ex} and λ_{vib}. Under these conditions, both incident and scattered photons are enhanced by the LSPR. This concept has been clearly illustrated in work by Wallace *et al*. who investigated the SERS EF of EBL-fabricated Au nanohole and nanodisc arrays with respect to the diameter of the nanostructured features.[121] When the gap spacing was maintained, the SERS enhancement increased with increasing nanohole diameter. The maximum SERS EF obtained at 785 nm excitation was for nanohole array which supported a LSPR at 790 nm. Therefore, the incident radiation was blue-shifted with respect to the nanostructure LSPR which was in agreement with the conclusions of Aussenegg and Van Duyne.[32, 120] The authors postulated that the increase in enhancement was due to the nanohole LSPR being better matched to the excitation wavelength highlighting that the magnitude of the electric field is heavily dependent on the LSPR.

1.5.2 Localised areas of high electric field enhancement

It is well-recorded that nanostructures have areas in which the local electric field enhancement is more intense than other areas. Generally, the sharp corners of nanostructures have been shown to generate a higher electric field as a result of the lightning rod effect.[122] Intense regions of electric field also arise as a result of coupling of gap SPPs between two metallic nanoparticles in close proximity. These areas of intense electric field have come to be known as hot-spots. The ability to predict the location of hot-spots in SERS substrates is hugely beneficial. Locating the analyte in the hot-spot areas should, in theory, result in more intense Raman scattering. This is especially important in single-molecule SERS detection.[123] There have been many studies published reporting the investigation into hot-spots in colloidal aggregates [124, 125] however less research has concentrated on hot-spot locations on SERS active nanostructures.

1.5.2.1 Predicating the location of hot-spots using simulations and modelling

The majority of the research in this area has focussed on the hot-spot location in dimer nanostructures due to their ease of modelling. The discrete dipole approximation (DDA) was employed to investigate the electric fields in Ag triangular prism dimer particles.[126] The greatest electric field enhancements were calculated to be at the point where the two prisms almost meet when excited at a wavelength in resonance with the LSPR. This observation has been corroborated in the literature.[127] This study was expanded by Lagugné-Labarthet *et al.* to investigate the electric field distribution in a hexagonal array of Au nanotriangles.[128] FDTD simulations demonstrated that the maximum electric field was localised at the vertices of the triangles as shown in Figure 1.14A. The authors noted that the electric field distribution was dependent on the irradiation wavelength and polarisation direction. It was concluded that a collective interaction between the nanotriangles in the array was responsible for the localisation of the electric field enhancement. The plasmon localisation on nanohole arrays has been investigated by Lee *et al.*[129] FDTD simulations predicted that the highest electric field was localised around the rim of the nanoholes as shown in Figure 1.14B.
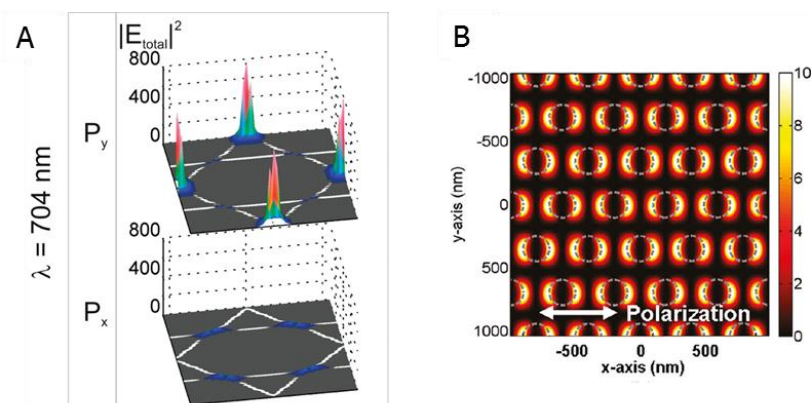
Figure 1.14 - Electric field simulations about A) Au nanotriangle array [128] and B) Ag nanohole array [129]

1.5.2.2 Experimental determination of hot-spot locations in nanostructured surfaces

Plasmon mapping of 2D nanostructures can correlate theoretical predications of the hot-spot localisation on nanostructures with experimental evidence. Electron energy-loss spectroscopy (EELS) has been used by several groups to experimentally map plasmon locations on single nanoparticles[130, 131] however this technique has not been well-utilised on 2D ordered nanostructured arrays. Maier *et al.* used EELS to map the plasmon location on Au bow-tie dimer and trimer structures.[132] The results, shown in Figure 1.15A, highlighted that plasmon hybridizations were located at the almost-touching triangle vertices and so were in good agreement with theoretical predications carried out on similar structures.
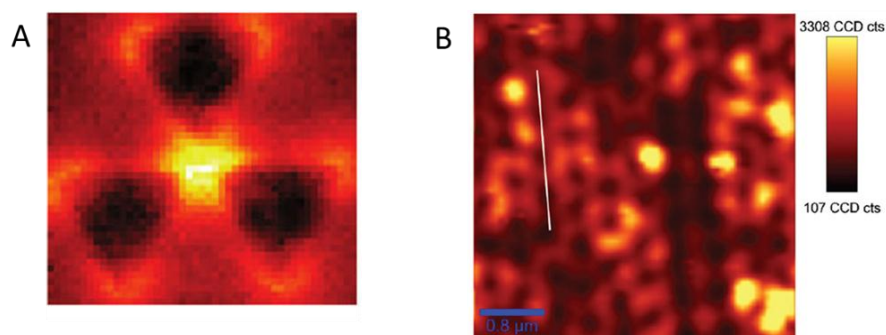
Figure 1.15 – A) Experimental integrated EELS signal map, over the range of 1.6 – 1.7 eV, of Au triangle trimer showing high regions of plasmon hybridization.[132] B) False colour SERS map of AuFON substrate showing regions of greater SERS intensity around the nanospheres.[133]

Hot-spot locations in Ag and Au nanotriangle arrays have been indirectly experimentally determined by Galarreta and co-workers.[134] This elegant approach used a photosensitive polymer film which upon irradiation at 532 nm, undergoes

deformation as a result of hot-spot excitation by the incident radiation. The deformation of the polymer was then imaged by atomic force microscopy (AFM) analysis. As predicted by calculations, the electric field was concluded to be most intense at the vertices of the nanotriangles.

Raman microscopy is a powerful experimental tool for visualising the hot-spot locations on nanostructures however only a handful of studies on this subject have been reported. It was first accomplished by Mirkin *et al.* who demonstrated that the areas of high SERS intensity on gapped nanowire substrates were in agreement with the predicted hot-spot locations.[135] Au[133] and AgFON[136] array substrates prepared by NSL have been analysed by Astilean and Farcau using scanning confocal SERS microscopy to investigate the lateral variations in SERS enhancement across the sample surface. The arrays consisted of polystyrene spheres of 450 nm diameter covered with a 100 nm Au or Ag layer. Figure 1.15B shows a false colour Raman map of a Au FON array. SERS enhancement was observed from the metal lattice surrounding the covered sphere with little enhancement resulting from the sphere itself. The SERS maps obtained were correlated with topographical information collected from AFM analysis. The authors identified two types of SERS enhancement; firstly, enhancement that originated from the metal lattice and had moderate intensity and secondly, randomly distributed intense SERS hot-spots.[136] This demonstrated that the overall SERS EF is a result of two magnitudes of electric field. Raman mapping has also been used to visualise hot-spots in Au nanogap arrays.[137] On excitation at 514.5 nm, the arrays showed a well-ordered square array pattern of high SERS intensity. Comparison of the SERS false colour maps and white light images suggested that the enhancement originated from the edges of the nanogaps. The areas of high SERS intensity were calculated to have EF in the region of $2x10^5$.

Raman mapping is a powerful imaging tool that can be used on a wide-range of substrates however, despite its potential, there have been few reports in the literature detailing the use of Raman mapping to visualise areas of intense electric field in ordered nanostructure arrays.

1.5.2.3 The use of ordered metallic arrays in SERS sensing applications

The use of colloidal nanoparticles in SERS analysis is ubiquitous and they are used in a wide-range of sensing applications.[138-141] However, advances in fabrication methods

34

and understanding of ordered SERS nanostructures have led them to being used in an increased number of chemical and biosensing SERS applications.

The development of SERS based detection using AgFON substrates has been championed by Van Duyne. In addition to high hot-spot density and ease of optical property tuning, metal FON substrates have a large surface area for analyte adsorption which makes them very effective SERS active substrates. His group have achieved rapid detection of anthrax spores below the anthrax infectious dose limit using a portable Raman spectrometer.[142] Addition of a sub-1 nm alumina over-layer by ALD to the AgFON substrates resulted in shorter analysis times and improved substrate stability.[143] The detection of the chemical warfare agent half-mustard has also been achieved using AgFON substrates highlighting the potential application for this class of substrate in real-life biological and chemical warfare agent sensing.[144] Van Duyne *et al*. demonstrated the use of AgFON substrates for *in-vivo* glucose monitoring in rats.[145] An AgFON chip was subcutaneously implanted and used to monitor the glucose concentration in the interstitial fluid by SERS. A mixed SAM was used to partition the glucose from the interstitial fluid and position it in close proximity to the SERS active surface. The SERS data collected correlated well with data obtained from the standard electrochemical measurements which were collected simultaneously. This research demonstrated the first *in-vivo* application of SERS.

AgFON substrates have also been utilised by other groups for biological and chemical SERS sensing applications demonstrating the great potential of this class of substrate.[146, 147] Liu and co-workers have developed a liposome-mediated immunoassay procedure in which the product from the liposome rupture was adsorbed onto an AuFON substrate and quantitatively detected by SERS.[148]

The effect of the distance between molecule and metallic nanostructure was probed by the Van Duyne group using atomic layer deposition (ALD) to create very thin multilayers of Al_2O_3 on top of AgFON substrates.[14] The use of ALD allowed precise deposition of the spacer layers with a thickness resolution of 3.2 Å. The results clearly demonstrated that an increase in distance between the analyte molecule and the metallic surface dramatically decreased the observed SERS intensity. However, it was also shown that SERS is a long-range effect and a SERS signal could still be detected when the molecule was almost 5 nm from the surface. It was calculated that a distance

of 2.8 nm between molecule and surface would decrease the SERS intensity by a factor of 10.

SERS sensing has also been achieved by numerous other groups on alternative ordered nanostructured substrates. Arrays of Ag nanorods have been used in the rapid and sensitive trace detection of viruses by SERS.[39] This class of substrate has a very large surface area and demonstrated highly reproducible SERS signals across samples. The detection of unlabelled Streptavidin on biotin-functionalised Au nanotriangle arrays by SERS was demonstrated by Galarreta and co-workers.[149] The local enhancement generated from the nanotriangles allowed the detection of vibrational signals from Streptavidin using short acquisition times. This work highlighted the use of nanostructured ordered arrays in molecular recognition applications. A field-portable SERS sensing system has been designed for chemical sensing of contaminants in doped ground-water samples.[150] The device used Au bow-tie arrays fabricated by EBL as the SERS active surface. Initial reports indicated that this device may be developed for field use however further work is required to improve the sensitivity before commercial applications can be exploited.

EBL-fabricated Au nanohole arrays have been used to probe protein orientation on bare and charged nanohole array surfaces using SERS.[151] Au nanocanals with AuNP that adhere to the canal inner walls have been designed by Tsukruk *et al*. and used for the detection of trace amounts of 2,4-DNT.[152] These 3D structures have a very large surface area available for hot-spot formation and analyte adsorption resulting in good sensitivity.

Biosensing using Au sphere segment void arrays has been applied to DNA research by Bartlett *et al*.[153] This proof-of-concept work showed that it was possible to discriminate between mutated versions of the same double stranded DNA at very low concentrations by SERS. These SERS active surfaces can also be used in electrochemical analysis leading to possible complementary analyses on the same sample.[153, 154] The commercially available substrate Klarite has also been used in DNA biosensing.[155] The hybridisation of dye-labelled single-stranded DNA to a single-stranded DNA-functionalised Klarite surface could be monitored by SERS. The authors reported good sample-to-sample reproducibility using this method.

Ordered nanostructured surfaces have found use in numerous other fields of analysis. Nanohole arrays have been used in optics,[156] photovoltaics[157, 158] and AFM applications.[159] Nanohole and nanotriangle arrays have been used in surface-enhanced fluorescence techniques.[160] [161]

Several plasmonic ordered nanostructured substrates have been used in SERS based biosensing applications; metal FON arrays in particular have shown great potential as sensitive SERS active substrates. However, with further optimisation, it may be possible to engineer ordered nanostructured substrates for the SERS detection of analytes at increasing levels of sensitivity and reproducibility.

1.6 Research Aims

NSL fabricated nanostructures have been used in the detection of many types of biomolecule. The ease of fabrication makes NSL fabricated substrates ideal for utilisation in sensing applications. There has been much research conducted into the physical and optical characterisation of Ag and Au nanotriangle and FON arrays. However substantially less research has been carried out on Ag and Au nanohole arrays. In addition, there have been no reports in the literature discussing the fabrication or use of film over etched nanosphere (FOEN) arrays. These arrays, prepared by modified NSL, are analogous in structure to FON arrays. Therefore, the optimal structure for SERS enhancement in the nanotriangle/nanohole and FON/FOEN series is still unknown.

This thesis details the investigation into NSL fabricated nanostructures for use as SERS substrates. The aim of this research was to:

- Fully characterise a series of FON/FOEN and nanotriangle/nanohole array substrates by physical and optical methods and investigate the Raman properties of these substrates to determine which factors exerted a strong influence on the Raman enhancement. The optimum nanostructures for use in SERS analysis were to be determined.
- Determine the regions of high electric field on the substrates using Raman microscopy.
- Investigate the use of substrates which exhibited high SERS enhancements in biosensing applications.

CHAPTER 2 - INVESTIGATION INTO THE PHYSICAL, OPTICAL AND RAMAN PROPERTIES OF ORDERED NANOSTRUCTURES PREPARED BY MODIFIED NSL

The aim of this research was to fully characterise the physical and optical properties of metal film over etched nanosphere (FOEN) and nanohole arrays and to determine the relationship between these properties and the observed Raman enhancement. Metal film over nanosphere (FON) and nanotriangle arrays have shown high Raman amplification in numerous applications.[142, 145, 146, 149] Modified NSL allows the preparation of a series of samples with identical periodicities but decreasing nanostructure feature diameters. The intention of this work was to determine the effect of etching the samples on the Raman enhancement. There has been no systematic study performed on nanostructures prepared by modified NSL and so optimum structures for Raman analysis have not been identified.

2.1 Experimental

2.1.1 Fabrication of FOEN and nanohole array substrates by modified nanosphere lithography (NSL)

All samples were prepared by collaborators in the Masson group at the Université de Montréal with the exception of Ag and Au FON and FOEN arrays of 450 nm periodicity.

2.1.1.1 Fabrication of FON and FOEN array substrates

Glass microscope coverslips (22 x 22 mm) were cleaned in piranha solution (3:1 v/v H_2SO_4:H_2O_2) for 90 min at 80 °C. As piranha solution is highly corrosive, special care was taken during this step. The glass coverslips were then thoroughly cleaned several times with 18 MΩ cm water in an ultrasonication bath. The substrates were then placed in a 5:1:1 v/v solution of H_2O, NH_4OH and H_2O_2 and sonicated for 60 minutes. Again, the coverslips were thoroughly cleaned in 18 MΩ cm water in an ultrasonication bath. The cleaned coverslips were stored in 18 MΩ cm water for several weeks, with the water being replaced every 48 hours.

The film over nanosphere (FON) arrays were prepared as follows. For nanospheres of 520 and 650 nm diameter (5000 series, Thermo Fischer particle technology, Nepean ON, Canada), nanosphere solution (37 µL) was drop-coated onto a cleaned glass microscope coverslip to form a well-ordered monolayer. The nanosphere solution compositions were as follows: for 520 nm nanospheres, 80 µL stock nanosphere solution was mixed with 160 µL ethanol and 760 µL water, for 650nm nanospheres, 120 µL stock nanosphere solution was mixed with 160 µL ethanol and 720 µL water. The drop coated solution was slowly evaporated under an ajar Petri dish to form a well ordered monolayer on the glass microscope coverslip.

For 220, 360, and 450 nm nanospheres, stock nanosphere solution (5000 series 10%w/v; Thermo Fischer particle technology, Nepean ON, Canada) was diluted with pure ethanol. The ratio of dilution was as follows: for 220 and 450 nm nanospheres, 30 µL of nanosphere solution was diluted with 30 µL of pure ethanol, while for 360 nm nanospheres, 30 µL of nanosphere solution was diluted with 50 µL of pure ethanol. These solutions were kept at room temperature for 2 hours prior to use. Glass coverslips were air-dried and 10 µL of the diluted nanosphere solution was drop coated on the glass slide. Immediately, the glass coverslip was transferred to the convex meniscus of Petri dish filled with 18 MΩ cm water resulting in the self-assembly of the nanospheres on the water-air interface. A drop of 2% sodium dodecylsulfate (Sigma-Aldrich) was added to compact the nanosphere monolayer. The monolayer was transferred to a clean, wet glass coverslip using Langmuir transfer and the coverslips were dried slowly under an ajar Petri dish.

To prepare FOEN arrays, the nanosphere masks were etched in an oxygen plasma (Harrick Plasma Cleaner PDC-32G, Pleasantville NY, USA). FON arrays did not undergo this etch step. The samples were etched at high power (18 W) for time periods between 0.5 and 10 min. Prior to the etching process, the vacuum was established for 20 min with an oxygen flow of 15 mL/min in the plasma chamber, which was maintained during the etching process. This was necessary to remove air gases and maintain a low pressure of nearly pure oxygen. Four replicate samples for each etch time (including 0 min) and nanosphere diameter were fabricated. The etching step decreased the nanosphere diameter, whilst maintaining the crystalline lattice. A metal film (Ag or Au as indicated in the results and discussion section) was deposited to a thickness of 125 nm with sputter coating (Cressington 308R, Watford, England, UK) on the etched

nanospheres to create FON or FOEN arrays. A 1 nm Cr adhesion layer was deposited prior to the Ag or Au film to promote adhesion.

2.1.1.2 Fabrication of nanotriangle and nanohole array substrates

Glass microscope coverslips were cleaned as described in section 2.1.1.1. Nanosphere stock solutions were supplied by Thermo Scientific Particle technologies (5000 series, 10% w/v, Nepean ON, Canada). The NSL masks were prepared as follows; for 650 nm spheres: a solution was prepared of 120 µl stock polymer sphere solution ,720 µl water and 160 µl ethanol. For 820 nm spheres: a solution was prepared of 37 µl stock polymer sphere solution, 200 µl water and 100 µl ethanol. For 1000 nm spheres: a solution was prepared of 45 µl stock polymer sphere solution, 200 µl water and 100µl ethanol. For 1500 nm spheres: a solution was prepared of 45 µl stock polymer sphere solution, 25 µl water and 25µl ethanol. All NSL mask solutions were allowed to sit at r.t. for 2 h prior to use. The drop-coating procedure was carried out using the following sphere solution volumes; 650 nm: 37 µl, 820 nm: 35 µl, 1000 nm: 37 µl and 1500 nm: 40 µl. The substrates were dried slowly under an ajar petri dish to encourage good monolayer formation.

Nanohole substrates were prepared by undergoing an etch step prior to metal deposition. The nanosphere masks were etched in an oxygen plasma (Harrick Plasma Cleaner PDC-32G, Pleasantville NY, USA). Nanotriangle arrays did not undergo this etch step. The samples were etched at high power (18 W) for time periods between 1 and 18 min. Prior to the etching process, the vacuum was established for 20 min with an oxygen flow of 15 mL/min in the plasma chamber, which was maintained during the etching process. Four replicate samples for each etch time (including 0 min) and nanosphere diameter were fabricated.

Metallization of the substrate was achieved by depositing a 1 nm Cr adhesion layer followed by a 125 nm Au or Ag layer or, for bimetallic arrays, 67.5 nm Ag followed by 67.5 nm Au. Finally, the NSL mask was removed by sonication in ethanol for a few seconds which resulted in nanohole arrays.

2.1.2 Physical characterisation of the arrays

All substrates prepared were physically characterised by atomic force microscopy (AFM) or scanning electron microscopy (SEM). AFM (WITec Alpha SNOM, Ulm, Germany) was carried out in contact mode using a force modulation cantilever with a spring constant of 3 N/m, resonant frequency of 60 kHz, a length of 225 μm, a width of 45 μm, a tip height of 14 μm and a curvature radius of < 10 nm. AFM analysis was used to physically characterise all nanotriangle and nanohole arrays. The AFM images obtained were processed using WITec project (WITec, Ulm, Germany) to determine the diameter of the holes. The average diameter values were based on the measured diameters of 10 nanoholes. SEM (Hitachi S-4700, Pleasanton CA, USA) was carried out at LASEM of École Polytechnique (Université de Montréal, Canada) and was used to characterise all FON and FOEN substrates. ImageJ software[162] was used to process the resultant SEM images and determine the nanosphere diameter. The calculated mean sphere diameter and standard deviation was based on the measured diameters of 20 spheres.

2.1.3 Addition of Raman reporter molecule

The array substrates were immersed in a 1 mM aqueous solution of cysteamine (Sigma-Aldrich) or 4-nitrobenzenethiol (4-NBT, Sigma-Aldrich) for 16 h. 4-NBT was initially dissolved in ethanol to aid dissolution and then diluted in 18 MΩ cm water to the required concentration. The samples were then thoroughly cleaned with water followed by ethanol, air dried or dried under an Argon flux and stored in the absence of light prior to the Raman analysis.

2.1.4 LSPR analysis

The plasmonic response of the FON/FOEN and nanotriangle/nanohole array substrates was measured in reflectance mode (epi-illumination configuration) using a 6 around 1 reflectance probe. The sample was illuminated with a halogen light source. The variable wavelength spectrophotometer (Ocean Optics, Dunedin FL, USA) was set to cover a spectral range of 400 to 900 nm. The spectrum obtained from flat Ag or Au was used as a reference spectrum. The LSPR peak was obtained by dividing the spectral values collected from the nanostructure by the spectral values collected from the reference. λ_{LSPR} was then determined by finding the minimum intensity value within the peak dip

range. The λ_{LSPR} reported is the mean λ_{LSPR} value as calculated from LSPR analysis of four replicate substrates.

2.1.5 Raman analysis

For each sample series (4 substrates per etch time), a Raman spectrum was measured with a Renishaw InVia Raman microscope using 633 and 785 nm excitation wavelengths and a 50x objective (numerical aperture, NA = 0.75). Raman analysis of FON/FOEN substrates was carried out using an acquisition time of 10 s and at either 0.1% or 0.05% of the laser power, resulting in 1 - 3 μW or 15 - 30 μW of laser power at the sample at 633 nm and 785 nm excitation, respectively. Raman analysis of nanotriangle or nanohole arrays was carried out at 1 % of the laser intensity, resulting in 35 μW for the 633 nm laser and 0.35 mW for the 785 nm laser and spectra were acquired for 10 s. The peak height values of the 1072 cm^{-1} peak of cysteamine and the 1573 cm^{-1} peak of 4-NBT were calculated and used for analytical purposes. The peak height values reported are the average values calculated from four replicate substrates for each etch time series. The standard deviations were also calculated from the four replicate substrates for each etch time. For comparison purposes, the Raman response was normalised to that of FON response for FOEN arrays (where FON = 1.0) or to the nanotriangle response for nanohole arrays (where nanotriangle = 1.0), prepared with the same NSL mask periodicity.

2.1.6 Investigation into the 4-NBT SERS signal over time

Three Ag nanohole arrays of 1000 nm periodicity and diameter/periodicity ratio (D/P) 0.68 (resulting from a 1 min etch period) were thoroughly cleaned with ethanol before immersion into a solution of 1 mM 4-NBT (Sigma-Aldrich) for 16 h. 4-NBT was initially dissolved in ethanol to aid dissolution and then diluted in doubly distilled water (ddH$_2$O) to the required concentration. After 16 h, the samples were thoroughly cleaned with water followed by ethanol, air dried and stored in the absence of light prior to Raman analysis. Raman analysis was performed using 514.5, 633 and 785 nm excitation wavelengths. Experiments using 514.5 nm excitation were performed on a Renishaw inVia Raman microscope equipped with a Leica DM/LM microscope and with a Modu-Laser of 514.5 nm excitation. Experiments using 633 and 785 nm excitations were performed on a Renishaw Ramascope equipped with a Leica DM/LM microscope and a Renishaw HeNe laser of 633 nm excitation and an Innovative Photonic Solutions

laser of 785 nm excitation. Identical parameters were used in all experiments: 50x objective (Leica, NPlan, NA = 0.75) and spectra were acquired for 1 s at 1 % of the total laser power. A spectrum was taken every 30 s over a period of 330 s from each of the three replicate substrates at each excitation wavelength.

2.1.7 Comparison to Klarite Raman response

Klarite 313 (Renishaw diagnostics, Glasgow, Scotland), a Ag nanohole array of 1000 nm periodicity and D/P 0.68 and a bimetallic nanohole array of 1000 nm periodicity and D/P 0.68 were thoroughly cleaned with ethanol prior to immersion in a 1 mM aqueous solution of 4-NBT for 16 h. 4-NBT was initially dissolved in ethanol to aid dissolution and then diluted in doubly distilled water (ddH$_2$O) to the required concentration. After 16 h, the samples were thoroughly cleaned with water followed by ethanol, air dried and stored in the absence of light prior to Raman analysis. Raman analysis was performed on a Renishaw Ramascope equipped with an Innovative Photonic Solutions laser of 785 nm excitation. Five replicate spectra were collected from different points across all substrates using 0.01 % laser power (equal to 0.24 mW of unfocussed laser power), a 50x objective (Leica, NPlan, NA = 0.75) and 10 s acquisition time. The mean 1573 cm^{-1} peak height and the standard deviation was calculated from the five replicate spectra obtained.

2.2 Results and Discussion

Metal FON substrates have been extensively characterised and used in numerous practical applications by Van Duyne and other groups.[14, 29, 143, 145, 148] By employing a modified NSL procedure, a series of metal film over nanosphere substrates can be prepared with decreasing sphere diameters. These have been named film over etched nanosphere (FOEN) substrates. It was postulated that by decreasing the diameter of the spheres, the SERS activity could be enhanced with respect to substrates of the same periodicity which had not undergone plasma etching as the LSPR of the etched substrates could be tuned to result in more efficient coupling between the substrate and the incident radiation which may have a large effect on the SERS enhancement.

A full investigation into the optical, physical and Raman enhancement properties of a series of FOEN substrates was carried out.

2.2.1 Initial investigation into FOEN arrays

Initial work focussed on Ag and Au FOEN substrates of 450 nm periodicity in order to optimise the fabrication and analysis methods. A series of FOEN substrates with 450 nm periodicity were prepared with varying etch times: 0, 1.5, 2.5, 4, 6 and 8 min.

2.2.1.1 Fabrication of FOEN substrates

Modified NSL was used to prepare the FOEN arrays. This fabrication method is not perfect: dislocations and defects interrupt the well-ordered structure where spheres have failed to self-assemble in the lowest energy configuration, where a sphere is missing or multilayers of spheres have formed. However, it is possible to fabricate large areas of nanostructure (10 - 100 μm^2) that are defect-free using this method. The polystyrene ordered monolayer is then etched using reactive oxygen plasma. The plasma generates ions which 'burn' the surface of the polystyrene spheres decreasing the diameter of the spheres but retaining the lattice spacing. The longer the etch time, the smaller the diameter of the spheres and the larger the gap between spheres. The etch process is inhomogeneous which results in the roughness of the sphere surface increasing with increasing etch time. The etch step is followed by a metallization step in which a 125 nm metal layer is deposited over the entire substrate. This process results in metal depositing in the interstitial voids between the spheres as well as forming a layer across the exposed face of the spheres. The deposited metal layer was thick

enough to connect the metal islands that form in the interstitial spaces between the polymer spheres and the metal layer that forms on top of the spheres. A 1 nm chromium layer was deposited prior to the Ag or Au layer to improve adhesion of the metal to the glass substrate.

2.2.1.2 Physical Characterisation

Physical characterisation of the samples was required to determine the dimensions and shape of the nanostructured FOEN arrays. Both factors are known to influence the LSPR peak and the electric field intensity therefore, it was paramount that the substrates were fully physically characterised in order to determine the structure-property relationship. In addition, physical characterisation provides a method to assess the uniformity of the fabricated surfaces.

Throughout this investigation, both atomic force microscopy (AFM) and scanning electron microscopy (SEM) were used to characterise the surfaces.

AFM

AFM is an analytical method capable of generating a high-resolution image of the sample surface. A nanometer tip mounted on a cantilever is used to probe the sample surface. The sample is supported on a piezoelectric stage which facilitates very small and precise movements. In contact mode, the tip is moved across the sample surface at variable rates depending on application. Changes in the sample topography result in deflection of the cantilever. This deflection is measured by a laser spot focussed on the top face of the cantilever and detected by photodiodes. In close-contact mode, the tip is in close proximity to the surface and vibrates at a set frequency. Forces between the tip and surface alter the vibration frequency resulting in deflection of the cantilever. AFM allows determination of dimensions in the *x*- and *y*-directions in addition to accurate measurements in the *z*-direction.

SEM

SEM is a form of electron microscopy which uses a beam of high energy electrons to scan the sample and produce an image of the surface. The beam electrons interact with the sample surface electrons and are reflected by elastic scattering into a detector. The beam electrons can also cause emission of secondary electrons from the sample by inelastic scattering which can be detected by a second detector. SEM produces images

at very high resolution however it can only be used to measure in the *x*- and *y*-directions.

AFM was the preferred method of physical characterisation in this investigation as it can provide information about the substrate topography. However, it was found that contact-mode AFM analysis of FOEN substrates of 450 nm periodicity resulted in damage to the samples. It was postulated that the AFM tip was 'popping-off' the spheres to give a structure that resembled a nanohole array. For this reason, SEM was used to physically characterise FON and FOEN arrays.

Figure 2.1 shows a large scale SEM image of an Ag FOEN array of 450 nm periodicity. The hexagonal close-packed structure of the spheres can clearly be seen. Dislocations and defects due to missing or smaller/larger spheres can be observed however, the structure is overall relatively uniform in nature.
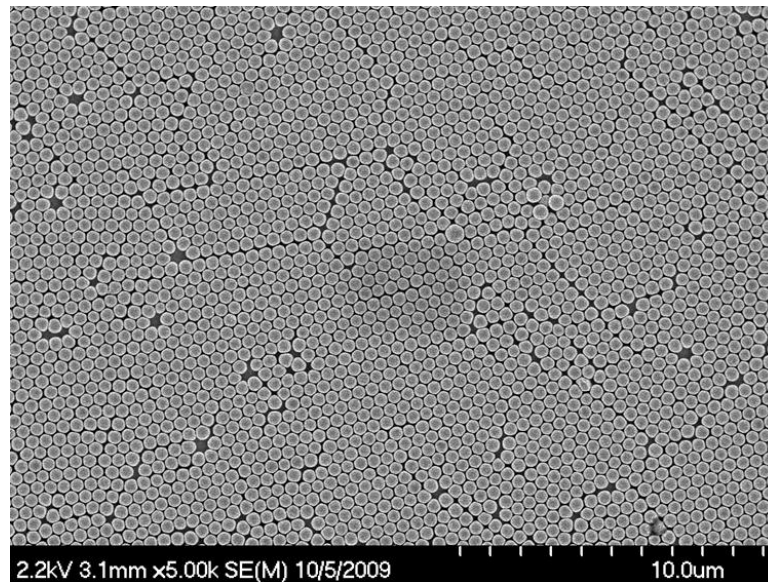

Figure 2.1 –Large scale SEM image of AgFOEN array of 450 nm periodicity and 0 min etch time. The scale bar represents 10 μm. The image was acquired using 2.2 kV and 5k magnification.

Samples with 450 nm periodicity and decreasing sphere diameter were analysed by SEM and the resulting images are shown in Figure 2.2.
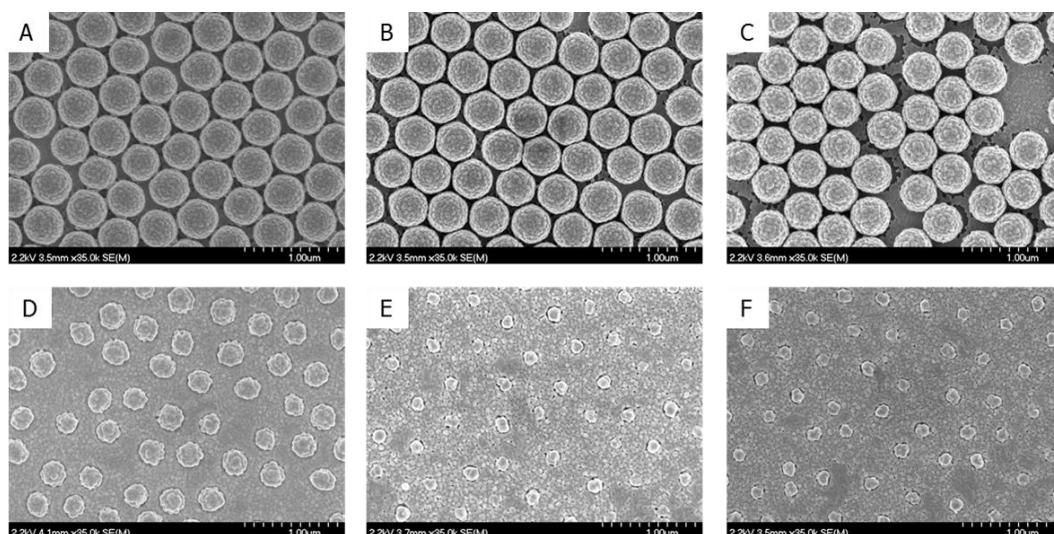
Figure 2.2 – SEM images of Ag FOEN arrays at A) 0 min etch time, B) 1.5 min etch tine, C) 2.5 min etch time, D) 4 min etch time, E) 6 min etch time, and F) 8 min etch time. The scale bar represents 1 µm in all images. . The images were acquired using 2.2 kV and 35k magnification.

The effect of increasing etch time is clearly demonstrated in Figure 2.2. As the etch time increases (images A to F), the diameter of the spheres decreases and the gap between the spheres increases. Initially, the spheres are relatively smooth but as the etch time increases, the surface becomes increasingly rough. The topography of the deposited metal layer between spheres can be observed in SEM images D, E and F and comprises of small metal islands. The average sphere diameters and the gap distances were evaluated using ImageJ software and are shown in Table 2.1.

Etch time – min	Diameter of spheres after metal coating - nm	Gap between spheres - nm	gap / diameter
0	443 ± 13	7	0.016
1.5	420 ± 18	30	0.071
2.5	402 ± 19	48	0.12
4	249 ± 23	201	0.81
6	139 ± 10	311	2.24
8	147 ± 13	303	2.06

Table 2.1 – Physical properties of Ag FOEN arrays of 450 nm periodicity. The error in the diameter of spheres measurement was calculated from the standard deviation of 20 sphere diameters.

The gap between spheres is the approximate gap between nanospheres as calculated by subtracting the average sphere diameter from the initial sphere diameter. The gap/diameter value was calculated to allow comparison of Raman response between

arrays of different periodicities and to aid predication of plasmon coupling between spheres. As discussed in the chapter 1, work by El-Sayed had determined that the decay length for plasmon coupling strength was approximately 0.2 units of the particle diameter.[82] Hence, plasmon coupling was predicted to occur in samples with a gap/diameter value of 0.2 or below and these samples were expected to exhibit the highest Raman response. The samples prepared had a range of gap/diameter values that would help corroborate this theory.

2.2.1.3 Optical Characterisation

It was important to fully characterise the optical properties of the arrays in order to determine the LSPR peak of the structures. As the substrates were opaque, LSPR spectroscopy was carried out in reflectance mode. This was advantageous as LSPR spectroscopy in epi-illumination mode is similar in instrumental set-up to that used for Raman spectroscopy. Figure 2.3A shows the LSPR response of the bare Ag FOEN arrays at various etch times (Panel A) and the Ag FOEN arrays after addition of a Raman reporter monolayer (Panel B).
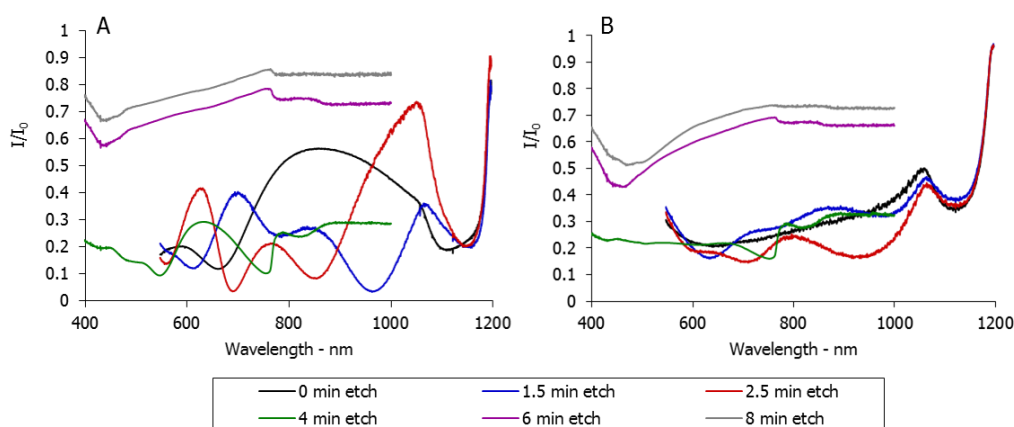
Figure 2.3 - LSPR response of 450 nm Ag FOEN arrays of varying etch time. A) LSPR response of bare arrays. B) LSPR response of arrays after addition of 4-NBT Raman reporter monolayer.

The effects of increasing the etch time on the LSPR wavelength can be determined from Figure 2.3B. The LSPR peak initially red-shifts which is indicative of plasmon coupling between the spheres.[82] This was observed for samples with etch times of 1.5 and 2 min. At longer etch times (6 and 8 min etch), the LSPR peak undergoes a blue shift, appearing at wavelengths below 600 nm, which suggests that plasmon coupling within the arrays is not occurring. Some samples exhibited multiple resonance peaks which could be attributed to more than one polar resonance in the structure.[135] It should also

be noted that as the etch time increases, the intensity of the LSPR peaks exhibited by the structures decreases. This is a result of the smaller nanospheres covering a smaller proportion of the actual surface area. The LSPR peak is sensitive to the environment at the metal surface. Figure 2.3B shows how the LSPR response of the substrates changed after immersion of the substrates in a solution of the Raman reporter molecule (4-NBT). The LSPR wavelengths have been tabulated in Table 2.2 for ease of discussion.

Etch time - min	λ_{LSPR} bare array - nm	λ_{LSPR} after reporter addition - nm
0	661	659
1.5	611, 962	633, 982
2.5	690, 853	710, 918
4	547, 745	752, 813
6	430	460
8	430	477

Table 2.2 - LSPR peak wavelengths before and after adsorption of 4-NBT to array surface of Ag FOEN arrays of 450 nm periodicity and varying etch times.

At all etch times, the LSPR peak undergoes a red-shift compared to the LSPR wavelength prior to Raman reporter addition. This is indicative of an increase in refractive index at the metal surface.[163] This peak shift implies that adsorption of the Raman reporter molecule to the metal surface has occurred. In order to achieve maximum SERS enhancement, the laser excitation wavelength used should be closely matched to the LSPR of the metal structure in the same form as it will be analysed by Raman spectroscopy. Therefore, the LSPR profile should be characterised after Raman reporter adsorption to maximise SERS enhancement.

2.2.1.4 Raman reporter choice

Several factors must be addressed when choosing a Raman reporter molecule. The Raman reporter must adsorb easily onto the SERS substrate, form a tightly packed self-assembled monolayer (SAM) and give a characteristic SERS spectrum that can be easily detected under standard conditions.

Two Raman reporter molecules were investigated; cysteamine and 4-nitrobenzenethiol (4-NBT). Cysteamine had been shown to form a tightly-packed monolayer on silver surfaces and give a characteristic SERS signal at 785 nm excitation.[164] There are several reports in the literature on the use of 4-NBT as a Raman reporter on Ag and Au surfaces.[165-167] Figure 2.4A shows the structure of cysteamine and three replicate

spectra from cysteamine adsorbed on three separate Ag FOEN arrays (P = 450 nm, etch time = 1.5 min) at 785 nm excitation. Figure 2.4B shows the structure of 4-NBT and the spectra obtained at 785 nm excitation from adsorbed 4-NBT on three separate Ag FOEN arrays (P = 450 nm, etch time = 2.5 min). Table 2.3 and Table 2.4 show the spectral assignments for the four main peaks of cysteamine and 4-NBT respectively.
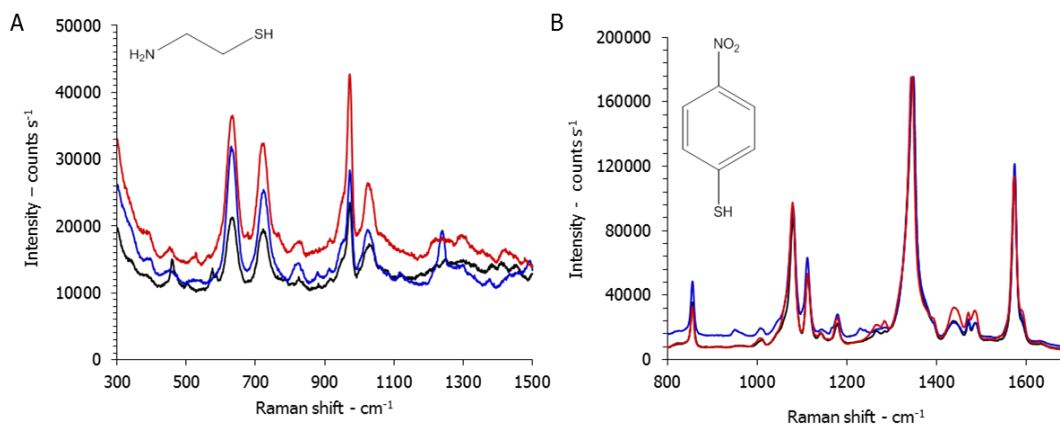
Figure 2.4 - A) The structure of cysteamine and three replicate SERS spectra from cysteamine adsorbed on Ag FOEN arrays at 785 nm excitation. B) The structure of 4-NBT and three replicate SERS spectra from 4-NBT adsorbed on Ag FOEN at 785 nm excitation.

Raman shift – cm^{-1}	Spectral assignment[164]
629	v(C-S)
723	v(C-S)
973	v(C-C(-N))
1027	v(C-C(-N))

Table 2.3 - Cysteamine spectral assignment.[164]

Raman shift – cm^{-1}	Spectral assignment[165]
1082	In-plane C-H bending mode
1110	In-plane C-H bending mode
1340	v_s(NO$_2$)
1573	C-C stretching mode

Table 2.4 - 4-NBT spectral assignment.[165]

Both cysteamine and 4-NBT exhibited good SERS responses on Ag FOEN arrays. The spectra obtained from 4-NBT adsorbed on separate Ag FOEN arrays resembled one another to a high degree highlighting the good signal reproducibility exhibited by this system.

4-NBT exhibited good SERS signals on Au FOEN arrays at both 633 and 785 nm excitation however no signal corresponding to cysteamine was observed from Au FOEN arrays under identical analysis conditions. Reports in the literature described the lack

of cysteamine SERS signal on Au sputter coated surfaces and the authors attributed this to weak charge transfer between cysteamine and the metal surface.[168] As both Ag and Au arrays were to be investigated, it was decided that 4-NBT would be used as the Raman reporter in all subsequent experiments.

SERS intensity of 4-NBT over time

The nitro group in 4-NBT is known to undergo surface-induced photo-reduction to an amine group under irradiation with a visible laser when adsorbed on a silver surface.[169] For this reason, it was important to choose a SERS peak for analysis that corresponded to a vibration that was not affected by the reduction reaction. The 1340 and 1573 cm^{-1} peak heights were investigated over a time period of 330 s using 514.5, 633 and 785 nm excitation.
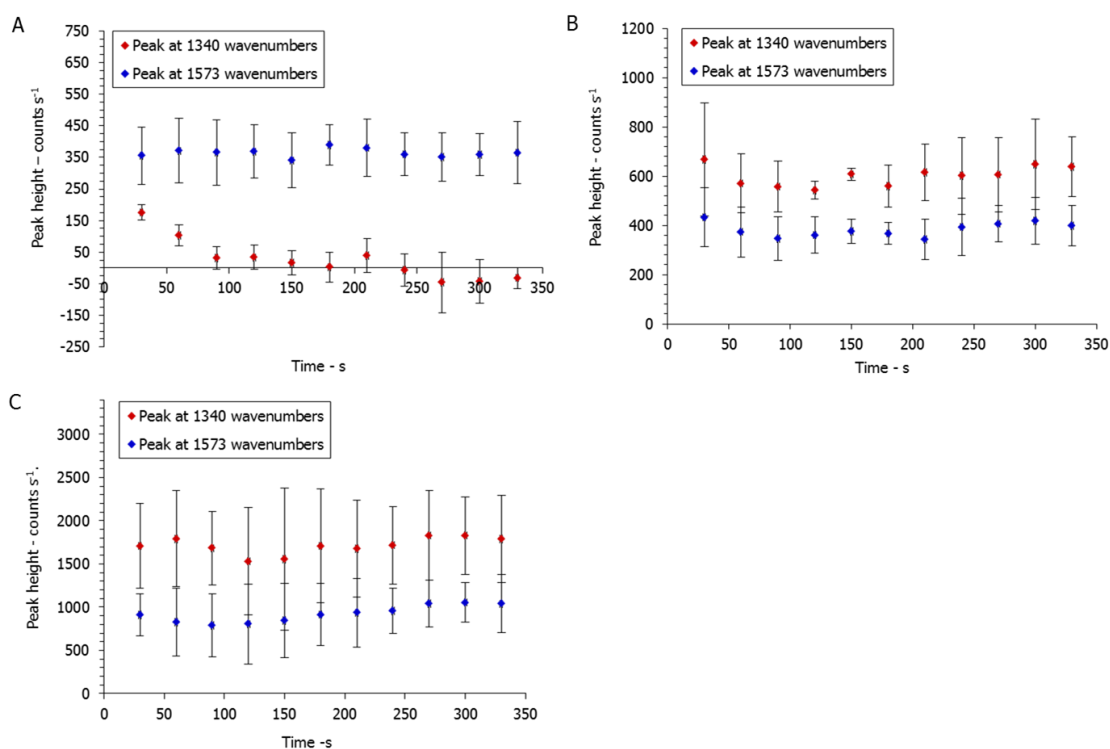
Figure 2.5 - 1340 cm^{-1}(red) and 1573 cm^{-1} (blue) mean peak height with respect to time at A) 514.5 nm excitation. B) 633 nm excitation. C) 785 nm excitation. Data points represent the mean peak height values calculated from three replicate experiments. The error bars represent two standard deviations about the mean. Identical parameters were used for all analyses: 50 x objective, 1 s acquisition time, and 1 % laser power.

Figure 2.5A shows the change in the 1340 and 1573 cm^{-1} peak height over the time course at 514.5 nm excitation. It can be clearly observed that the intensity of the 1340 cm^{-1} peak decreases rapidly, to below that of the noise level, whereas the peak intensity

of the 1573 cm^{-1} remains relatively unchanged. This is as expected as the peak at 1340 cm^{-1} corresponds to the nitro stretch which undergoes reduction to an amine group.

Figure 2.5B and C show the peak height profile with respect to time at 633 and 785 nm excitation respectively. The peak intensities remain relatively unchanged over the time course at both excitation wavelengths. Although the intensity of the 1340 cm^{-1} peak is greater, the error bars are also larger implying that analysis based on this peak would be less reproducible. Therefore, in experiments that used 4-NBT as the Raman reporter, analyses were based on the height of the 1573 cm^{-1} peak.

2.2.1.5 Metal

The Raman response exhibited by Ag FOEN arrays was compared to that exhibited by Au FOEN arrays. Figure 2.6 shows the mean peak height values calculated from four replicate samples at each gap/diameter. The average Raman response from each sample series was normalised to that of the unetched FON sample of the same metal resulting in the unetched FON sample having a value of 1.0 for the Raman response. This allowed clear examination of the effect of etching on the Raman response for each class of array.
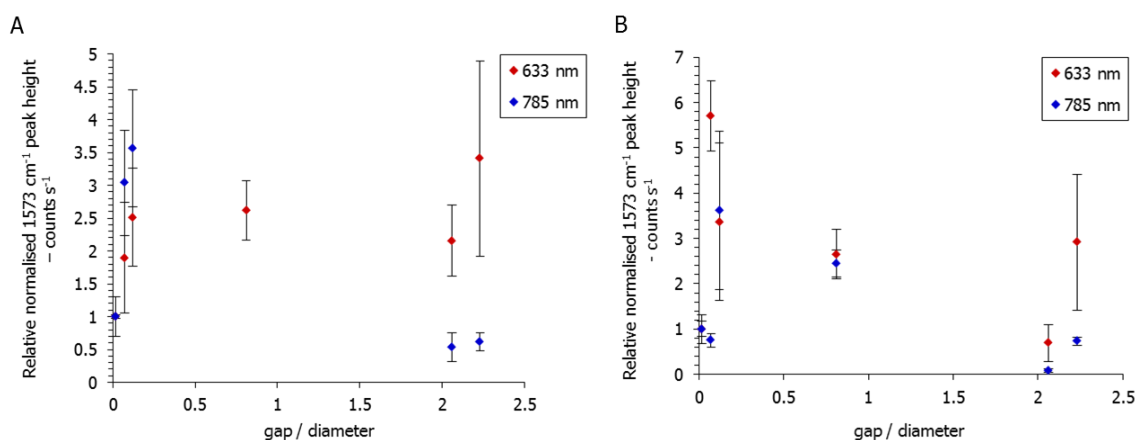
Figure 2.6 - A) Raman response of AgFOEN arrays of 450 nm periodicity at 633 (red) and 785 nm (blue) excitation. B) Raman response of AuFOEN arrays of 450 nm periodicity at 633 (red) and 785 nm (blue) excitation. The data points represent the mean height of the 1573 cm^{-1} peak calculated from four replicate substrates. The error bars represent two standard deviations about the mean.

It should be noted that due to missing data, there is a data point missing for the average Raman response of Ag FOEN array at 785 nm excitation with a gap/diameter value of 0.81. The Raman response graphs of the Ag and Au FOEN substrates resemble one another to a high degree. In both series, the Raman response with respect to the

unetched FON array increases to a maximum value followed by a decrease to below that of the FON sample. This indicated that there is an optimal etch time for each sample series. The only data points not to fit this trend were the Ag and Au FOEN arrays with a gap/diameter value of 2.23 at 633 nm excitation. At 633 nm excitation, optimum Raman response was obtained from Ag FOEN array with a gap/diameter of 2.23 and Au FOEN array with a gap/diameter of 0.071. Both Ag and AuFOEN arrays with a gap/diameter of 0.12 gave optimal response at 785 nm excitation. The raw Raman intensities of the optimum AgFOEN arrays were 219359 and 195471 a.u. respectively at 633 and 785 nm. The raw Raman intensities of the optimum Au FOEN arrays at 633 and 785 nm excitation were 111508 and 43000 a.u. respectively. Comparison of these values, all of which were obtained from analyses that used identical experimental parameters, demonstrated that, as predicted by literature, Ag SERS substrates exhibit more intense SERS enhancements than Au substrates.

This study had demonstrated that by etching the polymer spheres before metal deposition, an increased Raman response could be obtained. It was decided that this warranted further investigation with an expanded series of FON/FOEN arrays.

2.2.2 Full investigation into Ag FOEN arrays of varying periodicity

A systematic investigation was performed on a series of Ag FOEN substrates with 220, 360, 520 and 650 nm periodicities to probe the effect of sphere diameter and inter-particle distance on SERS activity. This study was designed to compare the Raman response of the unetched FON arrays to that of FOEN arrays etched for varying periods of time. The aim of this investigation was firstly to determine if a greater SERS enhancement could be achieved by etching the spheres before metal deposition and secondly, to understand the source of the enhancement. The fabrication and analyses of the substrates was carried out by collaborators at Université de Montréal.

The substrates fabricated were designed to cover a range of periodicities and gap/diameter values so the effect of both factors on Raman response could be fully investigated. The samples investigated are shown in Table 2.5.

Etch time - min	P = 220 nm D – nm (gap – nm) *gap/diameter*	P = 360 nm D – nm (gap – nm) *gap/diameter*	P = 520 nm D – nm (gap – nm) *gap/diameter*	P = 650 nm D – nm (gap – nm) *gap/diameter*
0	217 ± 12 (3) *0.014*	352 ± 22 (8) *0.023*	518 ± 29 (2) *0.004*	644 ± 24 (6) *0.009*
0.5	211 ± 13 (9) *0.043*	329 ± 18 (31) *0.094*	497 ± 15 (23) *0.046*	
1	201 ± 13 (19) *0.095*	315 ± 19 (45) *0.14*		
1.5	186 ± 10 (34) *0.18*	294 ± 23 (66) *0.22*	481 ± 20 (39) *0.081*	585 ± 27 (65) *0.11*
2.5	107 ± 8 (113) *1.05*	302 ± 10 (58) *0.19*	436 ± 19 (84) *0.19*	553 ± 26 (97) *0.18*
4	83 ± 7 (137) *1.65*	174 ± 10 (186) *1.06*	334 ± 19 (186) *0.56*	523 ± 27 (127) *0.24*
6		148 ± 13 (212) *1.43*	172 ± 16 (348) *2.02*	461 ± 17 (189) *0.41*
8			202 ± 14 (318) *1.57*	

Table 2.5 – Etch time, average sphere diameter, gap between spheres and gap/diameter values for Ag FON/FOEN substrates investigated. Average sphere diameter and standard deviation values are based on 20 spheres.

Table 2.5 shows the average sphere diameter after etching of the samples as evaluated from SEM images. As expected, an increase in etch time results in a decrease in sphere diameter and, hence, an increase in gap/diameter. It was not possible to fabricate FOEN arrays of 650 nm periodicity with a gap/diameter value larger than 0.41 as samples delaminated during the fabrication process. This effect was also observed in FOEN samples with smaller periodicities and large gap/diameter values but became more pronounced as the initial diameter of the spheres increased. As previously discussed, plasmonic coupling will occur in samples in which the gap between the nanostructured features is approximately 0.2 of the diameter of the nanostructured features. Hence, plasmonic coupling is predicted to occur in samples which have an approximate

gap/diameter of 0.2 or less: samples etched for 1.5 minutes or less in samples with 220 nm periodicity and 2.5 minutes or less in samples with 360, 520 and 650 nm periodicities.

2.2.2.1 Identification of LSPR wavelength

Optical characterisation of the FOEN substrates after the adsorption of 4-NBT was achieved using LSPR spectroscopy in reflectance mode. The LSPR wavelengths observed from each sample are tabulated in Table 2.6.

Etch time - min	P = 220 nm λ_{LSPR} - nm	P = 360 nm λ_{LSPR} - nm	P = 520 nm λ_{LSPR} - nm	P = 650 nm λ_{LSPR} - nm
0	566 865	554 733	634 824	607 808
0.5	529 757	523 641	708	
1	607	605 846		
1.5	605	532 633 835	880	818
2.5	571	551 778	633 846	640 782
4	550	549	617	733 873
6		563	507	OSR
8			517	

Table 2.6 – Observed LSPR peaks from Ag FON/FOEN substrates. OSR denotes that the LSPR peak is outside the spectral range of 400 - 900 nm.

The results of the optical characterisation demonstrate that etching the NSL masks has a significant effect on the excitation wavelength of the localised surface plasmon. Etching the NSL masks initially red-shifts the LSPR. A red-shift of the LSPR is indicative of plasmonic coupling between the metal-covered nanospheres. Therefore, it could be concluded that plasmon coupling occurred in samples etched for shorter etch times. The LSPR was then observed to blue-shift to shorter wavelengths, which is typical of a decrease in particle diameter.[170] The effect of periodicity on the LSPR could also be observed. Increasing the periodicity resulted in red-shifts of the LSPR wavelength,

except in samples with 220 nm periodicity. This trend was in agreement with previously reported studies on related substrates.[171]

2.2.2.2 Raman spectroscopy

All samples were analysed using 633 and 785 nm excitation and the results are shown in Figure 2.7 and Figure 2.8. One scan was taken from each of the four replicate samples prepared for each etch time. The average Raman response from each sample series was normalised to that of the unetched FON sample of the same periodicity. This allowed clear examination of the effect of etching on the Raman response (unetched FON sample has a value of 1.0 for the Raman response at each periodicity).

Figure 2.7 - A) Raman response of Ag FOEN arrays of 220 nm periodicity at 633 (red) and 785 nm (blue) excitation. B) Raman response of Ag FOEN arrays of 360 nm periodicity at 633 (red) and 785 nm (blue) excitation. The data points represent the mean height of the 1573 cm^{-1} peak calculated from four replicate substrates. The error bars represent two standard deviations about the mean.

The Raman response graphs of 220 and 360 nm periodicity Ag FOEN arrays follow the same trend. In both series, the Raman response with respect to the unetched FON array decreases slightly then increases to a maximum value followed by a decrease to below that of the FON sample. This indicates that there is an optimal etch time for each sample series and etching for a longer period of time results in a lower Raman response than that of the unetched FON substrate. The Raman response was determined to be optimal at a gap/diameter of 0.095 for FOEN of 220 nm periodicity and a gap/diameter of 0.22 for FOEN of 360 nm periodicity.
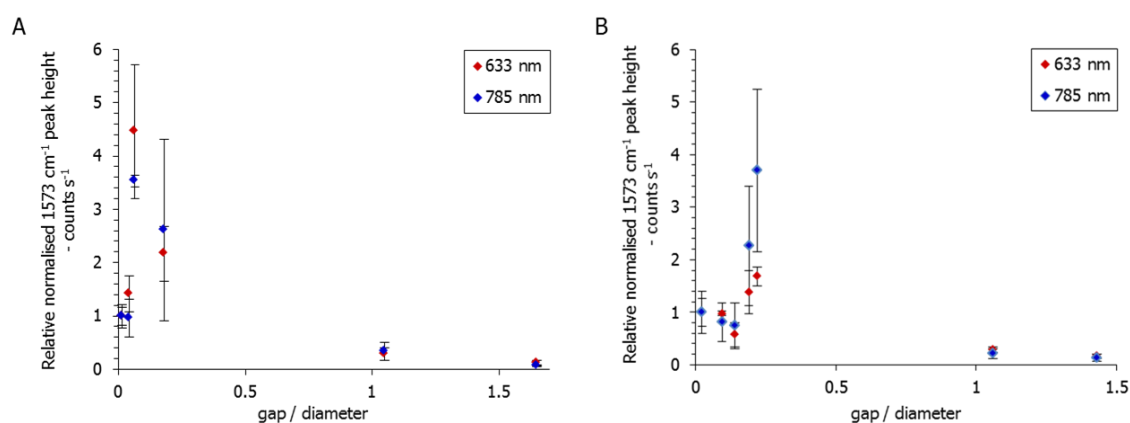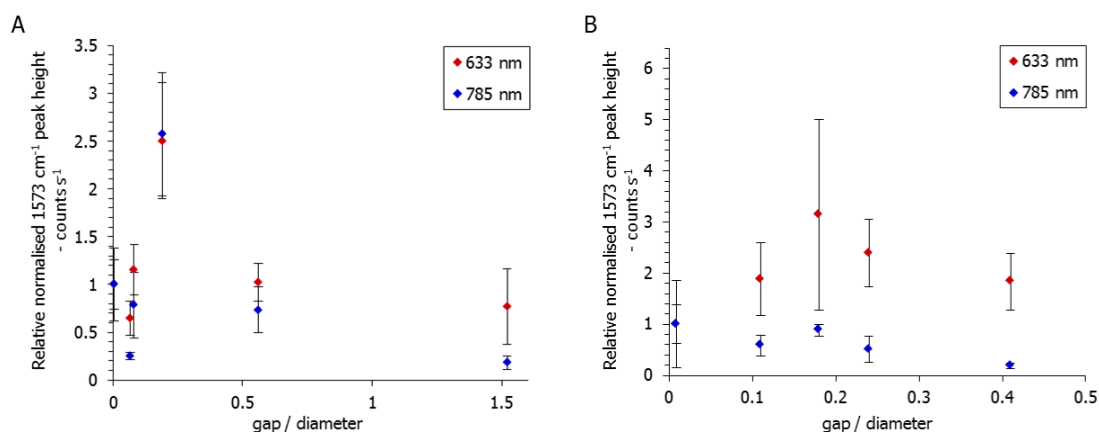
Figure 2.8 – A) Raman response of Ag FOEN arrays of 520 nm periodicity at 633 (red) and 785 nm (blue) excitation. B) Raman response of Ag FOEN arrays of 650 nm periodicity at 633 (red) and 785 nm (blue) excitation. . The data points represent the mean height of the 1573 cm^{-1} peak calculated from four replicate substrates. The error bars represent two standard deviations about the mean.

The Raman response of FOEN arrays fabricated from 520 nm spheres mirrored that of 220 and 360 nm FOEN arrays; the Raman response initially decreased before increasing to a maximum (at a gap/diameter value of 0.19) and subsequently decreasing to less than that of the unetched FON sample. In all previously discussed samples, the same pattern was closely adhered to regardless of excitation wavelength. However, the Raman response of FOEN arrays of 650 nm initial diameter excited at 785 nm is lower than that of the unetched FON arrays at every gap/diameter. The Raman response of the samples excited at 633 nm follows the same pattern as previously discussed.

To determine the factors that had the greatest influence on the Raman response of the FOEN substrates, the properties of the optimum substrates with respect to Raman response at each sphere diameter were compared. The properties of the optimum Ag FOEN substrates at 633 nm excitation are collated in Table 2.7.

Sphere diameter – nm	Etch time - min	gap/diameter	Raman intensity – a.u.	Relative response vs. FON	λ_{LSPR} - nm
220	1	0.095	517391	4.5	607
360	1.5	0.22	204678	1.7	532, 633, 835
450	6	2.24	219358	3.4	460
520	2.5	0.19	287930	2.5	633, 846
650	2.5	0.18	13964	3.1	640, 782

Table 2.7 – Properties of optimum Ag FOEN substrates based on Raman response at 633 nm excitation.

The optimal gap/diameter of all samples at 633 nm excitation, with the exception of AgFOEN of 450 nm periodicity, is less than 1. A gap/diameter value of around 0.2 is optimum for three of the sample series; 360, 520 and 650 nm. The LSPR wavelengths of these samples are also well-matched to the excitation wavelength. As discussed in section 1.5.1.2, maximum SERS enhancement is achieved when λ_{ex} is slightly blue-shifted with respect to λ_{LSPR} thus, in theory, very efficient coupling leading to large SERS enhancement would occur in the optimum AgFOEN substrates of 650 nm periodicity. Of the three substrates in which the LSPR is well-matched to the excitation wavelength (optimum substrates with 360, 520 and 650 nm periodicities), this substrate exhibited the greatest SERS signal intensity, relative to that of FON, and so confirms the theory. The LSPR wavelengths of the optimum substrates of 220 and 450 nm initial diameter were not close enough to the excitation wavelength to result in maximised SERS enhancement. However, the relative Raman responses with respect to the unetched FON substrate are highest for these samples. It was postulated that the small inter-particle distance (19 nm) in the 220 nm FOEN structure was responsible for the large Raman response. This theory was supported by reports in the literature of increasing electric field intensity as the inter-particle distance decreases towards very small distances.[83, 115] The Raman response of the optimal substrate of 450 nm periodicity may be in part explained by surface roughness. Longer etch times resulted in rougher surfaces as clearly demonstrated in the SEM images in Figure 2.2. Rougher surfaces

typically improve the Raman response and so the surface roughness contribution may be in part responsible for the intense Raman response observed from this sample.

Table 2.8 shows the properties of the optimal Ag FOEN substrates at 785 nm excitation.

Sphere diameter – nm	Etch time - min	gap/diameter	Raman intensity – a.u.	Relative response vs. FON	λ_LSPR - nm
220	1	0.095	641185	3.5	607
360	1.5	0.22	1130512	3.7	532, 633, 835
450	2.5	0.12	195472	3.6	710, 918
520	2.5	0.19	1306235	2.6	633, 846
650	2.5	0.18	79808	0.88	640, 782

Table 2.8 – Properties of optimum Ag FOEN substrates based on Raman response at 785 nm excitation.

The properties of the optimum substrates are very similar to those of the optimum arrays at 633 nm excitation; the gap/diameter values are 0.22 or less and the excitation wavelength is well matched to the LSPR wavelength of the substrates of 360, 520 and 650 nm initial diameter. The high Raman response of FOEN array of 220 nm initial diameter was again postulated to be a result of the small inter-particle gap present in the optimum substrate. The properties of the optimum substrate of 450 nm periodicity at 785 nm excitation differed to those of the optimum substrate at 633 nm excitation. The inter-particle gap was smaller (48 vs. 311 nm at 785 and 633 nm excitation, respectively). If the inter-particle distance was solely responsible for the increase in Raman response with respect to unetched FON, the same structure would exhibit optimal Raman response irrespective of excitation wavelength. Therefore, it was thought that a combination of factors was responsible for the observed SERS enhancement.

It can be concluded from investigation into the Raman responses exhibited by a series of optimal FOEN substrates that the increase in SERS enhancement observed, with respect to the unetched FON samples, was due to three factors: the inter-particle distance between spheres, efficient coupling between the excitation wavelength and the LSPR wavelength of the substrates and increasing roughness of the surfaces. However, these three factors do not contribute equally to the Raman response. The surface roughness has a minor contribution to the overall observed SERS enhancement.

If this factor had a large influence on Raman response, the substrates that had undergone long etch times (larger gap/diameter values) would be expected to exhibit the greatest Raman response as surface roughness increases with increasing etch time. Both the inter-particle distance and the coupling of the incident radiation with the surface plasmon heavily influence the SERS enhancement observed from the samples, albeit to differing degrees in different samples.

The results from this investigation demonstrate the importance of tuning the SERS substrate to the excitation wavelength and show the significance of the structure-property relationship. By controlling the size of the spheres and the gap between the spheres, the Raman response was shown to be improved by a factor of 4.5 at 633 nm excitation and 3.7 at 785 nm excitation. Thus, the use of modified NSL allowed the fabrication of optimal FOEN SERS substrates.

2.2.3 Nanohole arrays

Modified NSL can also be used to fabricate nanohole arrays. An analogous investigation into the structure-property relationship of nanotriangles and nanohole arrays was carried out to determine the optimum structures for SERS analysis and to investigate the factors that influenced the SERS enhancement. The fabrication and analysis of the substrates was carried out by collaborators at Université de Montréal.

Nanotriangle and nanohole arrays were prepared by modified NSL with a sphere removal step after metal deposition. An increase in etch time resulted in the transition of nanotriangle to nanohole array. The diameter of the hole decreased as the etch time period increased whilst still maintaining the lattice spacing. Nanostructures were fabricated using 650, 820, 1000 and 1500 nm polymer sphere masks. It was increasingly difficult to obtain complete sphere removal by sonication in samples that had undergone long etch times due to a strong point of contact between the metal layer on the polymer sphere and the metal deposited in the interstitial gaps. For this reason, the range of etch times investigated was limited. A full investigation into the optical properties of nanotriangle and nanohole arrays with 450 nm periodicity had been previously performed by the Masson group[74] and so this research focussed on arrays with larger periodicities.

For this investigation, the diameter/periodicity (D/P) ratio was used to compare arrays of different diameters and periodicities. The periodicity is dictated by the initial diameter of spheres used as the NSL mask and the diameter of the holes is dependent on etch time. The D/P ratio decreased as the etch time increased. The D/P ratio of analysed substrates ranged from 1.0 for unetched nanotriangle arrays to 0.43 for nanohole arrays of small hole diameter. A D/P ratio of 0 corresponds to a non-structured metallic film. Previous research by collaborators at Université de Montréal had demonstrated that the transition between nanotriangle and nanohole arrays occurred at D/P values between 0.75 and 0.6.[62]

2.2.3.1 Physical characterisation of the arrays

AFM analysis was used to physically characterise the nanotriangle and nanohole arrays. AFM was the preferred method of characterisation as it could be used to measure the height of the nanostructures in addition to measuring the diameter of the holes. In contrast to the physical characterisation of the FON/FOEN arrays, AFM did not damage the samples and so was used to analyse the topography of the nanotriangle and nanohole arrays. Figure 2.9 shows AFM images of a series of nanohole arrays fabricated from spheres of 1500 nm initial diameter.
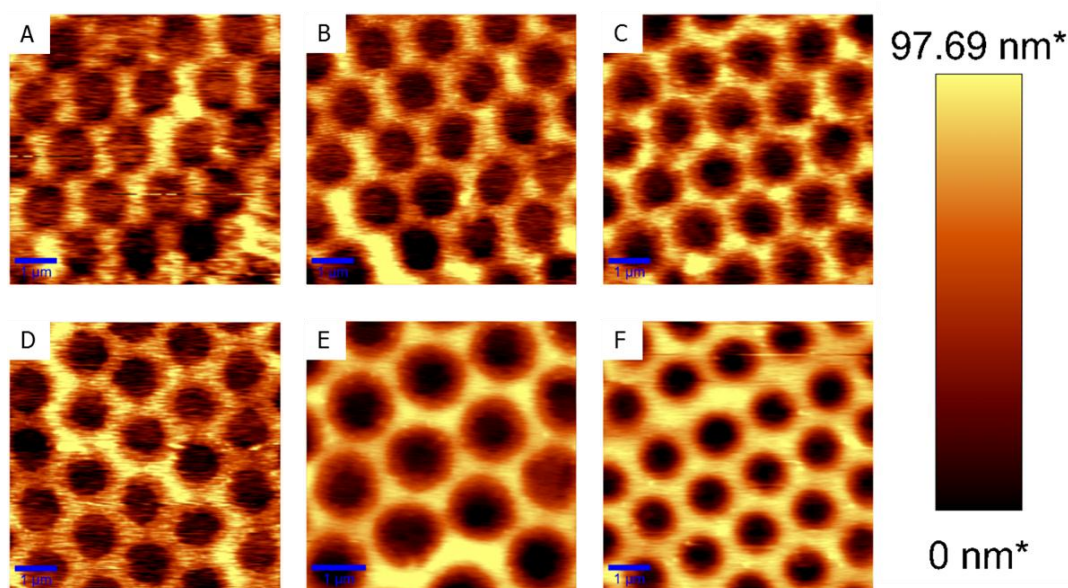

Figure 2.9 - AFM images of Ag nanoholes of 1500 nm periodicity. D/P A) 0.71 B) 0.69 C) 0.64 D) 0.64 E) 0.59 F) 0.53. The scale bar represents 1 μm in all images. The colour bar represents the vertical height of the arrays.

The AFM images show the transition from nanotriangle array (Images A and B), in which the metal triangles are isolated but almost touching, to nanohole array (Images C

to F), in which the metal triangles meet and eventually form a metal lattice as the D/P ratio further decreases.

The diameters of the nanoholes were evaluated from the AFM images and a mean diameter value was calculated for each substrate set. The physical properties of the nanotriangle and nanohole array substrates used in this investigation are shown in Table 2.9.

Etch Time - min	P = 650 nm		P = 820 nm		P = 1000 nm		P = 1500 nm	
	D - nm	D/P	D - nm	D/P	D - nm	D/P	D - nm	D/P
0	650	1.00	820	1.00	1000	1.00	1500	1.00
1	468	0.72	631	0.77	680	0.68		
2	390	0.60	566	0.69	610	0.61	1065	0.71
4	299	0.46	467	0.57	590	0.59	1035	0.69
6	293	0.45	459	0.56	530	0.53		
8	273	0.42	426	0.52	500	0.50	967	0.64
10			353	0.43	430	0.43		
12							956	0.64
15							885	0.59
18							795	0.53

Table 2.9 - Physical properties of Ag nanotriangle and nanohole arrays.

As expected, both the diameter of the holes and the D/P decrease with increasing etch time. As spheres of 1500 nm initial diameter were larger in size, longer etch times were required to achieve comparable D/P values. It should be noted that there are two substrate sets of 1500 nm periodicity with D/P 0.64. This is due to only a slight decrease in hole diameter between the substrates etched for 6 and for 8 min resulting in both substrate sets having a calculated D/P = 0.64.

Nanotriangle and nanohole arrays did not image as well as the FON/FOEN substrates in SEM analysis. This was thought to be due to the presence of a complete metal layer in FON/FOEN substrates which aided conductance of the beam and surface electrons preventing a build-up of charge and burning of the sample. As a result, AFM analysis was used to physically characterise all nanotriangle and nanohole substrates.

2.2.3.2 Optical characterisation of the arrays

The λ_{LSPR} exhibited by the samples is shown in Table 2.10.

P = 650 nm		P = 820 nm		P = 1000 nm		P = 1500 nm	
D/P	λ_{LSPR} - nm	D/P	λ_{LSPR} - nm	D/P	λ_{LSPR} - nm	D/P	λ_{LSPR} - nm
1.00	OSR	1.00	OSR	1.00	OSR	1.00	OSR
0.72	513	0.77	OSR	0.68	OSR	0.71	OSR
0.60	567	0.69	549 700	0.61	OSR	0.69	OSR
0.46	510 700	0.57	480 668 868	0.59	520	0.64	OSR
0.45	542 637	0.56	513 895	0.53	520	0.64	OSR
0.42	513 747	0.52	507 557 640	0.50	498 645 740 819	0.59	OSR
		0.43	528 670 807 842	0.46	498 645 740 819	0.53	649

Table 2.10 - LSPR wavelengths for Ag nanohole array samples. OSR denotes that the LSPR peak is outside the spectral range of 400 - 900 nm.

Variation of the periodicity and D/P resulted in tuning of the LSPR wavelength of the arrays from the visible to the IR wavelength region. However, this investigation was solely focussed on the optical properties of the arrays within the visible to near-IR spectral window as this region covers the commonly used Raman systems (514.5, 633 and 785 nm) hence LSPR spectroscopy was performed using a spectrometer that had a spectral range of 400 – 900 nm. The LSPR of nanotriangle samples and arrays of larger periodicities and D/P values were excited above 900 nm. This was expected as the LSPR has been reported to red-shift in samples with large periodicities.[171] Decreasing the D/P from 0.72 to 0.60 in arrays of 650 nm periodicity resulted in a LSPR red-shift indicative of plasmon coupling. When the D/P was decreased to within the nanohole array region (D/P < 0.6), the substrates supported a LSPR in the visible wavelength range however, as the D/P further decreased, the LSPR exhibited by the substrates did not significantly change. Multiple LSPR peaks were often observed from these samples as a result of the excitation of multiple plasmonic modes.[171] The observations noted from the optical characterisation of nanotriangle and nanohole arrays were in good agreement with results reported for similar substrates.[74, 170]

2.2.3.3 Raman spectroscopy

The nanotriangle and nanohole arrays were analysed under 633 and 785 nm excitation using identical parameters (50 x objective, 10 s acquisition time, and 1% laser power) to those used in the Raman analysis of the FON/FOEN arrays. The data obtained is shown in Figure 2.10.
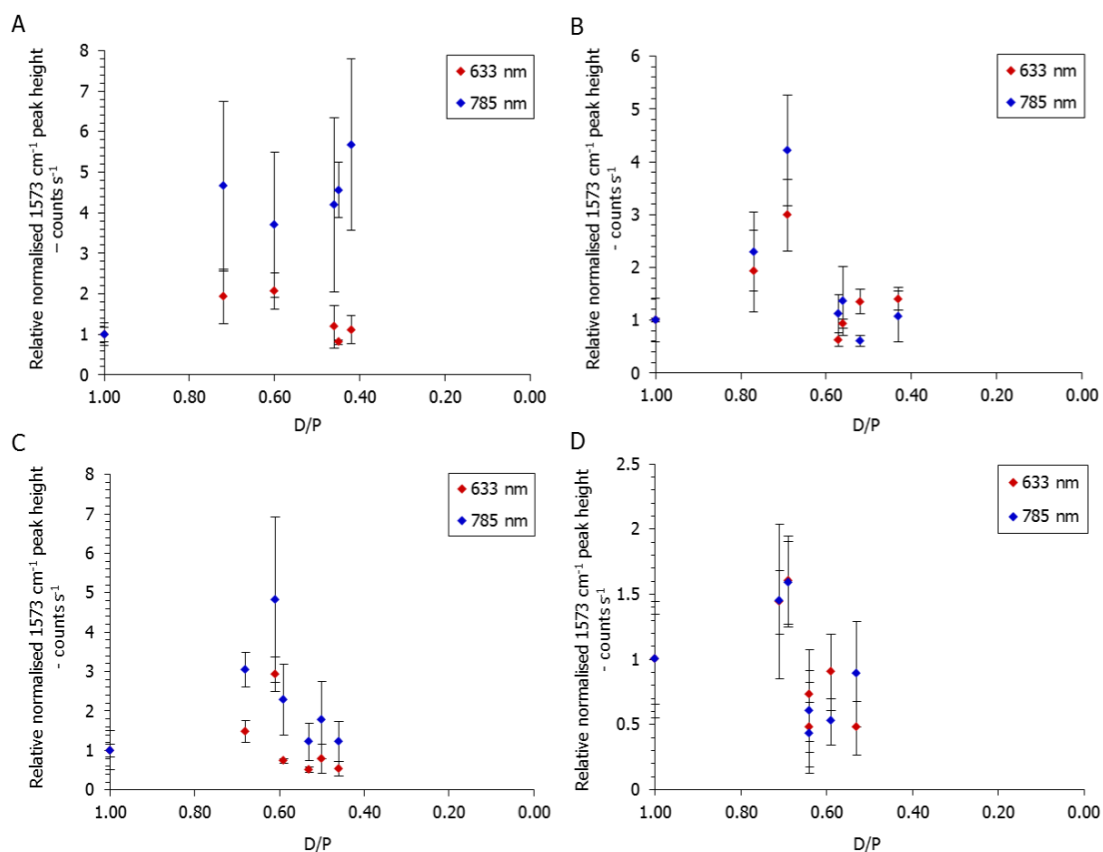

Figure 2.10 - Raman response of Ag nanotriangle and nanohole arrays at 633 (red) and 785 nm (blue) excitation. A) 650 nm periodicity B) 820 nm periodicity C) 1000 nm periodicity D) 1500 nm periodicity. The data points represent the mean height of the 1573 cm^{-1} peak calculated from four replicate substrates. The error bars represent two standard deviations about the mean.

The Raman response values are normalised with respect to the response observed from the unetched nanotriangle samples (D/P = 1.0) to ascertain the effect of decreasing the hole diameter and increasing the spacing between the holes on the Raman response. The Raman response data from all samples investigated evidently demonstrated that the D/P ratio has a significant effect on the SERS enhancement. The trend observed was similar for all analysed samples; the Raman response increased and reached maximum values for samples in the transition region (0.75 ≥ D/P ≥ 0.60) followed by a decrease to approximately the same values as those exhibited by unetched nanotriangle arrays. The only exception to this trend was the 650 nm

periodicity series excited at 785 nm in which the greatest Raman response was obtained from the samples with a D/P of 0.42. In general, the Raman response was higher when 785 nm excitation was used however; the reproducibility of the signals was poorer at this wavelength as highlighted by the larger error bars. The error bars for the 650 nm periodicity series were relatively large at 785 nm excitation and this variability may, in part, explain the differences in Raman response trend exhibited by this series of samples. Additionally, the substrate of 650 nm periodicity that exhibited maximum Raman response at 785 nm excitation supported a LSPR at 747 nm. Hence, efficient coupling between the excitation wavelength and the surface plasmon of the structure may further explain the high Raman response observed from this sample. The properties of the samples that exhibited optimum Raman response at both excitation wavelengths were examined in an attempt to understand the enhancement observed from these samples. The properties are shown in Table 2.11 and Table 2.12 for 633 and 785 nm excitation, respectively.

Sphere diameter – nm	Etch time - min	D/P	Raman intensity – a.u.	Relative response vs. nanotriangle	λ_{LSPR} - nm
650	2	0.60	27550	2.1	567
820	2	0.69	20560	3.0	549, 700
1000	2	0.61	2505	2.9	OSR
1500	4	0.69	16509	1.6	OSR

Table 2.11 - Properties of optimal Ag nanohole substrates based on Raman response at 633 nm excitation.

As discussed previously, the optimum substrates for all periodicities had a D/P ratio within the transition region (D/P 0.6 – 0.75). Optical characterisation of the substrates revealed that the majority of the arrays with a D/P ratio between 0.6 and 0.4 had LSPR bands that were close enough to the 633 and 785 nm excitation wavelengths to obtain efficient coupling. Therefore, these substrates would be expected to exhibit maximum Raman response. However, the experimental data did not support this theory. None of the optimum substrates supported a surface plasmon at a wavelength which would result in optimal coupling between the incident radiation and the surface plasmon. If the Raman response observed was wholly dependent on the coupling between excitation source and the sample surface plasmon, it would be expected that the samples of 1500 nm periodicity with a D/P ratio of 0.53 would give the optimum Raman response as these substrates supported a surface plasmon at 649 nm which would result in highly efficient coupling. However, the maximum Raman response

observed from samples of 1500 nm periodicity was for D/P ratio of 0.69 in which the LSPR wavelength was greater than 900 nm resulting in poor coupling between the incident radiation and the surface plasmons. Thus, closely tuning the excitation wavelength to the LSPR wavelength of the structures did not result in the optimal Raman response.

Sphere diameter – nm	Etch time - min	D/P	Raman intensity – a.u.	Relative response vs. nanotriangle	λ_{LSPR} - nm
650	8	0.42	2105	5.7	513, 747
820	2	0.69	12986	4.2	549, 700
1000	2	0.61	7430	4.8	OSR
1500	4	0.69	6318	1.6	OSR

Table 2.12 - Properties of optimal Ag nanohole substrates based on Raman response at 785 nm excitation.

Analysis of the optimal substrate properties for 785 nm excitation resulted in similar conclusions. Again, theory predicted that optimal coupling, and therefore greatest SERS enhancement, should occur in samples with low D/P ratios as the LSPR bands of these samples were closely matched to the excitation wavelengths. However, the optimum Raman response was exhibited by samples in the transition region and so was not a result of efficient coupling between the incident radiation and surface plasmon.

The highest Raman intensity at 633 and 785 nm excitation was observed for substrates of 650 nm periodicity with D/P 0.60 and 820 nm periodicity with D/P 0.69 respectively. This was in good agreement with the previously discussed research reported by Hatab and co-workers in which they concluded that maximum SERS enhancement was obtained when the periodicity of the nanostructured arrays was close to that of the wavelength of the excitation source.[30]

AFM analysis demonstrated that samples within the transition region consisted of a hexagonal array of almost-connected triangles. The distance between the triangles is much smaller than the diameter of the holes giving rise to plasmon coupling and an intense local electric field enhancement. Therefore it was concluded that the enhanced Raman responses exhibited by samples in the transition region was a result of the small inter-particle distance between triangles in the arrays.

Comparison of Raman response of Ag and Au nanohole arrays

Nanohole arrays of identical dimensions were used for this study. The arrays used were of 1000 nm periodicity and had been etched to give a D/P ratio of 0.61. Raman analysis was performed using 633 and 785 nm excitation. Figure 2.11 shows the mean peak height calculated from five replicate scans over the sample surface.
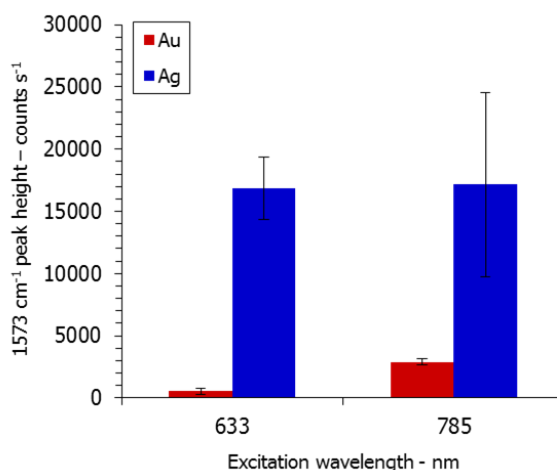

Figure 2.11 - Comparison of SERS response of Au (red) and Ag (blue) nanohole arrays of 1000 nm periodicity and D/P 0.61. Five replicate scans were collected, using an acquisition time of 10 s, from each substrate at each excitation wavelength. The error bars represent 2 standard deviations about the mean.

As expected, the Ag nanohole arrays exhibit a much larger Raman response than the analogous Au substrates. Greater SERS enhancement was observed from both metallic substrates at 785 nm excitation however poor signal reproducibility was attained from the Ag nanohole array at this excitation wavelength.

2.2.4 Comparison of properties of FOEN and nanohole arrays of same periodicity

It was of interest to compare the Raman response of the two types of array, of identical dimensions, that could be fabricated by modified NSL. The Raman responses of FOEN and nanohole substrates of 650 nm periodicity were compared at 633 and 785 nm excitation and the results were normalised to account for differences in laser power. The Raman intensities exhibited by the FOEN sample series of 650 nm initial sphere diameter were the lowest observed for the FOEN arrays investigated. This is in contrast to the nanohole arrays of 650 nm periodicity which showed the highest Raman intensities of the nanohole samples analysed. Figure 2.12 shows the results of the direct comparison between the two classes of substrate with respect to etch time.
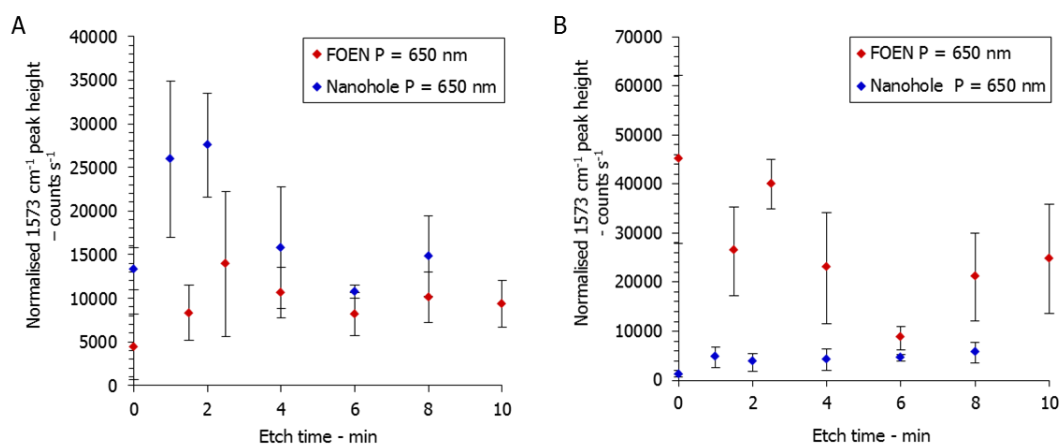
Figure 2.12- Comparison of SERS response from Ag FOEN (red) and Ag nanohole (blue) arrays of 650 nm periodicity at A) 633 nm excitation and B) 785 nm excitation. Each data point represents the mean 1573 cm^{-1} peak height calculated from four replicate analyses of four separate substrates. The error bars represent two standard deviations about the mean.

At 633 nm excitation, the Raman response of the nanohole and FOEN arrays follow the same trend however greater SERS enhancement was observed from the nanohole array substrate. At 785 nm excitation, the Raman response of the FOEN array was higher than that of the nanohole arrays. These observations were attributed to the LSPR of the substrates being well matched to the excitation wavelength; the nanohole substrates had LSPR within the range of 513 to 747 nm whereas the FOEN substrates had LSPR in the range of 607 to 873 nm. It was concluded that, in general, FOEN arrays exhibited larger Raman enhancements than nanohole arrays however both substrates investigated demonstrated good SERS activity and this study highlights that, depending on the application, the substrate can be selected to maximise the Raman response.

2.2.5 Optimal Substrates

The Raman response of nanohole substrates that had exhibited high SERS enhancement in previous studies was compared to that of Klarite, a commercially available SERS substrate. Klarite is a photolithography fabricated nanostructured silicon surface that consists of a square lattice of inverted square pyramidal pits covered by a layer of Au. Klarite has been shown to give large Raman enhancements and produce highly reproducible SERS signals.[172] This substrate has been often used by other groups as a comparison substrate when investigating the potential of their own SERS active surfaces.[173, 174] This investigation was performed using 785 nm excitation

as although Klarite exhibits good SERS enhancement at both 633 and 785 nm excitation,[172] the manufacturers advise that optimal performance of Klarite is achieved at 785 nm excitation.[175] A Ag nanohole array of 1000 nm periodicity and D/P ratio of 0.68 was used in this investigation. This substrate had been previously shown to exhibit good Raman response. The optical properties of bimetallic nanohole arrays had been previously investigated by the Masson group in which it was shown that they exhibited a similar optical response to single-layer metallic nanohole arrays.[74] It was further demonstrated that the bimetallic nanohole substrates showed an increased sensitivity to the bulk refractive index thus highlighting their possible use in SPR sensing. It was postulated that these bimetallic nanostructures may have the potential to be highly SERS active and so the Raman response was investigated alongside that of a Ag nanohole array of identical dimensions and Klarite.

All samples were coated with a 4-NBT SAM and analysed at 785 nm excitation under identical conditions. Figure 2.13 shows the mean 1573 cm^{-1} peak height calculated from five replicate scans taken across the sample area.
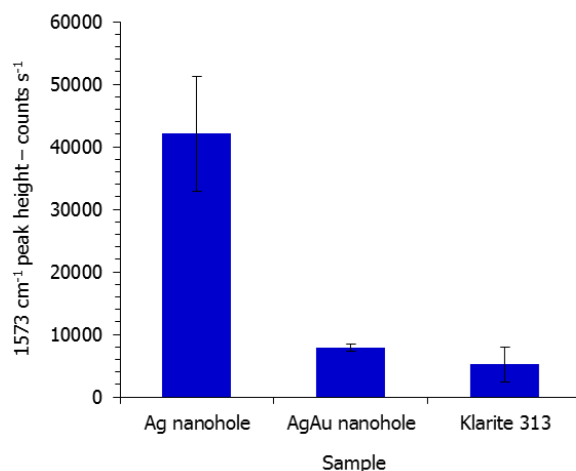

Figure 2.13 - Comparison of SERS activity of optimum substrates. Five replicate scans were collected using an acquisition time of 10 s from each sample at 785 nm excitation using 0.01 % laser power. The error bars represent 2 standard deviations about the mean.

The Raman response from the Ag nanohole array substrate was most intense. The bimetallic AgAu nanohole substrate and Klarite exhibited comparable SERS enhancement however the signal reproducibility was much lower from Klarite (the relative standard deviations were 8% and 53% for AgAu nanohole substrate and Klarite, respectively). It could be concluded that the nanohole arrays fabricated by NSL

exhibited both larger SERS enhancements and better signal reproducibility than the commercially available SERS substrate under the experimental conditions.

2.3 Conclusion

The etch step was determined to have significant influence on the physical, optical and Raman properties of both FOEN and nanohole arrays. Increasing the etch time decreased the feature diameter, increased the inter-particle gap and increased the roughness of the feature. This was demonstrated by the physical characterisation of the arrays by SEM and AFM analysis.

Etching of the polystyrene masks significantly altered the LSPR wavelength of the nanostructures. Short etch times resulted in a red-shift of the LSPR which was followed by a blue-shift at longer etch times. The red-shift that occurred when the samples were etched for short periods of time indicated that plasmon coupling was occurring between spheres/triangles.

The Raman response of both FOEN and nanohole arrays was improved by etching the NSL masks. An improvement of the Raman response with respect to unetched FON arrays of 4.5 at 633 nm excitation and 3.7 at 785 nm excitation was demonstrated by the optimal FOEN arrays. The optimal arrays both had a gap/diameter value of around 0.2 highlighting the importance of plasmon coupling. A similar effect was observed when the Raman response of a series of nanohole arrays was investigated. Substrates with etch times that resulted in a D/P ratio within the transition region (D/P between 0.75 and 0.6) were shown to exhibit maximum Raman response.

The improvement of the Raman response was attributed to two major factors: efficient coupling between the excitation wavelength and the LSPR peak of the substrate and tuning of the inter-particle gap to result in maximum plasmon coupling. Both factors are controlled by the etch time; etching the arrays alters both the LSPR wavelength and the inter-particle spacing. Thus, the use of modified NSL to fabricate nanostructures for use in SERS analysis shows great promise.

Results discussed in this chapter have been published in The Journal of Physical Chemistry C in 2010 (see the Appendix section for the full texts).

2.4 Further Work

The Raman responses for all substrates were calculated on the basis of the Raman signal collected from the illuminated area. The effect of surface area of the structures was, therefore, not taken into account when determining the optimum substrates as the study was designed to compare a range of substrates under the same analysis conditions. It would be interesting to calculate the enhancement factor of the substrates taking into account the differing surface areas to determine if comparable results were obtained. This would also allow direct comparison of the optimal FOEN and nanohole substrates with the wide-range of SERS substrates that have been reported in the literature.

CHAPTER 3 - MAPPING THE LOCATION OF THE RAMAN ENHANCEMENT IN NANOHOLE AND FOEN ARRAYS

Chapter 2 described the methodical investigation into the physical and optical bulk properties of FOEN and nanohole arrays. It was of great interest to investigate the electric field distribution and Raman properties of these arrays at the nanoscale.

Research in the literature has investigated the electric field intensity in nanotriangle and nanohole arrays using simulations to predict the location of maximum electric field.[128, 129] However, few studies has experimentally investigated the location of high electric field intensities in such arrays. Raman microscopy is a powerful tool to image the location of hot-spots in SERS substrates.

In an effort to visualise the SERS hot-spots, Raman maps of a series of arrays with varying D/P ratio were collected. This investigation would provide information on the frequency, density and shape of the hot-spots and aid the overall understanding of the Raman enhancement effect of the arrays.

3.1 Experimental

3.1.1 Sample Preparation

All substrates were prepared by Dr Debby Correia-Ledo at Université de Montréal using modified NSL as described in sections 2.1.1.1 and 2.1.1.2. Four identical, replicate samples for each periodicity and D/P were prepared. To form the Raman reporter SAM, the array samples were immersed in a 0.5 mM solution of 4-NBT (Sigma-Aldrich), initially dissolved in ethanol and further diluted in water, for 16 hours. The samples were then thoroughly washed with water followed by ethanol, dried under a stream of N_2 gas and stored in the dark prior to Raman mapping analysis.

3.1.2 Raman Mapping

Raman mapping was carried out using confocal WITec Alpha300 R instrumentation (WITec, Ulm, Germany) and either a 532 or 633 excitation laser (532 nm – WITec, full power = 37 mW; 633 nm – Research Electro-Optics, Boulder CO, USA, full power = 13 mW) This instrumental set-up allowed mapping of approximately 10 x 10 µm areas. A 10 x 10 µm area was mapped and a spectra taken every 100 nm. A 15 x 15 µm area was mapped on samples with a periodicity of 1500 nm. The laser power values were measured using a handheld LaserCheck power meter (Coherent, Santa Clara CA, USA). The approximate unfocussed powers of the 532 and 633 nm excitation lasers were 0.5 mW (1.4 % of total power) and 0.3 mW (2.3 % of total power) respectively. The parameters were set as follows: 0.005 s integration time, 100x objective (Olympus MPlan, NA = 0.9), which resulted in approximately 360 – 430 nm optically limited spatial resolution depending on the excitation wavelength used. The peak area of the v(C-C) stretch of 4-NBT at 1573 cm^{-1} was integrated and mapped, using WITec control software, resulting in a false colour image of the Raman intensity of this peak over the analysis area. Three maps were taken from three separate, identically prepared substrates at each etch time. WITec project 2.06 software was used for further data processing.

3.1.3 AFM analysis

The samples were analysed by AFM in close-contact mode on a NanoInk DPN5000 instrument (NanoInk, Inc., Skokie, IL USA). A close-contact Si, N-type tip with a force constant of 25 – 75 N/m (Applied NanoStructures, Inc., Santa Clara, CA, USA) was used. SPM Cockpit v3.3 software (Pacific Nanotechnology Inc., Santa Clara, CA, USA) was used to image the samples. Images were obtained using either low resolution parameters: 256 x 256 pixel resolution with a scan rate of 0.4 Hz or high resolution parameters: 512 x 512 pixel resolution using a scan rate of 0.2 Hz. The scanned areas intentionally included crystallisation defects and/or scratches to act as a point of reference between the AFM and Raman images. The scanned images were processed using SPIP software (Image Metrology, Hørsholm, Denmark) and involved a plane correction procedure followed by a filter being applied to the data to target noise. The resulting images were then adjusted to attain the optimum colour contrast.

3.1.4 FDTD simulations

Finite-Difference Time-Domain (FDTD) calculations were carried out by Anuj Dhawan and Tuan Vo-Dinh at Duke University, North Carolina, United States. The FDTD analysis on the nanohole array substrates was carried out using FullWAVE 6.0 software by R-Soft. The analysis was based on a periodic hexagonal array of nanoholes in 50 nm Ag film (with a 5 nm Ti adhesion layer underneath the Ag layer) fabricated on a silica substrate. The periodicity of the arrays was 1500 nm whilst the diameters of the nanoholes were varied between 300 and 1500 nm (using steps of 150 nm). The simulations were performed with the incident light (532 or 633 nm) being linearly polarized along the *x*-axis of the figures.

3.1.5 Selective immobilisation of analyte in regions of high electric field

Selective immobilisation using silylation chemistry

All chemicals were purchased from Sigma-Aldrich. Three Ag nanohole array samples of 1000 nm periodicity and D/P = 0.61 were incubated in a 1 mM solution of 1-hexadecanethiol (DMF was used as the solvent) for 16 h at r.t. After incubation, the samples were thoroughly washed with ethanol. The samples were then placed in a 1 mM solution of chloro(methyl)diphenylsilane in anhydrous dichloromethane (DCM). This solution also contained 1 mM of *N,N*-diisopropylethylamine, a hindered base, to scavenge free hydrogen ions and prevent hydrolysis of the silane. The samples were incubated for either 30 min or 4 h at r.t. After incubation, the samples were washed with anhydrous DCM, dried and analysed using the WITec microscope at 100x magnification.

Selective immobilisation using place-exchange method

The place-exchange method was based on a procedure published by Beeram and Zamborini.[176] All chemicals were purchased from Sigma-Aldrich except Streptavidin-dylight 633 which was purchased from Pierce (Rockford IL, USA). Bimetallic sample preparation followed the protocol described in section 2.1.1.2. Three bimetallic nanohole array samples of 1000 nm periodicity and D/P = 1.0 were incubated in a 1 mM ethanolic solution of 11-mercaptoundecanoic acid (11-MUA) for 16 h at r.t. These

samples were termed "pure MUA" samples. After incubation, the samples were thoroughly washed with ethanol and air-dried. The second set of samples, termed "place-exchange samples", were placed in a 1 mM ethanolic solution of 2-mercaptoethanol for 16 h at r.t. The samples were then washed with ethanol and immediately placed in a 5 mM solution of 11-MUA for 4 h at r.t. to allow the thiol exchange procedure to occur. After incubation in the 11-MUA solution, the samples were thoroughly washed with ethanol and air-dried. All samples were separately placed into an aqueous solution of 2 mM 1-ethyl-3-(3-dimethylaminopropyl)carbodiimide (EDC) and 5 mM N-hydroxysulfosuccinimide (sulfoNHS) for 1 h. After 1 h, all samples were rinsed with water, air-dried and placed into an aqueous solution of 5 µg/ml Streptavidin-dylight 633. The samples were incubated for 16 h at r.t. before being thoroughly washed with phosphate-buffered saline (PBS) pH 7.4 and air-dried. The samples were analysed by AFM in close-contact mode.

3.2 Results and Discussion

To fully investigate the SERS hot-spots, a series of samples with different periodicities and D/P ratios between 1.0 and approximately 0.4 were prepared by modified NSL, as detailed in section 2.1.1.2 and mapped using excitation wavelengths of 532, 633 and 785 nm. The intensity variation of the peak at 1573cm^{-1} was imaged across the mapped area resulting in false colour images. Three identical samples from each series were mapped and all maps for a particular sample series resembled each other to a high degree.

3.2.1 Experimental Considerations

3.2.1.1 Lateral Resolution

The features observed in the Raman maps were limited by the lateral resolution of the Raman instrument set-up. The lateral resolution of the set-up is dependent on the laser spot size which is in turn dependent on the excitation wavelength and the numerical aperture (NA) of the objective used for analysis. The diffraction limit of the instrumental set-up can be calculated to a good approximation using equation 3.1 where d is the laser spot diameter, λ is the excitation wavelength used and NA is the numerical aperture value of the objective.

$$d = \frac{\lambda}{2 \; x \; NA}$$

(3.1)

Using a 100x objective with a NA value of 0.9 and assuming no optical aberrations in the optical system, the approximate diffraction limits calculated for each excitation wavelength are shown in Table 3.1.

Excitation wavelength – nm (λ)	Calculated diffraction limit - nm
532	360
633	430
785	532

Table 3.1 - Calculated diffraction limits for the SERS experimental set-up using a 100 x objective (NA = 0.9) and excitation wavelengths of 532, 633 and 785 nm.

The calculated diffraction limit for 785 nm excitation is larger than the majority of features present in the series of nanohole and FOEN arrays. It was also found experimentally that the resolution of maps collected at this excitation wavelength was too poor to visualise any features. Therefore, only data collected using 532 and 633 nm excitation is included in this discussion.

3.2.1.2 The polarisation of the excitation source

It is important to note that in all cases, circularly polarised light was used. This explains why all the features in the false colour images obtained were symmetrical. The polarisation of the incident light has been shown to affect the magnitude and the location of the maximum electric field.[177, 178] However, the nature of this investigation was not to investigate how the polarisation of the light affected the electric field but instead to compare different structures of related arrays to determine if the location of electric field varied. Therefore, as all samples were analysed under identical conditions, the polarisation of the incident light was not an issue.

3.2.2 Raman maps of nanohole arrays at 532 and 633 nm excitation

The maps collected during this investigation clearly demonstrate that the locations of the regions of maximum Raman enhancement change as the transition from nanotriangle to nanohole array occurs. As this is a qualitative investigation into the location, shape and density of the hot-spots, all maps do not correspond to the same colour intensity scale. If this was the case, it would not be possible to observe the features in the false colour maps as the average intensity of the maps varies with the periodicity and D/P as discussed in Chapter 2. The region limits discussed were based on maps obtained from samples with 1500 nm periodicity as these maps exhibited the highest resolution.

Generally, all maps from samples with similar D/P ratios resemble one other to a high extent, irrespective of the periodicity of the array or excitation wavelength. Maps from samples with a periodicity of 1500 nm exhibited the best resolution as the features in these samples are larger than the instrumental set-up diffraction limit using excitation sources of 532 and 633 nm.

Table 3.2 and Table 3.3 show the SERS maps obtained at 532 and 633 nm excitation, respectively. The Raman maps collected from nanotriangle samples with a D/P of 1.0 suggest that the highest Raman intensity lies on the network of nearly connected triangles that surround the array of holes. For P = 650 nm and 820 nm, the resolution of the maps is too low to visualise the individual triangles. At P = 1000 nm and 1500 nm, the individual triangles can be observed. This result has been corroborated in recent work by Notingher *et al*. who performed combined AFM-Raman mapping of NSL-fabricated nanotriangle arrays at 532 nm excitation.[179]

As the D/P decreases to between 0.77 and 0.64, at the upper limit of the transition region, the maps obtained suggest that the maximum Raman enhancement is located on the metal lattice that surrounds the holes.

As the D/P further decreases to between 0.64 and 0.60, the location at which maximum Raman enhancement occurs alters. The experimental maps indicate that the highest Raman intensity lies around the rim of the nanohole resulting in a "donut"-like shape. This can be best observed in the map obtained for 1500 nm periodicity.

For samples in the nanohole region (D/P of 0.60 or below), the maximum Raman intensity appears to be located in the centre of the nanoholes. The bright spots in the Raman maps are arranged in a hexagonal pattern and have a centre to centre spacing that perfectly corresponds to the periodicity of the samples. The centre of the nanoholes has no metal and so would not be expected to be the source of SERS enhancement. It is postulated that the electric field is concentrated in the hole in samples with D/P < 0.60, leading to the centre of the hole acting as a point source for the maximum Raman enhancement.
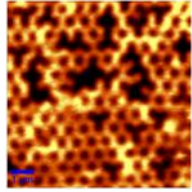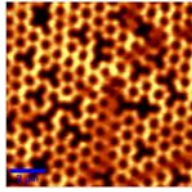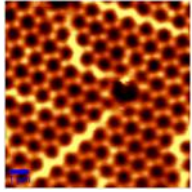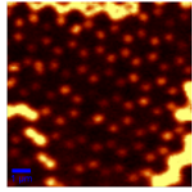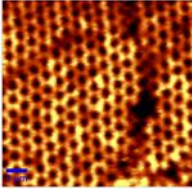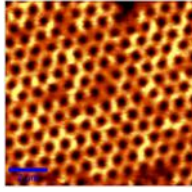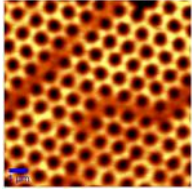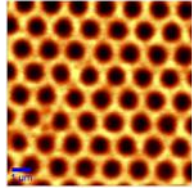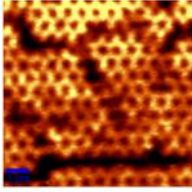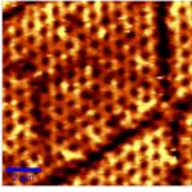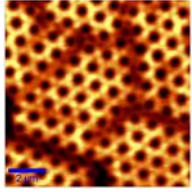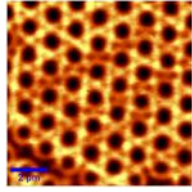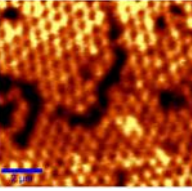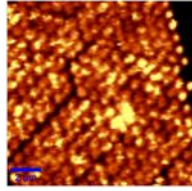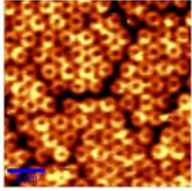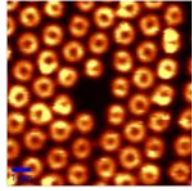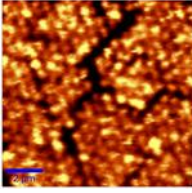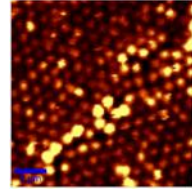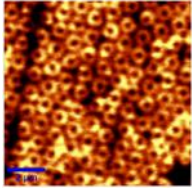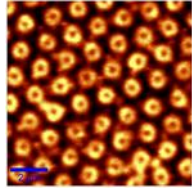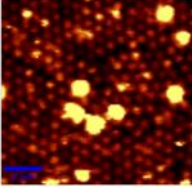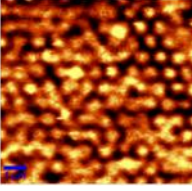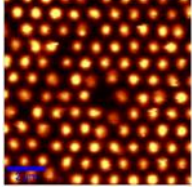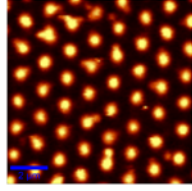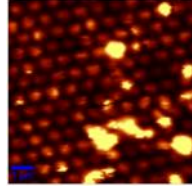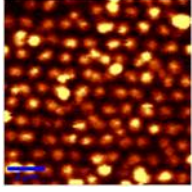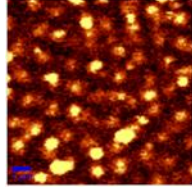
P	650 nm	820 nm	1000 nm	1500 nm
Nanotriangle D/P = 1.0				
Transition region 0.77 ≥ D/P ≥ 0.64				
Nanohole D/P < 0.64				

Table 3.2 - False colour Raman maps of the intensity of 1573 cm^{-1} peak across the sample area of a series of Ag nanotriangle and nanohole arrays with a deposited metal thickness of 125 nm and varying periodicities and D/P. All maps were obtained using an incident wavelength of 532 nm and a laser power of 0.5 mW. All images are 10 x 10 μm. All scale bars represent either 1 or 2μm.

81

P	650 nm	820 nm	1000 nm	1500 nm
Nanotriangle D/P = 1.0				*
Transition Region 0.77 ≥ D/P ≥ 0.64				*
Nanohole D/P < 0.64				

Table 3.3 - False colour Raman maps of the intensity of 1573 cm^{-1} peak across the sample area of a series of Ag nanotriangle and nanohole arrays with a deposited metal thickness of 125 nm and varying periodicities and D/P. All maps were obtained using an incident wavelength of 633 nm and a laser power of 0.3 mW. All images are 10 x 10 μm except P 1500 nm, D/P 1.0 and 0.71 (denoted by *) which are 15 x 15 μm. All scale bars represent either 1 or 2 μm.

The false colour images obtained suggest that the plasmon mode varies with decreasing D/P. At D/P = 1.00, the plasmon is localised on the triangular metallic islands that surround the network of holes. As the D/P decreases to between 0.77 and 0.64, the plasmon propagates along the honeycomb-like network of silver that surrounds the holes. Within the nanohole size regime (D/P < 0.64), the plasmon is localised to around the rim of the nanoholes at D/P 0.64 or at the centre of the nanoholes for lower D/P. This observation is in good agreement with reports in the literature of the plasmon mode present in similar structures.[170]

It is interesting to note the effect of array dislocations and defects on the SERS intensity; in samples with D/P = 1.0, dislocations and defects give an increased electric field enhancement as shown by yellow/orange lines in the false colour images. However, the defects and dislocations give a lower electric field enhancement in all samples of D/P < 1.0, with samples in the transition region showing moderate SERS enhancement from the defect areas as shown by the orange lines and nanohole samples showing low SERS intensity from the defected regions as illustrated by black lines. The reason for this is unclear.

3.2.3 Raman maps of FOEN arrays at 532 and 633 nm excitation

An analogous investigation into the location of the Raman enhancement in a series of FOEN arrays with decreasing D/P was undertaken. The results would provide an interesting comparison between the locations of the regions of maximum Raman enhancement in nanohole and FOEN arrays. For ease of comparison in this discussion, the FON and FOEN arrays are described by D/P as opposed to gap/diameter as used in Chapter 2. Ag FOEN arrays with periodicities of 650, 820, 1000 and 1500 nm and D/P of between 1.0 and 0.5 were prepared using modified NSL as outlined in section 2.1.1.1. FOEN arrays with a periodicity of 650 nm were difficult to prepare as samples with high D/P often delaminated during the wash steps in the fabrication process and the polystyrene spheres sometimes spontaneously "popped" off in samples with low D/P. As a result, only one sample with a periodicity of 650 nm and a D/P in the transition region was able to be prepared and mapped at 633 nm excitation. Samples were mapped using excitation wavelengths of 532 and 633 nm and the intensity of the C-C vibration at 1573 cm^{-1} was used to create a false colour image of the Raman

enhancement across the sample as shown in Table 3.4 and Table 3.5. As noted before, the false colour maps are not all to the same colour scale in order to aid clear visualisation of the features of the arrays.
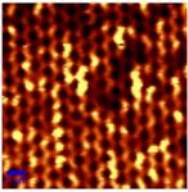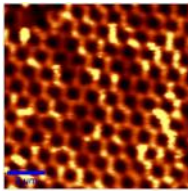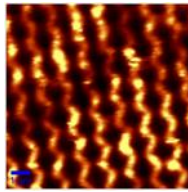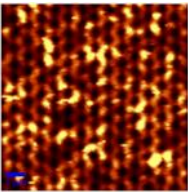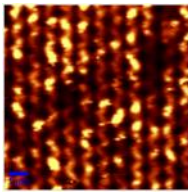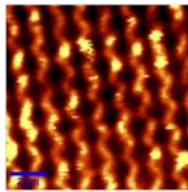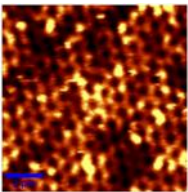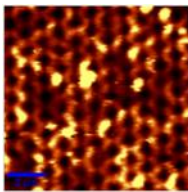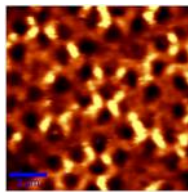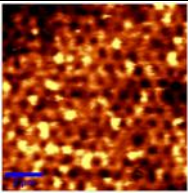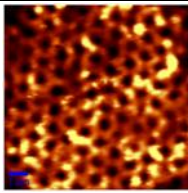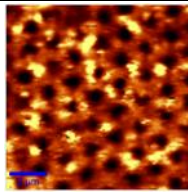
P	820 nm	1000 nm	1500 nm
FON D/P = 1.0			
Transition region 0.77 ≥ D/P ≥ 0.64			
FOEN D/P < 0.64			

Table 3.4 – False colour Raman maps of the intensity of 1573 cm^{-1} peak across the sample area of a series of Ag FON and FOEN arrays with a deposited metal thickness of 125 nm and varying periodicities and D/P. All maps were obtained using an incident wavelength of 532 nm and a laser power of 0.5 mW. All images are 10 x 10 μm. All scale bars represent 1 or 2 μm.
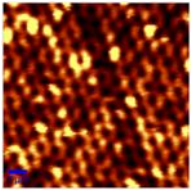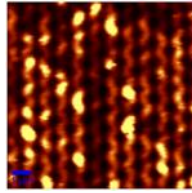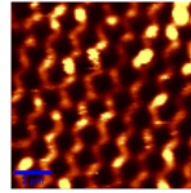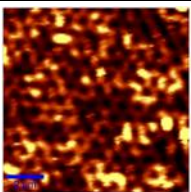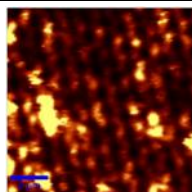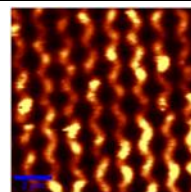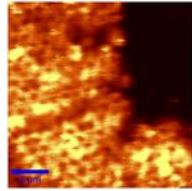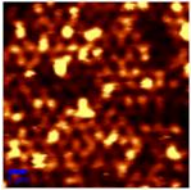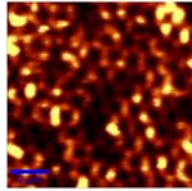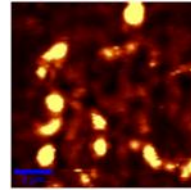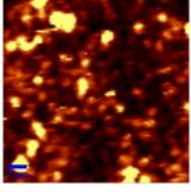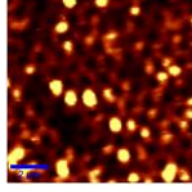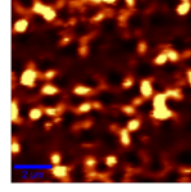
P	650 nm	820 nm	1000 nm	1500 nm
FON D/P = 1.0				
Transition region $0.77 \geq D/P \geq 0.64$				
FON D/P < 0.64				

Table 3.5 – False colour Raman maps of the intensity of 1573 cm^{-1} peak across the sample area of a series of Ag FON and FOEN arrays with a deposited metal thickness of 125 nm and varying periodicities and D/P. All maps were obtained using an incident wavelength of 633 nm and a laser power of 0.3 mW. All images are 10 x 10 µm. All scale bars represent 1 or 2 µm.

The results demonstrated that all false colour maps from FOEN samples are almost identical, irrespective of the periodicity of the array, the D/P or excitation wavelength used. All samples demonstrate the same pattern of high electromagnetic enhancement. It can be clearly observed that the regions of maximum Raman enhancement are located on the Ag lattice that surrounds the Ag-covered polystyrene spheres. In fact, in all maps obtained, little or no Raman enhancement was observed on the Ag-coated sphere. This suggests that the observed Raman enhancement is a result of an increase in electromagnetic field strength at the crevices and junctions where the nanostructured features are in closest proximity to one another due to the coupling of plasmons in this region. The results obtained correlated well with the findings of theoretical and experimental investigations conducted by Farcau and Astilean into the location of hot-spots in both Ag and Au metal film over sphere arrays.[133, 136] and with

computational calculations performed by García-Vidal and Pendry on roughened Ag nanostructures with a similar cross-section to that of metal FOEN substrates.[180]

3.2.3.1 Comparison of the SERS intensity pattern observed from nanohole and FOEN arrays

In order to compare the SERS intensity pattern from nanohole and FOEN arrays, a cross-sectional analysis was carried out on the false colour images obtained from Ag nanohole and FOEN arrays with a periodicity of 1500 nm at 532 nm excitation. This was achieved by marking a line over six holes in the nanohole arrays or six spheres in the FOEN arrays using the WITec software. All marked lines began at the same point on an array; the metal island adjacent to the widest part of a hole/sphere and traced across the diameter of six holes/spheres. The software then extracted the intensity of the 1573 cm^{-1} peak over the marked line resulting in a cross-section plot for each D/P which was stacked to create Figure 3.1 and Figure 3.2. It should be noted that due to the similarities in diameter of the nanoholes etched for 6 and 8 mins, both samples have a calculated D/P of 0.64 as discussed in section 2.2.3.1.
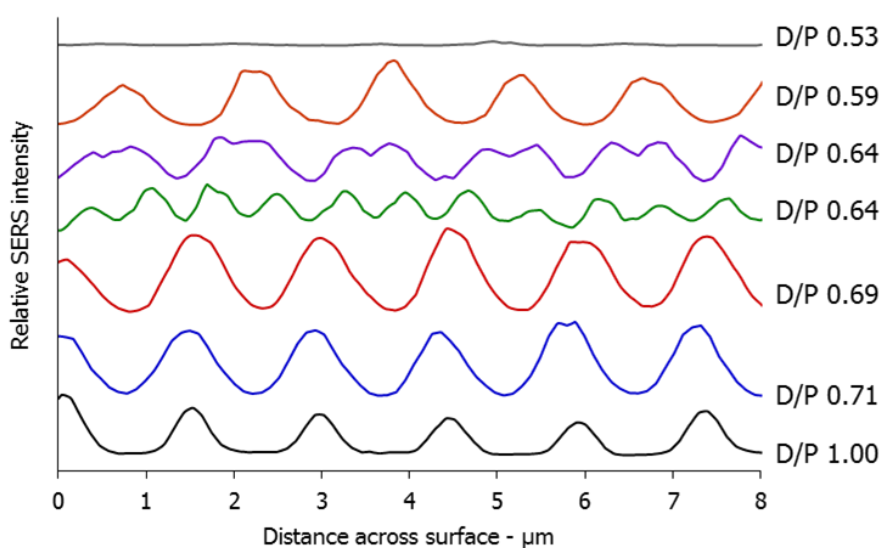
Figure 3.1 - Cross-section plot of Raman intensity across 1500 nm periodicity Ag nanotriangle and nanohole arrays of varying D/P and a deposited metal thickness of 125 nm. The Raman spectra were obtained using 532 nm excitation and 0.5 mW laser power.
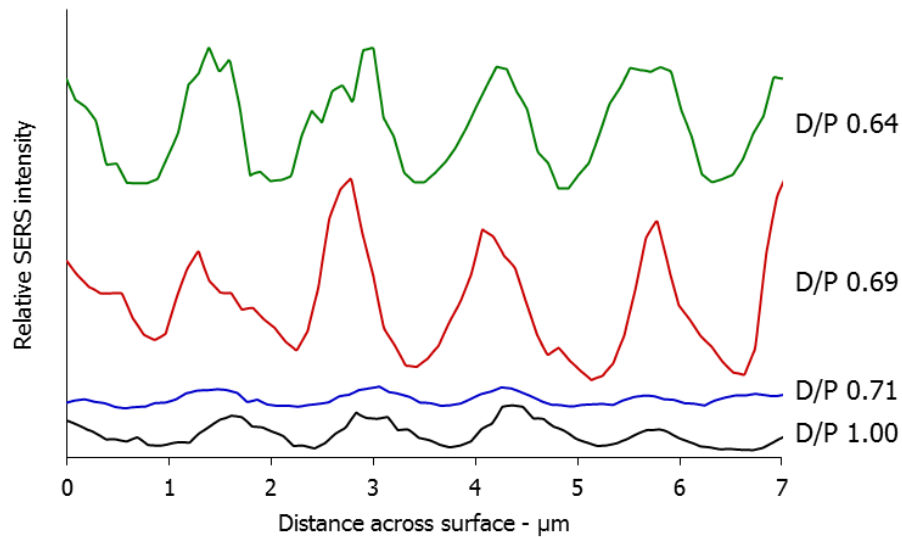
Figure 3.2 - Cross-section plot of Raman intensity across 1500 nm periodicity Ag FON and FOEN arrays of varying D/P and a deposited metal thickness of 125 nm. The Raman spectra were obtained using 532 nm excitation and 0.3 mW laser power.

The wave amplitudes highlight that the greatest SERS intensity was obtained at a D/P equal to 0.69 for both the nanohole and FOEN arrays. This observation correlated well with the findings of Chapter 2 in which the greatest SERS intensity was consistently attained from samples in the transition region.

Analysis of the SERS intensity cross-sections clearly highlights the differences in location of maximum SERS intensity on the arrays between nanohole and FOEN substrates. The cross-sectional analysis of the nanohole array substrates evidently demonstrates that the position of the maximum SERS intensity varies with decreasing D/P. As D/P decreases, the location of the SERS maximum intensity remains constant until D/P 0.69 when it shifts by 180° so that the position at which maximum intensity was attained in samples with D/P > 0.69 now gives minimum SERS enhancement. However, the cross-sectional analysis of FOEN arrays shows that the position of the maximum SERS intensity on the arrays does not vary with decreasing D/P indicating that the maximum electric field is always observed from the metal that surrounds the spheres

3.2.4 Raman and AFM correlation analysis

In order to prove where the Raman enhancement originated, it was necessary to conduct Raman analysis and a physical characterisation technique on the same area of the substrate. AFM was used to physically analyse the surface as it was thought that this technique would be compatible with scanning the same area as the Raman measurements were taken from. A Raman map was taken from an area on the substrate that included easily recognisable dislocations and defects. These features were then used to locate the same region under the AFM instrument microscope and scan it. By overlaying the Raman map and the AFM image, the spectroscopic information from the Raman map could be correlated with the topographical information from the AFM image elucidating the source of Raman enhancement. In addition, simultaneous cross-sectional analysis was carried out to allow clear correlation of the SERS intensity to the nanostructure topography across the surface.

The correlation of Raman maps and AFM images from FOEN array substrates had been described in the literature but no equivalent investigation had been reported for nanohole array substrates of varying D/P.[133] Correlated Raman and AFM analysis was performed on nanohole substrates with three different D/P ratios so as to fully investigate the differing origins of Raman enhancement as the transition of nanotriangle to nanohole progressed. Figure 3.3 shows the results of the correlated Raman and AFM analysis of a Ag nanohole array of 820 nm periodicity in the transition region (D/P = 0.69).

Raman   Raman /AFM overlay   AFM
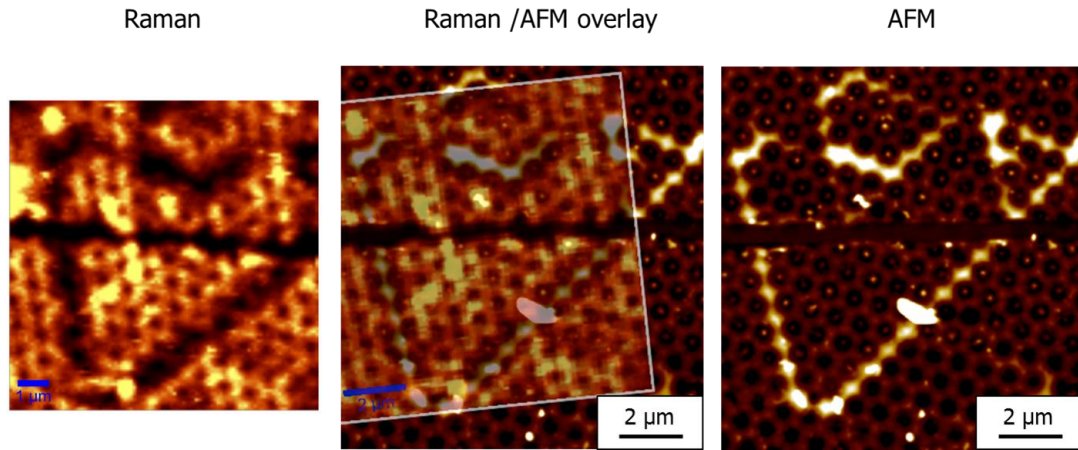
Figure 3.3 - Overlay of Raman false colour map and AFM image obtained from Ag nanohole array of 820 nm periodicity, a deposited metal layer thickness of 125 nm and D/P 0.69. The Raman map was obtained using an incident wavelength of 633 nm and a laser power of 0.3 mW.
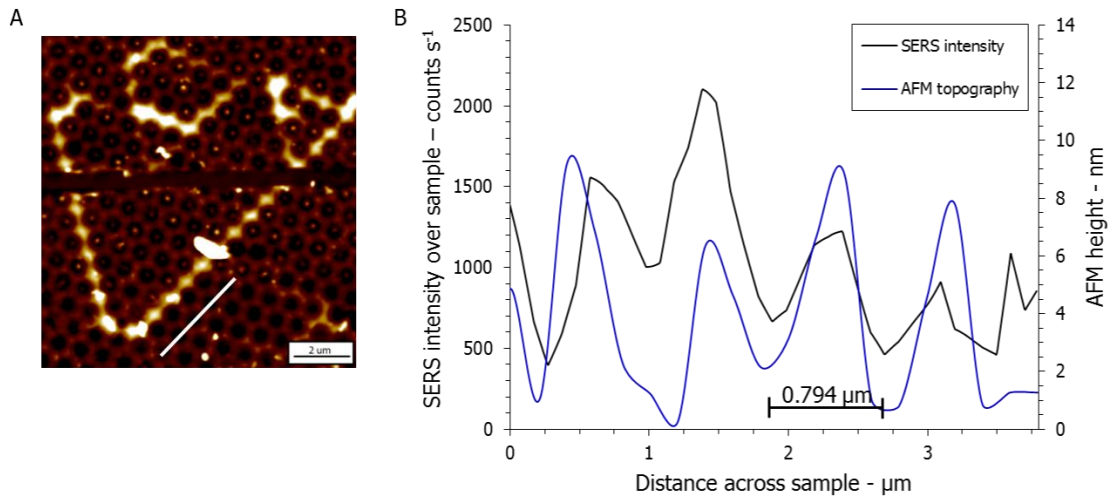
Figure 3.4 – A) AFM image obtained from Ag nanohole array of 820 nm periodicity and D/P 0.69. The white line marks the location of the cross-section taken from the Raman and AFM maps. B) Raman and AFM cross-section analysis of Ag nanohole array of 820 nm periodicity and D/P 0.69.

The Raman and AFM correlation analysis clearly illustrates that the areas of high Raman intensity in the Raman map match perfectly with areas of high topography in the AFM image. The cross-sectional analysis shown in Figure 3.4 confirmed that when the AFM height was high (on the Ag islands that surround the holes): the SERS intensity was at a maximum. It can be concluded from both analyses that the Raman enhancement originates from the islands of silver that surround the nanoholes in samples in the transition region.

The results of the correlation analysis of a Ag nanohole array of 1500 nm periodicity and D/P 0.64 are shown in Figure 3.5. This analysis was performed on an array with a

periodicity of 1500 nm as the "donut"-like areas of high Raman intensity were most clearly observed in samples with a larger periodicity.
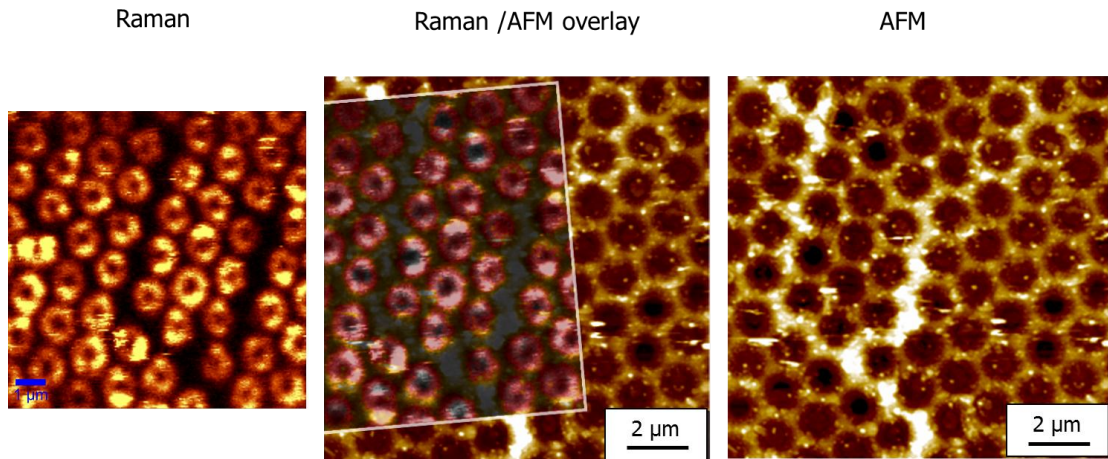
Figure 3.5 - Overlay of Raman false colour map and AFM image obtained from Ag nanohole array of 1500 nm periodicity, a deposited metal layer thickness of 125 nm and D/P 0.64. The Raman map was obtained using an incident wavelength of 633 nm and a laser power of 0.3 mW.
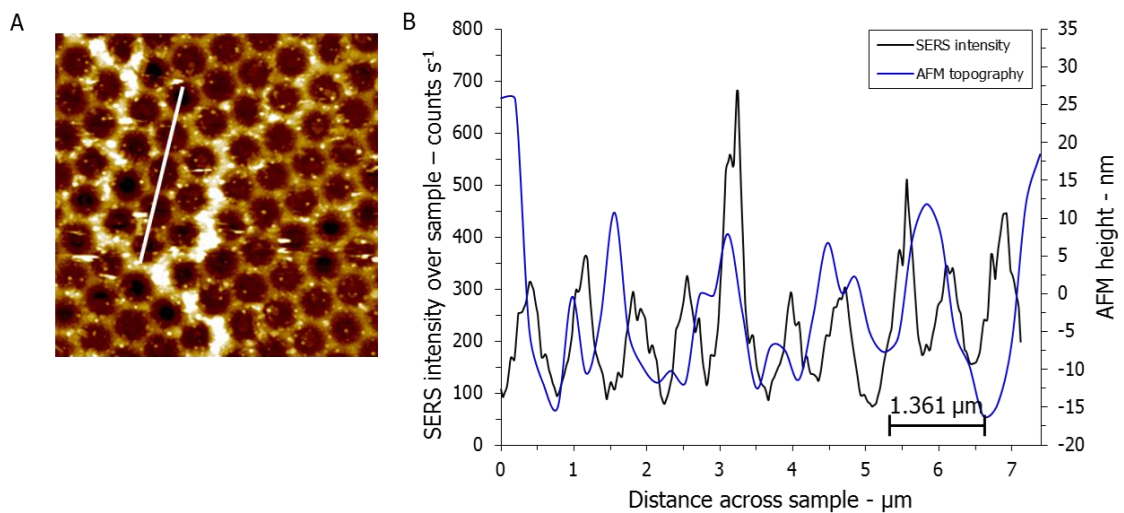
Figure 3.6 – A) AFM image obtained from Ag nanohole array of 1500 nm periodicity and D/P 0.64. The white line marks the location of the cross-section taken from the Raman and AFM maps. B) Raman and AFM cross-section analysis of Ag nanohole array of 1500 nm periodicity and D/P 0.64.

The areas of high Raman intensity in the Raman map perfectly correlate with the outer rim of the low topography regions in the AFM image. The cross-sectional analysis, shown in Figure 3.6, demonstrates that for every hole, there are two SERS intensity maxima that lie just to the inside of the hole region. From the results, it can be concluded that the plasmon originates on the rim of the nanohole in samples with a larger periodicity and a D/P ≤ 0.64. It is probable that this is the case in samples with a D/P value of approximately 0.64 and periodicities smaller than 1500 nm but the lateral

resolution limitations of the Raman instrument set-up prevent identification of the exact location of the plasmon.
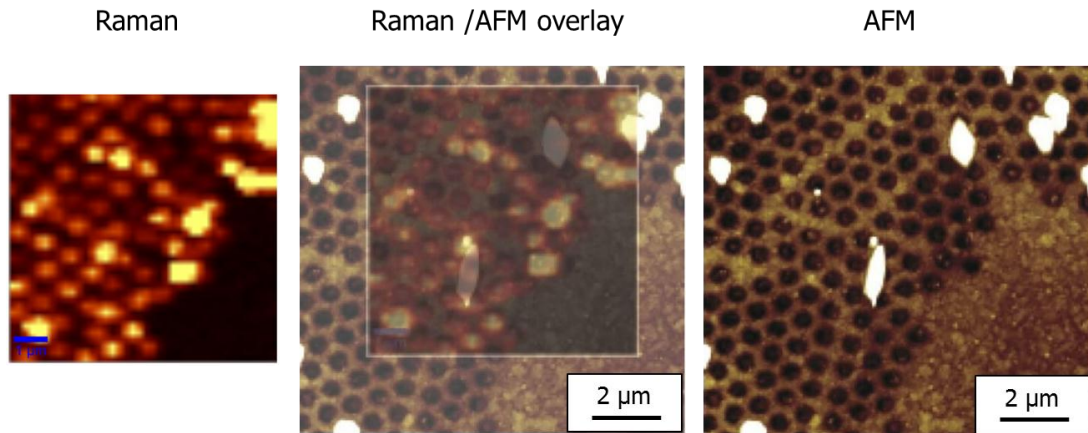
Figure 3.7 - Overlay of Raman false colour map and AFM image obtained from Ag nanohole array of 820 nm periodicity, a deposited metal layer thickness of 125 nm and D/P 0.43. The Raman map was obtained using an incident wavelength of 633 nm and a laser power of 0.3 mW.
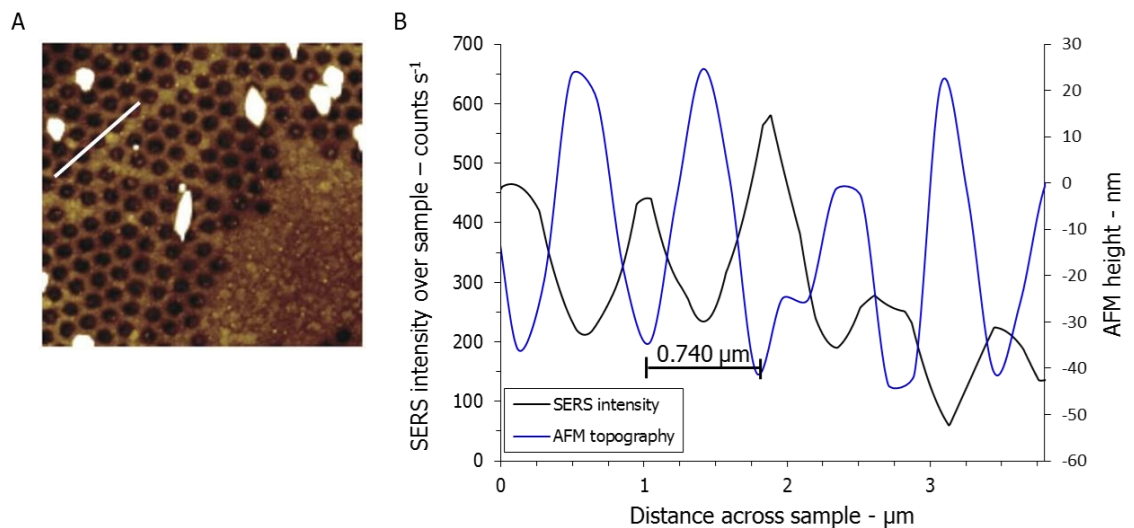
Figure 3.8 – A) AFM image obtained from Ag nanohole array of 820 nm periodicity and D/P 0.43. The white line marks the location of the cross-section taken from the Raman and AFM maps. B) Raman and AFM cross-section analysis of Ag nanohole array of 820 nm periodicity and D/P 0.43.

Figure 3.7 shows the results of the correlated Raman and AFM analysis of a Ag nanohole array of 820 nm periodicity in the nanohole region (D/P = 0.43). The analysis results show that the areas of high Raman intensity in the Raman map are well aligned with the areas of low topography in the AFM image. The cross-section analysis shown in Figure 3.8 clearly demonstrates that the maximum SERS intensity occurs when AFM

height is at a minimum. Therefore, the areas of high Raman enhancement are located in the hole region for samples with low D/P.

3.2.5 FDTD simulations

Finite-Domain Time-Difference (FDTD) calculations were applied to the nanotriangle and nanohole arrays in order to simulate the electric field distribution of the nanostructures. This technique has been employed by numerous research groups to calculate electromagnetic fields around a range of plasmonic materials, e.g. nanoparticles and nanopillar arrays.[181, 182] In this analysis, the diameters of the holes were varied so as to ascertain the effect that this parameter had on the electromagnetic field distribution of the substrates. The calculations were applied to hexagonal arrays fabricated on a glass substrate with the following parameters; periodicity of 1500 nm, Ti adhesion underlayer of 5 nm, Ag top layer of 50 nm. The diameters of the holes varied between 300 and 1500 nm with analysis carried out at 150 nm increments. The calculated FDTD simulations are shown in Table 3.6 alongside the corresponding experimental Raman maps. The FDTD calculations were carried out using an incident radiation wavelength of 532 and 633 nm. The results of simulations at both wavelengths are shown in Table 3.6.

	λ_{ex} = 532 nm		λ_{ex} = 633 nm	
	Raman map	FDTD	Raman map	FDTD
Nanotriangle D/P = 1.0			*	
Transition region 0.77 ≥ D/P ≥ 0.64			*	
Nanohole D/P < 0.64				

Table 3.6 - Raman false colour map and corresponding FDTD simulations at 532 (0.5 mW laser power) and 633 nm (0.3 mW laser power) excitation for Ag nanoholes of 1500 nm periodicity and varying D/P. All Raman maps are 10 x 10 μm except D/P 1.0 and 0.71 at 633 nm excitation (denoted by *) which are 15 x 15 μm. All scale bars represent either 1 or 2 μm. All FDTD simulated images are 3 x 3 μm.

The results of the FDTD simulations are in good agreement with the experimental Raman maps. Generally, the areas of predicted high electric field in the FDTD simulations (represented by light blue) correlate with the areas of high Raman enhancement (represented by yellow).

For nanotriangle arrays (D/P = 1.0), both simulations at λ_{ex} = 532 and 633 nm showed that the regions of highest electric field were at the junctions between two triangular metal islands. The FDTD analysis predicted that the maximum electric field would be along the edges of the triangle using an incident radiation of 532 nm and at the point where two triangle vertices meet using 633 nm excitation. The experimental SERS images suggest that the highest Raman enhancement is located on the triangles at both 532 and 633 nm excitation. The resolutions of the Raman maps are limited by the lateral resolution of the instrumental set-up preventing identification of the exact position of the localised enhancement on each individual nanotriangle. However, taking this into account, at D/P = 1, the FDTD simulations and experimental Raman maps are in good agreement with one another at both excitation wavelengths investigated.

As the D/P ratio decreases to between 0.77 and 0.69, the FDTD simulations at both excitation wavelengths predict that the maximum electric field lies at the rim of the holes. These results do not agree with what was observed experimentally. The Raman maps show that the largest Raman enhancement originates from the network of Ag between the holes. The discrepancy between the predicted and experimentally observed images may be a result of the lateral resolution limitations of the Raman mapping instrumental set-up.

As the D/P ratio further decreases, the FDTD simulations predict that the maximum electric field lies around the rim of the hole when 532 nm excitation was applied. When 633 nm excitation was used, the simulations predicted that the electric field lies toward the centre of the hole. The highest Raman intensity observed experimentally was located around the rim of the holes forming the aforementioned "donut" shapes. At this D/P, the simulations correlate well with the experimental Raman results.

For nanohole arrays (D/P < 0.64), the FDTD simulations at 532 and 633 nm excitation demonstrate that the maximum electric field is located in the centre of the nanoholes. Again, this result was in good agreement with the maps experimentally obtained.

The results of the FDTD analysis are largely well correlated to the experimental Raman maps. There are some discrepancies at D/P within the transition region (0.71 and 0.59). These discrepancies may be attributed to a combination of two factors. Firstly, the afore-mentioned lateral resolution limitations which prevent determination of the exact location of high Raman intensity in the experimental images. Secondly, the nature of NSL preparation of the samples results in a bowl-like hole in the Ag film. The tapered nature of the hole can be clearly seen in the SEM image shown in Figure 3.9.
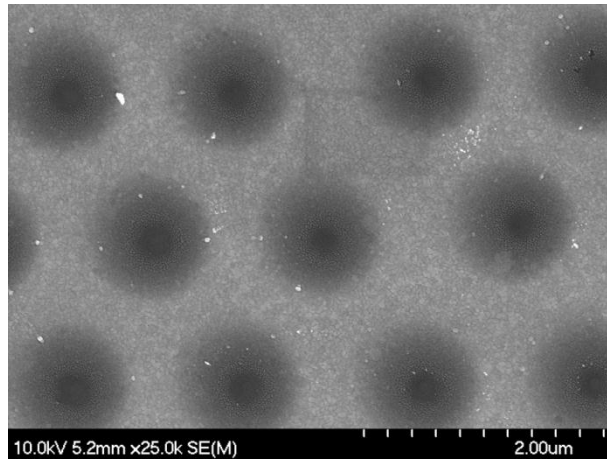
Figure 3.9 - SEM image of Ag nanohole array of 1500 nm periodicity with a D/P of 0.59. The scale bar represents 2 μm.

The diameter measurement used in the D/P calculation is measured at the surface of the hole. Therefore, the apparent D/P for the sample labelled at 0.59 is true for the surface of the nanohole, but the bottom of the nanohole will have a significantly smaller D/P. The FDTD simulations assume that the hole is cylindrical in nature and therefore the D/P is identical at the surface and the bottom of the nanohole. This concept is illustrated in Figure 3.10. The differences in hole shape between the experimental and theoretical samples may explain, in part, the discrepancies between the location of the predicted and observed maximum electric field.

Figure 3.10 – Cross-section of Ag nanohole to illustrate difference in structure between NSL fabricated hole and FDTD simulated hole. The red line represents the diameter at the surface of the hole whilst the blue line represents the diameter at the base of the hole.

3.2.6 Exploiting the regions of maximum Raman intensity for sensing applications

The information gained from the experimental Raman and AFM results and the FDTD calculations illustrate that different areas on the nanotriangle and nanohole arrays experience differing degrees of electric field. As discussed previously, both nanotriangle and nanohole arrays have been used as substrates for the detection of analytes by SERS.[149, 151] The sensitivity of the SERS analysis could, in theory, be improved by locating the molecule of interest on a region of the array that experiences the maximum electric field and therefore maximum Raman enhancement, as opposed to immobilisation of the analyte on the bulk surface of the nanostructure. Therefore, it was interesting and beneficial to investigate the selective immobilisation of analytes on regions that had been shown to give maximum Raman response.

Several selective immobilisation strategies were attempted to locate a molecule of interest in the regions of large electric field intensity in nanohole arrays. Initially, the use of silylation chemistry was investigated to modify the glass areas in the centre of nanoholes with a D/P of 0.64. It was postulated that conjugation of the biomolecule to the modified glass may result in placement of the target molecule in close proximity to the rim of the nanohole and therefore within the region of maximum Raman enhancement. However, the silylation conditions used resulted in damage to the nanostructured regions and were therefore deemed to be too harsh for this purpose.

Selective immobilisation was then attempted using a method based on work by Beeram and Zamborini.[176] They reported a place-exchange method in which selective immobilisation of an antibody was achieved on a Au triangular nanoplate by exploiting the lessened steric hindrance experienced by large biomolecules at the edges and vertices of the triangular nanostructures. It was thought that this methodology could be applied to nanotriangle samples with D/P = 1.0 to selectively functionalise the nanotriangle vertices with a molecule of interest. This would result in the molecule of interest, in this case a fluorescently-labelled protein; Streptavidin-dylight 633, being located in the "bow-tie" regions of the nanotriangle array which had exhibited maximum electric field intensity. Bimetallic nanotriangle arrays substrates with an Ag underlayer and an Au overlayer were used in this investigation so the method used by Beeram and Zamborini could be directly applied to the arrays. This strategy suffered from characterisation issues; Zamborini *et al.* had used AFM analysis to confirm the

presence of biomolecules at the nanostructure vertices however no immobilised biomolecules could be identified on the nanotriangle arrays using this analysis method. This may be attributed to the surface roughness of the nanotriangle arrays as the Au nanoplates used by Beeram and Zamborini had a relatively smooth surface thus facilitating analysis by AFM. For this method to be successfully applied to a SERS biosensing strategy, further investigation into the place-exchange immobilisation procedure and research into alternative characterisation methods would be required.

3.3 Conclusions

The research reported in this chapter has detailed the investigation into the location of maximum Raman enhancement in a series of nanohole and FOEN arrays with decreasing D/P. Confocal Raman mapping established that the maximum Raman enhancement, irrespective of array periodicity or D/P, is located on the Ag network that surrounds the spheres in FOEN arrays. Experimental evidence and FDTD calculations determined the site of high electric field varies with decreasing D/P in nanohole arrays. For samples with D/P = 1.0, the highest Raman intensity was observed at the point at which two metallic triangles, in the network of triangles that surround the holes, are in closest proximity. As the D/P decreased to within the transition region, between 0.77 and 0.64, the maximum SERS enhancement was found to be located on the network of silver surrounding the holes. As the D/P decreased to between 0.64 and 0.60, the maximum Raman intensity was located around the rim of the nanoholes. At D/P < 0.60, the electric field was found to be concentrated in the core region of the holes.

This comprehensive investigation has provided experimental evidence for the location of SERS hot-spots in both FOEN and nanohole arrays. The information gained from this study could have great implications in the development of SERS biosensing with enhanced sensitivity by locating analytes in the regions with maximum electric field.

Results discussed in this chapter have been published in Chemical Communications in 2011 and in The Journal of Physical Chemistry C in 2012 (see the Appendix section for the full texts).

3.4 Further Work

There are several methodologies that could be investigated to achieve the selective immobilisation of analyte molecules in the regions of maximum electric field enhancement.

The use of silylation chemistry to selectively modify the glass regions of nanohole arrays could be further investigated. For this strategy to be feasible, silylation conditions that did not damage the nanostructures would have to be developed.

As discussed previously, the place-exchange method reported by Beeram and Zamborini[176] has the potential to locate molecules of interest in the regions of high electric field on nanotriangle arrays. Initial investigations highlighted the difficulties in characterising the arrays after modification by AFM analysis. The use of larger molecules of interest may result in the detection of the immobilised molecules by AFM analysis. Alternatively, detection of the immobilised molecules could be achieved using a different characterisation method; SEM used alongside either cathodoluminescence (and a fluorescently-labelled target molecule) or X-ray microanalysis. Both techniques can result in a distribution image of molecules that emit fluorescent photons or distinct X-ray patterns (respectively) across the sample surface and hence may be used to successfully characterise the array surface after the place-exchange procedure.

Functionalization of the Cr adhesion layer is an alternate route that could be used to achieve the selective immobilisation of biomolecules in the hot-spot regions of nanohole arrays with a low D/P. There have been reports in the literature of the adhesion of carboxylic acid groups to Cr and this strategy could be used to functionalise the Cr selectively.[96, 183] This method would result in molecules being located in the core area of the holes as due to the metallization procedure; exposed Cr is only present in this region.

If these strategies were successful, this may result in enhanced sensitivity for the SERS detection of molecules of interest using metallic nanohole array substrates.

CHAPTER 4 - APPLICATIONS IN BIOSENSING

The previous chapters have described the results of fundamental investigation into the structure-property relationship of the FOEN and nanohole arrays. This chapter details research carried out to investigate if metallic FOEN and nanohole arrays had the potential to be used in the SERS sensing of biomolecules of interest.

4.1 Experimental

4.1.1 Sample Preparation

All substrates were prepared by Dr Debby Correia-Ledo at Université de Montréal. Bimetallic sample preparation followed the protocol described in section 2.1.1.2 with the exception of the metallisation step. Firstly a 1 nm layer of chromium was deposited to act as the adhesion layer. A layer of Ag was then deposited, 87.5 nm for the FOEN samples and 62.5 nm for the nanohole samples, followed by the deposition of Au to the same thickness as the Ag layer. Finally, preparation of the nanohole arrays was completed by sonication of the samples in ethanol for a few seconds to remove the polystyrene spheres.

4.1.2 SERS Instrumentation

All experiments were performed using either a Renishaw Ramascope equipped with a Renishaw HeNe laser of 633 nm excitation or an Innovative Photonic Solutions laser of 785 nm excitation, a Renishaw inVia Raman microscope equipped with a Modu-Laser of 514.5 nm excitation or a WITec Alpha 300 system equipped with a WITec laser of 532 nm excitation, a Research Electro-Optics laser of 633 nm excitation or a Toptica photonics diode laser of 785 nm excitation.

4.1.3 SERS characterisation of the substrates

Three bimetallic nanohole and three bimetallic FOEN arrays were thoroughly cleaned with ethanol and air-dried. All samples were analysed at 633 nm excitation using a 50x objective (Leica, NPlan, NA = 0.75), 10 % laser power and 10 s integration time. 5 replicate scans were collected from each substrate over the sample area.

4.1.4 SERS activity of substrates at 514.5, 633 and 785 nm excitation

Three bimetallic nanohole and three bimetallic FOEN arrays were thoroughly cleaned with ethanol and air-dried. All samples were incubated in a 0.5 mM solution of 4-NBT (Sigma-Aldrich) initially dissolved in ethanol and further diluted in water for 16 h at r.t. The samples were then thoroughly washed with ethanol and air-dried prior to analysis. Each sample was analysed at 532, 633 and 785 nm excitation using a 50 x objective, 10% laser power and 10 s integration time with 5 replicate scans being collected from each substrate over the sample area.

4.1.5 Dye choice

Three bimetallic nanohole arrays were thoroughly cleaned with ethanol and air-dried. All samples were incubated in a 72 µM solution of malachite green isothiocyanate (MG ITC, Invitrogen, Life Technologies, Grand Island NY, USA), initially dissolved in methanol and the further diluted in water, for 16 h at r.t. The samples were then thoroughly washed with ethanol and air-dried prior to analysis. Each sample was analysed at 532, 633 and 785 nm excitation using a 50 x objective, 10% laser power and 10 s integration time with 5 replicate scans being collected from each substrate over the sample area.

4.1.6 Surface Interaction - General Procedures

4.1.6.1 Labelling of Streptavidin with MG ITC

Streptavidin (ImmunoPure, Thermo Scientific, Waltham MA, USA) was reconstituted at 10 mg/ml in PBS. It then underwent a buffer exchange procedure. 10 µl streptavidin (10 mg/ml) and 90 µl 0.1 M sodium bicarbonate buffer pH 9.2 were added to a 50K MWCO centrifugal filter (Amicon Ultra – 0.5 ml, Millipore, Billerica MA, USA) and centrifuged at 13.4k rotations per minute (rpm) for 5 min (MiniSpin, Eppendorf, Stevenage, UK). 90 µl 0.1 M sodium bicarbonate buffer pH 9.2 was added and the centrifugation step repeated. The addition of buffer and centrifugation step was repeated for a third time before the centrifugal filter unit was inverted and placed in a fresh eppendorf and centrifuged at 1.0 k rpm for 5 min resulting in 40 µl 2.5 mg/ml streptavidin in 0.1 M sodium bicarbonate buffer pH 9.2 (assuming 100% recovery of protein). The freshly buffer-exchanged streptavidin was then conjugated to MG ITC. 6

mM MG ITC solution in anhydrous DMSO (33 µl) was prepared and added in 10 µl aliquots to a vortexing solution of streptavidin (2.5 mg/ml, 0.1 M sodium bicarbonate buffer pH 9.2). After all of the MG ITC had been added, the resulting solution was protected from light and agitated for 2 h at r.t. After 2 h, the solution was added to a 50K MWCO centrifugal filter and centrifuged for 5 min at 13.4k rpm, 100 µl PBS was added and the solution was centrifuged for 5 min at 13.4 k rpm. This step was repeated before the centrifugal filter unit was inverted and placed in a fresh eppendorf and centrifuged at 1.0 k rpm for 5 min resulting in 41 µM streptavidinMG (40 µl, 2.5 mg/ml – assuming 100% recovery of conjugate) in PBS. This solution was stored at 4°C until use.

4.1.6.2 Functionalization of array substrates with biotin

All steps were carried out at r.t.

Biotin-dPEG®₃-lipoic acid

The nanohole array samples were incubated in a 1 mM aqueous solution of Biotin-dPEG®₃-lipoic acid (thioctic acid-PEG$_3$-biotin linker, Quanta Biodesign, Powell OH, USA) for 18 h. After copious washings with ddH$_2$O, the samples were air dried and placed into an 16-well microarray chamber (Nexterion® 16-well incubation chamber – Schott, Jena, Germany) before interaction with StreptavidinMG.

(+)-biotinyl-3, 6, 9 – trioxaundecanediamine linker

A 16-MHA SAM was formed on the surface of the arrays by incubating the substrates in a 5 mM solution of 16-MHA (Sigma-Aldrich) in dimethyl formamide (DMF) for between 16 and 65 hours. The samples were then thoroughly washed with ethanol and dried before being placed into a microarray chamber. Activation of the carboxylic acid group to a NHS-activated ester was achieved by addition of 100 µl (per well) of a mixed aqueous solution of between 100 and 400 mM 1-ethyl-3-(3-dimethylaminopropyl) carbodiimide (EDC, Sigma-Aldrich) and 25 and 100 mM *N*-hydroxysulfosuccinimide (sulfo-NHS, Sigma-Aldrich). This solution was left to incubate for between 20 and 60 min. After activation, the wells were washed twice with 100 µl PBS pH 4.5. 100 µl 1 mM solution of (+)-biotinyl-3, 6, 9 – trioxaundecanediamine (amine-PEG$_3$-biotin, Thermo Scientific, Waltham MA, USA) dissolved in PBS was added to each well and the samples were agitated for 3 h before being washed 3 times with PBS. 100 µl 1 M ethanolamine.HCl (Sigma-Aldrich) pH 8.5 was added to each well and incubated for 1 h

with or without agitation. The wells were then washed three times with PBS prior to incubation with streptavidinMG.

4.1.6.3 Interaction of StreptavidinMG with the biotinylated surfaces

100 µl of either MG labelled streptavidin (streptavidinMG, 300 nM) or streptavidin that had been pre-reacted with 10 x excess free biotin for 1 h (control streptavidinMG - 300 nM), both diluted in phosphate-buffered saline with 0.05 % Tween (PBST, Tween was purchased from Sigma-Aldrich) was added to each well and incubated for between 5 min and 2 h either with or without agitation. The wells were then thoroughly washed with either PBS or PBST and the samples were removed from the microarray chamber and washed again with ddH$_2$O before being dried under a stream of nitrogen prior to analysis.

4.1.7 Aurora A Sensing

4.1.7.1 Labelling of Aurora A with MG ITC

Aurora A (Millipore, Billerica MA, USA) first underwent a buffer exchange procedure. 66.6 µl Aurora A (0.3 mg/ml) and 40 µl 0.1 M sodium bicarbonate buffer pH 9.2 were added to a 30K MWCO centrifugal filter (Amicon Ultra – 0.5 ml, Millipore, Billerica MA, USA) and centrifuged at 13.4k rpm for 5 min. 90 µl 0.1 M sodium bicarbonate buffer pH 9.2 was added and the centrifugation step repeated. The addition of buffer and centrifugation step was repeated for a third time before the centrifugal filter unit was inverted and placed in a fresh eppendorf and centrifuged at 1.0 k rpm for 5 min resulting in 45 µl 0.44 mg/ml Aurora A in 0.1 M sodium bicarbonate buffer pH 9.2 (assuming 100% recovery of protein). The freshly buffer exchanged Aurora A was then conjugated to MG ITC. 6 mM MG ITC solution in anhydrous dimethyl sulfoxide (DMSO) (33 µl) was prepared and added in 10 µl aliquots to a vortexing solution of Aurora A (45 µl, 0.44 mg/ml, 0.1 M sodium bicarbonate buffer pH 9.2). After all of the MG ITC had been added, the resulting solution was protected from light and agitated for 2 h at r.t. After 2 h, the solution was added to a 30K MWCO centrifugal filter and centrifuged for 5 min at 13.4k rpm, 100 µl PBS was added and the solution was centrifuged for 5 min at 13.4 k rpm. This step was repeated before the centrifugal filter unit was inverted and placed in a fresh eppendorf and centrifuged at 1.0 k rpm for 5 min resulting in 35 µl 0.57 mg/ml Aurora A MG (12 µM – assuming 100% recovery of conjugate) in PBS. This solution was stored at 4°C until use.

4.1.7.2 Functionalization of Array Substrates with Wild Type and Mutant peptides

The wild type (WT) and mutant peptides were custom ordered from Genscript (Piscataway NJ, USA). A 16-MHA SAM was formed on the surface of the arrays by incubating three nanohole substrates in a 5 mM solution of 16-MHA in DMF for 65 hours. The samples were then thoroughly washed with ethanol and dried under nitrogen before being placed into a microarray chamber. Activation of the carboxylic acid group to a NHS-activated ester was achieved by addition of 100 µl (per well) of a mixed aqueous solution of 400 mM EDC and 100 mM sulfo-NHS. This solution was agitated for 1 h at r.t. After activation, each well was washed twice with 100 µl PBS pH 4.5. 100 µl (per well) 2.5 mM solution of wild type peptide dissolved in PBS was added to the positive wells or 100 µl (per well) 2.5 mM solution of mutant peptide dissolved in PBS was added to the control wells. The samples were agitated for 3 h before being washed 3 times with PBS. 100 µl 1 M ethanolamine.HCl pH 8.5 was added to each well and incubated for 1 h with agitation. The wells were then washed three times with PBS prior to incubation with Aurora A MG.

4.1.7.3 Interaction of Aurora A MG with the peptide-functionalised surfaces

100 µl of MG labelled Aurora A (530 nM) was added to each well and incubated with agitation for either 30 or 60 min. After the incubation period, the wells were then thoroughly washed with PBST and the samples were removed from the microarray chamber and washed again with ddH$_2$O before being dried under nitrogen prior to analysis.

4.2 Results and Discussion

4.2.1 Substrate Choice

Two SERS active substrates based on arrays that had been previously studied were chosen for this investigation:

1. Bimetallic nanohole array - 1000 nm diameter, D/P = 0.6

    1 nm Cr adhesion layer

    62.5 nm Ag bottom layer

    62.5 nm Au top layer

2. Bimetallic FOEN array – 360 nm diameter, gap/diameter = 0.22

    1 nm Cr adhesion layer

    87.5 nm Ag bottom layer

    87.5 nm Au top layer

No prior investigation had been performed on the bimetallic nanohole substrates however the bimetallic FOEN array had demonstrated good Raman enhancement in previous studies.[184] The bimetallic nature of these substrates is advantageous for biosensing applications. The Ag bottom layer gives improved SERS response when compared to a similar Au layer as discussed in Chapter 2. The Au top layer has improved stability to oxidation when compared to a similar Ag layer. In addition, the Au top layer lends itself to straightforward functionalization with thiol-containing reagents.

4.2.2 SERS Characterisation of the substrates

The bare bimetallic nanohole and FOEN arrays were analysed at 633 nm excitation to characterise the intrinsic SERS signal of the substrates. Ideally, biosensing substrates should have little or no background signal so as to minimise interference in the analysis. Figure 4.1 and Figure 4.2 show a representative spectrum from the bare nanohole and bare FOEN arrays respectively.
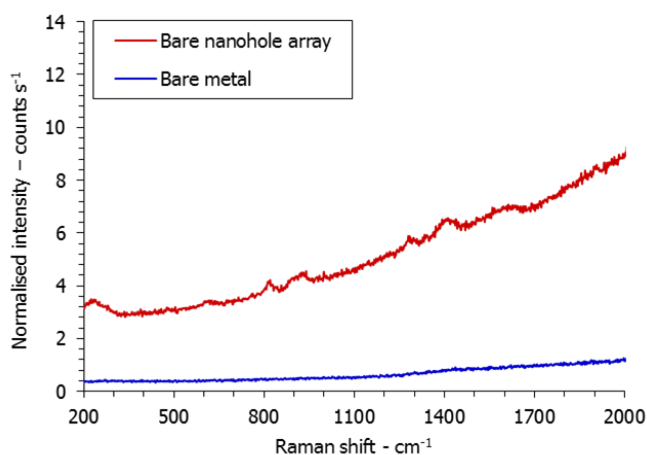
Figure 4.1 - Representative SERS spectrum obtained from bare bimetallic nanohole array of 1000 nm periodicity, a total deposited metal layer thickness of 125 nm and D/P 0.6 (red trace) and bare metal region of array (blue trace) using 633 nm excitation.
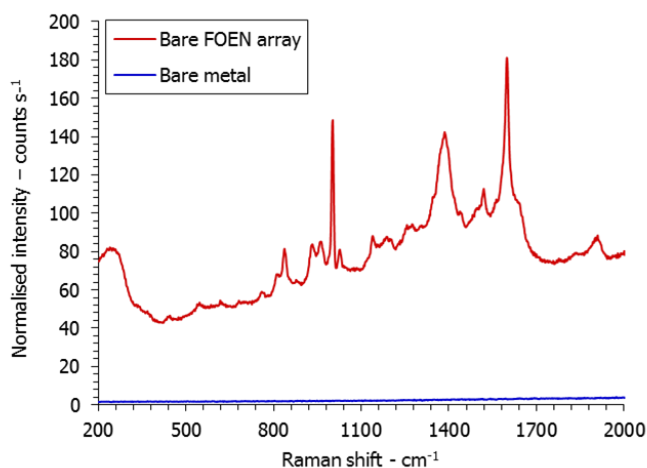
Figure 4.2 - Representative SERS spectrum obtained from bare bimetallic FOEN array of 360 nm periodicity, a total deposited metal layer thickness of 125 nm and a gap/diameter of 0.22 (red trace) and bare metal region of array (blue trace) using 633 nm excitation.

The blue traces in both figures are of a representative spectrum from an area on the sample with no nanostructure present. As expected, no SERS peaks were observed from these areas of flat metal.

The spectra of the bare nanostructured substrates clearly show that the bare nanohole arrays have almost no intrinsic Raman peaks whereas the spectra of the bare FOEN array show numerous distinct peaks. As the FOEN arrays consist of a metal layer over polystyrene spheres, it was probable that the SERS peaks present were due to polystyrene.

Experimentally observed Raman shift – cm⁻¹	Reported Raman shift[185] – cm⁻¹	Spectral assignment[185]
641	636	Radial ring stretching mode
828		
841		
940		
942		
1002 (s)	1014	Phenyl ring breathing mode
1029	1040	
1145		
	1172	C-H in plane bending mode
1389		
	1461	CH_2 vibrations
1521		
1600 (s)	1615	Ring stretching mode
1914		

Table 4.1 - Observed SERS peaks from bare bimetallic FOEN array of 360 nm periodicity and a gap/diameter of 0.22 at 633 nm excitation and reported spectral assignment of polystyrene SERS peaks at 514.5 nm excitation.[185]

Table 4.1 shows the experimentally observed peaks from the bare FOEN arrays alongside reported SERS peak values and assignments for polystyrene. The main peaks observed from the FOEN arrays (1002 and 1600 cm⁻¹) correspond to values reported for polystyrene on roughened Ag island films.[185] The peaks that do not correspond to the literature values for polystyrene where postulated to be from contaminants on the FOEN arrays as any SERS-active molecule at a high enough concentration could give a spectrum if in close enough proximity to the surface.

SERS Activity of the Substrates; 532, 633 and 785 nm Excitation

The Raman response at the three available excitation wavelengths was investigated to determine the optimum conditions for each substrate. Each array was incubated in a 0.5 mM solution of 4-NBT, initially dissolved in ethanol and further diluted in water, for 16 h to allow formation of a 4-NBT self-assembled monolayer (SAM). After thorough washing of each sample, the substrates were analysed using identical parameters at each excitation wavelength. Figure 4.3 shows the normalised peak height value for the 1573 cm⁻¹ peak of 4-NBT.
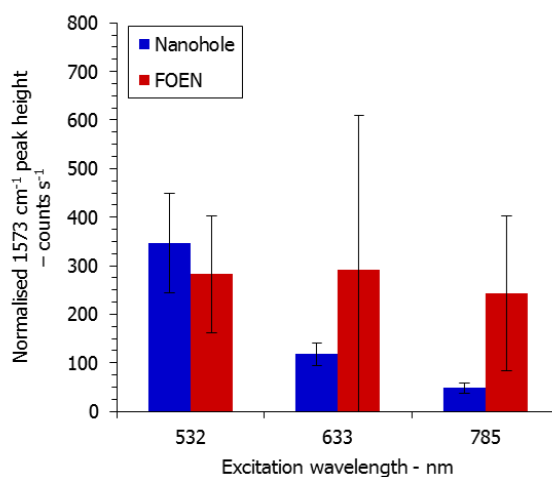
Figure 4.3 - SERS response of 4-NBT adsorbed on bimetallic nanohole array (blue) and bimetallic FOEN array (red) at 532, 633 and 785 nm excitation. The normalised peak height values represent the mean of five peak height values per array. The error bars represent two standard deviations about the mean.

Both the bimetallic nanohole and FOEN array substrates exhibited peaks corresponding to 4-NBT and hence are active at all excitation wavelengths investigated, albeit to differing degrees. The bimetallic nanohole array demonstrated the largest Raman response at 532 nm excitation whereas the FOEN array gave similar SERS signals at all three excitation wavelengths. The Raman response of the nanohole arrays was more reproducible at each excitation wavelength investigated than that of the FOEN array as highlighted by smaller error bars.

It was decided that for the development of a biosensing method, the bimetallic nanohole array substrates would be used for numerous reasons: it was shown that they were SERS active at all wavelengths investigated, they demonstrated low intrinsic SERS signals and they had better signal reproducibility when compared to the bimetallic FOEN arrays.

4.2.3 Dye Choice

It was postulated that selecting a dye with an absorbance peak close to that of one of the excitation laser wavelengths would result in a resonance contribution to the Raman enhancement from the dye, leading to more sensitive detection. For this reason, malachite green isothiocyanate (MG ITC) was chosen as it has an absorbance band at 625 nm[186] and is commercially available. Isothiocyanate reagents are often used to label biomolecules as they react rapidly and create a stable linkage between primary

amine groups on the biomolecule (the N-terminus or lysine side chains of peptides/proteins) and the required functional group e.g. dyes.

The nanohole array substrates were immersed in a solution of MG ITC to allow adsorption of MG to the arrays *via* the ITC group. The samples were thoroughly washed, dried and analysed using 532, 633 and 785 nm excitation lasers. This study was designed to determine the optimum excitation wavelength for analysis of MG labelled biomolecules. Figure 4.4 shows the structure of MG ITC and a representative spectrum obtained at each available excitation wavelength. Table 4.2 shows the spectral assignment of the peaks observed from MG ITC on the array surface. The observed Raman shifts correlate well to those reported in the literature.
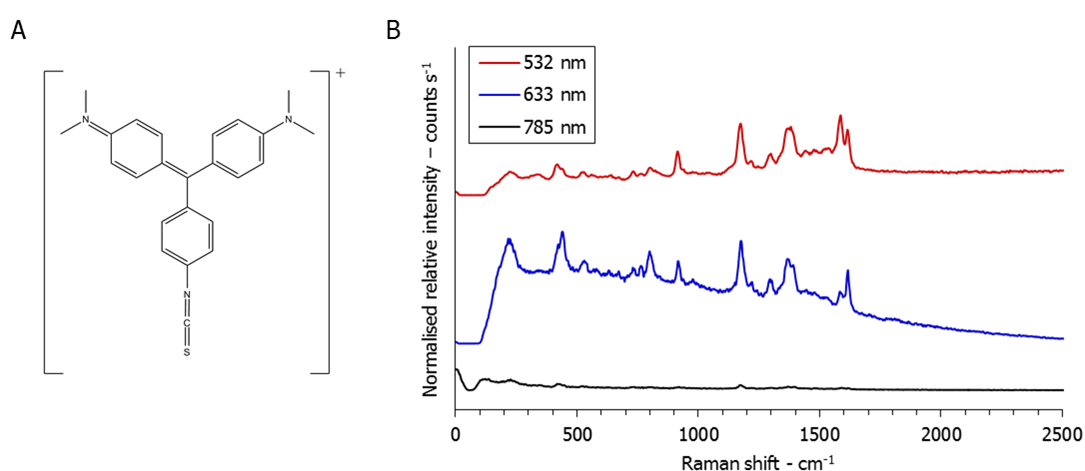
Figure 4.4 - A) Structure of MG ITC. B) Representative spectra collected from MG ITC functionalised bimetallic nanohole arrays at 532 (red trace), 633 (blue trace) and 785 nm (black trace) excitation.

Observed Raman shift – cm^{-1}	Reported Raman shift[187] – cm^{-1}	Spectral assignment
435	441	Benzene ring deformation
514	532	In-plane benzene ring deformation
730	736	In-plane benzene ring deformation and NH$_2$ stretch
757	762	NH$_2$ bend
796	806	C-H bend from benzene ring
916	919	in plane benzene vibration
1175	1177	Benzene in plane
1289	1297	In plane C-H and C-C-H
1364	1365	N-Ph ring stretch
1579	1586	In plane ring, stretch and bend
1614	1618	N-Ph ring and C-C stretch

Table 4.2 - Observed SERS peaks form MG ITC functionalised bimetallic nanohole arrays at 633 nm excitation and reported spectral assignment of MG ITC SERS spectra at 785 nm excitation.[187]

In order to quantify the SERS enhancement at each excitation wavelength investigated, the average height of the 1175 cm^{-1} peak was calculated. This peak was chosen at it was clear and well-defined. The peak height was calculated by subtracting the SERS intensity value at 1145 cm^{-1} from the SERS intensity maximum value at 1175 cm^{-1}. The peak height was then normalised for each experimental data set by dividing it by the laser power used for the analysis. This method was used for all subsequent experiments.
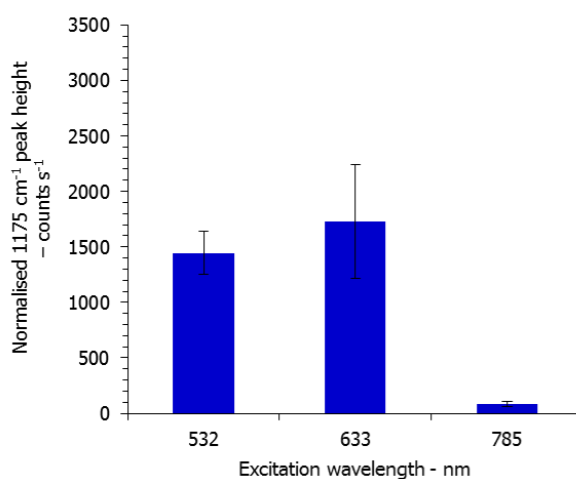
Figure 4.5 - SERS response of MG ITC functionalised bimetallic nanohole arrays at 532, 633 and 785 nm excitation. The peak height values represent the mean of five replicate scans and the error bars represent two standard deviations about the mean.

Good signal was observed at both 532 and 633 nm excitation as demonstrated in Figure 4.5. Excitation at 785 nm resulted in low signal. These observations were as expected as, stated previously, MG ITC has an absorption band at 625 nm which is very close to the 633 nm excitation line and close enough to the 532 nm excitation line to, in both cases, excite a resonant contribution from the dye giving rise to intense signal. The absorption band is not close enough to be excited by the 785 nm excitation laser resulting in less intense signal. It was decided that 633 nm excitation would be used to analyse the MG labelled Streptavidin as at 633 nm excitation, little background signal was exhibited by the bare nanohole arrays and intense signal was obtained from adsorbed MG.

4.2.4 Proof of concept initial work

The potential for carrying out a biological interaction on the bimetallic nanohole array was investigated using the interaction between a biotinylated linker and MG labelled

streptavidin. The biotin-streptavidin interaction was selected for the proof-of-concept investigation as it is well-documented, robust and often used in other proof-of-concept studies.[95, 188, 189] Streptavidin is comprised of four, identical monomeric units with each unit able to bind one biotin molecule.[190] The streptavidin-biotin interaction is one of the strongest known interactions in biology and exhibits a dissociation constant, K_d, of approximately 10^{-14} M.[191] The interaction occurs rapidly and the associated complex can only be disassociated under harsh conditions.[192, 193]

Conjugation of Streptavidin to malachite green isothiocyanate (MG ITC)

To facilitate the detection of streptavidin by SERS, it had to be labelled with a Raman active group. As discussed previously, MG was selected as the label of choice owing to its distinct Raman spectrum and high SERS activity at 633 nm excitation. The protocol used to label streptavidin with MG was based on methods described by Brinkley.[194] Briefly, streptavidin (10 mg/ml) was exchanged into a sodium bicarbonate buffer, pH 9.2, to ensure that the primary amine groups were not protonated as this hinders the cross-linking reaction. MG ITC (6 mM) was dissolved in anhydrous DMSO and added in 10 μl aliquots over 10 min to a vortexing solution of streptavidin. The reaction was agitated for 2 h. The ITC group hydrolyses in the presence of water and so a fresh solution of MG ITC in DMSO was prepared prior to every conjugation reaction. The resulting streptavidinMG conjugate was purified using a 50K molecular weight cut off (MWCO) gel filtration column. The conjugate was stored at 4°C until use.

Preliminary studies using a thioctic acid-PEG₃-biotin linker molecule

Preliminary studies were conducted using a commercially available thioctic acid-PEG₃-biotin linker (TA-biotin linker) molecule to functionalise the Au surface of the nanohole arrays with a biotin terminated group. The structure of the linker molecule is shown in Figure 4.6 and consists of a thioctic acid moiety (shown in blue) which anchors the linker to the Au surface *via* the sulphur atoms and a terminating biotin group (shown in red).
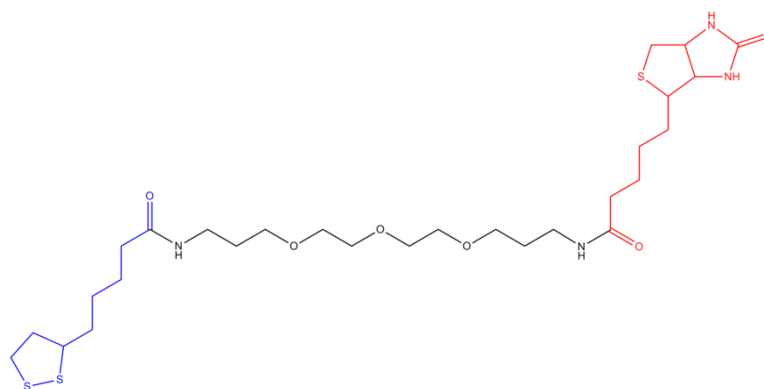
Figure 4.6 - Structure of thioctic acid-PEG₃-biotin linker.

The nanohole array samples were incubated in a 1 mM aqueous solution of the thioctic acid linker for 18 h. After copious washings with ddH$_2$O, the samples were air dried and placed into a microarray chamber. 100 µl of 300 nM streptavidinMG was added to each well and incubated for 2 h at r.t. with gentle agitation. The samples were then washed with PBS, dried and analysed using a 633 nm excitation laser. The results of this preliminary investigation demonstrated that a SERS signal corresponding to MG could be detected from the nanostructured areas on the nanohole array substrates as shown in Figure 4.7.
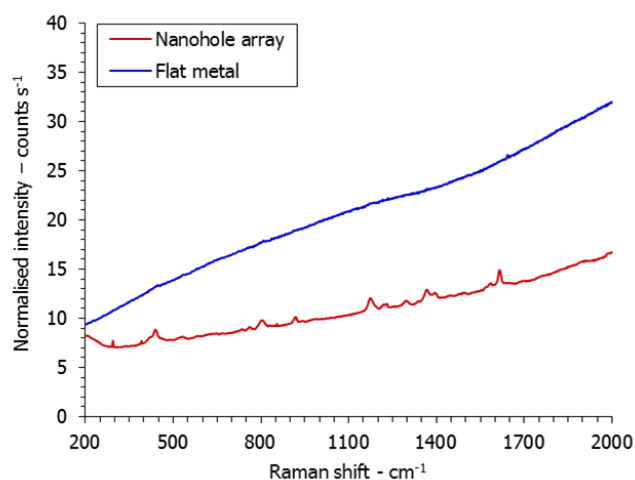
Figure 4.7 – Representative SERS spectra from nanostructure (red trace) and flat metal (blue trace) on bimetallic nanohole array of 1000 nm periodicity and D/P 0.6 obtained using 633 nm excitation, 10 s integration time, 50 x objective and 10% laser power.

Although peaks were observed, it was unknown if the signal was due to the specific interaction occurring or to non-specific binding. Further investigation with a control in which no binding between the biotinylated surface and streptavidinMG should occur was needed in order to confirm that the interaction was occurring as expected. No

peaks were detected from the flat metal areas of the arrays which indicated both that the signal observed was SERS rather than Raman or resonance Raman scattering and that SERS could only be observed on a surface with nanoscale roughened features. It should be noted that no peaks were observed from the flat metallic areas on the nanohole arrays in all subsequent experiments therefore all peaks observed were a result of SERS.

The use of the TA-biotin linker was limiting as it meant that only labelled streptavidin could be detected. To increase the range of interactions that could be investigated on the nanohole surface, a molecule was needed that could functionalise the Au surface with a reactive group which could in turn be used to bind to a biomolecule of choice. 16-mercaptohexadecanoic acid (16-MHA) was selected as it can anchor to the Au surface *via* the thiol group terminating in a free carboxylic acid group that can undergo amide bond formation with an amine group to link a biomolecule to the surface. 16-MHA is known to form a tightly packed SAM on Au surfaces and hence is used to functionalise surfaces in many biosensing applications.[154, 195, 196]

4.2.5 Interaction Method

The method used to develop a biosensing strategy on bimetallic nanohole arrays was based on procedures used in SPR assays and those used by other groups who had achieved biosensing on similar substrates.[62, 95, 197, 198] Firstly, a 16-MHA SAM was formed on the surface of the arrays by incubating the substrates in a 5 mM solution of 16-MHA in DMF for between 16 and 65 hours. The samples were then thoroughly washed with ethanol and dried before being placed into a 16-well microarray chamber. By placing the samples in the chamber, one array sample could be split into a maximum of 6 separate wells allowing multiple interactions on one array sample. The next step was to activate the carboxylic acid group to a NHS-activated ester using EDC and sulfoNHS. After activation, the wells were washed with PBS pH 4.5 to maintain stability of the NHS-activated ester group. A 1 mM solution of (+)-biotinyl-3, 6, 9 – trioxaundecanediamine (amine-PEG$_3$-biotin), a commercially available linker shown in Figure 4.8, with one end terminating in an amine group (blue) and the other end a biotin moiety (red), was then added.
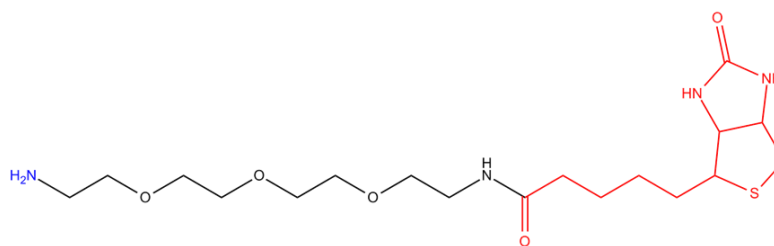
Figure 4.8 - Structure of (+)-biotinyl-3, 6, 9 – trioxaundecanediamine (amine-PEG$_3$-biotin).

The amine group reacts with the NHS-activated ester to form an amide bond between the 16-MHA SAM and the remainder of the linker molecule. To prevent any unreacted NHS-activated esters undergoing unwanted reactions, 1 M ethanolamine.HCl pH 8.5 was added to each well. This step blocks any unreacted NHS-esters in two ways; firstly, the amine group of ethanolamine can react with the NHS-ester to give an alcohol terminated group which should not react in the following steps; secondly, the increased pH of the solution promotes hydrolysis of the NHS-ester resulting in a carboxylic acid group which should also not react in the following steps. After the blocking step, the MG labelled streptavidin was added and incubated for between 5 min and 2 h. In order to determine if signal observed was due to the interaction occurring rather than non-specific binding, streptavidinMG that had been pre-incubated with excess free biotin for 1 h was added to the control experiments. By pre-reacting streptavidinMG with free biotin, all of the streptavidinMG binding sites should be fully saturated preventing reaction with any surface bound biotin therefore inhibiting binding. The wells were then thoroughly washed with either PBS or PBST and the samples were removed from the microarray chamber and washed again with ddH$_2$O before being dried and stored, in the absence of light, until analysis. Figure 4.9 shows the interaction in schematic form.
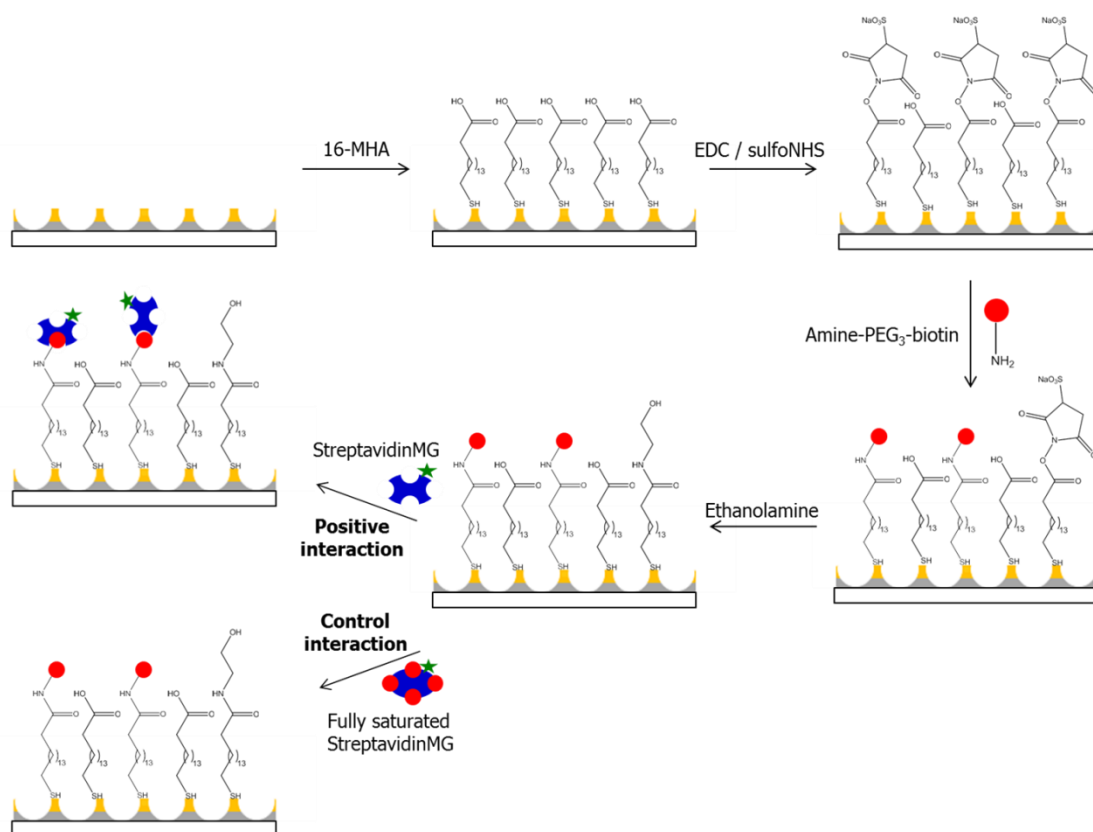
Figure 4.9 - Schematic of positive and control interaction of MG labelled streptavidin with biotin functionalised bimetallic nanohole array.

4.2.6 Evaluating the positive and control interactions

In all experiments discussed, the results were evaluated based on the discrimination obtained between the full positive and control interactions. The discrimination was defined as the difference between the lower limit of the mean peak height (mean value minus standard deviation) obtained from the positive interaction and the upper limit of the mean peak height (mean value plus standard deviation) obtained from the control interaction with both experiments performed under identical conditions.

4.2.7 Optimisation Experiments

Optimisation of the interaction process was investigated using the positive and control interactions as illustrated in Figure 4.9.

4.2.7.1 Optimising 16-MHA SAM formation time

In all biosensing strategies, the chemistry which occurs at the substrate surface is of paramount importance. It is necessary to have a well-packed SAM on the surface as this is the basis on which the rest of the interaction is built on. To ensure good SAM

formation, the substrates must be thoroughly cleaned before immersion into the monolayer solution, the reagents used must be of high quality and the formation time must be optimised for the specific system under investigation. The kinetics of SAM formation are very rapid and in general, an imperfect SAM is formed within 10 minutes of immersion of the sample.[199] However, longer incubation times are often used to ensure formation of a well-ordered, tightly-packed SAM. SAM formation times of 18 and 65 h were investigated.
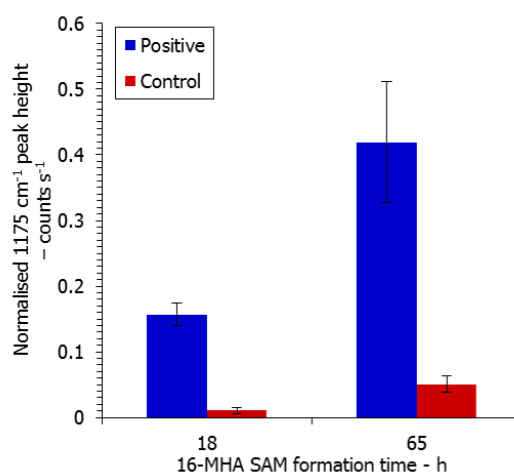
Figure 4.10 - Average SERS signal on 633 nm excitation exhibited by bimetallic nanohole array substrates after full interaction using SAM formation times of 18 or 65 h. Average peak height values were calculated from five replicate scans and the error bars represent two standard deviations about the mean.

It can be clearly observed from Figure 4.10 that good discrimination between the positive and control interaction was achieved in both cases. It was concluded that, as a result of the larger SERS signal obtained, a SAM formation time of 65 h was optimal for the system under investigation.

4.2.7.2 Optimising EDC/sulfoNHS conditions

The efficiency of amide bond formation *via* EDC/sulfoNHS coupling is low due to the competing hydrolysis of the NHS group.[200, 201] Therefore, as the degree of coupling governs the amount of amine-PEG$_3$-biotin linker on the surface, it is paramount to optimise the EDC/sulfoNHS coupling conditions in order to achieve the highest degree of coupling possible.

Three different sets of EDC/sulfoNHS coupling conditions were investigated and are shown in Table 4.3. For this experiment, a StreptavidinMG incubation time of 2 h was used.

Condition Set	[EDC] - mM	[sulfoNHS] - mM	Incubation time - min	Agitation
A	100	25	20	✘
B	400	100	30	✘
C	400	100	60	✓

Table 4.3 – EDC/sulfoNHS conditions investigated.

The results of this investigation are shown in Figure 4.11. The success of the coupling was evaluated by analysing the discrimination between the positive and control interaction. A separate surface was used for each set of coupling conditions and five replicate scans were taken from each surface.
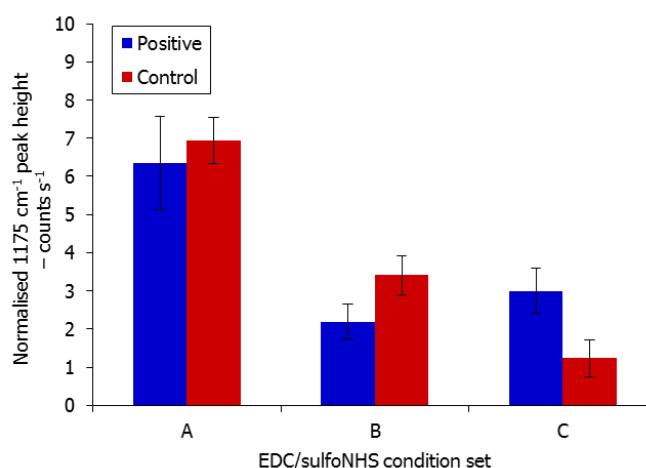
Figure 4.11 - SERS response from interactions using varying EDC/sulfoNHS coupling conditions on bimetallic nanohole arrays using 633 nm excitation. Average peak height values were calculated from five replicate scans and the error bars represent two standard deviations about the mean.

From this investigation, it could be concluded that discrimination between the positive and control experiments was only achieved using 400 mM EDC and 100 mM sulfoNHS and incubating this step for 1 h with gentle agitation. This set of conditions was therefore optimal and so used in all subsequent experiments.

4.2.7.3 StreptavidinMG Incubation Time Investigation

Reports in the literature of comparable biosensing strategies on similar surfaces describe varying lengths of incubation time, from 10 min to 4 h, for the streptavidin step.[87, 189, 198] Optimisation of this step was important as too short an incubation time would result in low amounts of streptavidin interacting with the biotinylated surface and too long an incubation time may result in increased levels of non-specific binding between the streptavidin analyte and the surface. StreptavidinMG incubation times of 5, 10, 15, 30 and 60 min were investigated. The optimal incubation time was determined by comparing the discrimination between positive and control interaction

for each streptavidinMG incubation time. The results from the streptavidinMG incubation time investigation are shown in Figure 4.12.
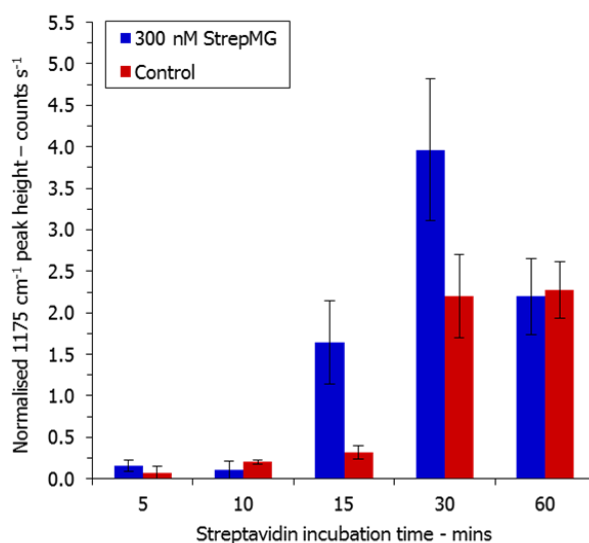
Figure 4.12 - SERS response from interactions of varying length of streptavidinMG incubation on bimetallic nanohole arrays using 633 nm excitation. Average peak height values were calculated from five replicate scans and the error bars represent two standard deviations about the mean.

From the results of this investigation, it could be determined that 5 and 10 min incubation times were not sufficiently long enough to achieve discrimination between the positive and control interaction. It could also be concluded that a 60 min incubation step resulted in no discernible discrimination which was attributed to excess amounts of non-specific binding in the control sample. Incubation times of 15 and 30 min gave good discrimination; 45% and 10% of the mean positive interaction peak intensity for 15 and 30 min incubation period, respectively. Initially, a 15 min incubation time was used as the best discrimination had been achieved using this incubation period. However, reproducible results were unable to be attained using this incubation time. The results from experiments in which a 30 min incubation time had been used showed both discrimination and good reproducibility (the signal was observed to vary by 19% between the five replicate scans collected). It was therefore decided that an incubation time of 30 min would be used in all further experiments.

Variability of signal between samples

The results of this experiment highlighted that the peak height values and therefore signal enhancement could vary between substrates. This was clearly observed in the 60 min incubation experiment. It was expected that a longer incubation time would result in higher intensity signals however; the normalised peak height values for both the

positive and control interaction with 60 min incubation were lower than that of 30 min incubation. This decrease in signal may be explained by the observation that some substrates are less SERS active than other substrates, even if the substrates originated from the same batch. This outcome had also been observed in previous experiments. It is unclear as to why this occurs and further investigation is needed to try and understand this effect. In an effort to avoid this occurrence, experiments which involved the comparison of specific conditions (e.g. concentration of streptavidinMG), were carried out, if possible, on the same substrate.

4.2.7.4 Evaluating the within and between sample coefficient of variation (CV)

To evaluate the variability of SERS intensity within and between substrates, coefficient of variation (CV) values were calculated. The CV is a measure of the spread of data and was calculated using equation 4.1

$$CV\ (\%) = \left(\frac{standard\ deviation}{mean}\right) \text{x } 100$$

(4.1)

Three positive and three control interactions were performed with each set (one positive, one control) on a separate substrate. Five replicate SERS spectra were collected from each interaction well. The results were analysed to determine the variability of SERS intensity both within a substrate and between three separate substrates.

Within substrate variability

The variability of SERS intensity within each of the three substrates investigated is shown in Figure 4.13.
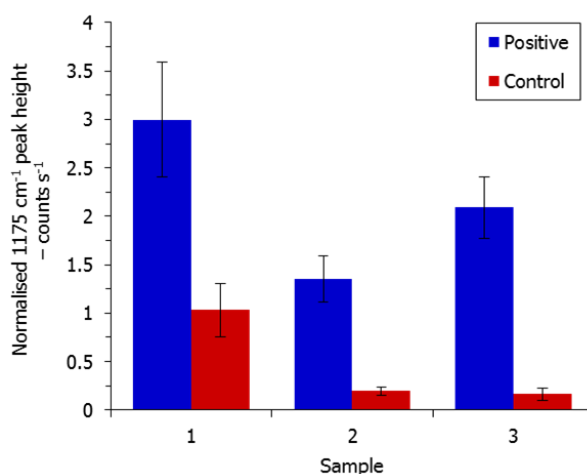
Figure 4.13 – The variation of SERS response at 633 nm excitation within three separate bimetallic nanohole array samples .The average peak heights were calculated from five replicate scans and the error bars represent two standard deviations about the mean.

In all samples, clear discrimination between the positive and the control interaction was achieved. The maximum CV values for the positive and the control interactions were 20 and 37%, respectively. There is a wide range of CV values reported in the literature for similar substrates; Norrod *et al.* reported a range of CV values for Ag SERS substrates ranging from 8 to 40%.[202] Stokes and co-workers reported a range of CV values between 9 and 35% for various dyes and dye-labelled DNA conjugates on Klarite.[155] Therefore, although the maximum CV values for the bimetallic nanohole substrates were relatively high, they were comparable to CV values reported for similar substrates in the literature.

Between sample variability

The variability of SERS intensity between the three substrates investigated is shown in Figure 4.14.
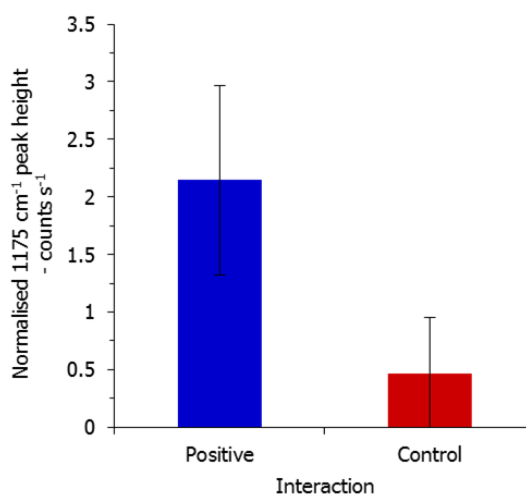
Figure 4.14 - The variation of SERS response at 633 nm excitation between three separate bimetallic nanohole array samples. The mean peak height values were calculated from spectra obtained from three separate substrates. The error bars represent two standard deviations about the mean.

The CV between the three samples was calculated to be 38% for the positive interaction and 106% for the control interaction. The calculated CV between the control samples was very high. It can be concluded that the Raman intensity varies moderately within substrates but to a greater extent between substrates and so experiments that compare variables, such as concentration of StreptavidinMG, should be performed on the same substrate to minimise the variability of the SERS intensity between samples.

Statistical analysis of the significance of the signal variability

Statistical analysis was carried out on the results of the signal variability investigation using the within substrate results to determine if the difference between the mean peak intensities observed from the positive and the control samples could be considered to be statistically significant (see section A1 for further details). The data from each replicate interaction was subjected to an individual F- and t-test. This would determine whether the positive and control mean intensity values observed from each replicate interaction differed as a result of the difference in interaction conditions as opposed to random error. For each replicate interaction, the results of a one-tailed t-test at a 95% confidence level showed the calculated value of t to be greater than the critical value of t ($t_{calc.} > t_{crit}$) and so the null hypothesis was rejected (H_0: the sample means of the

population do not differ significantly) hence the difference in mean peak intensities between the positive and control samples was significant and not due to random error.

4.2.7.5 Optimisation Investigation Conclusions

The results of the investigation into the optimal conditions for the SERS detection of labelled streptavidin on bimetallic nanohole arrays are summarised in Table 4.4.

Step	Concentration	Solvent	Time - h	Temperature - °C	Agitation
SAM formation	5 mM	DMF	65	r.t.	✘
EDC / sulfoNHS	400 mM / 100 mM	ddH$_2$O	1	r.t.	✔
Amine-PEG$_3$-biotin	1 mM	PBS	3	r.t.	✔
Ethanolamine pH 8.5	1 M	ddH$_2$O	1	r.t.	✔
StreptavidinMG	300 nM	PBST	0.5	r.t.	✔

Table 4.4 - Optimal conditions for proof-of-concept interaction on bimetallic nanohole array.

The discrimination between the positive and control interactions was maximised when the conditions outlined in Table 4.4 were used therefore these conditions were applied to all future experiments.

4.2.8 Signal variation with decreasing StreptavidinMG concentration

A biosensing system which is designed to detect an analyte at varying concentrations has to be validated over a dynamic range in order to determine the limits of the system. To validate the proof-of-concept biosensing system that had been developed on the bimetallic nanohole array substrates, the variation in height of the 1175 cm^{-1} peak was investigated with respect to decreasing concentration of streptavidinMG. It was postulated that a decrease in the concentration of streptavidinMG would result in a decrease in peak height. The optimised interaction method was followed using streptavidinMG concentrations of 300, 150 and 75 nM and a control streptavidinMG concentration of 300 nM. Three replicate samples at each concentration were prepared and analysed and 5 replicate scans from each sample were collected. The results of this investigation are shown in Figure 4.15.
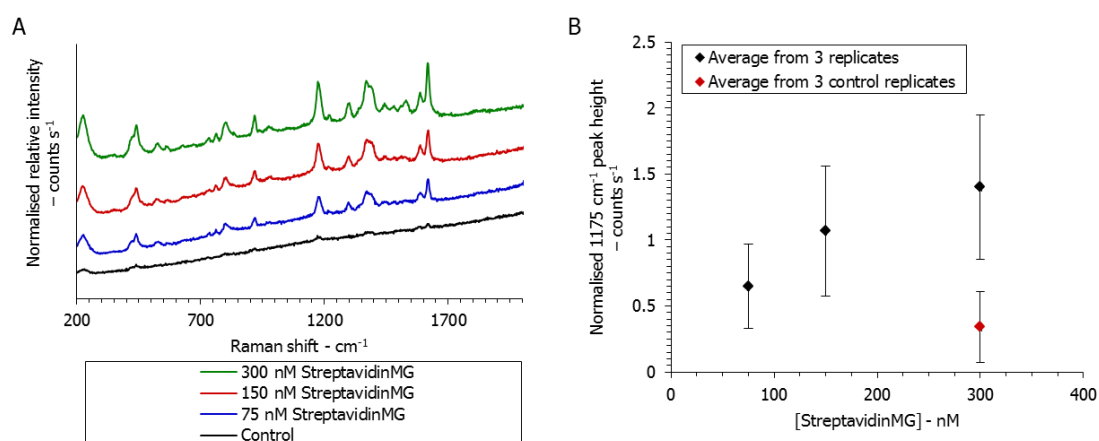
Figure 4.15 - A) Representative SERS spectra obtained from detection of 300 nM (green), 150 nM (red), 75 nM (blue) and in the absence (black) of streptavidinMG at 633 nm excitation. B) StreptavidinMG concentration dependence of SERS response.

Figure 4.15A shows a representative spectrum obtained from each streptavidinMG concentration investigated. The height of the 1175 cm^{-1} peak decreases with decreasing streptavidinMG concentration. Figure 4.15B shows the average peak height values from three experiments at each concentration investigated. It can be seen that although the peak heights clearly decrease with decreasing streptavidinMG concentration, the large standard deviations for each data point result in no discrimination between the different streptavidinMG concentrations investigated. To investigate the possible source of the large standard deviations, the results of the three replicate experiments performed on three separate samples were analysed as shown in Figure 4.16.
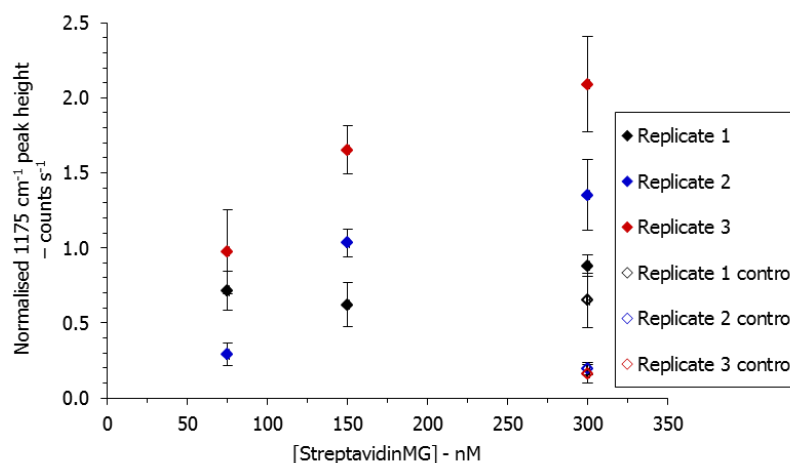
Figure 4.16 – The streptavidinMG concentration dependence of SERS response at 633 nm excitation from three separate replicate samples.

The results obtained from the replicate 1 experiment show no discrimination between any of the streptavidinMG concentrations investigated. This may be caused by the interactions being performed on a substrate with poor SERS activity. Discrimination was also not obtained between 300 and 150 nM streptavidinMG in both replicates 2 and 3 as illustrated by the overlap of error bars which represent the standard deviation. This may be caused by saturation of the biotinylated surface by streptavidinMG at concentrations above 150 nM. Further experiments using a dynamic range with an upper limit of 150 nM would be required to investigate this theory. However, replicates 2 and 3 both showed discrimination between the 150 nM streptavidinMG, 75 nM streptavidinMG and the control interaction indicating that the biosensing system is valid over a range of concentrations. As discussed previously, no discrimination was obtained from the average values calculated from the three separate experiments at each streptavidinMG concentration. Analysis of the peak height values from each separate interaction showed discrimination in two thirds of the experiments thus suggesting that the difference in SERS activity between the separate substrates was the reason that overall discrimination was not obtained. Further investigation with a larger number of replicate experiments could confirm this theory and improve the results obtained.

4.2.9 Increasing the distance between the SERS active substrate and the Raman reporter

It is known that in SERS, the further a molecule is away from the plasmonic surface, the lower the electric field experienced by the molecule and therefore the lower the SERS signal detected. This observation obeys the relationship described in equation 4.2 which states that the SERS intensity decreases as the distance between the surface and the analyte (r) increases.[24]

$$I_{SERS} = \left(\frac{a + r}{a}\right)^{-10}$$

(4.2)

By building up the interaction, investigation into both the effect of increasing the distance between the roughened metal surface and the Raman reporter on the SERS signal and the maximum distance tolerated before no signal can be detected could be accomplished. To achieve this, the amine-PEG$_3$-biotin linker was replaced with a biotinylated antibody. After interaction with streptavidinMG, the MG would be further

away from the array surface due to the increased size of the biotinylated antibody compared to the amine-PEG$_3$-biotin. The results obtained from this investigation were extremely variable with CV values ranging from 8 to 75%. The cross-linking of molecules via EDC/sulfoNHS coupling is not stereo-specific and so can result in the random orientation of the antibody to a surface.[203] Therefore, it was proposed that, as a result of the EDC/sulfoNHS coupling, the small biotin group may be "hidden" by the much larger antibody resulting in no interaction being able to occur between the biotin and labelled streptavidin molecule. The EDC/sulfoNHS coupling results in a random orientation of the biotinylated antibody and hence can explain why the results observed from this interaction were so variable. An alternative approach to the immobilisation of an antibody on the array surface would be required to further investigate the effect of distance between the SERS active substrate and the Raman reporter on signal enhancement.

4.2.10 Aurora A sensing

The method developed for sensing labelled streptavidin on a biotin-functionalised nanohole array substrate was shown to be successful at discriminating between a positive and a control interaction. It was thought that this proof-of-concept demonstration could be applied to a different system to determine if the procedure had the potential to be used in real-life biosensing applications. The system selected was Aurora A and C-terminal IKKβ peptides.

4.2.10.1 Aurora A

Aurora A is a kinase which is essential for the correct progression of cells through mitosis. It is also a target for the development of novel cancer therapies.[204] An interaction between Aurora A and the Inhibitory Kappa B kinase complex (IKK) has been shown in several studies.[205, 206] Preliminary work[207] has suggested that this interaction occurs at the C-terminus of the main IKK complex sub-unit IKKβ, in a region previously defined as the NEMO binding domain. The NEMO binding domain comprises of six amino acids, leucine-aspartic acid-tryptophan-serine-tryptophan-leucine (L-D-W-S-W-L), with the two central tryptophan residues being critical for any interaction.[208] Two short peptides (11 amino-acids) were created to represent the NEMO binding domain of IKKβ; a Wild Type (WT) with the NEMO binding domain sequence intact and a Mutant form in which the two critical tryptophan residues were mutated to alanine (A) residues, in theory, preventing any interaction from occurring. The binding of Aurora A to IKKβ had been previously investigated using SPR.[207] The results obtained suggested an interaction was occurring but further work was needed in order to confirm this theory. It was thought that the proof-of-concept work carried out on the biotin-streptavidin system could be applied to the Aurora A system to assess the binding of Aurora A to the WT and mutant forms of the peptide and, if successful, adding further confirmation of binding between these biomolecules.

4.2.10.2 Experimental method

The procedure used for the biotin-streptavidin proof-of-concept study was followed with two amendments; the amine-PEG$_3$-biotin linker was replaced by the WT peptide for the positive interaction or the mutant peptide for the control interaction and the MG-labelled streptavidin was replaced by MG-labelled Aurora A. The WT and mutant peptide were immobilised on the arrays surface *via* EDC/sulfoNHS conjugation of the

N-terminus of the peptides to the carboxyl group of the 16-MHA SAM. It was estimated that the Aurora A interaction with the WT peptide would not be as strong as the interaction between streptavidin and biotin and so in an attempt to maximise the binding, Aurora A MG was used at a higher concentration than that of streptavidinMG (530 nM vs. 300 nM respectively) and the Aurora A MG incubation time was investigated for two time points – 30 and 60 min. Three positive and three control interactions were performed at each incubation time, each in a separate well on the same substrate, and 8 replicate scans were taken from each well during SERS analysis.

4.2.10.3 Aurora A sensing results

Figure 4.17 shows the results of the Aurora A sensing experiment at both incubation time points.
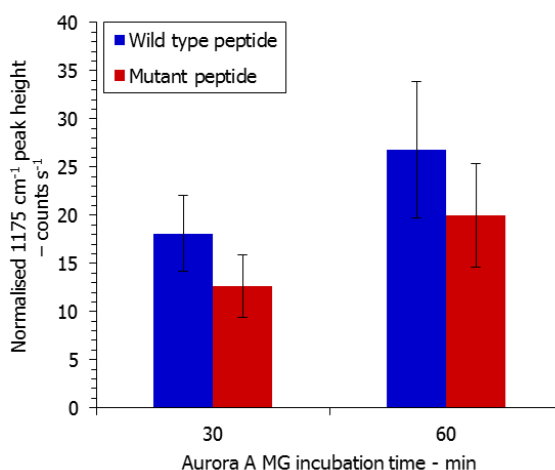
Figure 4.17 - Difference in SERS response at 633 nm excitation for 30 and 60 min Aurora A MG incubation time using peptide-functionalised bimetallic nanohole arrays. Peak height values represent the mean of three replicate samples and the error bars represent two standard deviations about the mean.

At both time points, the intensity of the 1175 cm^{-1} peak is higher for the WT peptide interaction compared to the mutant peptide interaction however no discrimination between the WT and the mutant peptide interactions was observed. At an incubation time of 60 min, both the signal observed from the WT and mutant peptide interactions was higher than that collected from the 30 min incubation time interactions. The CV values for the 30 min incubation time experiments were slightly smaller than those for the 60 min incubation (25% for the 30 min incubation period interaction compared to 27% for the 60 min incubation period interaction). These observations implied that increasing the incubation time, increased the amount of Aurora A MG that bound to the

surface and at longer incubation times, the binding is less uniform across the surface. This binding may be specific or non-specific in nature.

A one-tailed t-test at 95% confidence level was performed on the results of the 30 and 60 minute incubation study to determine whether the differences between the mean peak intensity values from the wild type peptide binding and the mutant peptide binding were statistically significant (see section A2 for full details). For both sample sets, t_{calc} was greater than t_{crit} ($t_{calc} > t_{crit}$) and so the null hypothesis was rejected; the difference between the wild type and mutant mean peak intensities was significant and not due to random error.

Although the statistical analysis concluded that the difference in mean peak intensity between the wild type and mutant peptide interaction at both 30 and 60 min incubation time points was significant, discrimination between the wild type and mutant peptide interactions was not achieved in either incubation time experiment. The lack of discrimination may be a result of an increase in non-specific binding between the peptide-functionalised surface and Aurora A MG however further work is required to investigate this theory.

The potential of a SERS-based method for assessing the binding of peptides to Aurora A

It can be concluded that the method investigated to assess the binding of a wild type and a mutant peptide to labelled Aurora A has the potential to be used in biological analysis. At both Aurora A MG incubation times, the SERS response obtained from the wild type peptide/Aurora A MG interaction was significantly higher than that obtained from the mutant peptide/Aurora A MG interaction. However, no analytical discrimination was obtained. As with all method development, optimisation is required for each specific system under investigation. It is possible that by optimising the conditions, e.g. incubation time, concentration of Aurora A MG, discrimination could be achieved between the wild type and mutant peptide experiments.

As the surface is functionalised with the peptide of interest, this method could be developed to analyse, on the same nanohole substrate, the binding of multiple different peptides with Aurora A hence creating a peptide screening method for use in the drug discovery process.

4.3 Conclusions

In conclusion, a method has been developed to detect MG labelled streptavidin on a biotin-functionalised bimetallic nanohole array using SERS at 633 nm excitation. Statistical tests demonstrated that the discrimination observed between the positive and control interactions was significant. A decrease in the concentration of streptavidinMG added to the surfaces resulted in a decrease in the height of the 1175 cm^{-1} peak demonstrating the method was valid at a range of streptavidinMG concentrations. The method was also successfully applied to a biological system of interest to assess the binding of a wild type peptide and a mutant peptide to MG labelled Aurora A.

4.4 Further Work

There is much scope for further work within this project.

4.4.1 Proof-of-concept Streptavidin detection

The dynamic working range of the proof-of-concept method should be investigated. Results demonstrated that discrimination could be obtained between 150 and 75 nM streptavidinMG and so further investigation should focus on concentrations below 75 nM as the results obtained suggested that at concentrations above 150 nM the surface was saturated with streptavidinMG.

In order to use this method to sense analytes, the substrate to substrate variability issue has to be addressed. The issue is thought to arise from the differences in SERS activity of each substrate. The inclusion of an internal standard in one well of each sample which could be used to calibrate the surfaces to account for any surface to surface variation may overcome this issue. In addition, the use of a micro-array chamber which could divide one surface into more than 6 wells would be advantageous as more experiments could be conducted under identical conditions on the same substrate.

4.4.2 Aurora A sensing

Optimisation of the interaction of MG labelled Aurora A with the wild type and mutant peptide is required to develop this method into a feasible biosensing strategy. The EDC/sulfoNHS coupling conditions, the method used to label Aurora A with MG, the Aurora A MG incubation time and concentration are all parameters that should be investigated to achieve a fully optimised interaction. If successful, the optimised method could be used to investigate the binding kinetics of the interaction and assess the binding of alternative peptides to Aurora A.

CHAPTER 5 - CONCLUSIONS

Metallic FON arrays and the related metallic nanotriangle arrays have demonstrated great potential as SERS substrates due to facile fabrication by NSL and the large Raman enhancement factors exhibited by these nanostructures.[28, 209] The use of modified NSL results in the closely related, but less investigated, FOEN and nanohole arrays. This research has detailed a systematic investigation into the structure-property relationship of FOEN and nanohole arrays in order to fully evaluate their potential as SERS substrates.

This research has concluded that significant improvements to the Raman response of FON and nanotriangle arrays could be obtained by the introduction of an etch step in the fabrication process, resulting in FOEN and nanohole arrays. The maximum Raman response was consistently exhibited by FOEN arrays with a gap/diameter of 0.2 or below and by nanohole arrays with a D/P of between 0.75 and 0.6 highlighting that the optimal substrates for Raman analysis could be predicted based on the physical properties of the array.

The outcome of tuning the nanostructure to specific properties results in maximum Raman enhancement and this is vital in the development of SERS active structures for use in sensing applications.

Hot-spots in SERS substrates are associated with large EF[210] however few studies have experimentally demonstrated the location of hot-spots or regions of high electric field in ordered 2D nanostructures. This research detailed the results of a fundamental investigation using SERS to probe the location of hot-spots on a series of nanotriangle/nanohole and FON/FOEN arrays. It was shown that the properties of the nanostructure resulted in the electric field being localised in different regions of the arrays. The results were in good agreement with the theoretical findings of numerous groups.[128, 129] The ability to map the hot-spots in SERS substrates is instrumental in the development of sensitive sensing strategies and paramount in the achievement of single-molecule SERS detection. Selective immobilisation of analyte molecules within the regions of intense electric field could have valuable implications in these research areas.

Successful development of a proof-of-concept SERS sensing strategy demonstrated that bimetallic nanohole arrays were suitable substrates for use in biosensing applications. Implementation of the developed methodology in a real-life biosensing situation highlighted the potential of this research for clinically-relevant biosensing applications.

This research has, through fundamental investigation of the structure-property relationship, demonstrated the great potential of metallic nanostructured arrays fabricated by NSL as useful, tuneable and sensitive SERS substrates for biosensing applications.

CHAPTER 6 - REFERENCES

1.   Le Ru, E. C.; Etchegoin, P. G., *Principles of Surface-Enhanced Raman Spectroscopy and related plasmonic effects*. First edition ed.; Elsevier: 2009.

2.   Willets, K. A.; Van Duyne, R. P. *Annual Review of Physical Chemistry* **2007,** 58, (1), 267-297.

3.   Lamprecht, B.; Krenn, J. R.; Schider, G.; Ditlbacher, H.; Salerno, M.; Felidj, N.; Leitner, A.; Aussenegg, F. R.; Weeber, J. C. *Applied Physics Letters* **2001,** 79, (1), 51-53.

4.   Aust, E. F.; Sawodny, M.; S, I.; Knoll, W. *Scanning* **1994,** 16, (6), 353-361.

5.   Sambles, J. R.; Bradbery, G. W.; Yang, F. *Contemporary Physics* **1991,** 32, (3), 173-183.

6.   Homola, J. *Chemical Reviews* **2008,** 108, (2), 462-493.

7.   Karlsson, R.; Fält, A. *Journal of Immunological Methods* **1997,** 200, (1–2), 121-133.

8.   Mernagh, D. R.; Janscak, P.; Firnam, K.; Kneale, G. G. *Biological Chemistry* **1998,** 379, 497-503.

9.   Bolduc, O. R.; Lambert-Lanteigne, P.; Colin, D. Y.; Zhao, S. S.; Proulx, C.; Boeglin, D.; Lubell, W. D.; Pelletier, J. N.; Fethiere, J.; Ong, H.; Masson, J. F. *The Analyst* **2011,** 136, (15), 3142-3148.

10.   Homola, J.; Yee, S. S.; Gauglitz, G. *Sensors and Actuators B: Chemical* **1999,** 54, 3-15.

11.   Haes, A. J.; Zou, S.; Schatz, G. C.; Van Duyne, R. P. *The Journal of Physical Chemistry B* **2003,** 108, (1), 109-116.

12.   Jung, L. S.; Campbell, C. T.; Chinowsky, T. M.; Mar, M. N.; Yee, S. S. *Langmuir* **1998,** 14, (19), 5636-5648.

13.   Svedendahl, M.; Chen, S.; Dmitriev, A.; Käll, M. *Nano Letters* **2009,** 9, (12), 4428-4433.

14.   Dieringer, J. A.; McFarland, A. D.; Shah, N. C.; Stuart, D. A.; Whitney, A. V.; Yonzon, C. R.; Young, M. A.; Zhang, X.; Van Duyne, R. P. *Faraday Discussions* **2006,** 132, 9-26.

15.   Smith, E.; Dent, G., *Modern Raman Spectroscopy: A Practical Approach*. Wiley: 2005; p 222.

16.   Fleischmann, M.; Hendra, P. J.; McQuillan, A. J. *Chemical Physics Letters* **1974,** 26, (2), 163-166.

17.   Jeanmaire, D. L.; Van Duyne, R. P. *Journal of Electroanalytical Chemistry and Interfacial Electrochemistry* **1977,** 84, (1), 1-20.

18.   Albrecht, M. G.; Creighton, J. A. *Journal of the American Chemical Society* **1977,** 99, (15), 5215-5217.

19.   Kneipp, K.; Kneipp, H.; Itzkan, I.; Dasari, R. R.; Feld, M. S. *Chemical Reviews* **1999,** 99, (10), 2957-2976.

20.   Moskovits, M. *Journal of Raman Spectroscopy* **2005,** 36, (6-7), 485-496.

21.   Le Ru, E. C.; Blackie, E.; Meyer, M.; Etchegoin, P. G. *The Journal of Physical Chemistry C* **2007,** 111, (37), 13794-13803.

22.   Grand, J.; de la Chapelle, M. L.; Bijeon, J. L.; Adam, P. M.; Vial, A.; Royer, P. *Physical Review B* **2005,** 72, (3), 033407.

23.   Tripp, R. A.; Dluhy, R. A.; Zhao, Y. *Nano Today* **2008,** 3, (3–4), 31-37.

24.   Kennedy, B. J.; Spaeth, S.; Dickey, M.; Carron, K. T. *The Journal of Physical Chemistry B* **1999,** 103, (18), 3640-3646.

25.   Brolo, A. G.; Irish, D. E. *Journal of Electroanalytical Chemistry* **1996,** 414, (2), 183-196.

26.   Stokes, R. J.; Macaskill, A.; Lundahl, P. J.; Smith, W. E.; Faulds, K.; Graham, D. *Small* **2007,** 3, (9), 1593-1601.

27.   Li, H.; Baum, C. E.; Sun, J.; Cullum, B. M. *Applied Spectroscopy* **2006,** 60, (12), 1377-1385.

28.   Haynes, C. L.; Van Duyne, R. P. *The Journal of Physical Chemistry B* **2003,** 107, (30), 7426-7433.

29.   Baia, L.; Baia, M.; Popp, J.; Astilean, S. *The Journal of Physical Chemistry B* **2006,** 110, (47), 23982-23986.

30.   Hatab, N. A.; Hsueh, C.-H.; Gaddis, A. L.; Retterer, S. T.; Li, J.-H.; Eres, G.; Zhang, Z.; Gu, B. *Nano Letters* **2010,** 10, (12), 4952-4955.

31.   Wang, C.; Ruan, W.; Ji, N.; Ji, W.; Lv, S.; Zhao, C.; Zhao, B. *The Journal of Physical Chemistry C* **2010,** 114, (7), 2886-2890.

32.   McFarland, A. D.; Young, M. A.; Dieringer, J. A.; Van Duyne, R. P. *The Journal of Physical Chemistry B* **2005,** 109, (22), 11279-11285.

33.   Brown, R. J. C.; Milton, M. J. T. *Journal of Raman Spectroscopy* **2008,** 39, (10), 1313-1326.

34.   Kerker, M.; Siiman, O.; Bumm, L. A.; Wang, D. S. *Applied Optics* **1980,** 19, (19), 3253-3255.

35.   Inoue, M.; Ohtaka, K. *Journal of the Physical Society of Japan* **1983,** 52, 3853-3864.

36.   Hildebrandt, P.; Stockburger, M. *The Journal of Physical Chemistry* **1984,** 88, (24), 5935-5944.

37.   Barhoumi, A.; Zhang, D.; Tam, F.; Halas, N. J. *Journal of the American Chemical Society* **2008,** 130, (16), 5523-5529.

38.   Casella, M.; Lucotti, A.; Tommasini, M.; Bedoni, M.; Forvi, E.; Gramatica, F.; Zerbi, G. *Spectrochimica Acta. Part A: Molecular and Biomolecular Spectroscopy* **2011,** 79, (5), 915-919.

39.   Shanmukh, S.; Jones, L.; Driskell, J.; Zhao, Y.; Dluhy, R.; Tripp, R. A. *Nano Letters* **2006,** 6, (11), 2630-2636.

40.   Inscore, F.; Shende, C.; Sengupta, A.; Huang, H.; Farquharson, S. *Applied Spectroscopy* **2011,** 65, (9), 1004-1008.

41.   Oo, M. K. K.; Chang, C. F.; Sun, Y.; Fan, X. *The Analyst* **2011,** 136, (13), 2811-2817.

42.   Wang, W.; Baohua, G. *Applied Spectroscopy* **2005,** 59, (12), 1509-1515.

43.   Driskell, J. D.; Kwarta, K. M.; Lipert, R. J.; Porter, M. D.; Neill, J. D.; Ridpath, J. F. *Analytical Chemistry* **2005,** 77, (19), 6147-6154.

44.   Thompson, D. G.; Enright, A.; Faulds, K.; Smith, W. E.; Graham, D. *Analytical Chemistry* **2008,** 80, (8), 2805-2810.

45.   Song, C.; Wang, Z.; Zhang, R.; Yang, J.; Tan, X.; Cui, Y. *Biosensors and Bioelectronics* **2009,** 25, (4), 826-831.

46.   Maiti, K. K.; Samanta, A.; Vendrell, M.; Soh, K. S.; Olivo, M.; Chang, Y. T. *Chemical Communications* **2011,** 47, (12), 3514-3516.

47.   Camden, J. P.; Dieringer, J. A.; Zhao, J.; Van Duyne, R. P. *Accounts of Chemical Research* **2008,** 41, (12), 1653-1661.

48.   Lal, S.; Grady, N. K.; Kundu, J.; Levin, C. S.; Lassiter, J. B.; Halas, N. J. *Chemical Society Reviews* **2008,** 37, (5), 898-911.

49.   Sepúlveda, B.; Angelomé, P. C.; Lechuga, L. M.; Liz-Marzán, L. M. *Nano Today* **2009,** 4, (3), 244-251.

50.   Rothschild, M.; Ehrlich, D. J. *Journal of Vacuum Science & Technology B: Microelectronics and Nanometer Structures* **1987,** 5, (1), 389-390.

51.   Andrew, T. L.; Tsai, H. Y.; Menon, R. *Science* **2009,** 324, (5929), 917-921.

52.   Fu, Y.; Zhou, W.; Lim, L. E. N.; Du, C.; Luo, X.; Zhao, Z.; Dong, X.; Shi, H.; Wang, C. *Optical Engineering* **2006,** 45, (10), 108001.

53.   Lin, Y.-Y.; Liao, J.-D.; Ju, Y.-H.; Chang, C.-W.; Shiau, A.-L. *Nanotechnology* **2011,** 22, (18), 185308.

54.   Ji, J.; O'Connell, J. G.; Carter, D. J. D.; Larson, D. N. *Analytical Chemistry* **2008,** 80, (7), 2491-2498.

55.   Clark, A. W.; Sheridan, A. K.; Glidle, A.; Cumming, D. R. S.; Cooper, J. M. *Applied Physics Letters* **2007,** 91, (9), 093109.

56.   Cao, W.; Elsayed-Ali, H. E. *Materials Letters* **2009,** 63, (26), 2263-2266.

57.   Nandwana, V.; Subramani, C.; Yeh, Y.-C.; Yang, B.; Dickert, S.; Barnes, M. D.; Tuominen, M. T.; Rotello, V. M. *Journal of Materials Chemistry* **2011,** 21, (42), 16859-16862.

58.   Aksu, S.; Yanik, A. A.; Adato, R.; Artar, A.; Huang, M.; Altug, H. *Nano Letters* **2010,** 10, (7), 2511-2518.

59.   Hulteen, J. C.; Van Duyne, R. P. *Journal of Vacuum Science and Technology A* **1995,** 13, (3), 1553-1558.

60.   Deckman, H. W.; Dunsmuir, J. H. *Applied Physics Letters* **1982,** 41, (4), 377-379.

61.   Hulteen, J. C.; Treichel, D. A.; Smith, M. T.; Duval, M. L.; Jensen, T. R.; Van Duyne, R. P. *The Journal of Physical Chemistry B* **1999,** 103, (19), 3854-3863.

62.   Live, L. S.; Bolduc, O. R.; Masson, J.-F. *Analytical Chemistry* **2010,** 82, (9), 3780-3787.

63.   Murray-Methot, M. P.; Menegazzo, N.; Masson, J. F. *The Analyst* **2008,** 133, (12), 1714-1721.

64.   Duyne, R. P. V.; Hulteen, J. C.; Treichel, D. A. *The Journal of Chemical Physics* **1993,** 99, (3), 2101-2115.

65.   Stuart, D. A.; Haes, A. J.; McFarland, A. D.; Nie, S.; Duyne, R. P. V. In *Refractive-index-sensitive, plasmon-resonant-scattering, and surface-enhanced Raman-scattering nanoparticles and arrays as biological sensing platforms*, 2004; Tuan, V.-D.; Zygmunt, G.; Joseph, R. L., Eds. SPIE: 2004; pp 60-73.

66.   Whitney, A. V.; Myers, B., D.; Van Duyne, R. P. *Nano Letters* **2004,** 4, (8), 1507-1511.

67.   Malinsky, M. D.; Kelly, K. L.; Schatz, G. C.; Van Duyne, R. P. *The Journal of Physical Chemistry B* **2001,** 105, (12), 2243-2350.

68.   Veinot, J. G. C.; Yan, H.; Smith, S. M.; Cui, J.; Huang, Q.; Marks, T. J. *Nano Letters* **2002,** 2, (4), 333-335.

69.   Han, S.; Briseno, A. L.; Shi, X.; Mah, D. A.; Zhou, F. *The Journal of Physical Chemistry B* **2002,** 106, (25), 6465-6472.

70.   Niu, D. X.; Zou, X.; Wu, J.; Xu, Y. B. *Applied Physics Letters* **2009,** 94, (7), 072501.

71.   Amaladass, E.; Eimüller, T.; Ludescher, B.; Tyliszczak, T.; Schütz, G. *Journal of Physics: Conference Series* **2010,** 200, (7), 072003.

72.   Bullen, H. A.; Garrett, S. J. *Nano Letters* **2002,** 2, (7), 739-745.

73.   Yi, D. K.; Kim, D.-Y. *Chemical Communications* **2003,** (8), 982-983.

74.   Murray-Méthot, M.-P.; Ratel, M.; Masson, J.-F. *The Journal of Physical Chemistry C* **2010,** 114, (18), 8268-8275.

75.   Ormonde, A. D.; Hicks, E. C. M.; Castillo, J.; Van Duyne, R. P. *Langmuir* **2004,** 20, (16), 6927-6931.

76.   Bartlett, P. N.; Birkin, P. R.; Ghanem, M. A. *Chemical Communications* **2000**, (17), 1671-1672.

77.   Haynes, C. L.; Van Duyne, R. P. *The Journal of Physical Chemistry B* **2001,** 105, (24), 5599-5611.

78.   Kosiorek, A.; Kandulski, W.; Glaczynska, H.; Giersig, M. *Small* **2005,** 1, (4), 439-444.

79.   Jensen, T. R.; Malinsky, M. D.; Haynes, C. L.; Van Duyne, R. P. *The Journal of Physical Chemistry B* **2000,** 104, (45), 10549-10556.

80.   Zhang, X.; Hicks, E. M.; Zhao, J.; Schatz, G. C.; Van Duyne, R. P. *Nano Letters* **2005,** 5, (7), 1503-1507.

81.   Mock, J. J.; Barbic, M.; Smith, D. R.; Schultz, D. A.; Schultz, S. *The Journal of Chemical Physics* **2002,** 116, (15), 6755-6759.

82.   Jain, P. K.; Huang, W.; El-Sayed, M. A. *Nano Letters* **2007,** 7, (7), 2080-2088.

83.   Romero, I.; Aizpurua, J.; Bryant, G. W.; García De Abajo, F. J. *Optics Express* **2006,** 14, (21), 9988-9999.

84.   Haynes, C. L.; McFarland, A. D.; Zhao, L.; Van Duyne, R. P.; Schatz, G. C.; Gunnarsson, L.; Prikulis, J.; Kasemo, B.; Käll, M. *The Journal of Physical Chemistry B* **2003,** 107, (30), 7337-7342.

85.   Su, K. H.; Wei, Q. H.; Zhang, X.; Mock, J. J.; Smith, D. R.; Schultz, S. *Nano Letters* **2003,** 3, (8), 1087-1090.

86.   Fromm, D. P.; Sundaramurthy, A.; Schuck, P. J.; Kino, G.; Moerner, W. E. *Nano Letters* **2004,** 4, (5), 957-961.

87.   Van Duyne, R. P.; Haes, A. J. *Journal of the American Chemical Society* **2002,** 124, (35), 10596-10604.

88.   Riboh, J. C.; Haes, A. J.; McFarland, A. D.; Yonzon, C. D.; Van Duyne, R. P. *Journal of Physical Chemistry B* **2003,** 107, (8), 1772 - 1780.

89.   Yonzon, C. R.; Jeoung, E.; Zou, S.; Schatz, G. C.; Mrksich, M.; Van Duyne, R. P. *Journal of the American Chemical Society* **2004,** 126, (39), 12669-12676.

90.   Haes, A. J.; Hall, W. P.; Chang, L.; Klein, W. L.; Van Duyne, R. P. *Nano Letters* **2004,** 4, (6), 1029-1034.

91.   Haes, A. J.; Chang, L.; Klein, W. L.; Van Duyne, R. P. *Journal of the American Chemical Society* **2005,** 127, (7), 2264-2271.

92.   Zhao, J.; Das, A.; Zhang, X.; Schatz, G. C.; Sligar, S. G.; Van Duyne, R. P. *Journal of the American Chemical Society* **2006,** 128, (34), 11004-11005.

93.   Hall, W. P.; Ngatia, S. N.; Van Duyne, R. P. *The Journal of Physical Chemistry C* **2011,** 115, (5), 1410-1414.

94.   Kreno, L. E.; Hupp, J. T.; Van Duyne, R. P. *Analytical Chemistry* **2010,** 82, (19), 8042-8046.

95.   Haes, A. J.; Van Duyne, R. P. *Journal of the American Chemical Society* **2002,** 124, (35), 10596-10604.

96.   Haes, A. J.; Hall, W. P.; Chang, L.; Klein, W. L.; Van Duyne, R. P. *Nano Letters* **2004,** 4, (6), 1029-1034.

97.   Haes, A. J.; Zou, S.; Zhao, J.; Schatz, G. C.; Van Duyne, R. P. *Journal of the American Chemical Society* **2006,** 128, (33), 10905-10914.

98.   Hiep, H. M.; Endo, T.; Kerman, K.; Chikae, M.; Kim, D.-K.; Yamamura, S.; Takamura, Y.; Tamiya, E. *Science and Technology of Advanced Materials* **2007,** 8, (4), 331-338.

99.   Lee, S.-W.; Lee, K.-S.; Ahn, J.; Lee, J.-J.; Kim, M.-G.; Shin, Y.-B. *ACS Nano* **2011,** 5, (2), 897-904.

100.   Raphael, M. P.; Christodoulides, J. A.; Mulvaney, S. P.; Miller, M. M.; Long, J. P.; Byers, J. M. *Analytical Chemistry* **2011,** 84, (3), 1367-1373.

101.   Brolo, A. G.; Gordon, R.; Leathem, B.; Kavanagh, K. L. *Langmuir* **2004,** 20, (12), 4813-4815.

102.   Stewart, M. E.; Yao, J.; Maria, J.; Gray, S. K.; Rogers, J. A.; Nuzzo, R. G. *Analytical Chemistry* **2009,** 81, (15), 5980-5989.

103.   Pang, L.; Hwang, G. M.; Slutsky, B.; Fainman, Y. *Applied Physics Letters* **2007,** 91, (12), 123112.

104.   Sharpe, J. C.; Mitchell, J. S.; Lin, L.; Sedoglavich, N.; Blaikie, R. J. *Analytical Chemistry* **2008,** 80, (6), 2244-2249.

105.   Eftekhari, F.; Escobedo, C.; Ferreira, J.; Duan, X.; Girotto, E. M.; Brolo, A. G.; Gordon, R.; Sinton, D. *Analytical Chemistry* **2009,** 81, (11), 4308-4311.

106.   Ferreira, J.; Santos, M. J. L.; Rahman, M. M.; Brolo, A. G.; Gordon, R.; Sinton, D.; Girotto, E. M. *Journal of the American Chemical Society* **2008,** 131, (2), 436-437.

107.   Meyer, S. A.; Le Ru, E. C.; Etchegoin, P. G. *Analytical Chemistry* **2011,** 83, (6), 2337-2344.

108.   Shkilnyy, A.; Souce, M.; Dubois, P.; Warmont, F.; Saboungi, M. L.; Chourpa, I. *The Analyst* **2009,** 134, (9), 1868-1872.

109.   Ko, H.; Singamaneni, S.; Tsukruk, V. V. *Small* **2008,** 4, (10), 1576-1599.

110.   Curto, A. G.; Abajo, F. J. G. d. *Nano Letters* **2008,** 8, (8), 2479-2484.

111.   Stuart, D. A.; Yonzon, C. R.; Zhang, X.; Lyandres, O.; Shah, N. C.; Glucksberg, M. R.; Walsh, J. T.; Van Duyne, R. P. *Analytical Chemistry* **2005,** 77, (13), 4013-4019.

112.   Litorja, M.; Haynes, C. L.; Haes, A. J.; Jensen, T. R.; Van Duyne, R. P. *The Journal of Physical Chemistry B* **2001,** 105, (29), 6907-6915.

113.   Zhang, X.; Yonzon, C. R.; Van Duyne, R. P. *Proceedings of SPIE* **2003,** 5221, 82-91.

114.   Whitney, A. V.; Elam, J. W.; Zou, S.; Zinovev, A. V.; Stair, P. C.; Schatz, G. C.; Van Duyne, R. P. *The Journal of Physical Chemistry B* **2005,** 109, (43), 20522-20528.

115.   Dhawan, A.; Norton, S. J.; Gerhold, M. D.; Vo-Dinh, T. *Optics Express* **2009,** 17, (12), 9688-9703.

116.   Chan, C. Y.; Xu, J. B.; Waye, M. Y.; Ong, H. C. *Applied Physics Letters* **2010,** 96, (3), 033104.

117.   Wang, L.; Cai, L.; Zhang, J.; Bai, W.; Hu, H.; Song, G. *Journal of Raman Spectroscopy* **2011,** 42, (6), 1263-1266.

118.   Li, G.; Chen, X.; Huang, L.; Wang, J.; Hu, W.; Lu, W. *Physica B: Condensed Matter* **2012,** 407, (12), 2223-2228.

119.   Oubre, C.; Nordlander, P. *The Journal of Physical Chemistry B* **2005,** 109, (20), 10042-10051.

120.   Félidj, N.; Aubard, J.; Lévi, G.; Krenn, J. R.; Hohenau, A.; Schider, G.; Leitner, A.; Aussenegg, F. R. *Applied Physics Letters* **2003,** 82, (18), 3095-3097.

121.   Yu, Q.; Guan, P.; Qin, D.; Golden, G.; Wallace, P. M. *Nano Letters* **2008,** 8, (7), 1923-1928.

122.   Kumar, P. S.; Pastoriza-Santos, I.; Rodriguez-Gonzalez, B.; Garcia de Abajo, F. J.; Liz-Marzan, L. M. *Nanotechnology* **2008,** 19, (1), 015606.

123.   Kleinman, S. L.; Ringe, E.; Valley, N.; Wustholz, K. L.; Phillips, E.; Scheidt, K. A.; Schatz, G. C.; Van Duyne, R. P. *Journal of the American Chemical Society* **2011,** 133, (11), 4115-4122.

124.   Weber, M. L.; Willets, K. A. *The Journal of Physical Chemistry Letters* **2011,** 2, (14), 1766-1770.

125.   Willets, K. A.; Stranahan, S. M.; Weber, M. L. *The Journal of Physical Chemistry Letters* **2012,** 3, 1286-1294.

126.   Hao, E.; Schatz, G. C. *The Journal of Chemical Physics* **2004,** 120, (1), 357-366.

127.   Marty, R.; Baffou, G.; Arbouet, A.; Girard, C.; Quidant, R. *Optics Express* **2010,** 18, (3), 3035-3044.

128.   Galarreta, B. C.; Norton, P. R.; Lagugné-Labarthet, F. *The Journal of Physical Chemistry C* **2010,** 114, (47), 19952-19957.

129.   Lee, S. H.; Bantz, K. C.; Lindquist, N. C.; Oh, S.-H.; Haynes, C. L. *Langmuir* **2009,** 25, (23), 13685-13693.

130.   Nelayah, J.; Kociak, M.; Stéphan, O.; García de Abajo, F. J.; Tencé, M.; Henrard, L.; Taverna, D.; Pastoriza-Santos, I.; Liz-Marzán, L. M.; Colliex, C. *Nature Physics* **2007,** 3, (5), 348-353.

131.   Guiton, B. S.; Iberi, V.; Li, S.; Leonard, D. N.; Parish, C. M.; Kotula, P. G.; Varela, M.; Schatz, G. C.; Pennycook, S. J.; Camden, J. P. *Nano Letters* **2011,** 11, (8), 3482-3488.

132.   Koh, A. L.; Fernández-Domínguez, A. I.; McComb, D. W.; Maier, S. A.; Yang, J. K. W. *Nano Letters* **2011,** 11, (3), 1323-1330.

133.   Farcau, C.; Astilean, S. *Journal of Physical Chemistry C* **2010,** 114, (27), 11717-11722.

134.   Galarreta, B. C.; Rupar, I.; Young, A.; Lagugné-Labarthet, F. *The Journal of Physical Chemistry C* **2011,** 115, (31), 15318-15323.

135.   Qin, L.; Zou, S.; Xue, C.; Atkinson, A.; Schatz, G. C.; Mirkin, C. A. *Proceedings of the National Academy of Sciences of the United States of America* **2006,** 103, (36), 13300-13303.

136.   Farcau, C.; Astilean, S. *Chemical Communications* **2011,** 47, (13), 3861-3863.

137.   Im, H.; Bantz, K. C.; Lindquist, N. C.; Haynes, C. L.; Oh, S.-H. *Nano Letters* **2010,** 10, (6), 2231-2236.

138.   Xie, W.; Qiu, P.; Mao, C. *Journal of Materials Chemistry* **2011,** 21, (14), 5190-5202.

139.   Schlücker, S. *ChemPhysChem* **2009,** 10, (9-10), 1344-1354.

140.   Zhang, Y.; Hong, H.; Myklejord, D. V.; Cai, W. *Small* **2011,** 7, (23), 3261-3269.

141.   Dougan, J. A.; Faulds, K. *The Analyst* **2012,** 137, (3), 545-554.

142.   Zhang, X.; Young, M. A.; Lyandres, O.; Van Duyne, R. P. *Journal of the American Chemical Society* **2005,** 127, (12), 4484-4489.

143.   Zhang, X.; Zhao, J.; Whitney, A. V.; Elam, J. W.; Van Duyne, R. P. *Journal of the American Chemical Society* **2006,** 128, (31), 10304-10309.

144.   Stuart, D. A.; Biggs, K. B.; Van Duyne, R. P. *The Analyst* **2006,** 131, (4), 568-572.

145.   Stuart, D. A.; Yuen, J. M.; Shah, N.; Lyandres, O.; Yonzon, C. R.; Glucksberg, M. R.; Walsh, J. T.; Van Duyne, R. P. *Analytical Chemistry* **2006,** 78, (20), 7211-7215.

146.   Deckert, V.; Zeisel, D.; Zenobi, R.; Vo-Dinh, T. *Analytical Chemistry* **1998,** 70, (13), 2646-2650.

147.   Chen, K.; Leona, M.; Vo-Dinh, K.-C.; Yan, F.; Wabuyele, M. B.; Vo-Dinh, T. *Journal of Raman Spectroscopy* **2006,** 37, (4), 520-527.

148.   Liu, X.; Huan, S.; Bu, Y.; Shen, G.; Yu, R. *Talanta* **2008,** 75, (3), 797-803.

149.   Galarreta, B. C.; Norton, P. R.; Lagugné-Labarthet, F. *Langmuir* **2011,** 27, (4), 1494-1498.

150.   Hatab, N. A.; Rouleau, C. M.; Retterer, S. T.; Eres, G.; Hatzinger, P. B.; Gu, B. *The Analyst* **2011,** 136, (8), 1697-1702.

151.   Yu, Q.; Golden, G. *Langmuir* **2007,** 23, (17), 8659-8662.

152.   Ko, H.; Tsukruk, V. V. *Small* **2008,** 4, (11), 1980-1984.

153.   Mahajan, S.; Richardson, J.; Brown, T.; Bartlett, P. N. *Journal of the American Chemical Society* **2008,** 130, (46), 15589-15601.

154.   Chen, S.; Svedendahl, M.; Kall, M.; Gunnarsson, L.; Dmitriev, A. *Nanotechnology* **2009,** 20, (43), 434015.

155.   Stokes, R. J.; Macaskill, A.; Dougan, J. A.; Hargreaves, P. G.; Stanford, H. M.; Smith, W. E.; Faulds, K.; Graham, D. *Chemical Communications* **2007**, (27), 2811-2813.

156.   Gauvreau, B.; Hassani, A.; Fehri, M. F.; Kabashin, A.; Skorobogatiy, M. *Optics Express* **2007,** 15, (18), 11413-11426.

157.   Reilly, T. H.; Van de Lagemaat, J.; Tenent, R. C.; Morfa, A. J.; Rowlen, K. L. *Applied Physics Letters* **2008,** 92, (24), 243304.

158.   Lohmüller, T.; Müller, U.; Breisch, S.; Nisch, W.; Rudorf, R.; Schuhmann, W.; Neugebauer, S.; Kaczor, M.; Linke, S.; Lechner, S.; Spatz, J.; Stelzle, M. *Journal of Micromechanics and Microengineering* **2008,** 18, (11), 115011.

159.   Kim, H.; Park, J. H.; Cho, I. H.; Kim, S. K.; Paek, S. H.; Lee, H. *Journal of Colloid and Interface Science* **2009,** 334, (2), 161-166.

160.   Brolo, A. G.; Kwok, S. C.; Moffitt, M. G.; Gordon, R.; Riordon, J.; Kavanagh, K. L. *Journal of the American Chemical Society* **2005,** 127, (42), 14936-14941.

161.   Ravi, K. K.; Dinish, U. S.; Chit, Y. F.; Gopalkrishna, H.; Malini, O.; Anandi, A. In *Metal enhanced fluorescence on silver nano-triangles*, Photonics Global Conference 2010; 2010; pp 1-5.

162.   Rasband, W. S. ImageJ. http://imagej.nih.gov/ij/

163.   Chen, H.; Shao, L.; Woo, K. C.; Ming, T.; Lin, H.-Q.; Wang, J. *The Journal of Physical Chemistry C* **2009,** 113, (41), 17691-17697.

164.   Kudelski, A.; Hill, W. *Langmuir* **1999,** 15, (9), 3162-3168.

165.   Skadtchenko, B. O.; Aroca, R. *Spectrochimica Acta Part A* **2001,** 57, 1009-1016.

166.   Shin, K. S.; Park, C. S.; Kang, W.; Kim, K. *Chemistry Letters* **2008,** 37, (2), 180-181.

167.   Kim, K.; Choi, J.-Y.; Lee, H. B.; Shin, K. S. *ACS Applied Materials & Interfaces* **2010,** 2, (7), 1872-1878.

168.   Merlen, A.; Gadenne, V.; Romann, J.; Chevallier, V.; Patrone, L.; Valmalette, J. C. *Nanotechnology* **2009,** 20, (21), 215705.

169.   Han, S. W.; Lee, I.; Kim, K. *Langmuir* **2002,** 18, (1), 182-187.

170.   Murray, W. A.; Astilean, S.; Barnes, W. L. *Physical Review B* **2004,** 69, (16), 165407.

171.   Felidj, N.; Grand, J.; Laurent, G.; Aubard, J.; Levi, G.; Hohenau, A.; Galler, N.; Aussenegg, F. R.; Krenn, J. R. *The Journal of Chemical Physics* **2008,** 128, (9), 094702.

172.   Perney, N. M. B.; Baumberg, J. J. *Optics Express* **2006,** 14, (2), 847-857.

173.   Ignat, T.; Munoz, R.; Irina, K.; Obieta, I.; Mihaela, M.; Simion, M.; Iovu, M. *Superlattices and Microstructures* **2009,** 46, (3), 451-460.

174.   Jiao, Y.; Ryckman, J. D.; Ciesielski, P. N.; Escobar, C. A.; Jennings, G. K.; Weiss, S. M. *Nanotechnology* **2011,** 22, (29), 295302.

175.   resources.renishaw.com/en/FAQ(19262)

176.   Beeram, S. R.; Zamborini, F. P. *Journal of the American Chemical Society* **2009,** 131, (33), 11689-11691.

177.   Brolo, A. G.; Arctander, E.; Addison, C. J. *The Journal of Physical Chemistry B* **2005,** 109, (1), 401-405.

178.   Paul, A.; Kenens, B.; Hofkens, J.; Uji-i, H. *Langmuir* **2012,** 28, (24), 8920-8925.

179.   Sweetenham, C. S.; Notingher, I. *Journal of Nanophotonics* **2011,** 5, (1), 059504.

180.   Garcia-Vigal, F. J.; Pendry, J. B. *Physical Review Letters* **1996,** 77, (6), 1163-1166.

181.   Liu, Y.; Sarris, C. D.; Eleftheriades. *Antennas and Propagation Society International Symposium 2006, IEEE* **2006**, 741-744.

182.   Potyrailo, R. A.; Dovidenko, K.; Le Tarte, L. A.; Surman, C.; Pris, A. *Proceedings of SPIE* **2009,** 7322, 73220M.

183.   Jung, D. R.; Czanderna, A. W. *Journal of Vacuum Science and Technology A* **1995,** 13, (3), 1337-1344.

184.   Correia-Ledo, D.; Masson, J. F. *Unpublished work, Universite de Montréal* **2011**.

185.   Hong, P. P.; Boerio, F. J.; Clarson, S. J.; Smith, S. D. *Macromolecules* **1991,** 24, (17), 4770-4776.

186.   Qian, X.; Emory, S. R.; Nie, S. *Journal of the American Chemical Society* **2012,** 134, (4), 2000-2003.

187.   Kamińska, A.; Dzięcielewski, I.; Weyher, J. L.; Waluk, J.; Gawinkowski, S.; Sashuk, V.; Fiałkowski, M.; Sawicka, M.; Suski, T.; Porowski, S.; Hołyst, R. *Journal of Materials Chemistry* **2011,** 21, (24), 8662-8669.

188.   Lee, K.-B.; Yoon, K. R.; Woo, S. I.; Choi, I. S. *Journal of Pharmaceutical Sciences* **2003,** 92, (5), 933-937.

189.   Nath, N.; Chilkoti, A. *Analytical Chemistry* **2004,** 76, (18), 5370-5378.

190.   Hendrickson, W. A.; Pahler, A.; Smith, J. L.; Satow, Y.; Merritt, E. A.; Phizackerley, R. P. *Proceedings of the National Academy of Sciences of the United States of America* **1989,** 86, 2190-2194.

191.   Chaiet, L.; Wolf, F. J. *Archives of Biochemistry and Biophysics* **1964,** 106, 1-5.

192.   Tong, X.; Smith, L., M. *Analytical Chemistry* **1992,** 64, (22), 2672-2677.

193.   Holmberg, A.; Blomstergren, A.; Nord, O.; Lukacs, M.; Lundeberg, J.; Uhlen, M. *Electrophoresis* **2005,** 26, (3), 501-510.

194.   Brinkley, M. *Bioconjugate Chemistry.* **1992,** 3, (1), 2-13.

195.   Techane, S. D.; Gamble, L. J.; Castner, D. G. *The Journal of Physical Chemistry C* **2011,** 115, (19), 9432-9441.

196.   Huang, F.; Qu, S.; Zhang, S.; Liu, B.; Kong, J. *Talanta* **2007,** 72, (2), 457-462.

197.   Aslan, K.; Luhrs, C. C.; Perez-Luna, V. H. *Journal of Physical Chemistry B* **2004,** 108, (40), 15631-15639.

198.   Chi, Y. S.; Byon, H. R.; Lee, B. S.; Kong, B.; Choi, H. C.; Choi, I. S. *Advanced Functional Materials* **2008,** 18, (21), 3395-3402.

199.   Bain, C. D.; Troughton, E. B.; Tao, Y.-T.; Evall, J.; Whitesides, G.; Nuzzo, R. G. *Journal of the American Chemical Society* **1988,** 111, (1), 321-335.

200.   Gong, P.; Grainger, D. W. *Surface Science* **2004,** 570, 67-77.

201.   Wolf, L. K.; Fullenkamp, D. E.; Georgiadis, R. M. *Journal of the American Chemical Society* **2005,** 127, (49), 17453-17549.

202.   Norrod, K. L.; Sudnik, L. M.; Rousell, D.; Rowlen, K. L. *Applied Spectroscopy* **1997,** 51, (7), 994-1001.

203.   Bonroy, K.; Frederix, F.; Reekmans, G.; Dewolf, E.; De Palma, R.; Borghs, G.; Declerck, P.; Goddeeris, B. *Journal of Immunological Methods* **2006,** 312, 167-181.

204.   Katayama, H.; Sen, S. *Biochimica and Biophysica Acta* **2010,** 1799, 829-839.

205.   Prajapati, S.; Tu, Z.; Yamamoto, Y.; Gaynor, R. B. *Cell Cycle* **2006,** 5, (20), 2371-2380.

206.   Irelan, J. T.; Murphy, T. J.; DeJesus, P. D.; Teo, H.; Xu, D.; Gomez-Ferreria, M. A.; Zhou, Y.; Miraglia, L. J.; Rines, D. R.; Verma, I. M.; Sharp, D. J.; Tergaonkar, V.; Chanda, S. K. *Proceedings of the National Academy of Sciences of the United States of America* **2007,** 104, (43), 16940-16945.

207.   Wilson, A.; Gamble, C.; Paul, A. *Unpublished work, University of Strathclyde* **2011**.

208.   Rushe, M.; Silvian, L.; Bixler, S.; Chen, L. L.; Cheung, A.; Bowes, S.; Cuervo, H.; Berkowitz, S.; Zheng, T.; Guckian, K.; Pellegrini, M.; Lugovskoy, A. *Structure* **2008,** 16, (5), 798-808.

209.   Haes, A. J.; Haynes, C. L.; McFarland, A. D.; Schatz, G. C.; Van Duyne, R. P.; Zou, S. *MRS Bulletin* **2005,** 30, (05), 368-375.

210.   Ru, E. C. L.; Etchegoin, P. G.; Meyer, M. *The Journal of Chemical Physics* **2006,** 125, (20), 204701.

Appendix

A1 F- and t-test calculations from section 4.2.7.4

The F_{calc} value was calculated using equation A1.

$$F_{calc} = \frac{s_1^2}{s_2^2}$$

(A1)

where $s_1 > s_2$.

The degrees of freedom (v) used to determine the F_{crit} value was calculated using equation A2.

$$v = (n - 1)$$

(A2)

F-test H_0 – the variances are equal.

If $F_{calc} < F_{crit}$, the F-test passes and the H_0 is accepted. In this case, the standard deviations are pooled to calculate the variation (s) of the experiment. This was calculated using equation A3.

$$s = \sqrt{\left(\frac{(n_1 - 1)s_1^2 + (n_2 - 1)s_2^2}{(n_1 + n_2 - 2)}\right)}$$

(A3)

The t_{calc} value was then calculated using equation A4.

$$|t_{calc}| = \left(\frac{\bar{x}_1 - \bar{x}_2}{s\sqrt{\left(\frac{1}{n_1} + \frac{1}{n_2}\right)}}\right)$$

(A4)

The degrees of freedom (v) for the t_{crit} value were calculated using equation A5.

$$v = (n_1 + n_2 - 2)$$

(A5)

t-test H_0 – the mean values are equal

If $F_{calc} > F_{crit}$, the F-test fails and the H_0 is rejected. The t_{calc} value was then calculated using equation A6.

$$|t_{calc}| = \frac{|\overline{x_1} - \overline{x_2}|}{\sqrt{\frac{s_1^2}{n_1} + \frac{s_2^2}{n_2}}}$$

(A6)

In this case, the degrees of freedom (v) used to determine the t_{crit} value was calculated using equation A7.

$$v = \frac{\left(\frac{s_1^2}{n_1} + \frac{s_2^2}{n_2}\right)^2}{\frac{s_1^4}{n_1^2(n_1 - 1)} + \frac{s_2^4}{n_2^2(n_2 - 1)}}$$

(A7)

t-test H_0 – the mean values are equal

Replicate interaction 1

	Normalised 1175 cm^{-1} peak height values from positive interaction – a.u.	Normalised 1175 cm^{-1} peak height values from control interaction – a.u.
	3.177	0.642
	2.041	1.179
	3.570	1.153
	3.350	0.868
	2.852	1.311
Average	**2.998**	**1.031**
Standard deviation	**0.355**	**0.073**

Table A1 – Raw data from positive and control replicate interaction 1.

F_{crit} ($v = 4$) = 6.388 (at 95% confidence level)

F_{calc} = 4.851 therefore $F_{calc} < F_{crit}$ and H_0 is accepted; The variances are equal.

t_{crit} ($v = 8$) = 1.860 (one-tailed, at 95% confidence level)

t_{calc} = 6.723 therefore $t_{calc} > t_{crit}$ and H_0 is rejected; The difference in mean values is significant and not due to random error.

Replicate interaction 2

	Normalised 1175 cm^{-1} peak height values from positive interaction – a.u.	Normalised 1175 cm^{-1} peak height values from control interaction – a.u.
	1.500	0.084
	1.668	0.226
	2.060	0.197
	2.427	0.113
	2.203	0.191
Average	**1.972**	**0.162**
Standard deviation	**0.146**	**0.004**

Table A2– Raw data from positive and control replicate interaction 2.

F_{crit} (v = 4) = 6.388 (at 95% confidence level)

F_{calc} = 39.803 therefore F_{calc} > F_{crit} and H_0 is rejected; The variances are not equal.

t_{crit} (v = 4) = 2.132 (one-tailed, at 95% confidence level)

t_{calc} = 10.458 therefore t_{calc} > t_{crit} and H_0 is rejected; The difference in mean values is significant and not due to random error.

Replicate interaction 3

	Normalised 1175 cm^{-1} peak height values from positive interaction – a.u.	Normalised 1175 cm^{-1} peak height values from control interaction – a.u.
	1.314	0.209
	1.693	0.250
	1.245	0.167
	1.156	0.160
	1.296	0.175
Average	**1.341**	**0.192**
Standard deviation	**0.043**	**0.001**

Table A3 – Raw data from positive and control replicate interaction 3.

F_{crit} (v = 4) = 6.388 (at 95% confidence level)

F_{calc} = 30.846 therefore F_{calc} > F_{crit} and H_0 is rejected; The variances are not equal.

t_{crit} (v = 4) = 2.132 (one-tailed, at 95% confidence level)

t_{calc} = 12.253 therefore t_{calc} > t_{crit} and H_0 is rejected; The difference in mean values is significant and not due to random error.

A2 F- and t-test calculations from section 4.2.10.3

The calculations noted in section A1 were used in the F- and t-tests described in section 4.2.10.3.

30 minutes Aurora A incubation time

	Normalised 1175 cm^{-1} peak height values from WT peptide interaction – a.u.	Normalised 1175 cm^{-1} peak height values from mutant peptide interaction – a.u.
	15.845	9.089
	18.524	8.930
	17.743	10.873
	15.540	7.514
	17.621	9.927
	17.949	15.249
	18.201	11.984
	22.702	11.816
	9.811	12.158
	10.452	9.951
	16.724	12.838
	14.876	17.512
	23.048	14.293
	11.420	8.775
	23.740	10.738
	17.860	13.163
	22.510	15.050
	20.646	15.048
	22.093	22.092
	17.853	13.659
	23.381	16.200
	16.879	11.622
	17.379	12.582
	21.191	11.407
Average	**18.083**	**12.603**
Standard deviation	**3.930**	**3.237**

Table A4 – Raw data from wild type and mutant peptide interaction with 30 min Aurora A incubation time..

F_{crit} (v = 23) = 2.014 (at 95% confidence level)

F_{calc} = 1.474 (one-tailed, at 95% confidence level) therefore F_{calc} < F_{crit} and H_0 is accepted; The variances are equal.

146

t$_{crit}$ (v = 46) = 1.679

t$_{calc}$ = 5.273 (one-tailed, at 95% confidence level) therefore F$_{calc}$ > F$_{crit}$ and H$_0$ is rejected; The difference between is mean values is significant and not due to random error.

60 minutes Aurora A incubation time

	Normalised 1175 cm^{-1} peak height values from WT peptide interaction – a.u.	Normalised 1175 cm^{-1} peak height values from mutant peptide interaction – a.u.
	23.260	17.662
	24.657	12.818
	22.097	17.611
	21.462	21.501
	24.610	13.023
	32.343	14.778
	29.282	16.791
	29.562	20.746
	17.633	19.784
	17.406	16.498
	18.038	15.018
	21.939	11.241
	22.182	14.040
	15.549	17.945
	20.728	29.405
	35.695	28.446
	35.542	22.032
	33.032	28.890
	36.449	26.318
	35.735	24.842
	32.045	24.119
	35.470	23.044
	36.246	18.340
	21.872	24.173
Average	**26.785**	**19.961**
Standard deviation	**7.096**	**5.350**

Table A5– Raw data from wild type and mutant peptide interaction with 60 min Aurora A incubation time..

F$_{crit}$ (v = 23) = 2.014 (at 95% confidence level)

F$_{calc}$ = 1.760 (one-tailed, at 95% confidence level) therefore F$_{calc}$ < F$_{crit}$ and H$_0$ is accepted; The variances are equal.

t_{crit} ($v = 46$) = 1.679

t_{calc} = 3.762 (one-tailed, at 95% confidence level) therefore $F_{calc} > F_{crit}$ and H_0 is rejected; The difference between is mean values is significant and not due to random error.

A3 Publications

1. *The Journal of Physical Chemistry C* **2010**, 114, (51), 22406-22412

Surface-Enhanced Raman Spectroscopy Amplification with Film over Etched Nanospheres

Jean-Francois Masson,*,† Kirsty F. Gibson,‡ and Audrey Provencher-Girard†

*Département de Chimie, Université de Montréal, C. P. 6128 Succ. Centre-Ville,
Montréal, Québec H3C 3J7, Canada, and Centre for Molecular Nanometrology, Department of Pure and
Applied Chemistry, University of Strathclyde, Glasgow G1 1XL, Scotland*

Received: July 12, 2010; Revised Manuscript Received: November 10, 2010

Polymer nanosphere lithography (NSL) masks were etched in oxygen plasma prior to metal deposition, which tunes the localized surface plasmon resonance (LSPR) and the interparticle distance resulting in greater Raman amplification than conventional film over nanosphere (FON). Various nanosphere masks were investigated, using nanosphere sizes of 220, 360, 450, 520, and 650 nm etched from 0 (conventional FON) to 10 min. Thereby, the film over etched nanospheres (FOEN) amplifies by up to a factor of 4 the Raman response of 4-nitrobenzenethiol (4-NBT) on Ag as compared to unetched FON. The LSPR response of FOEN and SEM analysis of the gap distance revealed that the optimal amplification results from a combination of tuning the gap (a gap/diameter of less than 1 improves the Raman response), matching the laser excitation wavelength (633 and 785 nm both investigated), and an increasing roughness of FOEN. Metal multilayers of Ag and Au were also deposited to investigate the effect on the Raman and LSPR response. While the LSPR response remains relatively invariable, the Raman signal from 4-NBT decreased significantly by increasing the number of layers when Ag is used as the outer layer. However, a bimetallic film composed of Ag underlayer with Au as an outerlayer further increased the Raman response by a factor of 1.6. Overall, the most intense Raman response for FOEN was obtained with 360 nm nanospheres, etched for 1.5 min to create a gap of 66 nm with an overall bimetallic film thickness of 175 nm, which was composed of an Ag underlayer of 87.5 nm and an Au outerlayer of 87.5 nm. Thus, by performing these simple modifications to FON, the Raman response can be increased by nearly 1 order of magnitude.

Introduction

Surface-enhanced Raman spectroscopy (SERS) has emerged as a useful tool for analytical chemistry,[1] specifically in the bioassay platform[2] and (bio)chemical diagnostics areas.[3] Early SERS experiments were performed on roughened Ag electrodes, with limited reproducibility hindering many analytical applications. This has triggered extensive research in fabricating structures exhibiting greater reproducibility, while providing large Raman amplification.[4] In particular, nanoparticles and nanostructured arrays are attractive as SERS substrates for their improved reproducibility. Among others, colloidal surfaces, anisotropic nanostructures, surfaces prepared by lithographic techniques, and dimer structures have been recently developed for SERS.[4] SERS surfaces consisting of an array of nanoparticles or nanostructures are especially interesting for a number of reasons: they provide high surface density leading to intense Raman response, they can be manufactured reproducibly with repeatable Raman response, they are easy to handle, and they can be treated as or they react similarly to solid-phase synthesis substrates, facilitating chemical reactions and purification. Some examples of SERS active surfaces include nanohole arrays,[5] surfaces prepared with glancing angle deposition,[6] nanotriangle arrays,[7] and film over nanospheres (FON).[8] Numerous applications using these substrates have been reported in the literature.[1]

FON have been extensively investigated due to simple fabrication methodology and good Raman amplification. Briefly,

a nanosphere lithography (NSL) mask, consisting of a monolayer of hexagonally packed polymer or silica nanospheres, is deposited on a substrate, typically a glass microscope slide. A metal film is deposited onto the NSL mask, resulting in a surface with a reproducible nanoscale pattern. Recently, several approaches have been investigated to modify NSL to create more complex nanostructured arrays. Among others, nanopores or nanowells[9,10] and nanohole arrays[11] were fabricated using similar techniques involving etching a NSL mask. Etching the NSL mask also creates an array of nanoshells,[12] and removing the mask following metal deposition creates nanohole arrays. Nanohole arrays fabricated using modified NSL have been investigated for plasmonic sensing[13–15] and for Raman spectroscopy.[16] A recent article by Lee et al. demonstrated an increased enhancement factor of 1 order of magnitude of nanohole arrays as compared to AgFON. The authors also demonstrated that electroless deposition of Ag further increased the enhancement factor.[16] Modified NSL is therefore appropriate to fabricate SERS surfaces with tailored optical properties.

Several interesting optical phenomena occur when nanostructures are in close proximity to one another. Metallic nanoparticles in close proximity will have their surface plasmon greatly shifted depending on the interparticle distance, which has been exploited as a molecular ruler[17] and for the colorimetric detection of DNA hybridization.[18] In the case of Raman spectroscopy, nanoparticle dimers exhibit a much greater electric field in the gap between two nanoparticles, leading to significantly enhanced Raman amplification.[19,20] Tuning the distance between particles greatly influences the plasmonic properties. As described by the plasmonic ruler model, the gap must be normalized by the diameter of the nanoparticle. Plasmonic coupling between

* Corresponding author. Phone: (514) 343-7342. Fax: (514) 343-7586. E-mail: jf.masson@umontreal.ca.
† Université de Montréal.
‡ University of Strathclyde.

SERS Amplification with Film over Etched Nanospheres

J. Phys. Chem. C, Vol. 114, No. 51, 2010 **22407**

adjacent nanoparticles occurs for structures separated by a gap smaller than or equal to the diameter of the nanostructure.[21]

A recent article demonstrated that the number of cores in aggregates composed of multiple nanoparticles did not influence the enhancement factor.[22] A single hot spot in an aggregate is sufficient for attaining optimal amplification of the Raman response of a molecular adsorbate. Unlike isolated nanoparticles, no correlation was observed between surface plasmon wavelength and enhancement factor. Ultrasensitive Raman detection for molecules adsorbed on nanoaggregates has enabled several applications including single molecule Raman detection.[23] One approach to fabricating nanoaggregates with controlled distance between particles involves the use of organic layers acting as spacers between nanoparticles.[24,25] Porter et al. investigated the effect of interparticle spacing on Raman amplification using a nanoparticle located at varying distances from a metal surface. The distance was controlled using different chemical layers, and it was reported that for this particular experiment, the Raman amplification was greater with a shorter chemical layer of 1.2 nm in height. Simulations support these results; the gap between a nanosphere dimer pair was varied resulting in a rapid increase in the electric field as the gap decreased.[26] Therefore, there has been an increased interest in fabricating and studying nanostructures exhibiting small interparticle distance to exploit their increased Raman amplification.

Many techniques, including modified nanosphere lithography, result in particles and surfaces with non-negligible roughness, while chemical synthesis of nanoparticles leads to relatively smooth surfaces, such as the work on particle dimers reported above. Nanostructures with controllable interparticle distances were designed using on-wire lithography, a process leading to non-negligible surface roughness. It was demonstrated that a gap distance of 30 nm provided the largest Raman amplification for Au nanodisks. This is in disagreement with theoretical calculations for the same structures, which predicted a 10 nm interparticle distance should exhibit the largest amplification.[27] It was thereafter demonstrated that surface roughness contributes significantly to the Raman amplification of nanoparticle dimers. The surface roughness therefore accounts for the discrepancies between the theoretically and experimentally determined optimal interparticle distance of Au nanodisks.[28] Moreover, the nonzero optimal gap was explained by the strong detuning to the red of the surface plasmon wavelength for the on-wire lithography. This result is of significance for nanostructures prepared with techniques that result in non-negligible roughness, such as modified NSL.

Investigating the Raman response of nanoparticle arrays in relation with different sizes of nanoparticles and gap distances is of great interest to design optimal SERS substrates. A report in the literature has demonstrated that Raman amplification increases for arrays of nanoparticles with shorter interparticle distances.[29] In this example, the gap is varied from 75 to more than 250 nm, for square arrays of nanoparticles of 200 nm diameter (similar to FON).[29] Another group reported the effect on the plasmonic properties of nanotriangle arrays of varying the gap (between 50 and 100 nm).[30] The effect of the gap on the Raman properties has not been reported for these nanotriangle arrays of variable gap. In addition, these arrays were not within the same gap regime as nanoparticle dimers (<10 nm) or on-wire lithography (gap between 5 and 160 nm). Thus, the determination of the optimal gap size for arrays of nanoparticle remains to be determined. Modified NSL is used in this report as the method of choice to investigate nanostructure arrays with

a wide range of gap distances. This investigation reports the results obtained from the study of a series of FOEN substrates.

Experimental Section

Fabrication of Film over Etched Nanospheres (FOEN). Glass microscope slides (22×22 mm) were cleaned in pirhana solution (75% v/v H_2SO_4:25% v/v H_2O_2) for 90 min at 80 °C. Caution: Pirhana solution is highly corrosive. The glass slides were then thoroughly cleaned numerous times with 18 MΩ water in an ultrasonication bath. Thereafter, the slides were placed in a 5:1:1 v/v solution of H_2O, NH_4OH, and H_2O_2 for 60 min in an ultrasonication bath. Again, the slides were thoroughly cleaned in 18 MΩ water in an ultrasonication bath. The cleaned slides were stored in 18 MΩ water for several weeks, with the water being replaced every 48 h.

The films over nanosphere (FON) were prepared as follows. For nanospheres of 520 and 650 nm (Thermo Fischer particle technology, 5000 series), a nanosphere solution (37 μL) was drop-coated onto the cleaned glass microscope slide to form a well-ordered monolayer. The solution compositions were as follows: for 520 nm nanospheres, 80 μL of stock nanosphere solution was mixed with 160 μL of ethanol and 760 μL of water; for 650 nm nanospheres, 120 μL of stock nanosphere solution was mixed with 160 μL of ethanol and 720 μL of water. The drop coated solution was slowly evaporated under a Petri dish to form a well-ordered monolayer on the glass microscope slide.

For 220, 360, and 450 nm nanospheres, stock nanosphere solution (10% as provided) was diluted with pure ethanol. The ratio of dilution was as follows: for 220 and 450 nm nanospheres, 30 μL of nanosphere solution was diluted with 30 μL of pure ethanol, while for 360 nm nanospheres, 30 μL of nanosphere solution was diluted with 50 μL of pure ethanol. This solution was kept at room temperature for 2 h prior to use. Glass slides were air-dried, and 10 μL of the diluted nanosphere solution was drop coated on the glass slide. Immediately, the glass slide was transferred to the positive meniscus of Petri dish filled with 18 MΩ water. The nanospheres self-assembled on the water–air interface, and a drop of 2% sodium dodecylsulfate (SDS) was added to compact the nanosphere monolayer. The monolayer was transferred to a clean, wet glass slide using the Langmuir transfer. The slides with the nanosphere monolayer were dried slowly under a Petri dish.

The nanosphere masks were etched in an oxygen plasma as previously reported.[14] A plasma cleaner (Harrick Plasma Cleaner PDC-32G) was used at high power (18 W) from 0 min (for unetched samples) to 10 min. Prior to the etching process, the vacuum was established for 20 min with an oxygen flow of 15 mL/min in the plasma chamber, which was maintained during the etching process. The nanosphere masks were etched for various times. FOEN samples for each etch time and nanosphere size were replicated four times. This etching process decreased the nanosphere diameter, while maintaining the crystalline lattice. A metal film (Ag or Au as indicated in the Results and Discussion) was deposited with sputter coating (Cressington 308R) on the etched nanospheres to create films over etched nanosphere (FOEN). A 1 nm Cr adhesion layer was deposited prior to the Ag or Ag film to promote adhesion. Scanning electron microscope (SEM, Hitachi S-4700) images were obtained for the FOEN at each etch time to determine the nanosphere diameter.

LSPR Measurements. The plasmonic response of FOEN substrates was measured in reflectance mode using a 6 around 1 reflectance probe. The sample was illuminated with a halogen
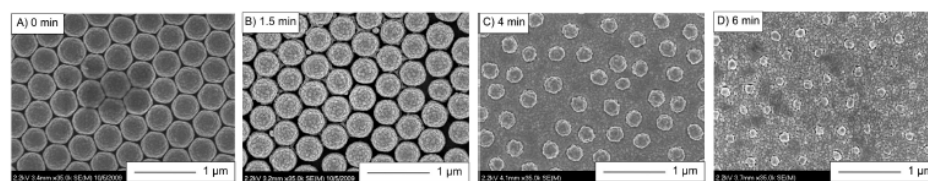
22408 *J. Phys. Chem. C, Vol. 114, No. 51, 2010* Masson et al.

Figure 1. SEM images at 35k magnification with films over nanospheres of (A) 0 min, (B) 1.5 min, (C) 4 min, and (D) 6 min. The nanospheres in this series were of 450 nm initial diameter.

TABLE 1: Average Diameter (in nm) for Individual Particles of FOEN with 125 nm Ag Film[a]

etch time (min)	220 nm diameter (nm)	gap/ diameter	360 nm diameter (nm)	gap/ diameter	450 nm diameter (nm)	gap/ diameter	520 nm diameter (nm)	gap/ diameter	650 nm diameter (nm)	gap/ diameter
0	217 ± 12 (3)	0.014	352 ± 22 (8)	0.023	443 ± 13 (7)	0.016	518 ± 29 (2)	0.004	644 ± 24 (6)	0.009
0.5	211 ± 13 (9)	0.043	329 ± 18 (31)	0.094			497 ± 15 (33)	0.066		
1	201 ± 13 (19)	0.065	315 ± 19 (45)	0.14						
1.5	186 ± 10 (34)	0.18	294 ± 23 (66)	0.22	420 ± 14 (30)	0.071	481 ± 20 (39)	0.081	585 ± 27 (65)	0.11
2.5	107 ± 8 (113)	1.05	302 ± 10 (58)	0.19	402 ± 16 (48)	0.12	436 ± 19 (84)	0.19	553 ± 26 (97)	0.18
4	83 ± 7 (137)	1.65	174 ± 10 (186)	1.06	249 ± 17 (201)	0.81	334 ± 19 (186)	0.56	523 ± 27 (127)	0.24
6			148 ± 13 (212)	1.43	139 ± 13 (311)	2.23	172 ± 16 (348)	2.02	461 ± 17 (189)	0.41
8					147 ± 12 (303)	2.06	202 ± 14 (308)	1.52		

[a] The number in parentheses is the approximate gap between nanospheres from the measured size; note the spheres had initially a CV < 3%.

light source. The variable wavelength spectrophotometer was set to cover a spectral range of 400–900 nm. Data were processed with Matlab to obtain the reflectance spectra using flat Ag or Au as the reference. The LSPR wavelength (λ_{LSPR}) was calculated using a minimum finding algorithm. This algorithm is based on modeling the LSPR peak with a second-order polynomial. The zero of the first derivative of the polynomial is λ_{LSPR}.

Raman Measurements. The FOEN substrates were immerged in 1 mM 4-nitrobenzene thiol (4-NBT) overnight. The samples were then thoroughly cleaned with water and air-dried prior to the Raman measurements. The Raman spectrum for each sample was measured using a Renishaw InVia Raman microscope using 633 and 785 nm laser excitation. Spectra were acquired for 10 s at either 0.1% or 0.05% of the laser power, resulting in a few tens of microwatts laser power at the sample. The Raman shift region covering 800–1800 cm^{-1} was monitored for the characteristic Raman peaks of 4-NBT (Figure S1). The peaks at 1082, 1112, 1350, and 1575 cm^{-1} were used to calculate every parameter reported in this Article. The data reported here are for the average from four identically prepared samples for the labeled Raman bands as shown in Figure S1. The Raman response was normalized to unetched FON, to compare FOEN with a common Raman substrate, and it is reported as a percentage of the response of FON (FON = 100%). We repeated a previously reported experiment[31] and found that the Raman intensity of FON prepared with various nanosphere diameters followed a pattern similar to the previously reported results.

Results and Discussion

There is increasing interest in fabricating ordered nanostructures with a controllable interparticle distance between adjacent nanoparticles, due to the increased Raman amplification when compared to isolated nanoparticles. Film over nanospheres (FON) substrates have been popularized due to large Raman amplification, good reproducibility, and simple fabrication procedure. This configuration does not facilitate "gap-enhanced"

Raman, due to the possible propagation of the surface plasmon in the continuous network of metal film. To facilitate gap-enhanced Raman, modified nanosphere lithography is a technique exploiting oxygen plasma to combust the polymer nanosphere mask, followed by metal deposition to result in FOEN. Etching the nanosphere mask does not influence metal deposition, as Ag films maintain their appearance of island-like structures on the surface (Figure S2). SEM images show that as etch time increases, the diameter of the spheres decrease as the gap between the spheres increases (Figure 1 and Table 1). The diameter of the nanospheres was obtained from the SEM images with image J (avalaible from NIH), and the gap can be obtained from this measurement. Etching for 30 s to 1 min created a gap in the order of 9–45 nm depending on the nanosphere diameter, while for 1.5–2.5 min etch time, the gap increased from 34 to 114 nm, and for etch times greater than 4 min, the structures exhibited gaps larger than 127 nm, up to >300 nm (Table 1). Because of the inherent variability of the NSL and plasma etching processes, there are defects on the substrate, and there is a range of average interparticle distance (gap) for FOEN. It does not seem that the presence of defects on the substrate causes a large change in the Raman properties of FOEN, as noted from the small standard deviations in the results below. The substrate is typically well oriented, and modified nanosphere lithography provides a simple method to tune the gap and to investigate several parameters influencing the Raman response.

The roughness of a substrate is another important factor in Raman spectroscopy. The increased roughness may be advantageous to create local hot spots. Initial experiments leading to the discovery of SERS were indeed performed on roughened surfaces.[32] In the present case, SEM images provide a good visualization of the surface roughness of the nanospheres on the FOEN. The surface of the nanospheres is initially smooth with very few defects. As etch time increases, the surface becomes increasingly rough. Plasma etching is not perfectly uniform; the polymer is etched at different rates depending on the location on the nanosphere. Hence, FOEN are significantly
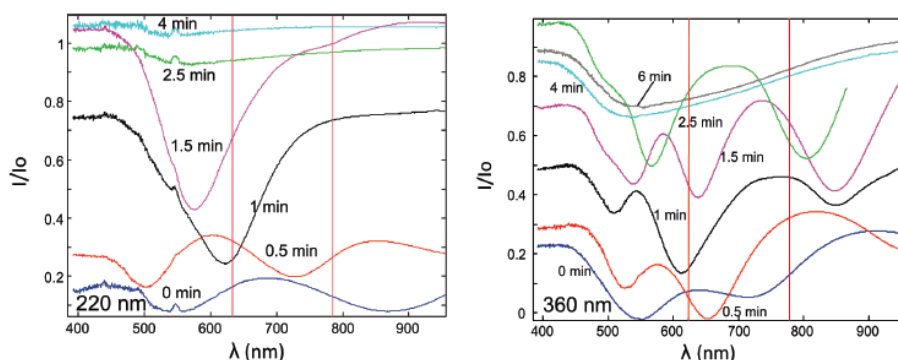
Figure 2. The reflectance spectra for 220 (left) and 360 nm (right) nanospheres are represented here, while the reflectance spectra for 450, 520, and 650 nm initial diameters are provided as Supporting Information. The LSPR bands are the minimum in the reflectance spectra and generally shift toward lower wavelength for longer etched samples. The red lines represent the excitation wavelength of the 633 and 785 nm lasers. Color legend: blue (0 min etching time), red (0.5 min), black (1 min), purple (1.5 min), green (2.5 min), light blue (4 min), and gray (6 min).

more granular and irregular for longer etch time (Figure 1). The effect of increased roughness on the Raman intensity is hard to predict as longer etch times will change both the particle size and thus the interparticle distance.

LSPR. Measuring the reflectance spectrum of FOEN provides the excitation wavelength of the surface plasmon of FOEN substrates. To provide a strong Raman response, the surface plasmon must be excited by the Raman laser.[33] It is well-known that the surface plasmon properties of nanoparticles are highly dependent on the size and shape of the nanoparticle,[7] but also on the distance to the nearest particle.[17] In the present case with FOEN, etching the nanosphere mask significantly changed the excitation wavelength of the surface plasmon. Etching the nanosphere mask using nanospheres with an initial diameter of 220 and 360 nm initially red-shifts the excitation wavelength for the shortest etch times. The surface plasmon then blue-shifts for longer etch times from nearly $\lambda = 900$ to 500 nm for 220 nm nanospheres and from $\lambda = 725$ to 500 nm for 360 nm nanospheres (Figure 2). The LSPR data for the other nanosphere sizes are shown in the Supporting Information. Smaller gaps lead to larger coupling, which translates to a red-shift of the plasmonic bands. Thus, in the case of FOEN, the larger plasmonic coupling was observed in the case of shorter etch times (surface plasmon excitation wavelength to the red of the spectrum), while longer etch times did not undergo plasmon coupling (gap/diameter $>$ 1) and exhibited an excitation wavelength closer to the blue (near $\lambda = 500$ nm). FOEN with nanospheres of 360 nm diameter exhibited multiple plasmonic bands, which have been previously reported to be associated with multipoles.[27] Lastly, the intensity of the plasmonic band decreased significantly with longer etch times, as the etching process maintains the density of nanospheres but decreases the actual area covered by the smaller nanospheres.

Raman Spectroscopy on FOEN. Etching the NSL mask prior to metal deposition significantly changes the physical and plasmonic properties of FOEN as compared to unetched FON. For FOEN of every size, the Raman response is optimal as compared to unetched FON, by up to 450% for the 633 nm laser and by 360% for the 785 nm laser with the optimal gap/diameter (Figure 3). Every sample studied followed the same pattern, where the Raman intensity increases to a maximum and then rapidly decreases to smaller responses than FON as the etch time increases. This indicates that there is an optimal etch

time for increased Raman response, and further increasing the etch time leads to performances poorer than FON. The optimal etch times for each nanosphere diameter are 1, 1.5, 4, 2.5, and 2.5 min for the 220, 360, 450, 520, and 650 nm nanospheres, respectively. Optimal etch times result in gap/diameter of less than 1, and the optimal gap/diameter was around 0.2 for many FOEN (Table 2). The variation of the Raman response with the etching time is mainly due to two factors: plasmon excitation by the laser and tuning the interparticle distance.

The excitation wavelength(s) of the surface plasmon on FOEN with optimal Raman amplification are all near the excitation lasers of 633 and 785 nm (Table 2). Thus, one important factor in attaining larger Raman amplification with FOEN involves matching the LSPR band with the Raman excitation laser. The tuneability of the LSPR response with FOEN is advantageous in this regard. Small differences in the plasmonic response of SERS substrates may lead to dramatic changes in Raman intensity. It was demonstrated by Van Duyne et al. that increased enhancement is obtained for an excitation laser at higher energy (lower wavelength) than the maximum of the plasmonic response.[33] The significant blue-shift of the plasmon resonances below the excitation lasers and the absence of multiple plasmonic bands for longer etch times leads to poor excitation of the surface plasmon. Hence, the Raman response becomes much smaller with longer etch time and significantly smaller than for FON.

The distance between two particles significantly changes their plasmonic properties and their Raman amplification. By etching the nanosphere mask, the gap is tuned from a few tens of nanometers to several hundreds nanometers, or when normalized to the actual diameter of the nanostructure, the ratio of the gap/diameter is varied from near 0 to more than 2. A ratio of less than 1 indicates that plasmon coupling is occurring according to the plasmon ruler equation, while a ratio of greater than 1 indicates plasmon coupling is not occurring.[21] As expected, the optimal gap/diameter is generally small, indicating that plasmon coupling is a significant factor in increasing the Raman response (Table 2). Moreover, tuning the plasmon wavelength to the excitation laser cannot solely explain the larger Raman response of FOEN, and the gap created contributes significantly to the larger Raman response of FOEN. For example, the Raman amplification of 220 nm nanospheres with the 785 nm laser excitation is much greater at 320% for FOEN etched for 1 min
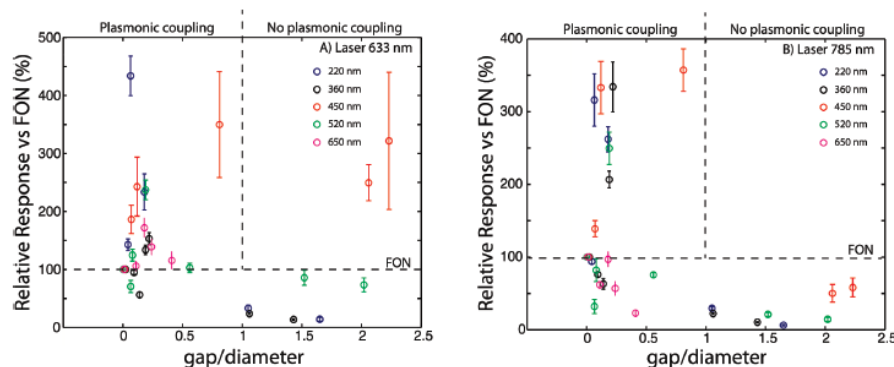
Masson et al.

Figure 3. Improvement of the Raman intensity for film over etched nanospheres for (A) excitation with 633 nm laser and (B) excitation with 785 nm laser. The Raman response for each series of different sphere size is normalized to unetched FON of the same size and reported as a percentage of the response versus FON (FON = 100%).

TABLE 2: Properties of Optimal Film over Etched Nanospheres for Various Nanosphere Diameters

sphere size (nm)	etch time (min)	relative response vs FON (%)		Raman intensity[a] (10^4 counts)		λ_{SPR} (nm)	gap/diameter
		633 nm	785 nm	633 nm	785 nm		
220	1	450	320	5.2	8.1	616	0.065
360	1.5	150	330	4.7	12.1	633 and 835	0.22
450	4	350	360	1.7	11.2	541 and 770	0.81
520	2.5	240	250	2.1	5.9	633 and 845	0.19
650	2.5	170	100	2.1	4.2	640 and 782	0.18

[a] Laser power: 785 nm, 35 μW; and 633 nm, 3.4 μW.

than with FON. This amplification occurs despite the presence of a plasmon band between $\lambda = 800$ and 900 nm for FON and the absence of a plasmonic band above 700 nm for the FOEN etched for 1 min (Figure 2). The gap/diameter for the FOEN of 220 nm etched for 1 min is very small at 0.065, indicating that the structure is within the high plasmon coupling region. Thus, large Raman amplification can still occur without coupling the laser light to near the maximum intensity of the surface plasmon. This result correlates well to a recent article published by Van Duyne et al. in which the authors reported that matching the laser excitation to the surface plasmon was not necessary to obtain large amplification for dimers in close proximity.[22] Another FOEN structure exemplifies the importance of the gap created with FOEN. The surface plasmon of FOEN of 520 nm etched for 2.5 min exhibits excitation bands in the same spectral region as the surface plasmon of FON of 520 nm (Figure S4). Despite this identical plasmonic response, the Raman response is much greater for the FOEN (gap/diameter of 0.19) than for FON by 240% and 250%, respectively, for the 633 and 785 nm lasers. Thereby, tuning the gap/diameter also leads to enhanced Raman response for FOEN.

Lastly, the surface roughness of the FOEN substrates increases with longer etch times, which can typically contribute to the improvement of the Raman response of SERS substrates. However, if the increase in substrate roughness had contributed significantly to the Raman response observed from the series of FOEN, the Raman response would have increased continuously with longer etch times instead of rapidly declining to values smaller than FON. The Raman response correlates more closely to the tuning of the gap/diameter and matching to a surface plasmon excitation band. The Raman amplification observed with FOEN is due to a combination of all three factors,

but with relative importance: tuning the plasmonic band to the excitation wavelength of the lasers (important factor), creating a gap capable of increasing the Raman amplification (important factor), and increasing the roughness of the sample (minor factor).

The raw intensity measured for FOEN with optimal etch time shows that for 633 nm, the intensity is larger for 220 nm nanospheres and decreases with larger nanospheres, while for
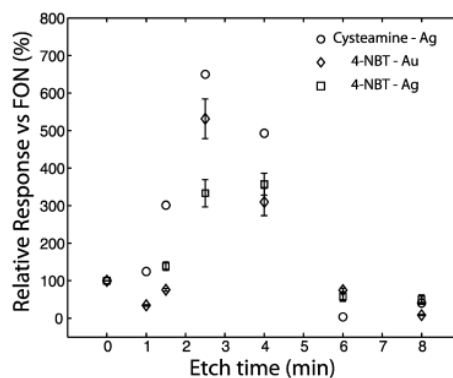

Figure 4. Raman response of film over etched nanospheres with cysteamine adsorbed on Ag and 4-NBT adsorbed on Au and Ag. These results show the effect of etch time on a 450 nm nanosphere mask, with a laser excitation of 785 nm. The response is normalized to FON and reported as a percentage of the response from FON (FON = 100%).
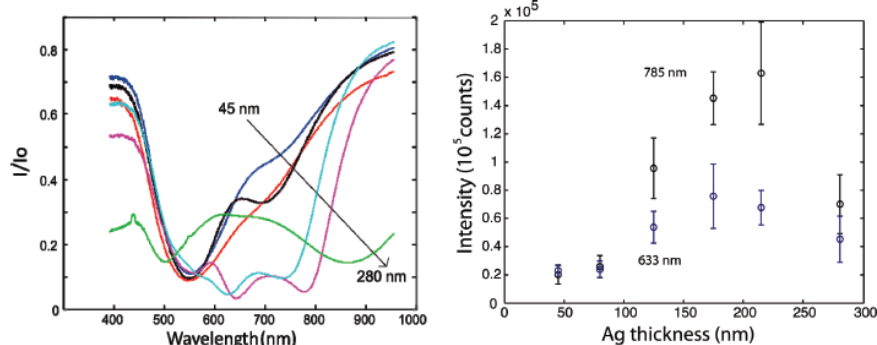
Figure 5. (Left panel) Reflectance spectrum of FOEN with 360 nm nanospheres and etched for 1.5 min. Different thicknesses of Ag were deposited: 45 nm (blue), 80 nm (red), 125 nm (black), 175 nm (purple), 215 nm (light blue), and 280 nm (green). (Right panel) The intensity of the 1340 cm^{-1} band of 4-nitrobenzenethiol is plotted for various Ag thicknesses with 633 (blue) and 785 nm (black) excitation lasers.
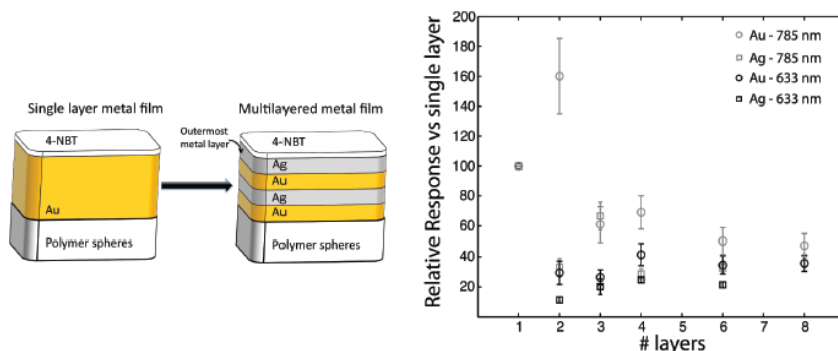

Figure 6. (Left panel) Schematic representation of multilayered metal films over nanospheres. The number of layers is varied by successive depositions of metal, with the overall thickness fixed at 175 nm. (Right panel) Improvement of the Raman response with multilayered metallic films, normalized to a single metal layer (response = 100%). The legend indicates the metal present on the outermost layer, on which 4-NBT is immobilized and the excitation wavelength of the laser employed to measure the Raman response.

785 nm laser, the intensity is optimal for 360 nm nanospheres and greater than for 633 nm laser. Thus, these results indicated that using the 785 nm laser with 1.5 min FOEN of 360 nm initial diameter yields the largest Raman amplification, and these conditions will be used for subsequent experiments.

Effect of the Metal Film Composition on Raman Amplification. Another important point to take into consideration is the Raman amplification with different metal surfaces as the metal composition directly influences the plasmonic properties of the nanoparticles. The amplification (with 785 nm laser) achieved by 4-NBT on Au and on Ag is greater for FOEN with etch times of 2.5−4 min as compared to unetched FON (Figure 4). Longer etch times lead to poorer Raman response with FOEN in comparison to FON. Au FOEN also exhibited a greater amplification as compared to Ag FOEN. It is also noteworthy to point out that the amplification is also molecule dependent. Ag FOEN with 450 nm nanospheres and 2.5 min etch time enhanced the Raman response of 4-NBT by 3.4 times as compared to the 6.5-fold enhancement of cysteamine both relative to the unetched substrates.

The thickness and composition of the metal film of FOEN are other important parameters to control for optimal Raman

amplification. The thickness of the Ag film can greatly change the plasmonic properties of FOEN (Figure 5, left). This study was conducted with the optimal FOEN of 360 nm nanospheres etched for 1.5 min. For thin Ag films, the plasmon is excited at $\lambda = 550$ nm, while plasmonic peaks appear near $\lambda = 633$ and 785 nm for thicker films. The Raman amplification is thus maximal for Ag films near 200 nm (Figure 5, right). Further increasing the thickness did not improve the Raman response. This is due to the plasmonic response of 280 nm thick Ag film red-shifting to nearly $\lambda = 900$ nm. These results are in agreement with the Ag thickness of 200 nm used by Van Duyne et al.[31] and the optimal thickness determined by Cullum et al. for Ag FON.[34]

There has been an increasing interest in fabricating multimetal layered nanoparticles. These exhibit stronger absorption of light, and the plasmonic properties are tunable according to the thickness and the composition of the metal films. Recently, it was also demonstrated that the intensity of enhanced transmission in nanohole arrays was improved for bimetallic films, using a Ag underlayer and a Au overlayer.[14] Other examples include FON substrates composed of Au multilayers with silver oxide island films.[35] The authors demonstrated that the films are more

154

stable to oxidation and they have an improved Raman response. Two series of FOEN with 360 nm nanospheres and 1.5 min etch were prepared: the first series had alternating layers of Au and Ag, terminating with an Ag overlayer (data represented by squares in Figure 6), while the second series still had layers of Ag and Au, with an Au overlayer (data represented by circles in Figure 6). The thickness of the metal layers was maintained at 175 nm, while the number of layers was varied from a single metal layer to 8 metal layers of equal thicknesses (Figure 6, left). Figure 6 (right panel) shows the Raman response for both 633 and 785 nm laser normalized to a single metal layer (single metal layer = 100% Raman response). The Raman response at 785 nm excitation for FOEN exhibited an increase of the Raman response to 160% with a bimetallic layer of Ag underlayer and Au overlayer. This result was repeated with two series of four identically prepared samples that had been analyzed weeks apart and is therefore reproducible. However, this result is unique in this study, as all other bimetallic FOEN exhibited a response lower than a single metal layer. Hence, Au on Ag bimetallic layers also exhibit analytical advantages for Raman amplification.

Conclusions

Modifying film over nanosphere (FON) sample preparation by etching the NSL mask prior to metal deposition exhibited several advantages as compared to unetched FON. The Raman amplification can be increased by nearly 1 order of magnitude by tuning the etch time, the initial diameter of the nanosphere, the metal composition, and the molecule adsorbed on the surface. FOEN were found to be optimal for 360 nm nanospheres etched for 1.5 min, with a film thickness of 175 nm and composed of 87.5 nm Ag as the underlayer and 87.5 nm Au overlayer. Characterization of these SERS substrates was performed using LSPR, SEM, and Raman spectroscopy. The greater Raman amplification of FOEN as compared to unetched FON is due to tuning the LSPR of the substrates to the excitation lasers, creation of a gap between adjacent nanospheres, and the increased roughness of FOEN generated by longer etching times. Thus, these surfaces are attractive to develop for analytical applications.

Supporting Information Available: Reflectance spectra for 450, 520, and 650 nm initial diameter nanospheres. This material is available free of charge via the Internet at http://pubs.acs.org.

References and Notes

(1) Stiles, P. L.; Dieringer, J. A.; Shah, N. C.; Van Duyne, R. R. *Annu. Rev. Anal. Chem.* **2008**, *1*, 601–626.

(2) Porter, M. D.; Lipert, R. J.; Siperko, L. M.; Wang, G.; Narayanana, R. *Chem. Soc. Rev.* **2008**, *37*, 1001–1011.

(3) Hering, K.; Cialla, D.; Ackermann, K.; Dorfer, T.; Moller, R.; Schneidewind, H.; Mattheis, R.; Fritzsche, W.; Rosch, P.; Popp, J. *Anal. Bioanal. Chem.* **2008**, *390*, 113–124.

(4) Banholzer, M. J.; Millstone, J. E.; Qin, L. D.; Mirkin, C. A. *Chem. Soc. Rev.* **2008**, *37*, 885–897.

(5) Brolo, A. G.; Arctander, E.; Gordon, R.; Leathem, B.; Kavanagh, K. L. *Nano Lett.* **2004**, *4*, 2015–2018.

(6) Tripp, R. A.; Dluhy, R. A.; Zhao, Y. P. *Nano Today* **2008**, *3*, 31–37.

(7) Jensen, T. R.; Malinsky, M. D.; Haynes, C. L.; Van Duyne, R. P. *J. Phys. Chem. B* **2000**, *104*, 10549–10556.

(8) Dick, L. A.; McFarland, A. D.; Haynes, C. L.; Van Duyne, R. P. *J. Phys. Chem. B* **2002**, *106*, 853–860.

(9) Whitney, A. V.; Myers, B. D.; Van Duyne, R. P. *Nano Lett.* **2004**, *4*, 1507–1511.

(10) Hicks, E. M.; Zhang, X. Y.; Zou, S. L.; Lyandres, O.; Spears, K. G.; Schatz, G. C.; Van Duyne, R. P. *J. Phys. Chem. B* **2005**, *109*, 22351–22358.

(11) Masson, J. F.; Murray-Methot, M. P.; Live, L. S. *Analyst* **2010**, *135*, 1483–1489.

(12) Lou, Y.; Lunardi, L. M.; Muth, J. F. *IEEE Sens. J.* **2010**, *10*, 617–620.

(13) Murray-Methot, M. P.; Menegazzo, N.; Masson, J. F. *Analyst* **2008**, *133*, 1714–1721.

(14) Murray-Methot, M. P.; Ratel, M.; Masson, J. F. *J. Phys. Chem. C* **2010**, *114*, 8268–8275.

(15) Canpean, V.; Astilean, S. *Mater. Lett.* **2009**, *63*, 2520–2522.

(16) Lee, S. H.; Bantz, K. C.; Lindquist, N. C.; Oh, S. H.; Haynes, C. L. *Langmuir* **2009**, *25*, 13685–13693.

(17) Sonnichsen, C.; Reinhard, B. M.; Liphardt, J.; Alivisatos, A. P. *Nat. Biotechnol.* **2005**, *23*, 741–745.

(18) Storhoff, J. J.; Elghanian, R.; Mucic, R. C.; Mirkin, C. A.; Letsinger, R. L. *J. Am. Chem. Soc.* **1998**, *120*, 1959–1964.

(19) Hao, E.; Schatz, G. C. *J. Chem. Phys.* **2004**, *120*, 357–366.

(20) McMahon, J. M.; Henry, A. I.; Wustholz, K. L.; Natan, M. J.; Freeman, R. G.; Van Duyne, R. P.; Schatz, G. C. *Anal. Bioanal. Chem.* **2009**, *394*, 1819–1825.

(21) Jain, P. K.; Huang, W. Y.; El-Sayed, M. A. *Nano Lett.* **2007**, *7*, 2080–2088.

(22) Wustholz, K. L.; Henry, A. I.; McMahon, J. M.; Freeman, R. G.; Valley, N.; Piotti, M. E.; Natan, M. J.; Schatz, G. C.; Van Duyne, R. P. *J. Am. Chem. Soc.* **2010**, *132*, 10903–10910.

(23) Kneipp, K.; Kneipp, H.; Kneipp, J. *Acc. Chem. Res.* **2006**, *39*, 443–450.

(24) Lal, S.; Grady, N. K.; Kundu, J.; Levin, C. S.; Lassiter, J. B.; Halas, N. J. *Chem. Soc. Rev.* **2008**, *37*, 898–911.

(25) Fan, J. A.; Wu, C. H.; Bao, K.; Bao, J. M.; Bardhan, R.; Halas, N. J.; Manoharan, V. N.; Nordlander, P.; Shvets, G.; Capasso, F. *Science* **2010**, *328*, 1135–1138.

(26) Dhawan, A.; Norton, S. J.; Gerhold, M. D.; Vo-Dinh, T. *Opt. Express* **2009**, *17*, 9688–9703.

(27) Qin, L. D.; Zou, S. L.; Xue, C.; Atkinson, A.; Schatz, G. C.; Mirkin, C. A. *Proc. Natl. Acad. Sci. U.S.A.* **2006**, *103*, 13300–13303.

(28) Li, S.; Schatz, G. C. *Mater. Res. Soc. Proc.* **2008**, *1087E*, V01–08.

(29) Gunnarsson, L.; Bjerneld, E. J.; Xu, H.; Petronis, S.; Kasemo, B.; Kall, M. *Appl. Phys. Lett.* **2001**, *78*, 802–804.

(30) Galarreta, B. C.; Harte, E.; Marquestaut, N.; Norton, P. R.; Lagugne-Labarthet, F. *Phys. Chem. Chem. Phys.* **2010**, *12*, 6810–6816.

(31) Zhang, X. Y.; Young, M. A.; Lyandres, O.; Van Duyne, R. P. *J. Am. Chem. Soc.* **2005**, *127*, 4484–4489.

(32) Fleischmann, M.; Hendra, P. J.; McQuillan, A. J. *Chem. Phys. Lett.* **1974**, *26*, 163.

(33) McFarland, A. D.; Young, M. A.; Dieringer, J. A.; Van Duyne, R. P. *J. Phys. Chem. B* **2005**, *109*, 11279–11285.

(34) Li, H. G.; Cullum, B. M. *Appl. Spectrosc.* **2005**, *59*, 410–417.

(35) Li, H. G.; Baum, C. E.; Sun, J.; Cullum, B. M. *Appl. Spectrosc.* **2006**, *60*, 1377–1385.

JP106450Y

2. *Chemical Communications* **2011**, 47, 3404-3406

COMMUNICATION

Correlated AFM and SERS imaging of the transition from nanotriangle to nanohole arrays†‡

Kirsty F. Gibson,§[a] Debby Correia-Ledo,§[b] Maxime Couture,[b] Duncan Graham[a] and Jean-Francois Masson*[b]

Mapping the transition of Ag nanotriangle to nanohole arrays revealed that the optimal SERS response was obtained near the transition. Correlated AFM and Raman imaging provided novel experimental proof that hot spots are located on Ag islands for nanotriangle arrays and in the core area of the hole for nanohole arrays, which is in agreement with previous theoretical predictions.

Surface-Enhanced Raman Scattering (SERS) is a sensitive, vibrational spectroscopic technique capable of giving rich, molecularly specific information.[1] The enhanced Raman scattering achieved by SERS over classical Raman spectroscopy is attributed to both electromagnetic and chemical enhancement mechanisms with the former having the major contribution to the overall enhancement.

SERS active nanostructures have generated great interest in recent years due to their substrate stability and reproducible Raman response.[2] Nanostructures comprised of metallic nanoparticles organised in a close-packed arrangement result in large Raman enhancement factors due to long range coupling between nanoparticles and a high 'hot spot' surface density.[3] The use of nanotriangle and nanohole arrays for sensitive detection of biomolecules has been demonstrated in the literature with enhancement factors of up to 10^8 having been reported.[4] Whilst these SERS substrates have been thoroughly investigated individually, there is no comparative investigation into their Raman response and the transition of nanotriangle arrays to nanohole arrays.

Nanohole arrays exhibit advantageous properties such as simple tuning of the plasmonic bands by varying the periodicity[5] and straightforward fabrication owing to recent advances in modified nanosphere lithography (NSL) techniques.[6] Nanohole arrays have also been shown to be mechanically stable over long periods of

time. Modified NSL was employed in this study to etch the polymer nanosphere mask (initial diameter of 820 nm) with a reactive oxygen plasma to decrease the diameter of the nanospheres while maintaining the crystalline lattice[6,7] (detailed protocol in ESI†). This technique was previously employed to investigate the transition from nanotriangle to nanohole arrays by surface plasmon resonance (SPR).[7,8] Raman mapping the transition of nanotriangle to nanohole arrays has not been performed and the optimal nanostructure for SERS is still unknown.

The localisation of hot spots on nanotriangle and nanohole arrays has only been demonstrated by theoretical calculations. These calculations revealed that the highest electromagnetic field was located at the junction of two adjacent triangles for nanotriangle arrays,[9] whilst the rim of the hole in nanohole arrays exhibited the highest field intensity.[10,11] Thus, in this investigation, correlated Raman imaging and Atomic Force Microscopy (AFM) was utilised to provide experimental evidence and further insight on hot spots and the homogeneity of the Raman response of nanotriangle and nanohole arrays.

The optical properties such as the surface plasmon and Raman intensity vary as both a function of the size and shape of nanostructure and the distance between nanostructures.[12,13] The transition from nanotriangle to nanohole arrays causes a significant change in the plasmonic properties. Related studies have demonstrated that the surface plasmon of nanotriangle arrays occurs at a higher wavelength than for nanohole arrays of the same periodicity and that the plasmonic properties of nanohole arrays remain relatively constant. It was also demonstrated that the transition of the plasmonic properties from nanotriangle to nanohole array occurs at a diameter/periodicity (D/P) of between 0.6 and 0.75.[7,8] A D/P of 1 corresponds to a nanotriangle array and D/P of 0 is for a non-structured metallic film.

For a D/P ratio of 1, no plasmonic bands were observed in the spectral range investigated (Fig. 1). This observation is consistent with Jensen *et al.*,[12] where a λ_{max} of 1125 nm was observed for nanotriangles prepared with nanospheres of 820 nm. Nanostructured SERS substrates with a D/P ratio of 0.69 (in the transition region) show two surface plasmon bands at 550 and 725 nm. As expected for nanohole arrays, the plasmonic response was almost identical for D/P ratios of 0.52 and 0.43 with three plasmonic bands at 500–550 nm, 650 nm and 800–850 nm. The two plasmonic bands at shorter wavelength (500–650 nm) are associated with the metal–solution interface and exhibit a

[a] *Centre for Molecular Nanometrology, WestCHEM, Department of Pure and Applied Chemistry, University of Strathclyde, Glasgow, UK G1 1XL.*
E-mail: duncan.graham@strath.ac.uk; Tel: +44 (0)141 548 4701
[b] *Department of Chemistry, Université de Montréal, C.P. 6128 Succ. Centre-Ville, Montréal, QC, Canada.*
E-mail: jf.masson@umontreal.ca; Fax: +1 514-343-7586; Tel: +1 514-343-7342
† Electronic supplementary information (ESI) available: Experimental procedure; Raman images. See DOI: 10.1039/c0cc05287f
‡ This article is part of a ChemComm web-based themed issue on Surface Enhanced Raman Spectroscopy.
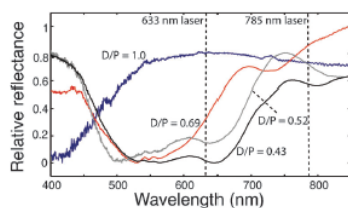§ These authors have contributed equally to this manuscript.

156

Fig. 1 Reflectance spectra for nanostructures prepared from 820 nm periodicity etched NSL masks. Color legend: diameter/periodicity (D/P) of 1.0 (0 min, blue), 0.69 (2 min, red), 0.52 (8 min, grey), and 0.43 (10 min, black).

sensitivity of 300 to 400 nm per RIU, while the plasmonic band near 800 nm has very low sensitivity to bulk refractive index, due to the excitation of the glass–metal interface.

In Raman spectroscopy, optimal response is generally obtained for an excitation laser at a slightly lower wavelength in relation to the surface plasmon, such that both the laser excitation and the Raman shifted photons are within the excitation boundaries of the plasmonic bands. The Raman intensity varies significantly as a function of the D/P for the 633 and 785 nm excitation wavelengths (Fig. 2). The Raman response of 4-nitrobenzenethiol (Raman spectrum provided in ESI†, Fig. S1) is reported as a relative response in comparison with nanotriangles (nanotriangles are normalised at 100%). When the D/P ratio approaches 0, no Raman amplification was observed, which is similar to the behaviour of a continuous film (for example, Ag layer deposited on a glass microscope slide). Nanohole arrays of D/P between 0.4 and 0.6 have plasmonic bands at slightly longer wavelength than the excitation laser. As previously stated, this scenario is generally optimal for the amplification of the Raman response.
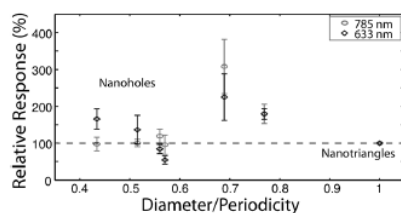

Fig. 2 Raman response of 4-nitrobenzenethiol for nanohole arrays of 820 nm periodicity; relative response *vs.* nanotriangles (100%).
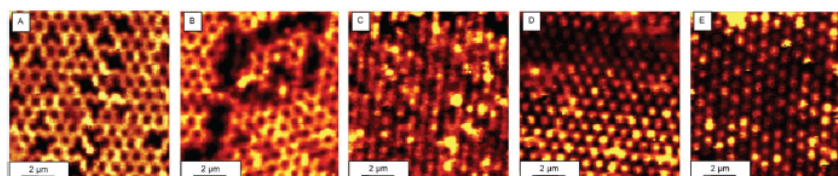
However, the optimal Raman response was with D/P of 0.69 with the improvement in Raman enhancement calculated to be 225% for 633 nm and 310% for 785 nm laser excitations in comparison to nanotriangles. This nanostructured sample corresponds to the size regime intermediate between nanotriangles and nanoholes.

These results demonstrate that the optimal amplification occurs at the transition between nanotriangle and nanohole arrays despite the fact that the lasers are not exciting the plasmonic band at the optimal wavelength (slightly shorter wavelength in relation to the plasmonic band). Within the size regime encompassed by the transition, the nanostructures are an array of nearly connected triangles, with a small gap between adjacent triangles. This gap created by etching the nanospheres enhances the electric field between the apex of the triangles, leading to significantly enhanced Raman response from molecules located in that region.[14] Tuning the surface plasmon of the SERS substrate to the laser wavelength cannot explain the larger Raman intensity of the SERS substrates at the transition point. Thus, the dominating factor in the enhanced Raman response is indeed the gap created between nearly connected triangle arrays, obtained with modified NSL.

The acquisition of Raman maps and AFM images on the same region of the SERS substrate was necessary to correlate spectroscopic information obtained from the Raman maps with the topographical information acquired with AFM. The Raman images clearly show the progression of nanotriangle to nanohole array (Fig. 3). The Raman image of D/P 1.0 and 0.69 shows a well ordered, crystalline lattice of dark holes. The correlated Raman map and AFM image shown in Fig. 4 revealed that the highest intensity Raman scattering, represented by the brighter areas on the inset image, can be clearly attributed to the network of Ag triangles (colored in red) that surround the dark holes (the holes demonstrated no Raman amplification) (Fig. 4, for higher resolution image, see Fig. S2 provided in ESI†). This observation correlates well to theoretical reports in the literature. Schatz *et al.* used discrete dipole approximation (DDA) to show that nanotriangle dimers in a tip-to-tip arrangement exhibit maximum local electric field enhancement at the interface between the two triangles.[9] These calculations have been corroborated numerous times in the literature.[14,15] The lateral resolution of the Raman map was limited by the experimental set-up to 350 nm thereby preventing identification of the exact position of the localised enhancement on each individual nanotriangle. Instead, a continuous network of Raman active sites is observed, leading to the appearance of dark holes and bright metallic nanotriangles.

The Raman maps of the nanohole arrays revealed a dark background with bright circular spots located where the holes

Fig. 3 Raman imaging data for (A) D/P 1.0, (B) D/P 0.69, (C) D/P 0.57, (D) D/P 0.56, and (E) D/P 0.43 substrates. False colour Raman map of intensity at 1574 cm^{-1}. λ_{ex} = 633 nm, 0.01 s integration time, 100× objective, 200 nm resolution. Images with smaller scanning areas (5 × 5 μm) for samples B and E are provided in ESI† (Fig. S4 and S5).
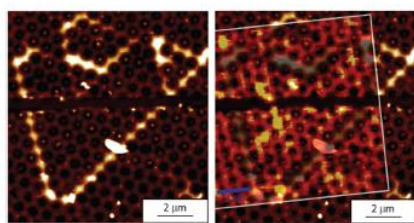
157

Fig. 4 $D/P = 0.69$ AFM and Raman imaging data. (Left) AFM image, (right) overlay graphic of AFM image and false color Raman map (framed inset).
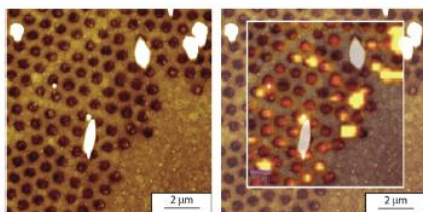

Fig. 5 D/P 0.43 AFM and Raman imaging data. (Left) AFM image, (right) overlay graphic of AFM image and false color Raman map (framed inset).

were assumed to be (Fig. 3). The bright spots in the Raman map are arranged in a hexagonal pattern, with a center to center spacing perfectly matching the periodicity of the nanohole arrays (820 nm). Correlated Raman and AFM analysis of D/P 0.43 samples showed that the bright red-yellow spots of the Raman image followed the same hexagonal pattern and well matched the dark holes in the AFM image. This observation confirmed that the maximum Raman scattering originates from the core area of nanoholes (Fig. 5, for higher resolution image, see Fig. S3 provided in ESI†). Theory predicts that in nanohole arrays, the electromagnetic field is concentrated around the edges of the nanoholes.[10] This agrees with the results observed experimentally in this study. Modified NSL results in "bowl-shaped" holes with the Ag wall tapered towards the centre of the hole. The hole shape and the diffraction limited spectral resolution can explain the pattern observed in the Raman image. In addition to electric field maximisation, surface roughness of the nanoholes also contributes to the overall Raman enhancement of the substrate. Etching the polystyrene spheres is an inhomogeneous process, which results in rougher surfaces as etch time increases. After metal deposition, the spheres are removed and the resulting nanoholes have a roughened metal surface, which is dictated by the roughness of the polystyrene mask after etching. Therefore, the nanohole surface roughness contributes to the overall Raman enhancement and furthermore, this effect is more pronounced in samples etched for longer times. Lastly, the Raman map of a D/P ratio of 0.57 has no distinctive pattern, which can be attributed to the nanostructured surface being a convolution of nanotriangle and nanohole arrays (Fig. 3).

Another important point is the relative homogeneity of the intensity across the Raman images. There are indeed regions of slightly larger intensity in some of the images, but generally the SERS substrates do not exhibit hot spots of extremely large intensity. Defects can be observed in some images, which are associated with the darkest zones in the Raman maps. Thus, this observation indicates defects are not the source of the large Raman intensity and that defect-free nanotriangle or nanohole arrays will lead to optimal SERS intensity.

In conclusion, the Raman intensity is optimal for a nanostructure near the transition (D/P ratio of 0.69) of nanotriangle to nanohole arrays; an improvement of 310% for 785 nm excitation and of 225% for 633 nm excitation. The AFM and Raman images correlate perfectly and prove that the maximum Raman enhancement originates from different sources in the two classes of substrate: from the metallic triangles for nanotriangle arrays and from the holes for nanohole arrays. Although this difference in enhancement origin has been predicated several times in the literature, this is the first experimental demonstration. This observation is significant in the understanding and design of SERS active substrates to maximise the Raman enhancement and allow greater sensitivity in the detection of molecules of interest.

Notes and references

1 D. L. Jeanmaire and R. P. Van Duyne, *J. Electroanal. Chem.*, 1977, **84**, 1.
2 R. M. Li, M. Z. Si, Y. P. Kang, X. F. Zi, Z. Q. Liu and D. Q. Zhang, *J. Colloid Interface Sci.*, 2010, **343**, 52; A. Wei, B. Kim, B. Sadtler and S. L. Tripp, *ChemPhysChem*, 2001, **2**, 743; X. Y. Zhang, J. Zhao, A. V. Whitney, J. W. Elam and R. P. Van Duyne, *J. Am. Chem. Soc.*, 2006, **128**, 10304.
3 D. A. Genov, A. K. Sarychev, V. M. Shalaev and A. Wei, *Nano Lett.*, 2004, **4**, 153.
4 A. G. Brolo, E. Arctander, R. Gordon, B. Leathem and K. L. Kavanagh, *Nano Lett.*, 2004, **4**, 2015; C. L. Haynes and R. P. Van Duyne, *J. Phys. Chem. B*, 2003, **107**, 7426.
5 T. Thio, H. F. Ghaemi, H. J. Lezec, P. A. Wolff and T. W. Ebbesen, *J. Opt. Soc. Am. B*, 1999, **16**, 1743.
6 J. F. Masson, M. P. Murray-Methot and L. S. Live, *Analyst*, 2010, **135**, 1483.
7 M. P. Murray-Methot, M. Ratel and J. F. Masson, *J. Phys. Chem. C*, 2010, **114**, 8268.
8 L. S. Live, O. R. Bolduc and J. F. Masson, *Anal. Chem.*, 2010, **82**, 3780; W. A. Murray, S. Astilean and W. L. Barnes, *Phys. Rev. B: Condens. Matter Mater. Phys.*, 2004, **69**, 165407.
9 E. Hao and G. C. Schatz, *J. Chem. Phys.*, 2004, **120**, 357.
10 S. H. Lee, K. C. Bantz, N. C. Lindquist, S. H. Oh and C. L. Haynes, *Langmuir*, 2009, **25**, 13685.
11 M. E. Stewart, C. R. Anderton, L. B. Thompson, J. Maria, S. K. Gray, J. A. Rogers and R. G. Nuzzo, *Chem. Rev.*, 2008, **108**, 494; Q. M. Yu, S. Braswell, B. Christin, J. J. Xu, P. M. Wallace, H. Gong and D. Kaminsky, *Nanotechnology*, 2010, **21**, 355301.
12 T. R. Jensen, M. D. Malinsky, C. L. Haynes and R. P. Van Duyne, *J. Phys. Chem. B*, 2000, **104**, 10549.
13 C. Sönnichsen, B. M. Reinhard, J. Liphardt and A. P. Alivisatos, *Nat. Biotechnol.*, 2005, **23**, 741.
14 B. C. Galarreta, E. Harte, N. Marquestaut, P. R. Norton and F. Lagugne-Labarthet, *Phys. Chem. Chem. Phys.*, 2010, **12**, 6810.
15 R. Marty, G. Baffou, A. Arbouet, C. Girard and R. Quidant, *Opt. Express*, 2010, **18**, 3035; P. J. Schuck, D. P. Fromm, A. Sundaramurthy, G. S. Kino and W. E. Moerner, *Phys. Rev. Lett.*, 2005, **94**, 017402.

158

3. *The Journal of Physical Chemistry C* **2012**, 116, 6884-6892

Assessing the Location of Surface Plasmons Over Nanotriangle and Nanohole Arrays of Different Size and Periodicity

Debby Correia-Ledo,[†] Kirsty F. Gibson,[‡] Anuj Dhawan,[§,⊥,‖] Maxime Couture,[†] Tuan Vo-Dinh,[⊥,‖,○] Duncan Graham,[‡] and Jean-Francois Masson*[,†,△]

[†]Department of Chemistry, Universite de Montreal, C.P. 6128 Succ. Centre-Ville, Montreal, Quebec, Canada, H3C 3J7

[‡]Centre for Molecular Nanometrology, WestCHEM, Department of Pure and Applied Chemistry, University of Strathclyde, Glasgow, United Kingdom, G1 1XL

[§]Department of Electrical Engineering, Indian Institute of Technology—Delhi, New Delhi, India, 110016

[⊥]Department of Biomedical Engineering, [‖]Fitzpatrick Institute for Photonics, and [○]Department of Chemistry, Duke University, Durham, North Carolina, United States, 27708

[△]Centre for self-assembled chemical structures (CSACS)

Ⓢ Supporting Information

ABSTRACT: The increasing popularity of surface plasmon resonance (SPR) and surface enhanced Raman scattering (SERS) sensor design based on nanotriangle or nanohole arrays, and the possibility to manufacture substrates at the transition between these plasmonic substrates, makes them ideal candidates for the establishment of structure−property relationships. This work features near diffraction-limited Raman images and finite-difference time-domain (FDTD) simulations of nanotriangle and nanohole array substrates, which clearly demonstrate that the localization of the hot spot on these SERS substrates is significantly influenced by the ratio of diameter/periodicity (D/P). The experimental and simulation data reveal that the hot spots are located around nanotriangles ($D/P = 1$), characteristic of localized SPR. Decreasing the D/P ratio to 0.75−0.7 led to the creation of nanohole arrays, which promoted the excitation of a propagating surface plasmon (SP) delocalized over the metal network. The optimal SERS intensity was consistently achieved at this transition from nanotriangles to nanoholes, for every periodicity (650 nm to 1.5 μm) and excitation wavelength (633 and 785 nm) investigated, despite the presence or absence of a plasmonic band near the laser excitation. Further decreasing the D/P ratio led to excitation of a localized SP located around the rim of nanohole arrays for D/P of 0.5−0.6, in agreement with previous reports. In addition, this manuscript provides the first evidence that the hot spots are positioned inside the hole for D/P of 0.4, with the center being the region of highest electric field and Raman intensity. The compelling experimental evidence and FDTD simulations offer an overall understanding of the plasmonic properties of nanohole arrays as SERS and SPR sensors, which is of significant value in advancing the diversity of applications from such surfaces.
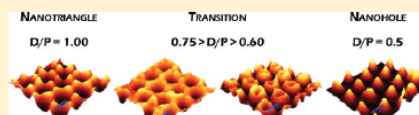
Nanostructured surfaces have found use in various fields such as optics,[1] chemical and biological sensing,[2] photovoltaics,[3,4] and surface-enhanced spectroscopies.[5] The exquisite surface sensitivity of surface plasmons on nanostructured substrates is at the origin of optical phenomena, such as surface-enhanced Raman scattering (SERS). SERS is a versatile and highly sensitive analytical technique, which is capable of producing a vibrational fingerprint of the molecule under study.[6] Significant literature supports the theory of Raman enhancement in SERS. A major contribution to the Raman enhancement can be attributed to the excitation of the localized surface plasmon resonance (LSPR) that occurs on nanostructured surfaces.[7] As a result, an intense electromagnetic field is confined to specific regions on SERS substrates.[7,8] Molecules located within these regions of high electric field (so-called hot spots) contribute a major portion to the overall response of the substrate, without being the only contribution. The hot spots are significantly influenced by the

size and shape of the nanostructured substrate and by geometrical parameters, such as the distance between nanoparticles (gap-effect).

Among the plethora of nanostructured surfaces that have been designed,[9] nanotriangle[10] and nanohole arrays[11] exhibit good sensitivity to refractive index and so are suitable for SPR sensing. In addition, these nanostructures give large Raman enhancement factors necessary for SERS studies. Nanotriangle array-based sensors have been shown to be reliable and versatile substrates for LSPR sensing[12] and SERS.[10] In particular, nanohole arrays present a strongly enhanced light transmission at specific wavelengths that can be attributed to various plasmonic modes. As a result, an amplified electrical field is generated when an active plasmonic mode is excited, which can

6884

The Journal of Physical Chemistry C

be of use in SERS and SPR experiments.[13] Nanohole and nanotriangle arrays owe their interest to the availability of several fabrication methods capable of producing large areas of nearly defect-free substrates. The possibility of creating nanostructures ranging from nanotriangle to nanohole arrays by modified nanosphere lithography (NSL) has provided a tool to study the plasmonic properties at the transition between these nanostructures.[14−16] While nanotriangle and nanohole arrays have been reported numerous times in the literature, no comparative studies have established their relative plasmonic properties.

Tuning the physical properties of nanostructured substrates, such as the diameter, height, thickness, and interparticle spacing engineers the plasmon dispersion, which influences the excitation wavelength of the LSP, the sensitivity to refractive index, the SERS enhancement, and SP mode (propagating or localized). For example, the modification of the size of Au nanoparticles on silicon substrate or of crescent-shape metallic nanoparticles resulted in the full control of tuning the SP excitation wavelength over a range from visible to infrared region.[17] Furthermore, the plasmonic resonance of Ag nanocylinders was blueshifted by either increasing the height or reducing the diameter, which often results in the increase of optical absorption losses within the metal.[18] Surface plasmon frequency can be engineered using double metallic configurations[19] or metallo-dielectric configurations.[20] These examples demonstrated the strong influence of the substrate geometry on the LSP.

Substrates with surface features of a length scale longer than the dissipation length of the surface plasmon polariton exhibit properties characteristic of propagating surface plasmons. Some substrates, such as nanohole arrays, have features with length scales both in the nanoregime and the macroregime. Studying their plasmonic properties is thus of importance. The transition between localized and propagating SP modes was reported in nanovoid substrates supported on a metallic film by changing the normalized thickness of the voids.[21] Nanovoids were prepared by nanosphere lithography (NSL) on a metallic film, leading to structures of relative similarity to nanotriangle and nanoholes. For example, structures with small normalized thickness resemble to nanotriangle arrays on a metallic film, while nanovoid substrates of large normalized thickness are similar to nanohole arrays. It was demonstrated that propagating SP modes were excited for small normalized thickness, which transition to localized SP mode located inside the voids for large normalized thickness. The excitation of localized and propagating SP modes was reported in nanotriangle and nanohole substrates based on sensitivity to refractive index and SPR spectra in the Kretschmann configuration.[14,22,23] However, nanotriangle and nanohole arrays are commonly excited by extinction or transmission spectroscopy for SPR and SERS experiments. It is thus important to establish the properties of these plasmonic substrates for fundamental knowledge and sensor design.

In addition to experimental properties, there is a strong interest in correlating the plasmonic properties to the predicted theoretical response. Recently, significant efforts have been undertaken to predict the localization of the regions with the strongest electromagnetic enhancement on the substrate, often referred to as "hot spots". These hot spots are major contributors to the SPR and SERS response from molecular adsorbates. Thus, it is important to understand the structure−property relationship for different plasmonic substrates in order

to better control the localization of molecular receptors on the surface of the substrate. Enhanced sensitivity may be accessible due to binding of the analyte at specific locations of a nanostructured substrate.[24] Numerical solutions have produced significant predictions for the localization of hot spots. For example, Schatz et al. performed discrete dipole approximation (DDA) calculations on triangular dimers separated by a gap of 2 nm.[25] It was found that the hot spots were located at the tips of the triangles in nanotriangle substrates. In the case of triangle dimers, it was demonstrated that the maximum electric field enhancement occurs at the tip-to-tip region of the dimers. For nanohole arrays, simulations revealed that the hot spots were located around the rim of the nanohole.[26] Essentially, all simulations were performed on nanohole arrays, in which the diameter was nearly half the periodicity. No complete set of simulations has demonstrated the evolution of the hot spot localization in the transition from nanohole arrays.

Correlating simulations with experimental results provides compelling proof of the localization of the hot spots on nanostructures. Raman microscopy, although a very powerful analytical tool, has not been extensively exploited to image the localization of the regions of high Raman intensity on SERS substrates. These regions can be attributed to hot spots. Hot spots were first imaged by Qin et al. for barcodes of different spacing to understand the effect of plasmonic coupling on the SERS response.[27] The Raman images of film over etched nanospheres showed experimental evidence that the hot spots were indeed in regions where nanospheres were at closest proximity.[28] We have recently achieved correlated AFM and SERS images for nanotriangle and nanohole arrays,[29] which provided compelling evidence of the localization of hot spots on the SERS substrates. The Raman images map the regions of high plasmonic field and, thus, can provide evidence of the plasmonic mode excited on substrates. In the work presented here, the measurement of SPR properties, SERS response, Raman images, correlated atomic force microscopy (AFM) and Raman images, and electric field distribution calculations obtained by finite-difference time-domain (FDTD) for nanotriangle and nanohole arrays of various periodicities provide a comprehensive overview of the plasmonic properties of these important substrates.

■ EXPERIMENTAL SECTION

Fabrication of the Nanotriangle and Nanohole Arrays. Nanosphere lithography (NSL) is a simple method used to fabricate several different types of size-tunable nanoparticle arrays as it provides great control over the size, shape, and interparticle distance (gap). While some defects are present and depend on the deposition conditions,[30] crystalline regions composed of several domains with different orientation of the crystal lattice can create useful substrates of several square millimeters up to a square centimeter. NSL has been utilized to fabricate nanotriangle arrays,[31] and by adding a reactive ion etching step, nanohole arrays can be created by reducing the size of the polymer nanospheres without altering the crystalline lattice of the NSL mask.[13,32,33] Thus, in this work, modified NSL was employed to investigate the surface plasmon properties[15,16] and SERS properties[29] of the transition from nanotriangle to nanohole arrays.

Glass microscope slides of 22 mm × 22 mm were first cleaned in a piranha solution (75% v/v H_2SO_4: 25% v/v H_2O_2) at 80 °C for 90 min. After thoroughly rinsing with 18 MΩ·cm water, they were sonicated in a 5:1:1 v/v solution of water/

160

H_2O_2/NH_4OH for 60 min. The glass slides were once again thoroughly rinsed with 18 MΩ·cm water and stored in water for extended periods of time, with replacement of the water every 48 h. Nanosphere lithography (NSL) was employed to fabricate the nanohole arrays of various periodicity and diameter.[13,16] Using the clean glass slides as the substrate, NSL masks were prepared by drop coating of the nanospheres in solution. Considering the periodicity, a specific drop coating solution was prepared by mixing respectively water (18 MΩ·cm Milli-Q), ethanol (ACS grade), and a nanosphere stock solution (Thermo Scientific Particle technologies, 5000 series; 10% w/v) in different volume proportions (Table S3 in the Supporting Information (SI)). The drop size used in the drop coating process was also dependent on the periodicity. Finally, well-ordered regions were formed by drying the deposit at room temperature by covering the coverslip with the drop coating solution with a Petri dish slightly raised by a pipette tip.

The size of the nanospheres was then tuned by etching the NSL masks with an oxygen plasma using a plasma cleaner (Harrick Plasma Cleaner PDC-32G) at high power (18 W) for 0−10 min for periodicities ranging from 650 to 1000 nm and for 0−18 min for 1500 nm nanospheres under a continuous oxygen flow of 15 mL/min. A 20-min vacuum step prior to etching was necessary to remove air gases and to leave a low pressure of nearly pure oxygen.

Metallization of the substrate was achieved by depositing a 1 nm Cr adhesion layer followed by a 125 nm Au or Ag layer. Finally, removing the NSL mask by sonication in ethanol for a few seconds resulted in the nanostructured arrays. Four identical samples were prepared for each series for analytical purposes, and the size (diameter and depth) of the nanoholes was estimated by atomic force microscopy (AFM) in contact mode and scanning electron microscopy (SEM).

Plasmonic Properties. The plasmonic properties were determined by reflectance measurements at normal incidence using a 6 around 1 reflectance probe. Illumination under a halogen light source allowed the measurement of a reflectance spectrum ranging from 400 to 900 nm. For each sample, a spectrum was prepared by processing the reflectance data using a smooth Ag or Au film as the reference. Reflectance measurements were preferred due to the similarity of the Raman spectra measurements with an epi-microscope. Sensitivity was measured with sucrose solutions of different refractive indices, using transmission measurements with a custom-built flow cell and optical setup.

Raman Spectroscopy Measurements. Nanohole arrays were first immersed in an aqueous solution of 0.5 mM 4-nitrobenzene thiol (4-NBT) overnight. The 4-NBT was chosen as a control molecule because its Raman behavior is well-known. The samples were then rinsed with water followed by ethanol, dried under an argon flux, and stored in the dark prior to their use. For each series (4 samples for each etch time), a Raman spectrum was measured with a Renishaw InVia Raman microscope using 633 and 785 nm excitation wavelengths. Spectra were acquired for 10 s at 1% of the laser intensity, resulting in 35 μW for the 633 nm laser and 35 mW for the 785 nm laser. Four characteristic Raman peaks of 4-NBT (1082, 1112, 1350, and 1575 cm^{-1}) were used to investigate the intensity of the Raman response for each nanohole array sample. For comparison purposes, the Raman response was reported as a percentage compared to the nanotriangle response (where nanotriangle = 100%), prepared with the same NSL mask.

Near-Diffraction Limited Raman Microscopy Measurements. Raman analyses were carried out using WiTec alpha300 instrumentation, which facilitated the mapping of approximately 10×10 μm areas. The false color Raman maps of intensity were obtained using a 532, 633, or 785 nm excitation laser. The approximate powers of the 532, 633, and 785 nm excitation lasers were 0.57 (1.2% of total power), 0.33 (1.5% of total power), and 1.2 mW (1.5% of total power), respectively. The laser power density was estimated at 0.84 MW/cm² for the 532 nm laser and at 0.34 MW/cm² for the 633 nm laser, with an illuminated area of approximately 0.068 μm² for the 532 nm laser and 0.097 μm² for the 633 nm laser. The parameters were set as following: 0.005 s integration time and 100× objective (Olympus MPlan, NA = 0.9), which resulted in approximately 300−500 nm spatial resolution. The intensity of the ν(C−C) stretch of 4-NBT at 1575 cm^{-1} was mapped resulting in a false color image of the Raman enhancement over the analysis area. Three maps were taken from three separate, identically prepared samples for each etch time and all maps from samples with the same etch time resembled one another to a high degree highlighting the reproducibility of the Raman response from the substrates.

Contact mode AFM analysis was performed on a NanoInk DPN5000 instrumentation. Images were obtained at 512×512 pixel resolution using a scan rate of 0.2 Hz. The scanned areas intentionally included crystallization defects and/or scratches to act as a point of reference between the AFM and Raman images.

Finite-Difference Time-Domain (FDTD) Simulations. In the work described in this paper, the FDTD technique was employed for numerically calculating electromagnetic (EM) fields around nanotriangle and nanohole arrays in metallic thin films (Ag thin films) so as to study the effects of the diameters (D) and periodicities (P) of the nanohole arrays on the EM fields. We have previously employed FDTD for modeling EM fields around metallic nanostructures such as nanoparticles and nanopillar arrays.[14,17] While FDTD algorithms[18] analyze structures by solving the differential form of coupled Maxwell's equations, analyses described in these calculations incorporate the effects of dispersion relations, e.g. the effects of wavelength dependence of the dielectric constants of the metallic structures. Here, we employed an FDTD software called FullWAVE 6.0 by R-Soft to carry out the FDTD analysis for the nanohole arrays. This software enables FDTD analysis of the metallic media to include Debye or Lorentz models of dispersion relations of the dielectric constants of the metals.

In the FDTD simulations, we used an extended Debye dispersion model for determining the dielectric constants for silver.[14] 3D FDTD solutions were obtained for electromagnetic fields around periodic hexagonal arrays of nanoholes (having different diameters and periodicities) in Ag films (50 nm thick Ag film, having a 5 nm thick Ti adhesion layer underneath the Ag film) deposited on a silica substrate. Electromagnetic fields (e.g., E and H fields in the x, y, and z directions) in the vicinity of the nanohole arrays were calculated assuming plane wave illumination being normally incident on the nanohole arrays, the wavelengths of the incident radiation being 532 and 633 nm. The magnitude of the incident electric fields was taken to be unity and the enhancement of electromagnetic fields, around the nanohole arrays, evaluated. The time steps employed in these simulations were selected to be small enough such that the Courant stability criterion[18] was satisfied for the different grid sizes employed. For FDTD calculations involving the

161

Article

nanohole arrays, the grid sizes in the x, y, and z directions (Δx, Δy, and Δz) were selected to be such that the value of the E field intensities around the nanohole arrays became independent of the grid sizes. In these simulations, the grid sizes in the x, y, and z directions were 5, 5, and 30 nm, respectively. The FDTD simulations were performed with the incident light being linearly polarized light along the x-axis of the figures (see bottom row of Figure 4). In our simulations, the diameters of the nanohole arrays in the Ag film varied between 300 and 1500 nm (steps of 150 nm), while the periodicity of the nanohole arrays was 1500 nm.

■ RESULTS AND DISCUSSION

General Properties of Nanohole Arrays. Nanohole arrays of different periodicities and diameters were fabricated by modified nanosphere lithography (NSL).[13,16,33] The initial size of the polystyrene spheres dictates the periodicity, while the duration of the etching process controls the diameter of the holes. A diameter/periodicity (D/P) ratio allows simple comparison of arrays of different periodicities. For example, a D/P of 1 corresponds to a nanotriangular structure, while a D/P of 0 is observed for a continuous film. It has been reported that the SERS, SPR, and LSPR results demonstrate that the transition from triangle to hole arrays occurs within a D/P ratio ranging from 0.75 to 0.60.[29] Therefore, a matrix of nanohole array samples was constructed with periodicities ranging from 650 to 1500 nm. Samples with D/P between 0.4 and 1.0 were investigated (Table 1). The investigation was limited to a lower

Table 1. Surface Plasmon Resonance Wavelength for Nanohole Arrays of Different Periodicities

650 nm		820 nm		1000 nm		1500 nm	
D/P	λ_{LSPR} (nm)	D/P	λ_{LSPR} (nm)	D/P	λ_{LSPR} (nm)	D/P	λ_{LSPR} (nm)
1.00	OSR[a]	1.00	OSR[a]	1.00	OSR[a]	1.00	OSR[a]
0.72	513	0.77	OSR[a]	0.68	OSR[a]	0.71	OSR[a]
0.60	567	0.69	549, 700	0.61	OSR[a]	0.69	OSR[a]
0.46	510, 700	0.57	480, 668, 868	0.59	520	0.64	OSR[a]
0.45	542, 637	0.56	513, 895	0.53	520	0.64	OSR[a]
0.42	513, 747	0.52	507, 557, 640	0.50	498, 645, 740, 819	0.59	OSR[a]
		0.43	528, 670, 807, 842	0.46	498, 645, 740, 819	0.53	649

[a]OSR: Outside spectral range of 400–950 nm.

boundary of D/P equal to 0.4 as the modified NSL method is incompatible with the fabrication of nanohole arrays of smaller D/P ratios. The transition region is of particular interest, as it exhibited an improved Raman response for nanohole arrays of 820 nm.[29] The physical aspect of the substrate changes significantly in this transition region. AFM images of samples with 1000 nm periodicity clearly demonstrated that samples with D/P ratio ranging from 0.74 to 0.77 consist of a network of nearly interconnected triangles, while a D/P with values around 0.60–0.63 exhibits a continuous network of holes (Figure 1). Therefore, these values of D/P will be used to define the upper and lower limit of the transition zone. To better understand the properties of plasmonic substrates in this transition region and to determine optimal SERS substrate
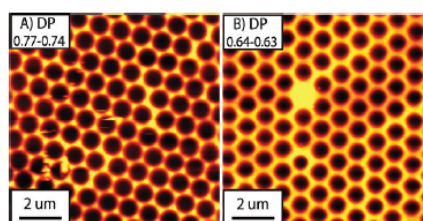

Figure 1. AFM images (10 μm × 10 μm scan) of nanohole arrays with 1000 nm periodicity, for which the D/P corresponds to the (A) upper and (B) lower boundaries of the transition region, respectively.

among nanotriangle and nanohole arrays, a comprehensive characterization of nanohole arrays was undertaken.

The D/P ratio and the periodicity are two factors that significantly affect the optical properties of nanohole arrays. The excitation wavelength of the surface plasmon[34] and the sensitivity to refractive index of nanohole arrays are proportional to the periodicity; higher excitation wavelength and sensitivity are achieved with a larger periodicity.[35] While the plasmonic properties can be extended to the IR region,[36] this study focuses on the optical properties of nanohole arrays within the visible–near-infrared region ranging from 400 to 950 nm, as this region covers the plasmonic properties of Au and Ag and also spans the range of most common Raman systems (e.g., λ = 488, 514, 532, 633, and 785 nm). As expected, the surface plasmons (SPs) of nanotriangle arrays (D/P of 1.0) and of nanohole arrays of larger periodicities (e.g., 1000 and 1500 nm) are excited above λ = 1 μm (Table 1). Indeed, for nanotriangle arrays, decreasing the D/P ratio promotes plasmon coupling, and redshifting the plasmonic band to lower energies (higher wavelengths). For nanohole arrays, decreasing the D/P ratio does not significantly influence the excitation wavelength but increases the intensity of the plasmonic band. The observations noted here have also been reported for other periodicities of nanotriangle and nanohole arrays.[15,16] As for samples with small D/P ratios or short periodicities, a plasmonic band in the visible region of the light spectrum was observed. Hence, the majority of samples prepared using 650 and 820 nm periodicities support an SP in the target spectral region, while the SP of samples with 1000 and 1500 nm periodicities could not be excited under experimental conditions. Samples with lower D/P ratios feature multiple plasmonic bands associated to the several modes excited in the spectral region probed. The sample set was designed to evaluate the influence of the SP excitation wavelength on the Raman properties of nanohole arrays.

Bulk Plasmonic Properties: From Nanotriangle to Nanohole Arrays. The D/P ratio significantly impacts the Raman response of SERS substrates. Importantly, the Raman response reported here is for the illumination of a surface of constant area on the substrates, regardless of the geometrical shape of the substrate, providing a direct comparison of the Raman intensity. The Raman response is normalized to that of nanotriangle array (D/P = 1.00) of the same periodicity for comparison purposes. In the nanohole region, for D/P ratios smaller than 0.60, the Raman response is essentially equivalent to that of nanotriangle arrays. A distinct exception to this observation concerns the nanohole arrays of 650 nm periodicity
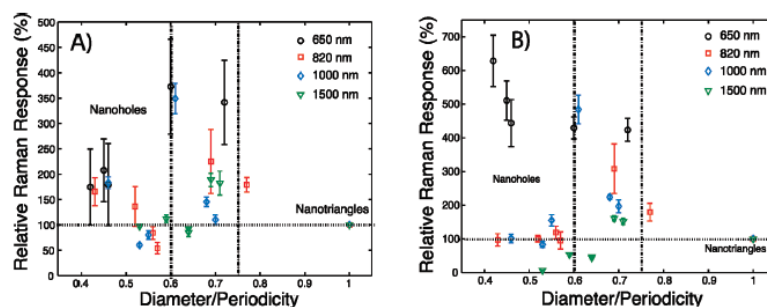
162

Figure 2. Influence of the diameter/periodicity (D/P) ratio of nanohole arrays on the amplification of the Raman response for an excitation wavelength of (A) 633 and (B) 785 nm.

excited at λ = 785 nm (Figure 2, right). By featuring a strong plasmonic band near λ = 700 nm, the response is amplified to about a factor of 6 in comparison to nanotriangle arrays. Otherwise, for every periodicity and excitation laser (λ = 633 and 785 nm), the Raman response is maximal for SERS substrates within the transition region with D/P of 0.75 to 0.6 (Figure 2). Particularly, the largest Raman responses were observed for D/P ratios of 0.60, 0.69, 0.61, and 0.69 for substrates of 650, 820, 1000, and 1500 nm periodicities, respectively. The SERS substrates obtained from 650 and 1000 nm periodicities exhibited the highest relative Raman improvement in the transition region. The amplification factor is approximately 3.5 and almost 5 for the excitation wavelengths of 633 and 785 nm respectively. A smaller amplification factor is observed for SERS substrates of 820 and 1500 nm periodicities; a factor of 2.5−3 and 1.5−2 for excitation wavelengths of 633 and 785 nm was achieved, respectively.

The raw intensity of the Raman response for the illumination of a fixed geometrical area of the optimal nanostructure of each periodicity was constant for λ = 633 nm excitation. In contrast, the Raman response at λ = 785 nm was most intense for substrates with 1000 nm periodicity where the response was 50% more intense compared to that of other periodicities. Overall, on our system (Renishaw InVia Raman microscope), we observed a larger raw intensity per unit power for the λ = 633 nm laser. However, the λ = 785 nm Raman laser is available with ten times more intensity and has the additional advantage of decreasing the fluorescence with longer wavelengths. Therefore, the nanostructures of 1000 nm periodicity with a D/P ratio of 0.69 excited at a 785 nm wavelength yielded the most intense response among the ones tested in this study.

While the Raman response is essentially constant for nanohole arrays (D/P < 0.6), the sensitivity to refractive index is a factor of D/P for these nanostructured substrates. Although the theoretical equations describing the sensitivity of nanohole arrays do not take into consideration the diameter of the holes,[35] it was previously reported that the sensitivity is indeed modulated by the diameter of Ag nanoholes with 450 nm periodicity.[16] Here, the sensitivity of Au nanohole arrays of 820 and 1000 nm periodicities also strongly depend on the diameter of the nanoholes within the region of D/P ratios comprised between 0.40 and 0.60. The sensitivity measured with sucrose solutions of refractive index (RI) ranging from 1.33 to 1.37 RIU region varied between 196 and 428 nm/RIU

and reached a maximum for a D/P of 0.44 for nanohole arrays of 820 nm periodicity (Figure 3). For the nanohole arrays of
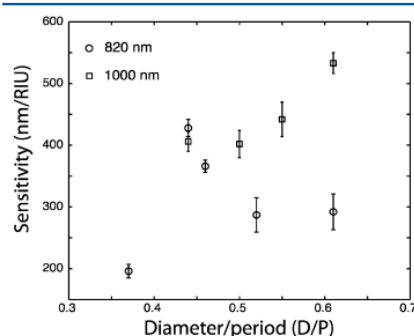

Figure 3. Sensitivity to refractive index of sucrose solutions (RI range: 1.33−1.37) measured for nanohole arrays with 820 (circles) and 1000 nm (squares) periodicities at different D/P ratios in the nanohole region, e.g. D/P < 0.60.

1000 nm periodicity, the sensitivity increased linearly as a function of D/P to reach a value of 533 nm/RIU for a D/P ratio of 0.6 (Figure 3). The absence of a plasmonic band in the λ = 400−950 nm region for larger D/P values prohibited the measurement of sensitivity of these substrates. In comparison, Au exhibited a constant sensitivity for 450 nm periodicity.[16] The various trends resulting from the relationship of the sensitivity as a function of the D/P ratio are not only useful for understanding the plasmonic properties of nanohole arrays but also for predicting the behavior and analytical properties of these arrays as well.

While the sensitivity of SPR sensors with nanohole arrays strongly depends on the D/P ratio and the periodicity, the SERS response follows similar trends for the periodicities and D/P ratios investigated here. By comparing the values in Table 1 with the data plotted in Figure 2, it is possible to argue that the presence of a strong first order SP band is not necessary to achieve an enhanced Raman response especially at the transition region from nanotriangle to nanohole arrays, since
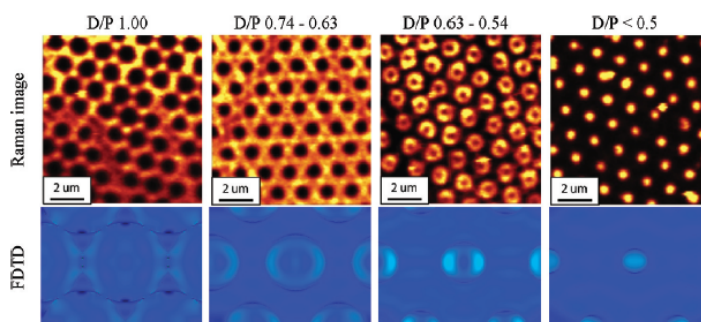
163

Figure 4. (top row) False color Raman microscopy images of a 10 μm × 10 μm region for nanohole arrays of decreasing D/P ratios from left to right, respectively. (bottom row) FDTD images of a 3 μm × 3 μm region for nanohole arrays corresponding to the same D/P regions as for the Raman images. For the Raman images and the FDTD simulations, the periodicity of the nanohole arrays is 1500 nm, illuminated with a 532 nm laser.

Raman lasers are likely to excite higher-order plasmon bands on substrates of larger periodicities. Thus, other factors such as plasmonic coupling from tip-to-tip geometry are major contributors to the improvement of the Raman response in the transition region of $0.75 > D/P > 0.60$.

Imaging the Hot Spots of Nanotriangle and Nanohole Arrays. Imaging Raman scattering of samples with different periodicities, but similar D/P ratios, may provide an overview of the localization of the hot spots on the SERS substrate. The strong correlation between geometrical factors of the samples and the strong Raman response could be explained by the similarities of the hot spots. By measuring high-resolution confocal Raman microscopy images of the SERS substrates, the localization of the enhanced electric field and, thus, the identification of the regions with the highest intensity for the Raman response on those nanostructures can be precisely mapped and correlated to the physical aspects of the SERS substrates. Confocal Raman microscopy allows near diffraction-limited resolution images of the samples. In the case of laser excitation at $\lambda = 532$, 633, and 785 nm investigated here, the diffraction limited lateral resolution of the Raman images with a 100× dry objective (NA = 0.9) are 360, 430, and 532 nm, respectively. A monolayer of 4-nitrobenzenethiol (4-NBT) uniformly covers the samples to alleviate any surface concentration effect that could have arisen from irregular coating of the SERS substrate with the reporter. As expected, the lateral resolution with the $\lambda = 785$ nm laser was inadequate to measure Raman images with sufficient details. Due to their better lateral resolution, Raman images of the SERS substrates with the 532 and 633 nm lasers provide detailed images of the localization of the region of high Raman intensity (Figure 4; complete set is provided in the SI). Four distinct patterns can be observed: (1) islands of high Raman response correlated to the location of the triangles for a D/P of 1.00, (2) a network of high Raman response colocalized with the network of nearly interconnected triangle arrays at a D/P ratio ranging from 0.74 to 0.63, (3) "donut-shaped" regions of high Raman response around the rim of the nanoholes for $0.63 > D/P > 0.54$, and (4) the core area of the nanoholes acts as a point-source of the high Raman response for smaller D/P ratios. It is important to note that the images were acquired with circularly polarized light,

explaining the symmetrical nature of the hot spots. By decreasing the periodicity, the quality of the images is lowered due to a poorer ratio of feature size/spatial resolution (Tables S1 and S2 in the SI). Nonetheless, the Raman images revealed that the location of the hot spots is similar for substrates with constant D/P, regardless of the periodicity and the presence or absence of a plasmonic band being excited by the Raman laser.

The highest Raman intensity is observed near the transition between the network of interconnected triangles and the substrates with a high electric field around the rim of the nanoholes. The network of nearly interconnected triangles exhibited a region of high plasmonic coupling,[37,38] due to the presence of a network of dimers. It is expected that the high electric field will lead to significantly improved Raman response at the tip-to-tip region of this substrate. Figure 4 (second panel) presents faint areas near the center of the triangles as well as regions of slightly higher intensity. The contrast is quite poor between these regions, which may be due to the spatial resolution being much larger than the actual hot spots. Nonetheless, this structure of nearly interconnected nano-triangle arrays (or so-called bowtie arrays) provides significantly improved Raman response in relation to conventional nano-triangle and nanohole arrays.

As expected, the SERS images clearly demonstrate the localized SP excited in nanotriangle arrays. The structure-dependent properties of a nanohole array substrate are evident from the different SERS images obtained depending on the D/P ratio. The delocalization of the region of high Raman response on the metallic network near the transition from nanotriangle to nanohole arrays is characteristic of a propagating SP. We observed in our previous studies that a propagating SP can be excited on the substrate at the transition from nanotriangle to nanohole arrays.[14] In addition, the nanovoid substrates prepared by Kelf et al, which resemble the nanohole arrays, also exhibited a propagating SP at low normalized thickness.[21] Low normalized thickness corresponds to large D/P ratios. Further decreasing the D/P ratio leads to a localized SP located around the rim of the nanohole, which becomes highly focused inside the nanohole at lower D/P ratios. This transition from propagating to localized SP was also reported in nanovoids substrates. Thus, the plasmonic

164

properties of nanohole arrays are very similar to nanovoids. In summary, the transition from nanotriangle to nanohole arrays is characterized by a localized SP at high D/P for triangle arrays, which propagates near the transition to nanohole array and is localized for nanohole arrays of smaller D/P.

Despite the imperfect nature of NSL for fabricating nanohole arrays, the simplicity of the technique, the low cost of fabrication, and facile tuning of the geometrical parameters of the substrate makes it an interesting alternative to photo-lithography, E-beam lithography, or focused ion beam milling. Most importantly, SERS images demonstrate that the response is relatively homogeneous across the sample; a 10–30% coefficient of variation was observed on the intensity of the hot spots across the Raman images. This confirms that most of the sample contributes to the overall Raman response, unlike the nanoparticle aggregates for which the majority of the signal may originate from one particular hot spot. Another important observation resides in the intensity observed at the point defects of the samples. The boundary of a dislocation between two regions of different crystalline orientations is more intense than perfectly oriented regions for the triangle arrays (D/P of 1.0). These same boundaries in nanohole arrays exhibit smaller Raman responses, suggesting that the highest Raman response for nanohole arrays will be for samples perfectly oriented.

Correlated AFM and SERS images on the same location of a nanostructured substrate provide valuable insights on the structure–property relationship of these arrays. It was previously reported that for a transition state of nearly connected nanotriangles for substrates of 820 nm periodicity for a D/P ratio of 0.69, the network of metallic triangle is colocated with the one of intense Raman areas.[29] In addition, the point source-like areas of high Raman intensity for nanohole arrays of $D/P = 0.43$ correlated with the center of the core area of the nanoholes.[29] Here, correlated AFM and SERS images confirmed that the "donut-shaped" region of high Raman intensity is perfectly colocalized with the rim of nanohole arrays of 1.5 μm periodicity with a D/P of 0.64 (Figure 5). The dark region of low Raman response at the
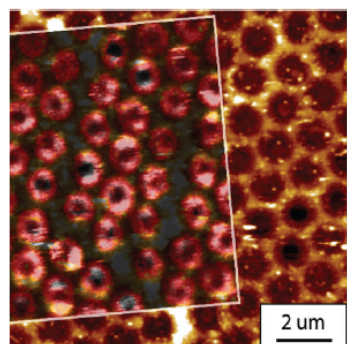

Figure 5. Correlated AFM and SERS images of a nanohole array with a D/P ratio of 0.64. The false color Raman image (pink) was acquired at 633 nm, which is delimited by the white boundaries. The ring attributed to the high Raman intensity is colocalized with the rim of the nanohole, which is in agreement with the FDTD calculations.

center of the donut is about 400 nm across for 1500 nm periodicity. This region is close to the diffraction-limited resolution of the $\lambda = 532$ and 633 nm lasers, explaining that it was only observed for the 1000 (only with $\lambda = 532$ nm) and 1500 nm (with both lasers) periodicities (Tables S1 and S2 in the SI). We anticipate that these regions also exist for nanohole arrays of smaller periodicity, but the spatial resolution of the measurement did not provide direct evidence of this dark core, as it is below the diffraction limit for smaller periodicities.

Finite-Difference Time-Domain (FDTD) Simulations. Calculations to map the electric field distribution of SERS substrates correlate well with the experimental SERS images (Figure 4 (bottom row); Tables S1 and S2 in the SI). The FDTD simulations were performed with linearly polarized light along the x-axis of the figures. As predicted by numerical simulations,[33,37] the alignment of the areas of high electric field with the orientation of the polarized light is expected. Both simulations at $\lambda = 532$ and 633 nm show that the region of high electric field surrounds the nanotriangles for substrates exhibiting a D/P ratio of 1.0; therefore, matching with the SERS image showing the triangles as being the regions of high Raman intensity. FDTD simulations are also in strong agreement with the experimental data for the nanohole array substrate with a $0.74 > D/P > 0.63$. The SERS image and the FDTD simulation for a $0.63 > D/P > 0.54$ demonstrate that the region of high electric field and intense Raman response is located around the rim of the nanoholes. By decreasing the D/P ratio of the FDTD simulations to 0.3, the center of the nanoholes becomes a point-source region of high electric field, fitting very well with the experimental SERS image for smaller D/P.

The slight discrepancy between the experimental and simulated D/P, in particular for smaller D/P values, is due to the imperfect nature of the samples prepared with NSL. Indeed, the experimental D/P measured by AFM and the simulations do not consider the tapered nature of the nanohole wall. In fact, the nanoholes are more bowl-like, instead of cylindrical. Therefore, the apparent D/P for the sample labeled $0.57 > D/P > 0.50$ is true for the top of the nanohole, but an SEM image of this sample demonstrates that the bottom of the nanohole had a smaller D/P ratio of approximately 0.3 (Figure S1 in the SI), which is in good agreement with the simulations. Measuring the diameter of the region of high Raman response for the smallest nanohole diameter also results in a D/P of 0.3, once again in agreement with the SEM image and the FDTD simulation. To our knowledge, it is the first time that such result demonstrates that if the nanohole diameter is small in comparison to the periodicity, the region of high electric field is not located at the edge of the rim of the nanohole (so-called donut-shape), but rather at the center of the nanohole (typically made of glass, rather than metal), where molecules are not expected to absorb in common biosensing strategies. It also explains the lower Raman intensity measured for these samples, despite the excitation of the plasmonic band. The electric field is concentrated in a region where very few molecules are located, resulting in a lower Raman intensity.

The deviation between the FDTD simulations and the experimental SERS images for a D/P near 0.7 is another example of the influence of the imperfect nature of the samples prepared by NSL. The AFM image of the sample with a $0.77 > D/P > 0.74$ shows a lower topography at the tip-to-tip region (Figure 1), due to the shadow effect of the NSL mask during the deposition of the metal layer. This imperfection in the tip-

165

Article

to-tip region may promote high electric field at this region, as observed in the experimental SERS image, instead of the rim of the nanoholes as simulated.

FDTD simulations performed at $\lambda = 532$ nm provide images with better lateral resolution than the ones at $\lambda = 633$ nm (Tables S1 and S2 in the SI). While this is in agreement with experimental Raman images, FDTD simulations are not diffraction-limited and so this does not explain the poorer definition of the hot spots with the longer wavelength. The simulations were performed with substrates of 1500 nm periodicity, such that there is no presence of plasmonic bands due to periodic hexagonal array of nanoholes (Table 1). Therefore, the influence of the D/P ratio can be clearly seen in the interpretation of the Raman images. One possible explanation involves fringes resulting from the excitation of the substrate. Fringes arise from the excitation of a surface plasmon polariton (SPP) around an individual nanohole by the incident electric field in the zero-order excitation. This SPP propagates radially from the individual nanoholes,[39,40] and an interference pattern is created from the SPP of adjacent nanoholes, which can be observed in the FDTD simulations.

■ CONCLUSIONS

Raman spectroscopy, confocal Raman microscopy, surface plasmon resonance, and FDTD simulations have been employed to extensively characterize the transition from nanotriangle to nanohole arrays. For every periodicity sampled (650−1500 nm), the largest Raman response was observed at the transition state between nanotriangle and nanohole arrays. This transition occurs within a D/P region ranging from 0.75 (nearly interconnected triangle) to 0.60 (network of nanoholes). The SERS images of the hot spots on the nanostructures vary as the transition from nanotriangle to nanohole occurs. The hot spots were observed to be a delocalized area of high Raman intensity, which perfectly matches the metallic network of the array at a D/P ratio of nearly 0.7 and a donut-shape region of high Raman response (nanohole array), which correlates very well with the edges of the nanoholes. Thereby, the SERS images demonstrate the presence of a localized SP in nanotriangle arrays, a propagating SP for the substrate at the transition from nanotriangle to nanohole arrays and a localized SP in nanohole arrays. These changes in structure were demonstrated by correlating the AFM results and Raman microscopy images with one another. For the first time to our knowledge, it was observed that by further decreasing the D/P ratio, the region of high electric field for nanohole arrays is positioned at the center of the nanoholes, with a center-to-center spacing perfectly matching the periodicity. This observation has significant implications for biosensing applications in terms of optimal placement of bioanalytes. The experimental SERS images are in good agreement with the FDTD simulations, and the outcome provides a comprehensive study of the plasmonic properties of nanohole arrays, from understanding the different locations of the hot spots to demonstrating the largest potential for SERS and SPR sensing applications.

■ ASSOCIATED CONTENT

Ⓢ Supporting Information
Complete set of Raman images for all the periodicities (650−1500 nm) for 535 and 633 nm excitation wavelengths as well as their matching FDTD images, SEM image attesting to the bowl-like shape structure of nanoholes, and summary of drop coating conditions as a function of the periodicity. This material is available free of charge via the Internet at http://pubs.acs.org/.

■ AUTHOR INFORMATION

Corresponding Author
*E-mail: jf.masson@umontreal.ca. Tel.: +1-514-343-7342. Fax: +1-514-343-7586.

Notes
The authors declare no competing financial interest.

■ REFERENCES

(1) Gauvreau, B.; Hassani, A.; Fehri, M. F.; Kabashin, A.; Skorobogatiy, M. *Opt. Express* **2007**, *15*, 11413.
(2) Ferreira, J.; Santos, M. J. L.; Rahman, M. M.; Brolo, A. G.; Gordon, R.; Sinton, D.; Girotto, E. M. *J. Am. Chem. Soc.* **2009**, *131*, 436.
(3) Lohmüller, T.; Müller, U.; Breisch, S.; Nisch, W.; Rudorf, R.; Schuhmann, W.; Neugebauer, S.; Kaczor, M.; Linke, S.; Lechner, S.; Spatz, J.; Stelzle, M. *J. Micromech. Microeng.* **2008**, *18*, 115011.
(4) T. H. Reilly, I.; Lagemaat, J. v. d.; Tenent, R. C.; Morfa, A. J.; Rowlen, K. L. *Appl. Phys. Lett.* **2008**, *92*, 243304.
(5) Bahns, B. T.; Yan, F.; Qiu, D.; Wang, R.; Chen, L. *Appl. Spectrosc.* **2006**, *60*, 989.
(6) Fan, M.; Brolo, A. G. *Phys. Chem. Chem. Phys.* **2009**, *11*, 7381.
(7) Guerrini, L.; Izquierdo-Lorenzo, I.; Garcia-Ramos, J. V.; Domingo, C.; Sanchez-Cortes, S. *Phys. Chem. Chem. Phys.* **2009**, *11*, 7363.
(8) Hering, K.; Cialla, D.; Ackermann, K.; Dörfer, T.; Möller, R.; Schneidewind, H.; Mattheis, R.; Fritzsche, W.; Rösch, P.; Popp, J. *Anal. Bioanal. Chem.* **2008**, *390*, 113.
(9) Stewart, M. E.; Anderton, C. R.; Thompson, L. B.; Maria, J.; Gray, S. K.; Rogers, J. A.; Nuzzo, R. G. *Chem. Rev.* **2008**, *108*, 494.
(10) Stiles, P. L.; Dieringer, J. A.; Shah, N. C.; Van Duyne, R. P. *Annu. Rev. Anal. Chem.* **2008**, *1*, 601.
(11) Gordon, R.; Sinton, D.; Kavanagh, K. L.; Brolo, A. G. *Acc. Chem. Res.* **2008**, *41*, 1049.
(12) Willets, K. A.; Van Duyne, R. P. *Annu. Rev. Phys. Chem.* **2007**, *58*, 267.
(13) Masson, J.-F.; Murray-Méthot, M.-P.; Live, L. S. *Analyst* **2010**, *135*, 1483.
(14) Live, L. S.; Bolduc, O. R.; Masson, J. F. *Anal. Chem.* **2010**, *82*, 3780.
(15) Murray, W. A.; Astilean, S.; Barnes, W. L. *Phys. Rev. B* **2004**, *69*.
(16) Murray-Methot, M.-P.; Ratel, M. P.; Masson, J.-F. *J. Phys. Chem. C* **2010**, *114*, 8268.
(17) Das, N. C. *J. Appl. Phys.* **2011**, *110*, 046101.
(18) Henson, J.; Dimakis, E.; DiMaria, J.; Li, R.; Minissale, S.; Dal Negro, L.; Moustakas, T. D.; Paiella, R. *Opt. Express* **2010**, *12*, 21322.
(19) Zhao, H.; Zhang, J.; Liu, G.; Tansu, N. *Appl. Phys. Lett.* **2011**, *98*, 151115.
(20) Paiella, R. *Appl. Phys. Lett.* **2005**, *87*, 111104.
(21) Kelf, T. A.; Sugawara, Y.; Cole, R. M.; Baumberg, J. J.; Abdelsalam, M. E.; Cintra, S.; Mahajan, S.; Russell, A. E.; Bartlett, P. N. *Phys. Rev. B* **2006**, *74*.

166

Article

(22) Live, L. S.; Masson, J. F. *J. Phys. Chem. C* **2009**, *113*, 10052.

(23) Live, L. S.; Murray-Methot, M. P.; Masson, J. F. *J. Phys. Chem. C* **2009**, *113*, 40.

(24) Beeram, S. R.; Zamborini, F. P. *J. Phys. Chem. C* **2011**, *115*, 7364.

(25) Hao, E.; Schatz, G. C. *J. Chem. Phys.* **2004**, *120*, 357.

(26) Stewart, M. E.; Mack, N. H.; Malyarchuk, V.; Soares, J.; Lee, T. W.; Gray, S. K.; Nuzzo, R. G.; Rogers, J. A. *Proc. Natl. Acad. Sci. U.S.A.* **2006**, *103*, 17143.

(27) Qin, L. D.; Zou, S. L.; Xue, C.; Atkinson, A.; Schatz, G. C.; Mirkin, C. A. *Proc. Natl. Acad. Sci. U.S.A.* **2006**, *103*, 13300.

(28) Farcau, C.; Astilean, S. *J. Phys. Chem. C* **2010**, *114*, 11717.

(29) Gibson, K. F.; Correia-Ledo, D.; Couture, M.; Graham, D.; Masson, J. F. *Chem. Commun.* **2011**, *47*, 3404.

(30) Kumnorkaew, P.; Ee, Y.-K.; Tansu, N.; Gilchrist, J. F. *Langmuir* **2008**, *24*, 12150.

(31) Jensen, T. R.; Malinsky, M. D.; Haynes, C. L.; Duyne, R. P. V. *J. Phys. Chem. B* **2000**, *104*, 10549.

(32) Murray-Methot, M. P.; Menegazzo, N.; Masson, J. F. *Analyst* **2008**, *133*, 1714.

(33) Lee, S. H.; Bantz, K. C.; Lindquist, N. C.; Oh, S.-H; Haynes, C. L. *Langmuir* **2009**, *25*, 13685.

(34) Thio, T.; Ghaemi, H. F.; Lezec, H. J.; Wolff, P. A.; Ebbesen, T. W. *J. Opt. Soc. Am. B* **1999**, *16*, 1743.

(35) Lee, K. L.; Wang, W. S.; Wei, P. K. *Plasmonics* **2008**, *3*, 119.

(36) Coe, J. V.; Heer, J. M.; Teeters-Kennedy, S.; Tian, H.; Rodriguez, K. R. *Annu. Rev. Phys. Chem.* **2008**, *59*, 179.

(37) Galarreta, B. C.; Harte, E.; Marquestaut, N.; Norton, P. R.; Lagugne-Labarthet, F. *Phys. Chem. Chem. Phys.* **2010**, *12*, 6810.

(38) Hao, E.; Schatz, G. C. *J. Chem. Phys.* **2004**, *120*, 357.

(39) Nerkararyan, S.; Nerkararyan, K.; Janunts, N.; Pertsch, T. *Phys. Rev. B* **2010**, *82*.

(40) Nikitin, A. Y.; Garcia-Vidal, F. J.; Martin-Moreno, L. *Phys. Rev. Lett.* **2010**, *105*.

167

4. *Analytical and Bioanalytical Chemistry*, published online July 2012.

ORIGINAL PAPER

Angle-dependent resonance of localized and propagating surface plasmons in microhole arrays for enhanced biosensing

Ludovic S. Live · Anuj Dhawan · Kirsty F. Gibson ·
Hugo-Pierre Poirier-Richard · Duncan Graham ·
Michael Canva · Tuan Vo-Dinh · Jean-François Masson

Abstract The presence of microhole arrays in thin Au films is suited for the excitation of localized and propagating surface plasmon (SP) modes. Conditions can be established to excite a resonance between the localized and propagating SP modes, which further enhanced the local electromagnetic (EM) field. The co-excitation of localized and propagating SP modes depends on the angle of incidence (θ_{exc}) and refractive index of the solution interrogated. As a consequence of the enhanced EM field, enhanced sensitivity and an improved response for binding events by about a factor of 3 to 5 was observed with SPR sensors in the Kretschmann configuration for a set of experimental conditions (λ_{SPR}, θ_{exc}, and η). Thus, microhole arrays can improve sensing applications of SPR based on classical prism-based instrumentation and are suited for SP-coupled spectroscopic techniques.

L. S. Live · H.-P. Poirier-Richard · J.-F. Masson (✉)
Département de chimie, Université de Montréal,
C.P. 6128 Succ. Centre-Ville,
Montreal, QC H3C 3J7, Canada
e-mail: jf.masson@umontreal.ca

A. Dhawan · T. Vo-Dinh
Fitzpatrick Institute for Photonics, Duke University,
Durham, NC 27708, USA

A. Dhawan · T. Vo-Dinh
Department of Biomedical engineering, Duke University,
Durham, NC 27708, USA

A. Dhawan
Department of Electrical Engineering,
Indian Institute of Technology-Delhi,
New Delhi 110016, India

K. F. Gibson · D. Graham
Centre for Molecular Nanometrology, WestCHEM, Department of
Pure and Applied Chemistry, University of Strathclyde,
Glasgow G1 1XL, UK

M. Canva
Laboratoire Charles Fabry, Institut Optique Graduate School,
Université Paris Sud, CNRS,
91127 Palaiseau, France

T. Vo-Dinh
Department of Chemistry, Duke University,
Durham, NC 27708, USA

J.-F. Masson
Center for Self-Assembled Chemical Structures,
Montreal, QC H3C 3J7, Canada

🍦 Springer

Introduction

The properties of plasmonic materials emerge from the
electromagnetic (EM) field generated by the surface plas-
mon (SP) waves (or polaritons), which are the collective
oscillation of free electrons at the metal/dielectric interface
[1, 2]. Arising from this enhanced EM field, the plasmonic
materials exhibit high sensitivity to refractive index (RI) and
to the presence of molecules at the vicinity of their surface,
which makes them particularly well suited for label-free
optical sensing of bioanalytes [1–4]. In addition, other appli-
cations exploit the excitation of the SP on the metallic
surface to greatly increase the EM field generated for vari-
ous applications in surface-enhanced spectroscopies
(Raman (SERS) [5–7]; fluorescence (MEF) [8, 9]; and in-
frared (SEIRAS) [10, 11]), sub-diffraction limit microscopy
(apertureless near-field scanning optical microscopy
(NSOM)) [12], photothermal treatments [13], and drug de-
livery [14] in biomedicine. The increasing interest in plas-
monic materials underlines the importance of further
understanding and controlling the plasmon effects.

Distinct underlying principles are characteristic of the
size of plasmonic materials: radiative localized SP for
nanomaterials are excited directly by light and explained
by the Mie theory [4], while classical SP resonance for
thin Au films has been explained by the reflectivity of
thin films and the Fresnel equations [15]. The locally
enhanced EM field arising from the generation of SP
polaritons in nanomaterials leads to enhanced detection of
molecular adsorbates in localized SP resonance (LSPR) [16]
or surface-enhanced spectroscopies [17]. The exquisite sen-
sitivity of propagating SPR to RI changes has given rise
to a large market of SPR instrumentation, with major
implications in bioanalysis and biosensing [18]. While
both LSPR and propagating SPR relies on the excitation
of free electrons in metals, they differ in instrumentation
(transmission (or extinction) measurement vs. angle- or
wavelength-scanning instrumentation), excitation mode (di-
rect vs. prism coupling or diffraction), theory (Mie scattering
vs. Bragg resonances or Fresnel equations), and sensitivity
(surface vs. bulk). Understanding the principles of the transi-
tion between localized and propagating SPR will contribute
not only to the development of a new generation of plasmonic
materials with enhanced spectroscopic properties but also to
bridge the gap in knowledge between LSPR and propagating
SPR.

Although for most plasmonic materials the nature of the
SP dictates if excitation is produced by direct illumination or
by prism-coupling, localized SP can be excited in the
Kretschmann configuration with nanostructured substrates
[19, 20]. Both localized and propagating SP can be excited
simultaneously, as previously demonstrated for nanovoids
supported on a metallic film [21], by the extraordinary
transmission of sub-wavelength holes directly excited by
light [22], and with nanoporous membrane excited in total
internal reflection [23]. Of particular interest, nanovoids
feature localized or propagating SP depending on the exci-
tation angle. At a specific excitation angle, a resonance
between these modes can be established (i.e., the localized
SP mode can be coupled to the propagating mode or vice
versa), leading to an enhancement of the SP polariton reso-
nances as demonstrated in Raman spectroscopy [21, 24].
Co-exciting localized and propagating SP improves the
enhancement factor in SERS experiment [25, 26], which
can be achieved by tuning the resonance frequency of the
propagating SP and localized SP to be matched [25]. De-
spite the enhancement demonstrated in Raman spectrosco-
py, plasmonic sensors exploiting the resonance between
localized and propagating SPR modes have not been
demonstrated.

Due to their features in the size regime intermediate to
classical propagating SPR and LSPR substrates, it is antic-
ipated that similar SP modes interactions can be excited in
SPR with micro-patterned substrates, thus combining the
strong sensitivity of localized EM fields with the powerful
analytical properties of propagating SP. Recently, it was
demonstrated that microhole arrays support a propagating
SP with high sensitivity to RI [27, 28], providing solid
evidence to further investigate plasmonic metamaterials.
Microhole arrays are also adapted for use with classical
SPR instruments or with LSPR configuration. Hole arrays
are known substrates for Raman enhancement, and thus,
should be for other SP-coupled spectroscopies.

This paper elucidates that a resonance between a
localized and a propagating SP modes supported on
microhole arrays enhances SPR sensing, which can be
established by tuning the angle of incidence of the light
beam. The interacting SP modes generate localized EM
fields observed in SERS. The resonant interaction be-
tween the localized and propagating SP modes generates
a highly sensitive SPR response at specific experimental
conditions (λ_{SPR}, θ_{exc}, and η). This enhanced sensitivity
is applicable to biosensing while preserving the integrity
of the current continuous thin film-based SPR method.
A better understanding of the distinct micro-plasmonic
properties cannot only improve SPR biosensors but also
lead to broader applications based on a novel class of
materials.

169

Angle-dependent resonance of localized and propagating SP

Materials and methods

SP resonance and Raman microscopy measurements on microhole arrays

The method for the fabrication and characterization of the microhole arrays was adapted from previous reports [27, 29, 30], and is explained in details in supporting information. Briefly, microhole arrays were prepared using a modified nanosphere lithography (NSL) method, where the periodicity is controlled by the initial diameter of the microsphere and the diameter of the hole depends on the duration of the etching process. A gold film of about 65-nm thickness was sputtered on the NSL mask, which was then removed by sonication to create the microhole array. SPR measurements were performed on an angulo-spectral instrument from 400 to 900 nm and with angles ranging from 70° to 77° (details in supporting information).

Raman microscopy measurements were performed at 633 nm laser excitation with a ×100 dry objective, which provides near-diffraction limited spatial resolution (details in supporting information). The white light images of the microhole arrays were performed with the same experimental setup as for the Raman microscopy by replacing the laser source with a broadband white light. A monolayer of 4-nitrobenzenethiol was formed on the microhole arrays to image the distribution of the electric field on the microhole arrays.

Enhanced biosensing with microhole arrays was demonstrated with the detection of IgG with a substrate functionalized with anti-IgG (details in supporting information), in comparison to the response from a thin Au film of 50-nm thickness. Angle-resolved multi-wavelengths SPR response of the immobilization of anti-IgG and the detection of IgG at various excitation angles optimized the response of microhole arrays. Thus, real-time kinetic measurements of the IgG detection were performed at 72.6° for microhole arrays of (65 ± 10) nm depth, with at least four identically prepared substrates. The IgG biodetection was performed for concentrations of 0.1, 1, 10, 100, and 1,000 nM in phosphate-buffered saline (PBS) solution.

RCWA simulations

3-D rigorous coupled-wave analysis (RCWA) calculations [31, 32] of reflectance from the microhole array structures were carried out using DiffractMOD 3.1 software. In the RCWA calculations carried out for the microhole array structures, TM-polarized plane waves (at different wavelengths and angles of incidence) were incident on the hexagonal array of microholes in a thin gold film and the reflectance calculated as a function of the incident angle or wavelength. In the simulations, the thickness of the gold films was modeled at

70 nm—the gold films being deposited on a 1-nm thick chromium adhesion layer which is deposited on BK7 glass substrates having RI of ~1.517. Other experimental details are provided in supporting information.

Results and discussion

Metamaterials with features of a length scale greater than the incident wavelengths of light and shorter than the propagation distance of the SP polariton in a continuous Au film (typically greater than 10 μm) [2] are not well understood. These metamaterials are also characterized by a length scale that is explained by neither SP theories. Thus, the plasmonic properties of metamaterials need to be defined, for which enhanced sensitivity was observed with microhole arrays. This can enable the design of microhole array based plasmonic substrates with optimal enhanced sensitivity.

To answer this important question about the plasmonic properties of metamaterials, a modified SPR instrument in the Kretschmann configuration is well suited for understanding the SP interactions involved in sensitivity enhancement of microhole arrays compared with conventional continuous films. A polychromatic light source allows an angle-scanning SPR instrument to record dispersion curves with experimental boundaries of 450–950 nm and excitation angles at the substrate plane of 70–77° (for details, Fig. S1 in the Electronic supplementary material (ESM)). Thus, the influence of experimental parameters (λ_{SPR}, θ_{exc}, and η) on the plasmonic properties of microhole arrays can be systematically investigated. Here, we focus on microhole arrays of 3.2-μm periodicity with hole diameter of 1.8 (±0.2) μm and a depth of 65 (±10) nm fabricated on a BK7 glass substrate (SEM image of the microhole arrays is provided in Fig. S2 in the ESM). The influence of experimental parameters on the plasmonic and analytical properties of microhole arrays was established, and potential biosensing applications of microhole arrays were explored.

Localized and propagating SP waves in microhole arrays

The SPR dispersion relation well characterizes the plasmonic properties of materials. The SPR dispersion relation refers to the momentum matching conditions of the SP polaritons for several excitation angle and wavelength couples. In continuous films, the influence of the excitation angle from 70° to 77° in water ($\eta=1.333$ RIU) on the minimum intensity in the SPR spectra, attributed to the excitation of a propagating SP, is clearly observed in the SPR dispersion relation (Fig. 1, left). The momentum-matching conditions of light and SP are met around $\lambda=600$ nm for excitation angles near 77° and λ increases as θ_{exc} decreases from 77° to 70° (dashed line). This

170

Fig. 1 SPR dispersion in water environment (RI=1.333 RIU) of continuous films and microhole arrays. *Left*, propagating SP mode (*dashed line*) is present on continuous films, while 65 nm depth microhole arrays (*right*) present localized SP (*dotted line*) and propagating SP modes
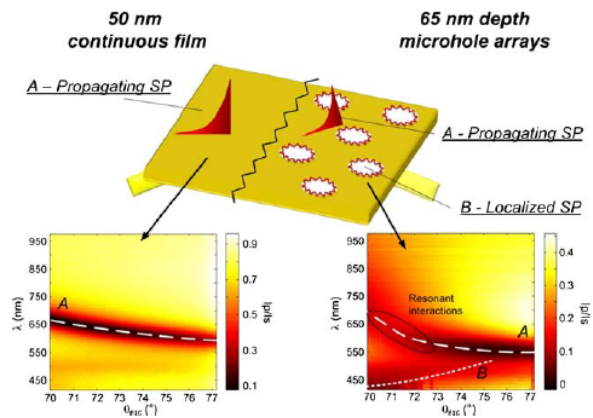
strong dependence of the excitation wavelength with respect to the angle of the incident beam of light characterizes propagating SP.

The dispersion relation of microhole arrays revealed that a propagating SP is excited in these metamaterials (Fig. 1, right). The propagating SP of microhole arrays is blue-shifted by about 50 nm in comparison to the one observed for a continuous film in the θ_{exc} range of 73° to 77° (Fig. S3 in the ESM). The symmetry of the response between microhole arrays and continuous films is broken for $\theta_{exc}<73°$. The angular sensitivity of the propagating SP of microhole arrays exceeds the one of continuous films, such that microhole arrays are resonant at wavelengths greater than continuous films at 70°. The divergence between the response of microhole arrays and continuous films demonstrates particular properties of microhole arrays that may be at the origin of their enhanced sensitivity.

In addition, microhole arrays exhibit a second plasmonic band that is resonant at around $\lambda=500$ nm and is observed for $\theta_{exc}<75°$ (Fig. 1, right dotted line). The weak sensitivity of this plasmonic band at higher energy (or shorter wavelength) to the excitation angle is characteristic of localized SPR supported by nanoparticles [33, 34]. Thus, at $\theta_{exc}<75°$, localized and propagating SP modes are co-excited in microhole arrays.

This result clearly indicates that microhole arrays can support simultaneously a localized and propagating SP for a given set of experimental conditions. The sudden increase of the resonant wavelength of microhole arrays at $\theta_{exc}<73°$ originates from resonant interactions between localized and propagating SP, similar to the one reported for metallic nanovoids [21]. Nanovoids featured resonance between the localized or delocalized SP, which occurs when the excitation angle and wavelength coincide for the propagating and

localized SP modes. Thereby, the resonance led to an enhancement of the SP polariton resonances [21, 35]. In the conditions described in this paper, it is also anticipated that a resonance between the localized and propagating SP can be established, with the consequence of enhanced EM fields in microhole arrays. While the dispersion curve provides solid evidence of the presence of a localized and propagating SPs in microhole arrays, other techniques must be employed to confirm this hypothesis. Hence, SERS imaging should reveal the position of stronger EM field generated by localized SP in microhole arrays.

Concentration of SP waves into holes

SERS imaging is an exquisite tool to observe the localization of EM fields in plasmonic substrates [36, 37]. It has been predicted [38] and experimentally demonstrated [39] that the SP supported by nanohole arrays is confined around the rim of the holes. The presence of high energy localized SP increases the local sensitivity to RI changes [40, 41]. It is anticipated that the zero order excitation of microhole arrays would occur in the near- to mid-IR regions [22, 42] due to the periodicity of microhole arrays. While the lower mode of excitation (such as (1,0), (0,1), and (1,1) of hole arrays) cannot be excited in the visible spectral range for microhole arrays, higher modes of localized SP or grating modes of the microhole arrays are accessible by direct illumination. The reflectance spectrum of microhole arrays measured under a ×100 objective shows the presence of SPR modes between 500 and 800 nm (Fig. S4 in the ESM). These modes can be excited in SERS imaging experiments to reveal the presence of an increased localized EM field [43].

SERS imaging provides information on the enhanced SP location on microhole arrays as regions of high Raman

171

intensity are correlated to the highest EM field [43]. A reference image can be collected from the laser line scattering. This technique is possible with microhole arrays since these are much larger than the diffraction limit resolution of Raman microscopes. Thus, a monolayer of 4-nitrobenzenethiol (4-NBT) was formed at the surface of microhole arrays and a SERS image of the 1,573 cm^{-1} vibration (C-C vibration) was collected for 632.8 nm laser excitation (A SERS spectrum for 4-NBT on microhole arrays is provided in Fig. S5 in the ESM). The Raman images show evidence of a localized SP, with donut-shaped regions of high field intensity (Fig. 2), similar to the previously reported experimental images and prediction by numerical simulations for nanohole arrays [43, 44]. The Raman images are reported for non-background corrected images of the integrated intensity area of the vibrational band at 1,571 cm^{-1}. The reflectance image of the laser produces a high-resolution reference image of the microhole substrate. The superimposition of the SERS and reflectance image ($S+R$) from the same region clearly indicates the position of a localized EM field into the microholes. The close correlation of the FDTD and experimental images reported by Correia-Ledo et al. strongly support that the enhanced EM field around the rim of the hole is accurately measured and not the result of roughness from the rim of the hole. The results reported here are in agreement with the FDTD and Raman images obtained for nanohole arrays of 1,500 nm periodicity and a D/P ratio of 0.6 [43].

The comparison of the SERS intensity on the rim of microhole arrays (region of highest intensity) and the terrace reveals a significant amplification of the SERS signal of 4-NBT (Fig. S5 in the ESM) at the rim of the microhole. No SERS signal was observed on the terrace, while the characteristic bands of 4-NBT were observed with a signal to noise

ratio of about 10 at the rim of the microhole (Fig. S5 in the ESM). The low intensity observed for microhole arrays can be attributed in part, to the direct excitation being a relatively weaker phenomenon in microhole arrays than for triangular nanoparticles or sub-wavelength gratings where the Raman signal is amplified in the order of 100–1,000 times [45, 46]. In addition, the resonance between localized and propagating SP delocalizes the energy between the terrace and the rim of the microholes. Nanohole arrays with smaller periodicity would improve the enhancement factor of SERS on this substrate. Otherwise, plasmon coupling with labeled Au NP would also provide further enhancement of the SERS response on microhole arrays. While microhole arrays shall not be regarded as superior SERS substrate, it provides excellent SPR sensitivity and better SERS than thin Au films. Therefore, it is anticipated that both the exquisite surface sensitivity of localized SPR and the excellent analytical properties of propagating SPR can be obtained in the microhole array sensor by establishing a resonance between both plasmonic modes.

Imaging the SP in reflectance spectroscopy with near diffraction-limited optics provide a clear picture of the plasmonic properties with exquisite spatial resolution (Fig. 3). As expected, the SPR spectra on the terrace and holes differ mainly by the intensity of the reflected light (Fig. S4 in the ESM). In addition, monitoring the position of the SP band of the minimum near 630 nm reveals that the SPR band redshifts inside the hole by 1–2 nm (Fig. S6 in the ESM). Imaging the position of this plasmonic band provides a startling picture of the variation of the excitation wavelength of the plasmon band on the terrace and in the hole of the microhole arrays (Fig. 3, right). These reflectance images of the SP, the SERS images, and the previously published FDTD data [43] reveal that the microhole are the location of enhanced EM fields and slight shifts in SP excitation wavelength.
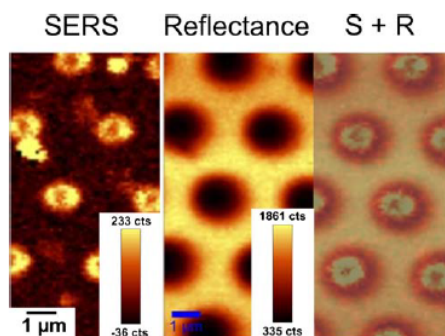
Influence of the dielectric medium on the RI sensitivity

As demonstrated, the presence of microholes in thin films allows simultaneous excitation of localized and propagating SP modes, which interact resonantly at specific experimental conditions. In addition to the angle and the wavelength of light entering resonance, the RI of the solution also changes the momentum-matching conditions of the SP. The calibration curves of microhole arrays excited in the Kretschmann configuration of SPR reveal regions of anomalous SPR dispersion relation at different θ_{exc} (Fig. 4). The SPR wavelength of continuous films monotonously increases with the RI from 1.33 to 1.37 RIU. However, the excitation wavelength of microhole arrays diverges from the one of continuous films within a specific range of RI.

Microhole arrays exhibit regions of sensitivity equivalent to continuous films (regions A and C in Fig. 4) and a region

SERS   Reflectance   S + R

233 cts   1861 cts

1 µm   -36 cts   1 µm   335 cts

Fig. 2 Surface-enhanced Raman scattering (*SERS*) imaging of the microhole arrays highlighting the enhanced EM field into the holes. A reference image in reflectance was collected simultaneously to the SERS image from the 632.8 nm laser scattering. Parameters, ×100, NA=0.9 microscope objective−cone angle of 65°
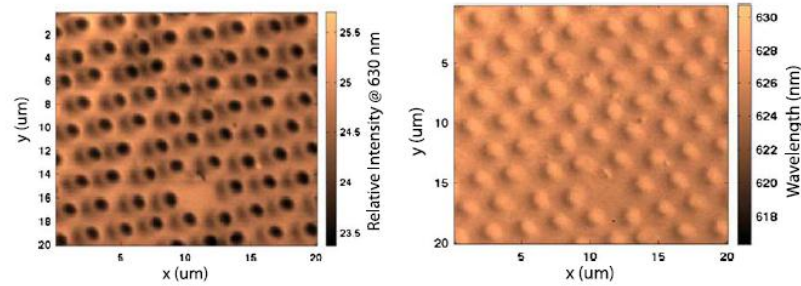
172

Fig. 3 *Left,* the *white light* reflectance image of the microhole arrays for the spectral region near 630 nm correlates with the laser reflectance image in SERS. *Right,* the image of the minimum wavelength in the reflectance spectrum shows a shift in the plasmon excitation wavelength for the location of the microholes. Parameters, ×100, NA=0.9 microscope objective−cone angle of 65°

covering approximately 10 mRIU of enhanced sensitivity (region B of Fig. 4). It is important to note that the region of enhanced sensitivity is expected when the resonant conditions between the localized and propagating SP are met (which are governed by the physical aspect of the microhole arrays, excitation wavelength and RI of the solution). This clearly demonstrates that the impact of enhanced EM field is emerging from this resonance and leads to increased sensitivity in SPR.

The region of enhanced sensitivity changes with the excitation angle and the RI of the solution. For example, enhanced sensitivity was observed for solutions of 1.335 to 1.345 RIU interrogated at an excitation angle of 70.6°, while the region of enhanced sensitivity shifts by 5 mRIU for an increase of 1.3° of θ_{exc} (Fig. 4). This influence of several experimental parameters on the enhanced sensitivity may raise the question about linearity of the SPR sensors based on microhole arrays. To answer this question, a closer look at the range of refractive indices comprised between 1.334 and 1.344 RIU highlights the greater sensitivity of microhole arrays and linearity of the SPR response ($\Delta\lambda_{SPR}$) for both plasmonic materials (Fig. 4, right). In the 10-mRIU range investigated, the sensitivity of

microhole arrays is greater by more than two times the sensitivity of continuous films, while microhole arrays exhibit a similar linearity in comparison to continuous Au films, shown by the similar correlation coefficient (R^2). As demonstrated below, a 10-mRIU range is sufficient for biosensing applications. Generally, the range of $\Delta\lambda_{SPR}$ observed in the course of a biosensing experiment is on the order of 10–20 nm for experiments. Microhole arrays were linear for at least $\Delta\lambda_{SPR}$=80 nm. Hence, the linearity of the SPR response with microhole arrays substrate is suited for biosensing applications. A small difference in the response of microhole arrays as compared with continuous films is a weaker and slightly broader absorption band, which can be attributed to the scattering of photons in the microhole array substrate (Fig. S7 in the ESM).

In order to identify the optimal resonant conditions for a set of RI and excitation angles, the SPR response was measured at every 10-mRIU step between 1.33 and 1.36 RIU. The enhanced SPR sensitivity to RI change of the dielectric environment of microhole arrays was quantified by a ratio of $\Delta\lambda_{SPR}$ with microhole arrays divided by $\Delta\lambda_{SPR}$ observed for continuous films (amplification factor dielectric (AFd)) (Fig. 5, left).
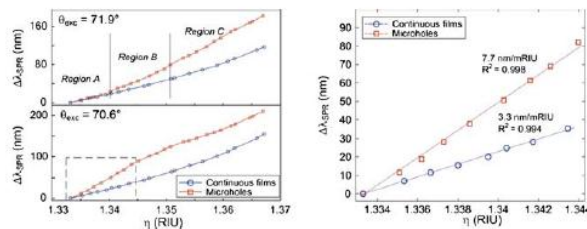
Fig. 4 Microhole arrays (*red line*) and continuous films (*blue line*) calibration curves at two different excitation angles. *Left,* various SP response range (regions A, B, and C) highlighting the non-linear response of structured samples over the complete RI range studied. *Right,* a focus on a 10-mRIU range (θ_{exc}=70.6°, *dashed line*) shows the sensitivity enhancement of microhole arrays and comparable linearity to continuous films

Angle-dependent resonance of localized and propagating SP

Fig. 5 *Left*, quantification of the improvement in SPR response for microhole arrays. A greater sensitivity was observed in comparison to continuous films at multiple θ_{exc} ($n<4$ samples) for different RI ranges. *Right*, SPR response of microhole arrays simulated by RCWA for 10-mRIU steps
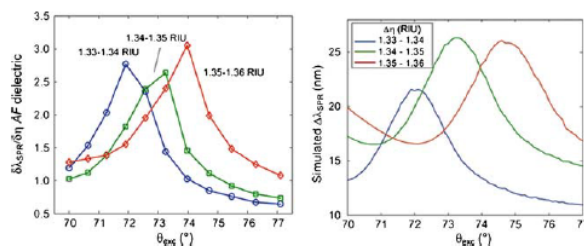
As observed, the optimal excitation angle increases with RI Interestingly, the AFd remained constant at around 3 for the various sets of experimental conditions. In addition, the range of excitation angles for which the AFd is about 3 is generally tolerant to variations of ±0.5°. Thus, this relaxes any constraint of highly accurate angle precision that would be required on SPR instruments using the microhole arrays. This result signifies that different excitation angles will be optimal for different biological media (Fig. S8 in the ESM).

As expected, λ_{SPR} at which the resonance between the localized and propagating SP is established remained constant for different refractive indices of the solution. It is observed that the optimal propagating λ_{SPR} is redshifted by approximately 100 nm in comparison to the localized SP. The independence of the excitation wavelength for enhanced SPR is a consequence of the requirement of using a wavelength that excites both the localized and propagating SPs to achieve the enhanced plasmonic properties. This observation further supports the evidence of the resonance between localized and propagating SP leading to enhanced sensitivity.

The properties of microhole arrays are captured by RCWA, as RCWA considers the diffraction of the electric fields at the surface of microhole arrays and propagating SPs. RCWA simulations revealed a similar enhanced $\Delta\lambda_{SPR}$, which was dependent on the excitation angle and RI of the solution (Fig. 5, right). We observed that RCWA predicts a slightly weaker $\Delta\lambda_{SPR}$ than observed experimentally. In addition, a small variation of the optimal excitation angle, at specific refractive indices emerged from the simulations in comparison to the experimental data. This small discrepancy is attributed to the orientation of the microhole array lattice (rotational angle φ) with respect to the incident photon beam, and therefore the existence of different directions of propagation of SPs in the microhole array. The SP modes excited on the microstructure are significantly affected by the lattice orientation as demonstrated in metallic nanovoids [21]. Simulations capturing the different φ must be undertaken with synthetic microhole arrays prepared with lithographic techniques, which is not the object of the present work. Thus, the optical properties measured here were an average of multiple φ orientations, as the lattice orientation cannot be controlled with microhole arrays prepared by modified nanosphere lithography. It is thus important to mention that the RCWA simulations were performed considering φ at 0°. Nonetheless, RCWA simulations are valuable to estimate resonant SP mode conditions at specific excitation angles and RI.

As previously mentioned, exploitation of the enhanced SPR sensitivity of microhole arrays does not require instrumentation with great excitation angle accuracy, as the resonant SP modes conditions are observed within a range of about 1°. RCWA further exemplifies this property of microhole arrays. For example, a variation of 3 % on $\Delta\lambda_{SPR}$ was calculated with RCWA (Fig. 5, right, blue solid line) for $\Delta\theta_{exc}$ of 1°; simulated for RI around 1.33 to 1.34 RIU corresponding to the resonant conditions. Thus, microhole

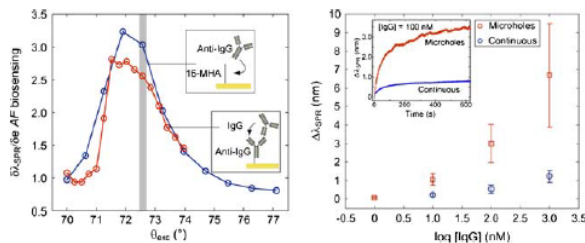Fig. 6 *Left*, angular SPR response characterization sensitivity to local RI changes to the immobilization of anti-IgG for microhole arrays (*blue line*) and biodetection of IgG (*red line*). *Right*, biosensing SPR response of microhole arrays (*red*) and continuous films (*blue*) to various concentration of IgG over 10 min and sensorgram at 100 nM (*inset*). The *error bars* correspond to one standard deviation

174

arrays present a great potential as an enhanced SPR biosensing platform due to the adjustable resonant conditions, the significantly larger SPR shifts observed and the linearity of the SPR signal. Thus, the potential of microhole arrays as a substrate for biosensing assays must be validated with the calibration of a biosensor to detect a specific biomolecule.

Enhanced IgG biosensing

The applicability of the enhanced properties of microhole arrays was evaluated with a biosensor for IgG. Enhanced sensitivity for molecular adsorbate was supported by RCWA simulations, which predicted that the formation of a thin molecular adsorbate would yield enhanced SPR sensing around $\theta_{exc}=71.5°$ (Fig. S9 in the ESM). The simulations were performed for a 1-nm thick layer of a molecular layer having a RI of 1.5. Here, the local RI of the target bonded to the substrate surface is referred as "ε" instead of "η," which define the complete volume probed in the dielectric environment. The RCWA simulations demonstrate that the molecular adsorption processes are also subject to enhanced SPR sensing for a specific excitation angle range.

Experimentally, the $\Delta\lambda_{SPR}$ for the immobilization of 153 nM anti-IgG to the SPR sensor and the biodetection of 100 nM IgG were both enhanced by a factor of nearly 3 with microhole arrays in comparison to continuous Au films (Fig. 6, left). Due to the slow process of acquiring the SPR spectra at each excitation angles, the data in Fig. 6 required measurements calculated from the $\Delta\lambda_{SPR}$ of PBS solution before and after the 10-min kinetic process. The experimental enhancement for the immobilization of anti-IgG and detection of IgG were observed at higher excitation angles than predicted by the simulations (near 72.5°), due to the thicker biological layer formed by anti-IgG and IgG (approximately 5–10 nm) [47], in comparison to the simulation of a 1-nm thick layer. The *AF biosensing* (AFb) of 3 with microhole arrays is as the one previously quantified for the dielectric medium sensitivity (AFd).

Although useful to determine the optimal excitation angle, calibration of the SPR sensor for IgG was required to assess the potential of microhole arrays as a biosensing substrate. Therefore, a calibration curve was established at $\theta_{exc}=72.6°$ (gray line), an angle very close to the one of SPR using a dove prism (72.8°) (Fig. 5, right) [48]. The sensorgrams for the detection of 100 nM of IgG with microhole arrays (top trace) and continuous films (lower trace) show the greater response generated of microhole arrays (inset). Moreover, microhole arrays revealed a limit of detection (concentration corresponding to three times the noise on a blank sensorgram) an order of magnitude better than continuous film. The constant AFb of 5.7±0.4 for sensing 10 nM to 1 μM implies that the SPR response of microhole arrays was co-linear with the one of continuous films substrates. Thereby, enhanced biosensing based on microhole arrays was demonstrated. The SPR response of IgG concentration was

increasing to concentrations up to 1,000 nM. The non-linearity of the calibration curve is predicted by the Langmuir isotherm. In addition, the AFb observed with microhole arrays is comparable to the ones reported for other nanostructured films [49]. The larger error on the measurements with microhole arrays in comparison to thin Au film is due to the fabrication process with nanosphere lithography, which is not perfectly reproducible. We recently observed that by regenerating a single microhole substrate, the error on multiple measurements of IgG becomes less than 5 %. Improving the reproducibility of the fabrication method will significantly improve the error on the measurement. Thus, microhole arrays are suitable as an enhanced SPR biosensing substrate.

Conclusions

Plasmonic metamaterials present unique optical properties with a tremendous potential to improve current SPR sensing based on continuous films. By establishing the resonance between the localized and propagating SP modes supported by microhole arrays, the sensitivity was enhanced by a factor of 3 to five times compared with continuous films, which lead to an order of magnitude lower detection limit of IgG biodetection. The presence of localized SPs is characterized by regions of higher EM fields on the substrate in SERS imaging, thus indicating the potential of such plasmonic material for surface-enhanced spectroscopy. Enhancements were observed for bulk sensitivity measurements as well as sensitivity to molecular adsorption processes, making microhole arrays a substrate of interest to enhance the performance of SPR sensors.

References

1. Homola J (2003) Present and future of surface plasmon resonance biosensors. Anal Bioanal Chem 377(3):528–539. doi:10.1007/s00216-003-2101-0
2. Homola J, Yee SS, Gauglitz G (1999) Surface plasmon resonance sensors: review. Sens Actuators B 54(1–2):3–15
3. Haes AJ, Van Duyne RP (2002) A nanoscale optical biosensor: Sensitivity and selectivity of an approach based on the localized surface plasmon resonance spectroscopy of triangular silver nanoparticles. J Am Chem Soc 124(35):10596–10604. doi:10.1021/ja020393x
4. Jain PK, El-Sayed IH, El-Sayed MA (2007) Au nanoparticles target cancer. Nano Today 2(1):18–29
5. Fan MK, Andrade GFS, Brolo AG (2011) A review on the fabrication of substrates for surface enhanced Raman spectroscopy and their applications in analytical chemistry. Anal Chim Acta 693(1–2):7–25. doi:10.1016/j.aca.2011.03.002
6. Vo-Dinh T, Wang HN, Scaffidi J (2010) Plasmonic nanoprobes for SERS biosensing and bioimaging. J Biophotonics 3(1–2):89–102. doi:10.1002/jbio.200910015
7. Tripp RA, Dluhy RA, Zhao YP (2008) Novel nanostructures for SERS biosensing. Nano Today 3(3–4):31–37

175

Angle-dependent resonance of localized and propagating SP

8. Aslan K, Gryczynski I, Malicka J, Matveeva E, Lakowicz JR, Geddes CD (2005) Metal-enhanced fluorescence: an emerging tool in biotechnology. Curr Opin Biotechnol 16(1):55–62. doi:10.1016/j.copbio.2005.01.001

9. Lakowicz JR (2001) Radiative decay engineering: Biophysical and biomedical applications. Anal Biochem 298(1):1–24. doi:10.1006/abio.2001.5377

10. Lal S, Grady NK, Kundu J, Levin CS, Lassiter JB, Halas NJ (2008) Tailoring plasmonic substrates for surface enhanced spectroscopies. Chem Soc Rev 37(5):898–911. doi:10.1039/b705969h

11. Osawa M (2001) Surface-enhanced infrared absorption. In: Kawata S (ed) Near-field optics and surface plasmon polaritons. Topics in applied physics, vol 81. Springer, Berlin, pp 163–187

12. Reilly TH, van de Lagemaat J, Tenent RC, Morfa AJ, Rowlen KL (2008) Surface-plasmon enhanced transparent electrodes in organic photovoltaics. Appl Phys Lett 92 (24). doi:10.1063/1.2938089

13. Cobley CM, Chen J, Cho EC, Wang LV, Xia Y (2011) Gold nanostructures: a class of multifunctional materials for biomedical applications. Chem Soc Rev 40(1):44–56

14. Yavuz MS, Cheng Y, Chen J, Cobley CM, Zhang Q, Rycenga M, Xie J, Kim C, Song KH, Schwartz AG, Wang LV, Xia Y (2009) Gold nanocages covered by smart polymers for controlled release with near-infrared light. Nat Mater 8(12):935–939, http://www.nature.com/nmat/journal/v8/n12/suppinfo/nmat2564_S1.html

15. Knoll W (1998) Interfaces and thin films as seen by bound electromagnetic waves. Annu Rev Phys Chem 49(1):569–638. doi:10.1146/annurev.physchem.49.1.569

16. McFarland AD, Van Duyne RP (2003) Single silver nanoparticles as real-time optical sensors with zeptomole sensitivity. Nano Lett 3 (8):1057–1062. doi:10.1021/nl034372s

17. Bantz KC, Meyer AF, Wittenberg NJ, Im H, Kurtulus O, Lee SH, Lindquist NC, Oh SH, Haynes CL (2011) Recent progress in SERS biosensing. Phys Chem Chem Phys 13(24):11551–11567. doi:10.1039/c0cp01841d

18. Schasfoort RBM, Tudos AJ (2008) Handbook of surface plasmon resonance. The Royal Society of Chemistry, Cambridge

19. Byun KM, Jang SM, Kim SJ, Kim D (2009) Effect of target localization on the sensitivity of a localized surface plasmon resonance biosensor based on subwavelength metallic nanostructures. J Opt Soc Am a-Opt Image Sci Vis 26(4):1027–1034

20. Kim SA, Byun KM, Kim K, Jang SM, Ma K, Oh Y, Kim D, Kim SG, Shuler ML, Kim SJ (2010) Surface-enhanced localized surface plasmon resonance biosensing of avian influenza DNA hybridization using subwavelength metallic nanoarrays. Nanotechnology 21 (35). doi:10.1088/0957-4484/21/35/355503

21. Kelf TA, Sugawara Y, Cole RM, Baumberg JJ, Abdelsalam ME, Cintra S, Mahajan S, Russell AE, Bartlett PN (2006) Localized and delocalized plasmons in metallic nanovoids. Physical Review B 74 (24)

22. Coe JV, Heer JM, Teeters-Kennedy S, Tian H, Rodriguez KR (2008) Extraordinary transmission of metal films with arrays of subwavelength holes. Annu Rev Phys Chem 59(1):179–202. doi:10.1146/annurev.physchem.59.032607.093703

23. Yu F, Ahl S, Caminade A-M, Majoral J-P, Knoll W, Erlebacher J (2006) Simultaneous excitation of propagating and localized surface plasmon resonance in nanoporous gold membranes. Anal Chem 78(20):7346–7350. doi:10.1021/ac060829h

24. Baumberg JJ, Kelf TA, Sugawara Y, Cintra S, Abdelsalam ME, Bartlett PN, Russell AE (2005) Angle-resolved surface-enhanced Raman scattering on metallic nanostructured plasmonic crystals. Nano Lett 5(11):2262–2267. doi:10.1021/nl051618f

25. Du L, Zhang X, Mei T, Yuan X (2010) Localized surface plasmons, surface plasmon polaritons, and their coupling in 2D metallic array for SERS. Opt Express 18(3):1959–1965

26. Liu Y, Xu S, Li H, Jian X, Xu W (2011) Localized and propagating surface plasmon co-enhanced Raman spectroscopy based on evanescent field excitation. Chem Commun (Camb) 47(13):3784–3786. doi:10.1039/c0cc04988c

27. Live LS, Masson JF (2009) High sensitivity of plasmonic microstructures near the transition from short-range to propagating surface plasmon. J Phys Chem C 113(23):10052–10060. doi:10.1021/jp9020273

28. Live LS, Murray-Methot MP, Masson JF (2009) Localized and propagating surface plasmons in gold particles of near-micron size. J Phys Chem C 113(1):40–44. doi:10.1021/jp8104419

29. Live LS, Bolduc OR, Masson JF (2010) Propagating surface plasmon resonance on microhole arrays. Anal Chem 82(9):3780–3787. doi:10.1021/ac100177j

30. Live LS, Masson JF (2010) High sensitivity of SPR with microplasmonic structures. Plasmonics in Biology and Medicine Vii 7577. doi:10.1117/12.840745

31. Dhawan A, Canva M, Vo-Dinh T (2011) Narrow groove plasmonic nano-gratings for surface plasmon resonance sensing. Opt Express 19(2):787–813

32. Moharam MG, Gaylord TK (1983) Three-dimensional vector coupled-wave analysis of planar-grating diffraction. J Opt Soc Am 73(9):1105–1112

33. Willets KA, Van Duyne RP (2007) Localized surface plasmon resonance spectroscopy and sensing. Annu Rev Phys Chem 58:267–297. doi:10.1146/annurev.physchem.58.032806.104607

34. Halas NJ, Lal S, Chang W-S, Link S, Nordlander P (2011) Plasmons in strongly coupled metallic nanostructures. Chem Rev (Wash) 111(6):3913–3961. doi:10.1021/cr200061k

35. Teperik TV, Popov VV, de Abajo FJG, Abdelsalam M, Bartlett PN, Kelf TA, Sugawara Y, Baumberg JJ (2006) Strong coupling of light to flat metals via a buried nanovoid lattice: the interplay of localized and free plasmons. Opt Express 14(5):1965–1972. doi:10.1364/oe.14.001965

36. Galarreta BC, Rupar I, Young A, Lagugnee-Labarthet F (2011) Mapping hot-spots in hexagonal arrays of metallic nanotriangles with azobenzene polymer thin films. J Phys Chem C:null–null. doi:10.1021/jp204402f

37. Qin LD, Zou SL, Xue C, Atkinson A, Schatz GC, Mirkin CA (2006) Designing, fabricating, and imaging Raman hot spots. Proc Natl Acad Sci U S A 103(36):13300–13303. doi:10.1073/pnas.0605889103

38. Stewart ME, Mack NH, Malyarchuk V, Soares J, Lee TW, Gray SK, Nuzzo RG, Rogers JA (2006) Quantitative multispectral biosensing and 1D imaging using quasi-3D plasmonic crystals. Proc Natl Acad Sci U S A 103(46):17143–17148. doi:10.1073/pnas.0606216103

39. Gibson KF, Correia-Ledo D, Couture M, Graham D, Masson JF (2011) Correlated AFM and SERS imaging of the transition from nanotriangle to nanohole arrays. Chem Commun (Camb) 47 (12):3404–3406. doi:10.1039/c0cc05287f

40. Gordon R, Sinton D, Kavanagh KL, Brolo AG (2008) A new generation of sensors based on extraordinary optical transmission. Acc Chem Res 41(8):1049–1057. doi:10.1021/ar800074d

41. Kwak ES, Henzie J, Chang SH, Gray SK, Schatz GC, Odom TW (2005) Surface plasmon standing waves in large-area subwavelength hole arrays. Nano Lett 5(10):1963–1967. doi:10.1021/nl051339s

42. Teeters-Kennedy S, Williams SM, Rodriguez KR, Cilwa K, Meleason D, Sudnitsyn A, Hrovat F, Coe JV (2006) Extraordinary infrared transmission of a stack of two metal micromeshes. J Phys Chem C 111(1):124–130. doi:10.1021/jp063745l

43. Correia-Ledo D, Gibson KF, Dhawan A, Couture M, Vo-Dinh T, Graham D, Masson J-F (2012) Assessing the location of surface plasmons over nanotriangle and nanohole arrays of different size and periodicity. J Phys Chem C 116(12):6884–6892. doi:10.1021/jp3009018

44. Lee SH, Bantz KC, Lindquist NC, Oh S-H, Haynes CL (2009) Self-assembled plasmonic nanohole arrays. Langmuir 25(23):13685–13693. doi:10.1021/la9020614

45. Hou Y, Xu J, Li W, Wang X (2011) Coupled subwavelength gratings for surface-enhanced Raman spectroscopy. Phys Chem Chem Phys 13(23):10946–10951

46. McFarland AD, Young MA, Dieringer JA, Van Duyne RP (2005) Wavelength-scanned surface-enhanced raman excitation spectroscopy. J Phys Chem B 109(22):11279–11285. doi:10.1021/jp050508u

47. Zhang J, Lakowicz JR (2007) Metal-enhanced fluorescence of an organic fluorophore using gold particles. Opt Express 15(5):2598–2606. doi:10.1364/oe.15.002598

48. Bolduc OR, Live LS, Masson JF (2009) High-resolution surface plasmon resonance sensors based on a dove prism. Talanta 77(5):1680–1687. doi:10.1016/j.talanta.2008.10.006

49. Hoa XD, Kirk AG, Tabrizian M (2009) Enhanced SPR response from patterned immobilization of surface bioreceptors on nano-gratings. Biosens Bioelectron 24(10):3043–3048. doi:10.1016/j.bios.2009.03.021

177